PHYSICAL AND NUMERICAL MODELLING OF GROUTED NAILS IN CLAY

by

Jonathan David Morris

A thesis submitted for the Degree

of Doctor of Philosophy at the

University of Oxford

Magdalen College

Hilary Term, 1999

PHYSICAL AND NUMERICAL MODELLING OF GROUTED NAILS IN CLAY

J.D. Morris
Magdalen College, University of Oxford

A thesis submitted for the Degree of Doctor of Philosophy
Hilary Term, 1999

ABSTRACT

The research described in this thesis focussed on the bond resistance of grouted soil nails in clay. Physical modelling took the form of large scale element tests in the laboratory of drilled and grouted nails in a stiff clay. Nails were installed under different boundary stresses; testing was conducted at different constant rates of pull-out and also under sustained load conditions. Observed behaviour was compared with that predicted by measurements of interface shear resistance obtained in a conventional shear box.

Numerical modelling was carried out in an attempt to improve understanding of the effects of installation processes on nail performance, and to investigate the trends in behaviour observed during the laboratory tests. For this purpose, a one-dimensional finite element computer program was developed to include the effects of consolidation and the out-of-plane soil displacements associated with nail axial loading.

The physical modelling showed that the loading rate has a significant effect on bond resistance. This has consequences for the interpretation of data from constant rate of displacement pull-out testing, the conventional method of verifying bond resistance in the field. It is suggested that this type of testing is inappropriate in low permeability soils, because capillary suctions develop which lead to increased bond resistance. Results from laboratory sustained load tests show that lower values of bond resistance are mobilised under the static load conditions more likely to exist in a real soil nailed structure.

The numerical modelling confirms the behaviour observed during the laboratory tests, and shows that the mechanisms by which bond is mobilised are complex, depending critically on the dilation and consolidation characteristics of the soil. Nail installation procedures are modelled, and grout pressures are shown to strongly influence bond resistance.

Interface tests show trends in behaviour similar to those observed during pull-out testing. However, difficulties exist in the qualitative use of interface test data to predict nail bond resistance.

Acknowledgements

I would like to express sincere thanks to my present employers Kvaerner Cementation Foundations for their financial support over the last three years. In particular, I would like to thank Dr David Greenwood, who was instrumental in organising the sponsorship agreement, and was also the source of much encouragement. Thanks are also extended to the current members of the technical department, and in particular to Mr Rab Fernie, Dr Martin Pedley and Mr Tony Suckling for their useful comments and support over the last two months.

I am in the debt of many people in the Engineering Department at Oxford. First and foremost, I would like to express my sincere gratitude to my supervisors Dr Harvey Burd and Dr George Milligan (now of GCG in London). Their guidance and patience has been invaluable, and is greatly appreciated. I would also like to thank Professor Guy Houlsby for his advice and encouragement in all areas, and particularly in relation to the finite element work.

Other people at Oxford whom I would particularly like to thank are: Clive, Bob, Chris, Maurice, Ken and John H. for their help with the apparatus and other matters; Gwyn for proof reading the manuscript; Neil for asking awkward questions; Scott for Keble lunches; Charles for Friday beers; Nic for always being helpful; and Ramon for much needed escapes from Oxford in the summer months.

Finally, I would like to thank Freya, my family and my friends for all the support they have given me over the last three years. Without you all, I would never have got this finished.

CONTENTS

Chapter 1. INTRODUCTION AND LITERATURE REVIEW

1.1. Introduction

The technique of soil nailing is established in many countries throughout the world as a method of stabilising cut and natural slopes in a variety of ground conditions. It is a versatile and cost-effective alternative to more traditional methods when the ground displacements inherent to the passive action of soil nails are tolerable. Although many methods of design for the construction of soil nailed slopes have been successfully employed, a major area of uncertainty remains in the assessment of resistance to pull-out of the soil nail from the passive zone.

Methods of determining the bond resistance of soil nails for design include: analysis of in-situ test data; analysis of laboratory test data; pull-out tests on trial nails; and the use of previously obtained tabulated data correlated to basic soil properties. Theoretical analyses are complex, due to the difficulty of assessing the stress conditions around a nail following the installation process. In all cases, it is generally considered good practice to check nail performance by testing a number of nails on site (preferably extra nails installed specifically for this purpose) once construction has started. However, the loading conditions and rate of pull-out may be very different in a site test to those prevailing in a failing soil-nailed structure.

At present, the use of soil nailing for permanent geotechnical structures is mostly confined to granular soils, soft rocks and low plasticity cohesive soils. Experience of working with these soils has shown that the careful application of suitable design methods leads to few problems in construction and performance of the finished structure (although insufficient time has elapsed to confirm the design lifetime of such structures). Very little use of the technique had been made in clays, where there is concern regarding possible large deformations and low bond stresses. It may prove impossible to deploy nails in bulk deposits of these clays economically, but one of the advantages of the technique is its

applicability to heterogeneous ground conditions. It would be beneficial to understand the nail behaviour in these soils since they are often encountered during construction in otherwise straightforward material.

The research described in this thesis focussed on the bond resistance of grouted soil nails in clay. Physical modelling took the form of large scale element tests in the laboratory of drilled and grouted nails in a medium plasticity clay. Nails were installed under different boundary stresses; testing was conducted at different constant rates of pull-out and also under sustained load conditions. Observed behaviour was compared with that predicted by measurements of interface shear resistance obtained in a conventional shear box. Numerical modelling was carried out in an attempt to improve understanding of the effects of installation processes on nail performance, and to investigate the trends in behaviour observed during the laboratory tests. For this purpose, an existing in-house finite element analysis computer program was modified to include the effects of consolidation and the out-of-plane soil displacements associated with nail axial loading.

This thesis is divided approximately equally between the physical and numerical modelling. The physical modelling is described before the numerical modelling, then the results from both are discussed together towards the end of the thesis.

1.2. Literature review

1.2.1. Bond resistance

A section through a typical soil nailed slope is shown in figure 1.1. Line AB in the figure represents the position of the points of maximum tension in each nail under service loading, and divides the soil into active and passive zones. During construction of the slope, the soil undergoes lateral stress relief, putting the nails into tension. Provided that nails are long and are placed at near horizontal inclinations, the contribution of shear and bending forces in the nails to the overall slope stability at the serviceability limit state (SLS) is negligible, and the nails continue to operate almost entirely in tension. Previous work in the laboratory and the field has confirmed this, Pedley et al. (1990).

Although a nail acts in tension along its entire length, the stress conditions in the soil are very different in the two zones, figure 1.2. In the passive zone, the soil is stable, and the nail is being pulled from the soil towards the slope face. In the active zone, relative movement of soil and nail is in the opposite direction, and the soil can be considered to be flowing past the nail towards the slope face. Generally it is the pull-out capacity of the nails in the passive zone that dictates the overall design. However, in cases where a structural facing to the slope is not provided, sufficient bond capacity in the active zone is essential to prevent failure of the soil near the slope surface, and this should be considered in the design, Barley (1999). In the remainder of this thesis, the terms *bond resistance* or *skin friction* should be taken as meaning the resistance to pull-out of a nail installed in a passive soil mass, expressed in terms of the shear stress acting on the outer surface of the nail grout.

1.2.2. Previous research into pile shaft friction

The geometry of soil nails has much in common with that of piles (and some important differences which are discussed later in this section). In particular, the development of pile shaft friction is similar to the development of soil nail bond resistance in the passive zone. Piles have been used extensively in clay soils, and there is an abundance of published material on shaft friction, where there is little equivalent information available for soil nails. Research on pile shaft friction also started earlier, and results from this research have formed the basis for many later soil nailing design theories. Therefore, work on piles will be discussed first, before moving on to 'dedicated' nailing research.

Early theories linked the shaft friction, τ_s, to the average undrained in-situ shear strength of the clay, s_u, e.g. Skempton (1959):

$$\tau_s = \alpha s_u \qquad (1.)$$

The accumulation of a large amount of field data, and the determination of empirical corrections for specific soil and pile types has meant that this total stress method is still useful in many cases. However, the behaviour of soil is controlled by effective stresses,

and advances were made towards considering the problem in these terms. Chandler (1968) and Burland (1973) sought to relate τ_s to the in-situ horizontal effective stress σ'_h:

$$\tau_s = c' + \sigma'_h \tan\phi'_d \qquad (2.)$$

Failure was assumed to take place within the clay for fully rough piles (concrete, as opposed to steel piles which were considered smooth), but allowance was made for remoulding of the clay close to the shaft surface during installation. Hence ϕ'_d represents the effective friction angle of the remoulded, or 'disturbed' soil. It was suggested that c' (considered as the effective cohesion) should be ignored on account of this remoulding.

The main problem with this approach was that it required an accurate estimate of σ'_h around the pile. The approach of both Chandler and Burland was to assume that σ'_h was directly proportional to the vertical effective stress σ'_v, this being the more accurately determinable effective stress. This led to τ_s being expressed in terms of σ'_v:

$$\tau_s = \beta\sigma'_v \qquad (3.)$$

where $\beta = K \tan\phi'_d$ and K is the ratio of horizontal and vertical effective stresses. Although derived from different assumptions, (3.) was not significantly more useful to designers than (1.) since both equations related τ_s to soil properties measured before construction; neither took any account of changes to these properties caused by pile installation or loading.

The desire to use driven piles for new offshore applications in the late 1970s prompted a large amount of research towards a more fundamental understanding of pile capacity. The behaviour of a pile was seen to depend crucially on its history, which Randolph and Wroth (1982) divided into three main sections: pile installation; consolidation, as excess pore pressures generated during installation dissipate; and pile loading. Attention was focussed on these processes as they related to driven piles, but the same processes are seen to be relevant to the installation of bored piles or soil nails, except that installation includes three further processes: boring; consolidation of the soil during the period between boring and grouting; and grouting.

Randolph and Wroth (1981) compared the behaviour of soil around a pile during loading with that of soil in the simple shear apparatus, figure 1.3. They suggested that the strain path followed by the soil in both cases was similar, and therefore attempted to

predict the shear stress at failure in simple shear, τ_f, from more commonly available material properties. Reasonable agreement was found between experimental data for various normally and lightly overconsolidated clays and the expression:

$$\frac{\tau_f}{(s_u)_{tc}} = \frac{(3-\sin\phi')\cos\phi'}{3} \qquad (4.)$$

Here $(s_u)_{tc}$ is the undrained shear strength measured in triaxial compression. They went on to estimate values of $(s_u)_{tc}$ from overconsolidation ratio (OCR) and the ratio of the critical state parameters κ and λ using the Cam-clay material model. By substituting these values of $(s_u)_{tc}$ into (4.) they once more found broad agreement with experimental data for τ_f at low values of OCR (4 or less), but suggested that the model would overestimate strengths for more heavily overconsolidated soils.

When considering shaft resistance in heavily overconsolidated clay, Randolph and Wroth (1982) stated that allowance should be made for the possibility of slip occurring between the pile and the adjacent soil, a mode of failure not observed during simple shear testing. In this case, they observed that the bond was purely frictional, and suggested that the approach described by Burland (1973) would be more appropriate, expressed in the form:

$$\tau_s = \sigma'_r \tan\delta_{int} \qquad (5.)$$

where δ_{int} is the effective angle of friction between the pile surface and the soil.

Several attempts have been made to model the behaviour of piles in clay experimentally at reduced scale in the laboratory. Three separate studies of this type are described by Steenfelt et al (1981), Chandler and Martins (1982) and Francescon (1983). All of the studies used Speswhite kaolin consolidated from slurry. The method of pile installation described by Chandler and Martins was devised to minimise the disturbance caused to the clay sample, leaving the pile in as close to a 'wished in place' condition as possible. The reason for this being done was that the study was concerned with the fundamental mechanisms of pile shaft friction, and the authors wished to eliminate any possible installation effects. The other studies used jacked piles, and investigations into the effects of installation were seen as important parts of the research. Specifications of the three studies are shown in Table 1.1.

	Steenfelt, Randolph and Wroth (1981)	Chandler and Martins (1982)	Francescon (1983)
Pile installation method	Jacked	Minimal disturbance	Jacked
Pile diameter (*mm*)	19.05	15.0	18.9
Clay sample diameter (*mm*)	300	102	250 (series A) and 850 (series B)
Total boundary stress control	Triaxial	Triaxial	Triaxial (A)and uniaxial (B)
Pile instrumentation	Axial load and pore pressure transducers	Radial stress (1 test only)	Radial stress, axial load and pore pressure transducers
Pile loading rate	0.2 *mm/s*	~0.3 *mm/hr*	0.003 to 0.33 *mm/s*
OCR	1, 2, 8	1, 5	1,2,4,8 (A) 1,2,4.2,8.3,17,50 (B)

Table 1.1 – Specifications of laboratory studies on model piles

Steenfelt et al. (1981) compared the behaviour of model piles installed in clay samples prepared at varying overconsolidation ratios, but at the same final water content. This was done to create samples of nominally the same undrained shear strength, so that the effects of OCR could be studied in isolation. τ_f was found to lie close to $(s_u)_{tc}$ in all cases, i.e. $\alpha \approx 1$, with a tendency of α to increase slightly with OCR. Corresponding β values increased with OCR from 0.2 to 1.15. Unfortunately the instrumentation did not allow measurement of the radial stress acting on the pile, so it was not possible to deduce the local effective stress state.

The study reported by Chandler and Martins (1982) concentrated on the effects of initial stress ratio, *K*, on shaft friction. All the tests were performed at a very low displacement rate, and so were assumed to be fully drained. They found that α increased with *K*, and recorded a higher bond strength, but lower α value for one test at OCR = 5. Measurements of radial stress at the pile face during loading were made during one test, and showed a reduction of 15% at peak load, followed by an increase and then another decrease towards the end of the test. The stress was observed to remain within approximately 85 to 100% of the initial value at all times during the test.

The ratio of peak to residual pile load was found to be approximately the same for all tests. Considering this result along with the radial stress measurements, and assuming that the final shear stress corresponded to residual conditions for which a value of $\phi'_r = 11.5°$ had been measured in ring shear, they concluded that the angle of friction at the pile-soil interface, δ_{int}, was independent of K and equal to approximately 22°. This value compared closely to $\phi' = 23°$ measured for kaolin in triaxial compression.

Examination of thin sections taken from the pile-soil interface at the end of tests revealed a narrow (~0.01*mm* thick) continuous cylindrical displacement discontinuity within the soil approximately 0.5*mm* from the pile surface, along which clay particles were strongly oriented. This confirmed that residual conditions were reached at large displacements. The piles were 'grouted' in place using epoxy resin, which clearly created a sufficiently rough pile surface to prevent slippage at the boundary itself.

Francescon (1983) measured α values that decreased with OCR. The extensive instrumentation allowed the calculation of pile-soil friction angle directly. Values of δ_{int} were found to depend on shaft roughness, a lower value of $\delta_{int} = 15°$ being measured when the pile was completely smooth. Roughening the surface by gluing sand onto it (the increase in effective diameter was accounted for) increased δ_{int} to 17°, but this was still well below the triaxial $\phi' = 23°$ measured for undisturbed kaolin. This low value was attributed to failure having initially occurred on a horizontal plane. From the Mohr's circle, figure 1.4, δ_i is in this case given by:

$$\tan \delta_{int} = \frac{\sin \phi' \cos \phi'}{1 + \sin^2 \phi'} \qquad (6.)$$

which gives $\delta_{int} = 17°$ for $\phi' = 23°$.

During loading, the radial effective stress next to the pile was found to vary only slightly, in the range $\pm 0.25\, s_u$. The drop in bond strength after peak was attributed to the formation of a vertical rupture plane, on which the residual friction angle was mobilised. This mechanism was assumed to prevent the measurement of higher friction angles, in

particular $\delta_{int} = \phi'$, which could in theory be mobilised if the stress state were to rotate at constant p' to point P in figure 1.4[†].

In summary, the following results are noted from the piling literature:

- Simple empirical methods are generally used to predict shaft friction from ground conditions for different pile installation techniques.
- The described effective stress method of design relies on accurate estimates of in-situ horizontal effective stress and pile/soil friction coefficient, $\tan\delta_{int}$.
- Experimental studies on model piles have deduced that although σ'_r next to the pile may depend substantially on the method of installation, changes during loading are relatively small.
- δ_{int} values recorded during model tests show a range of values, but these were approximately constant for each test series. Higher values were recorded from the piles installed with minimal disturbance compared to the jacked piles.
- Post peak reductions in shaft friction may be attributed to the mobilisation of low residual friction angles on a cylindrical rupture surface running parallel to the pile.

1.2.3. Previous research into the bond resistance of soil nails

The relationship between the results from pull-out tests, direct shear tests of nailed soil, and interface tests was examined by Tei (1993). The tests were performed in sands of different grade and at different relative densities. Results from the different types of test were compared using an apparent friction coefficient, f^*, defined by

$$f^* = \frac{\tau_{max}}{\sigma_m} \tag{7.}$$

where σ_m was the initial normal stress acting at the shear surface. Higher values of f^* were calculated from the pull-out tests than from the direct shear tests on nailed sand. The interface tests gave the lowest values of f^*. This trend was attributed to the reducing degree of restrained dilatancy in the soil surrounding the reinforcement. Lower values of

---

[†] It is noted that this assumes that the intermediate stress σ'_2 lies halfway between σ'_1 and σ'_3. This is a reasonable estimate if the soil is assumed to be deforming in simple shear, Randolph and Wroth (1981).

f^* were also recorded for a nail of larger diameter. This can be explained by assuming that the thickness of the zone of soil under shear around a cylindrical inclusion is constant regardless of diameter, Houlsby (1991).

Tei also found that f^* depended critically on the surface roughness of the reinforcement. For a perfectly smooth surface, values of less than $(\tan\phi'_{cv})$ were recorded, whereas values of two to four times $(\tan\phi'_{peak})$ measured during direct shear were observed during pull-out tests on rough nails. Examining the sand in the interface tests by X-ray techniques, he found that the thickness of the rupture plane at the interface for smooth reinforcement was considerably thinner than for rough reinforcement. These results were all attributed to the dilation behaviour of the soil.

A series of large scale element tests has recently been carried out at Oxford University by Chang. A $1m$ long nail was instrumented with four load cells capable of measuring radial and shear stresses acting on the grout-soil interface during installation and pull-out testing. The final diameter of the nail after grouting was $100mm$. The nail was installed in saturated fine sand, which was able to withstand the formation of an unsupported borehole for a short time before grouting. A brief description of the apparatus and instrumentation is given by Milligan et al. (1997), which also describes some typical results. Tests were performed at normal (gravity pressure only) and elevated grout pressures. Unfortunately, the majority of this work is not yet published, and it is currently unclear how grout pressure affected the stresses measured around the nail.

The results given in the above paper show some interesting features, however. Direct measurement of the stresses on the nail during grout setting and curing proved that large reductions from original in-situ values occur as a result of forming the borehole. The vertical and lateral boundary stresses during the test illustrated in the paper were $200kPa$ and $100kPa$ respectively, whereas the average value of normal stress measured on the nail surface after 38 hours' curing was approximately $40kPa$.

Increases in normal stress to above the original in-situ values were subsequently observed during loading, due to dilation. This allowed the mobilisation of high shear stresses, while the angle of friction (calculated directly from the local normal and shear stress values) remained approximately constant. It is interesting to note that the shear

stresses measured locally exceeded the average value calculated from the total pull-out resistance; the reason for this is unclear, but it could be due to a reduction in boundary stresses near the ends of the tank due to wall friction. This would result in the mobilisation of lower shear stresses towards the end of the nail. (The load cells were grouped midway along the length of the nail.)

Little attention has so far been given to stress conditions in the soil surrounding the nail in the active zone. The loading of the soil on the nail in this region is different to that experienced in the passive zone, as the soil is unloading (in a direction parallel to the nail axis), and soil displacements are likely to exceed nail displacements. An attempt to model this situation in the laboratory using a modified triaxial apparatus is described by Standing (1997). The apparatus is similar to that described by Chandler and Martins (1982), and nails were installed using the same method, leaving them in a 'wished in place' condition. Radial stress cells were incorporated into the model nail, but unfortunately these were not developed in time for use in the tests performed in clay.

Nails were installed into consolidated kaolin and fixed to the bottom of the triaxial cell. To simulate active zone conditions, the radial stress was held constant, and the axial stress reduced, indirectly loading the nail in tension. The nature of this loading made results difficult to interpret, since the relative nail-soil displacement was only known at the top and bottom of the sample, and varied in an unknown fashion in between. Micro-fabric studies similar to those described by Chandler and Martins confirmed the existence of displacement discontinuities within the clay adjacent to the nail. These were confined to the top section of the nail where nail-soil relative displacements were greatest.

In summary,

- In granular soils, the stress conditions around nails have been shown to depend critically on soil dilation, and the degree to which it is confined during loading. Dilation increases the effective stress acting normally to the nail, and allows the mobilisation of higher interface shear stresses.
- The radial stress acting on a drilled and gravity grouted nail after installation is likely to be significantly reduced from the original in-situ value.

- Values for interface friction angle are strongly influenced by the surface roughness of the nail. The angles measured are approximately constant even at large displacements.

It should be stressed that the above observations are based upon tests in sand. However, the drained behaviour of overconsolidated clays has much in common with that of sands, and it is suggested that dilative movements of such clays under loading, although considerably smaller in magnitude, might lead to similar trends in behaviour.

1.2.4. Soil nail field data

One of the earliest descriptions of data from pull-out tests performed in the field was given by Cartier and Gigan (1983). Tests were performed during the construction of an 11.6*m* high cutting in cemented sand, at varying heights, and hence at varying vertical effective stress. The wall was nailed using driven, ungrouted, steel angle sections. They compared the test results in terms of unit skin friction, expressed as the pull-out force per metre length of nail:

$$T_f = Pc' + 2D\sigma_v\mu^* \tag{8.}$$

where P is the perimeter of the steel angles, D is the width of an equivalent flat reinforcement strip, c' is the soil cohesion (estimated as 30*kPa*) and μ^* is the effective friction coefficient. μ^* took values of greater than unity near the top of the wall, but dropped to a constant value of approximately $\mu^* = 0.5\tan\phi$ below a depth of 5*m*. They suggested that this was due to greater dilation of the soil at lower vertical stress.

An example of pull-out data obtained from grouted nails in cohesive soils is described by Heymann et al. (1992). Results are presented from forty pull-out tests, in residual soils of low to intermediate plasticity. The tests were all performed at a rapid rate of pull-out, with the final nail displacement of around 30*mm* being achieved in 10 to 15 minutes. Results from the pull-out tests are compared with values from the equation

$$\tau_f = c' + \sigma'_n \tan\phi' \tag{9.}$$

where the soil properties c' and ϕ' were obtained from drained shear box tests, and σ'_n is the average stress acting normally on the nail surface. It was found that predictions using this equation underestimated the measured pull-out strengths by a factor of approximately

two for residual andesite (a cohesive clayey silt), but the method of calculating σ'_n is not given in the paper. Results are also presented showing the variation of ultimate bond resistance in andesite with depth. Values of approximately $200kPa$ were obtained for all depths up to $6m$.

Another reported case of nailing in cohesive soil is given by Gässler (1995). Pull-out tests were performed on nails installed in weak clay silt stone. Some of the nails tested were strain gauged to measure axial stresses at various locations along their length. This enabled the distribution of shear stress acting along the length of the nails to be determined. The nails used for supporting the slope excavation were very long (15 to $24m$), but the grouted length of the test nails was kept to a maximum of $10m$. Even at this length, the distribution of axial stress during pull-out showed that the extensibility of the nail influenced the result. At low pull-out forces, the bond resistance was mobilised more at the upper end of the grouted section, where nail-soil relative displacements were greatest. At the far end of the nail, low axial stresses in adjacent strain gauge locations indicated that little relative displacement, and hence low bond resistance had been mobilised. This made it difficult to assess the maximum possible bond resistance, but the average value, calculated by assuming uniform mobilisation along the nail length, was sufficient to satisfy the design requirements. This problem was avoided by Heymann et al. (*loc. cit.*) by the use of short ($1m$ long) nails installed separately for testing purposes.

A full scale test on a nailed wall constructed in consolidated highly plastic clay is described by Gässler (1992). No data on bond resistance are given, but the paper is interesting as it shows that the time-dependent behaviour of cohesive soils must be considered if they are to be proposed for stabilisation by soil nailing. The horizontal displacement of the top of the wall increased steadily under load to a value of $36mm$ (0.6% of the wall height) over a 14 day period. Extending the trend of these results over a 1 year period suggested that the horizontal displacement at this time would be approximately $200mm$ (3.3% of the wall height), suggesting that serviceability of such a wall would be extremely doubtful.

1.2.5. Design methods for calculating nail bond resistance

BS8081: 1989 – *Code of practice for ground anchorages*

Although this code was written specifically for the design of ground anchorages, the part dealing with bond resistance may equally well be applied to soil nails. In cohesive soils, the design method is based on the simple α equation originally derived for bored piles (1.). It is stated that α values higher than 0.45 can be mobilised, but recommends that these are verified by proving tests. Otherwise, the values of α are the same as those employed for piling.

Results from field tests presented in the code show that increases in bond resistance of 25 to 50% may be achieved for anchors grouted at high pressures. The greatest benefit to bond resistance is shown to be achieved by post-grouting (secondary injections performed after initial stiffening of primary grout). The grout pressures described are very high (1000 to 4000*kPa*), and it is unlikely that pressures of this level could be used safely on most soil nailing projects, due to the lack of overburden and consequent risk of ground heave or rupture. The general principle of employing grout pressures is relevant to soil nailing, however; this is discussed further in section 1.2.6.

U.K. Highways Agency advice note HA 68/94 – *Design methods for the reinforcement of highway slopes by reinforced soil and soil nailing techniques*

This method is different from the others described here, in that it is based upon effective stresses for both cohesive and non-cohesive soils. The general equation given for pull-out resistance of reinforcement (in terms of the force for each layer) is

$$P_{des} = \lambda_p L_e \left(\sigma'_n \tan \phi'_{des} + c'_{des}\right) \qquad (10.)$$

where the expression within brackets represents the shear stress mobilised for design, and the subscripts indicate the use of design values for soil strength. L_e is the length of nail within the passive zone and λ_p is a non-dimensional pull-out factor, which accounts for the nail perimeter, horizontal spacing and one other variable which relates interface strength parameters to unreinforced soil parameters (both sets measured by direct shear testing before construction).

As with piling design, the major uncertainty when using equation (10.) is the determination of the in-situ effective stress surrounding the nail. The approach used by the advice note is to assume the lateral effective stress (acting parallel to the slope) is related to σ'_v by the coefficient K_L, so that the average radial effective stress, σ'_n, acting along the pull-out length of the nail is given by

$$\sigma'_n = \frac{1}{2}(1 + K_L)\sigma'_v \qquad (11.)$$

Assuming active conditions develop perpendicular to the slope, it is suggested that a suitable formula for K_L is

$$K_L = \frac{1}{2}(1 + K_a) \qquad (12.)$$

where K_a is the coefficient of active earth pressure, taken as

$$K_a = \frac{1 - \sin\phi'_{des}}{1 + \sin\phi'_{des}} \qquad (13.)$$

It is noted that the equation for σ'_n may underestimate in-service values for granular soils, as a result of the beneficial effects of dilation, and that the equation might overestimate values for soils with appreciable cohesion, as a result of stresses arching around the nail. In the latter case, it is recommended that 'design values are checked by a drained pull-out trial on site, or that the nails are pressure grouted or expanding grout used.' Examination of equations (11.), (12.) and (13.) reveals that higher values of σ'_n are predicted for lower values of ϕ'_{des}. However, if the first term in the brackets in equation (10.) is plotted against ϕ'_{des}, it is seen that the overall effect of increasing ϕ'_{des} is to increase bond resistance, as expected. This trend is shown in figure 1.5; the y-axis is normalised by the in-situ vertical effective stress.

In cohesive soils of plasticity index greater than 25%, attention is drawn to the possibility of low residual friction angles being mobilised at larger displacements, particularly in the case of flexible nails. This seems reasonable, since the soil shear strain at the near end of a flexible nail is likely to be large at working loads, due to the extension of the nail and the narrowness of the shear zone. At the far end of the nail, the displacement of the nail relative to the soil, and hence the shear strain, will be smaller. A

consequence of this is that once the bond shear stress at the far end of the nail has reached peak, the shear strain at the near end may be large enough for soil particle alignment to have occurred along a rupture surface, leaving only residual soil shear strength to resist nail movement. If the bond resistance has been designed assuming uniform conditions along the nail, it is probable that pull-out failure will occur by this mechanism (progressive failure, sometimes called progressive de-bonding in the nailing literature).

For steel nails, differences in nail-soil relative displacements along a nail are likely to be small, and the Advice Note recommends the use of constant volume post-peak parameters.

BS8006: 1995 – *Code of practice for strengthened/reinforced earth and other fills*

This is a very general document which provides little specific advice for the design of soil nail bond resistance. It does, however, note that the use of the total stress method (α values) is best suited to design in cohesive soils, but that if an effective stress method is to be used, values of friction angle between soil and reinforcement, δ_{int}, should be determined from in-situ pull-out tests or interface shear box tests.

U.S.A. Federal Highways Administration (1996) – *Manual for design and construction of soil nailed walls*

A total stress method is again recommended for cohesive soils. α values are stated to vary between 0.25 to 0.75, the lower factors being associated with stiffer, harder clays. Typical values of bond resistance for design are listed for different cohesive soils – values for stiff clay are stated to lie in the range 40 to 60kPa. Concerns are mentioned regarding the creep behaviour of softer clay soils, and the possible softening of sensitive clays following increases in water level following construction.

Recommendations *Clouterre* (1991)

The French practice of soil nailing is described in this comprehensive document. Bond resistance is determined in the first instance by relation to pressuremeter test results. The range of values indicated for bond resistance in clays is 50 to 125kPa. These values

are confirmed during construction by testing of nails in-situ. Details of procedures for both constant rate of pull-out and sustained loading tests are specified. The latter are compulsory for inspection tests on nails installed in soils having plasticity index of greater than 20%, to check on creep* behaviour. No theoretical method for calculating bond resistance is given.

1.2.6. High pressure grouting – cavity expansion

The design code for ground anchorages (previous section) describes how bond resistance may be significantly increased by the use of high grout pressures. HA 68/94 also recognises that high pressure grouting may have a beneficial effect on bond in soils with appreciable cohesion, but does not give any information regarding the mechanism by which this benefit is obtained. In fact, there is little published material on the practical methods of using high pressures during the grouting of nails (the pressures necessary, and the duration for which the pressure should be maintained) and the increases in bond resistance that might be expected following the implementation of such methods.

High values of shaft friction of post-grouted micro piles (diameter 100 to 150*mm*) installed in London clay are described by Jones and Turner (1980). Micro piles carry only a small amount of load through end bearing, and hence act in a manner similar to grouted soil nails. In the paper, results from constant load and constant rate of penetration tests on 150*mm* diameter piles up to 19*m* long are presented. Piles were initially grouted under gravity pressure in the normal way. After 24 hours, extra grout was introduced at several locations (below 5m ground depth to prevent excessive heave) along the length of each pile by a system of tubes fitted before installation. Pressures employed were in the range 1000 to 1500*kPa*, and typically 400*kg* of extra grout was injected. Information on initial in-situ effective stresses is not given, but it may be assumed that these grouting pressures were approximately an order of magnitude greater than σ'_h.

* It is not clear from *Clouterre* whether the phenomenon to which this term refers is actually viscous creep or time dependent nail movement due to consolidation of the soil in the shear zone. Time dependent effects are discussed in Chapter 9.

Typical design values of α for bored piles in London clay lie in the range 0.3 to 0.45. Analysis of the results from field tests on the piles described above gave α values in the range 0.7 to 1.0. (The higher values of α were obtained for shorter piles, since these were less susceptible to the progressive mode of failure associated with elastic shortening of the pile under load.) Again, it is not clear from the paper whether the enhanced load-carrying capabilities of these piles were due to increases in pile diameter, fissuring and consolidation of the soil around the pile, a combination of these two factors or other entirely separate mechanisms. It is also unclear how the grouting operations affected the shape of the finished piles, in particular whether the extra grout increased the diameter locally around the injection points, or caused a uniform increase in diameter of the whole post-grouted length.

If it is assumed that the main effect of high pressure grouting is to increase pile diameter, it is possible to model the resultant soil loading as a process of cylindrical cavity expansion. This process has previously attracted a great deal of attention in relation to the installation of driven piles, e.g. Randolph et al (1979a), Francescon (1983). Francescon measured increases in σ'_h of 20 to 80% following the driving of model piles into overconsolidated kaolin.

The action of grouting is likely to differ significantly from pile driving, however, since both the inner boundary conditions and the magnitude of soil radial displacements are different in the two cases. In theory, the pile driving process involves infinite cavity expansion from $r = 0$ to $r = r_i$, where r_i is the pile radius. The inner boundary is most suitably modelled as impermeable, and the expansion there modelled as displacement controlled. During nail grouting, however, the inner boundary is pressure controlled, and the high water content of the grouts used implies that water can flow across the boundary while the grout remains fluid (approximately 4 to 6 hours for a typical mix). Under pressure control, it is unlikely that large increases in cavity radius are obtainable before rupture occurs, particularly in stiffer and fissured clays.

In summary, nails installed using high grout pressures might be expected to mobilise higher bond resistance than gravity grouted nails, although to date little research specific to soil nails has been carried out. Elevated grout pressure on the inner boundary of

a nail borehole may act to enlarge the cavity; this could be modelled as a cavity expansion process using suitable boundary conditions. The application of very high grout pressures in the field is likely to be problematic, since a large proportion of nails are necessarily installed near ground level, and rupture of the borehole could have serious consequences. Lower grout pressures of magnitude approximately equal to the overburden stress might, however, have a beneficial effect, although it is probable that the pressure would have to be maintained until the grout had set to achieve a permanent increase in effective stress around the nail.

1.2.7. Finite element modelling

The finite element technique has been widely applied to the analysis of soil nailing problems. However, the majority of published results are from analyses of nailed slopes or walls, e.g. Unterreiner et al. (1997); little or no attention has been paid to the modelling of individual nails. An interesting example of equivalent research into pile shaft resistance is described by Potts and Martins (1982). The mobilisation of shear stress along a rough pile shaft in normally consolidated clay was considered in terms of the effective stresses acting in the clay. Two elasto-plastic constitutive laws based on Modified Cam Clay were used to model the soil under undrained and fully drained loading conditions. A direct consequence of this type of model is that the peak angle of friction that can be mobilised along a pile shaft is independent of initial stress conditions, and is given by

$$\delta_{int} = \tan^{-1}(\sin\phi') \qquad (14.)$$

The implied Mohr's circle at failure is shown in figure 1.6. This was found to agree well with the experimental data obtained by Chandler and Martins (1982).

Analyses of piles loaded under drained conditions indicated that large reductions in mean effective stress in the soil adjacent to the piles would occur, and that these would be accompanied by a corresponding decrease in the radial effective stress. Consideration of undrained pile loading indicated that the generation of excess pore pressure was likely to be highly localised, and would dissipate rapidly, raising the question of whether pile loadings are drained or undrained in practice. All analyses predicted large shear strain

concentrations in the soil adjacent to loaded piles, implying that residual conditions would quickly be approached after peak.

It is important to note that the above study examined the behaviour of piles in normally consolidated clays only, and also that the material model was unable to predict any shear stress reduction once a peak value had been reached. The stiff clays into which it is hoped to extend the technique of soil nailing are often heavily overconsolidated; dilation might have a considerable effect on bond resistance in these soils.

1.2.8. Summary

To date, the majority of nailing projects in the UK and abroad have been confined to granular soils. This is mainly due to concerns regarding low bond resistance in cohesive soils, and possible large deformations in service caused by creep. To understand how bond resistance is mobilised in these and other soils, it is necessary to examine the changes in effective stress in the soil around nails during installation and loading, and consider the effect that these changes will have on the bond resistance mobilised. Previous research has shown that the stress paths followed during each of these processes is likely to be complex, and will depend on many different factors. Simple design methods are not able to take all of these factors into account, but in some cases they may still be unnecessarily conservative.

Although a large amount of research has been carried out into the behaviour of nails in granular soils, little to date has concentrated on mechanisms of nail bond resistance in clay. Research into the shaft resistance of axially loaded piles in clay has provided some interesting insights into behaviour, but the boundary conditions relating to soil nails are likely to be quite different. The pressure used during grouting is likely to have a significant effect on bond resistance – this area in particular has attracted little attention. The use of elevated grout pressures in clays might increase bond resistance sufficiently to make the nailing technique economic in these soils, even taking into account the additional overhead in equipment.

The standard method of checking the bond resistance of nails in the field is the pull-out or constant rate of displacement test. While this method may be suitable for nails installed in granular soils, the low permeability of some clays suggests that typical rates for these tests may lead to substantially undrained behaviour. In these cases, it is unclear how the test results pertain to conditions within a real nailed structure under service conditions, where loading is more likely to be fully drained. The analysis of clay samples taken adjacent to model piles at failure, however, suggests that the zone of sheared soil may in fact be extremely narrow, and is likely to behave in a drained fashion under most loading rates encountered.

1.3. Aims of research project

It is impossible to consider all the possible influences on bond resistance in one research programme. The laboratory research described in this thesis has focussed on the bond resistance of grouted nails in clay. Three areas in particular are investigated:

Mechanisms of nail-soil bond

The stress conditions around a loaded nail are complex. If the variations in bond resistance recorded in different soils, using different installation processes, and under various loading conditions are to be explained, a model of the effective stresses and pore water pressures in the soil is needed. Current design methods for soil nailing are often oversimplified, and may therefore be over-conservative or even unsafe in some instances. An understanding of the mechanisms by which bond resistance develops underlies the development of rational design procedures which in turn leads to the construction of efficient and safe geotechnical structures.

Field testing procedures

The method of testing soil nails in the UK is not standardised. There is concern that different results might be obtained from the various test procedures followed, and also that these results may not be relevant to the conditions pertaining in a real nailed structure.

If the results from field tests are to be compared or used to validate design assumptions, it is essential that the influence of the testing procedure on the quantities measured is adequately understood, and that the most appropriate type of test is used.

The use of interface tests to predict bond resistance

A simple test whereby the shear strength of a grout-soil interface is directly measured might provide a suitable method for predicting the bond resistance of grouted nails installed in the same soil. Since this type of test can be performed in the laboratory, it would represent a simple and cost-effective method of obtaining parameters for design.

The methods used to research these areas were as follows:

Laboratory pull-out and sustained load testing

A large laboratory nailing apparatus was devised to investigate the variations in behaviour of grouted nails loaded under different conditions. The desired specifications for these tests may be summarised:

- The diameter of the grouted nails should be comparable to those typically used in the field to avoid possible effects of scale. The diameters used in the field range from approximately 75 to 200*mm*, and are generally towards the lower end of this range.
- The soil used for the tests should be a stiff clay; it is unlikely that softer clays would be considered for nailing due to excessive displacements of the structure as a whole. The sample should be quick to prepare, so that a sufficient number of tests can be performed to allow the observation of trends in behaviour under different in-situ and loading conditions. The sample size should be sufficient to accommodate the nails used with minimal boundary effects.
- The method of installation of nails should be as close as possible to the methods typically used on site.
- The nail loading system should be capable of applying loads at varying rates of displacement to model standard pull-out testing methods, and should also be able to apply and maintain constant loads.

- A computer based data acquisition system should be used to allow the collection of test data over the varying durations of the different types of test planned.

Interface testing

The potential links between interface and pull-out test results were investigated by a series of small interface tests on the same soil and grout used during the nailing tests. The method of preparation of samples had to be representative of the grouting procedure employed during the nailing tests, which implied that the grout should be allowed to set while in contact with the soil. The standard direct shearing apparatus was considered to be the most suitable starting point for these tests, since it was able to meet the specifications for loading at different rates, and for the application of varying surcharge levels.

Finite element modelling

A finite element model was developed to examine trends observed during the laboratory tests, and to investigate further the mechanisms of bond resistance in terms of soil effective stresses. The specification of these analyses is given separately in Chapter 6, but the essential desirable features were: an ability to model the effects of installation procedures, including the use of high grout pressures; a material model capable of including the effects of plasticity and dilation; the ability to explain the trends observed in the laboratory, and to extrapolate these trends where it was not possible to perform sufficient numbers of laboratory tests.

Chapter 2. TEST APPARATUS

2.1. Introduction

This chapter describes the development of a test apparatus for measuring the bond resistance of drilled and grouted soil nails in clay soil. It also describes the selection of a suitable soil for use in these tests. The main apparatus had to include the following components:

- A tank to contain a large sample of clay soil under vertical load, with a sealable hole to allow installation and pull-out of nails.
- Loading systems to apply both the distributed vertical load to the sample and direct point load to the nail head.
- Instrumentation to measure loads, displacements and pressures developed during pull-out.
- Data acquisition systems to log output from the instrumentation.
- Drilling equipment to form holes in the prepared soil sample.
- Fittings and mixing equipment to place the grout around the nail.

2.2. Test soil: Methods of soil sample preparation

2.2.1. Background

A commonly used method to prepare clay soil samples in the laboratory is by consolidation from slurry. The advantage of this method is that a uniform sample can be produced with known stress history. The main disadvantage is the excessive time required to achieve a clay of reasonable strength. To prepare samples in the large tank selected for this testing programme, it was estimated that a minimum of six weeks per sample would be needed, assuming drainage at top and bottom boundaries. Substantial modification to the

tank would also be required, as the pre-consolidation volume of the sample would be in the region of twice the final volume.

To keep the average test time below two weeks, the possibility of using previously consolidated material was investigated. The clay would ideally be stiff and highly plastic as this is typical of the material found in embankments and cuttings formed from London Clay. It was thought that a straightforward, rapid method of sample preparation would be to use unfired clay bricks.

The method of producing samples using unfired bricks was first employed by Rogers (1985) at Nottingham University. Here they were used to simulate a road foundation on clay in which pipelines were buried. Rogers used blocks supplied by Butterley Brick Company (see below) formed from Keuper Marl. The bricks were placed in layers in a $2m$ deep pit and compacted into place using a triple-headed tamper. Each layer was thoroughly scarified after compaction between layers to remove horizontal interfaces. The pit took four weeks to fill and was left for five months to allow the pore pressures to reach equilibrium. Reasonable continuity of strength and water content was achieved throughout the sample. Rogers reports several advantages in using unfired bricks (as opposed to other mechanically retrieved clay), including: ease of handling, reduction of air voids to a minimum thereby increasing homogeneity, and the production of a flat surface to aid compaction.

Rogers left the bricks for five months before testing. During the current research, however, it was not going to be practicable to leave them for this long before testing, due to the number of tests planned. However, it was hoped that by standardising a test preparation schedule based on a much shorter consolidation time it would be possible to obtain good comparative data for different testing conditions.

2.2.2. Selection of brick type

Three separate brickworks were contacted, and trial bricks were obtained from two of these. The first load of trial bricks were donated by London Brick Company of Stewartby near Bedford (now part of Hanson Brick), where the material had been extracted

from the Lower Oxford Clay beds exposed locally. In manufacture, the material is first crumbled, then pressed into dense bricks, which are then able to support their own weight in large stacks as they progress through the kiln. On testing samples in the small Casagrande direct shear apparatus, the undrained shear strength was measured to be in the region of $300kPa$. This was considered too high for testing purposes, and the remaining bricks were discarded.

On the recommendation of the technical services department at Stewartby, Butterley Brick in Ripon, Derbyshire (also one of the Hanson group of companies) were contacted with a view to obtaining lower strength clay. Butterley bricks are made from clays won from several local strata. The clay is taken in large batches, consisting of perhaps one weeks' mining, and then stored in bulk ready for processing. The material may be left for periods of up to a year before manufacture. The brick manufacturing process involves: grinding of the clay into gravel-sized pieces; sieving to a maximum granule size of $3mm$; hydration to approximately 20% to plasticise; then extrusion to shape before firing in small batches. The bricks do not have to support themselves in large stacks, so are generally not required to be as strong as those from Stewartby. Coal Measure Shale is one of the softer clays used and was thought to be the most suitable of those available. The main disadvantage of using Derbyshire clay was the distance from Oxford, but the price of the unfired bricks was very low if collected direct from the brickworks. Another benefit was the willingness of Butterley to extrude the clay in larger blocks equivalent in size to three standard house bricks. This allowed for better (more continuous) samples and less time stacking bricks in place.

The initial appearance of these bricks was more encouraging. The surface of the bricks could easily be indented with a finger, as opposed to the Stewartby bricks which could only just be indented with a thumbnail. Rolling small fragments between the fingers indicated that the material was near the plastic limit, and also revealed a small quantity of coarse sand and fine gravel present throughout. The colour was a light grey as opposed to the dark green of the other bricks, and the overall texture indicated that the material was more continuous and uniform, and showed much less tendency to crumble.

2.2.3. Assessment of brick suitability

Index tests indicated that the blocks as delivered were at the plastic limit with a moisture content of 18%. The plasticity index was 22%, and the liquid limit was 40%, placing the soil in the medium plasticity inorganic clay bracket. A small scale trial pull-out test was performed using a simple plate steel tank to contain a 428*mm* by 463*mm* by 450*mm* high sample, figure 2.1. The sample was prepared without surcharge, and a 50*mm* diameter hole drilled through using a hand auger. A length of 10*mm* diameter reinforcing bar was grouted into the hole, left for 2 days to cure, then pulled out vertically using a manually operated hoist. The load displacement behaviour was recorded using a load cell at the 'nail' head and a dial gauge measuring the relative movement of hoist and sample box..

A peak shear stress (averaged over the surface of the nail in contact with soil) of around 60*kPa* was measured after 12*mm* of pull-out. A series of shear vane tests were then carried out in conjunction with moisture content tests throughout the sample. The shear vane results gave s_u values in the range 83 to 110*kPa*, with the majority of readings around 100*kPa*. Two quick undrained triaxial tests gave slightly higher values of 122 and 135*kPa*.

On the basis of these tests, the Butterley Bricks were selected for use in the main testing programme. The material had proven easy to manipulate into the test tank, being easily cut with simple hand tools. The tests confirmed that the clay was of high-medium plasticity. Ideally, a high plasticity soil such as London Clay would have been used, but no brickworks were identified that used this material. The Coal Measure Shale was therefore considered to be the best available.

2.3. Soil tank

The tank used for the main test series is shown in figure 2.2 and Plate 1. It had to be reasonably large to model the nail diameter at close to full scale. The former Large Direct Shear Apparatus (LDSA) constructed by Palmeira (1984) was the largest tank

available in the Oxford laboratory at the start of the project. It was originally designed to be used both as a large shear box and as a pull-out tank for testing geogrid and geotextile reinforcement. The LDSA had undergone significant modifications in the period 1984 to 1995. Originally, the vertical load was applied by means of a pressure bag in the top platen, reacted by horizontal beams spanning the length of the apparatus. This was later replaced by a hydraulic vertical loading system, employing hydraulic jacks at each corner of the box, powered by an accumulator charged from a gas bottle. A concrete slab replaced the original one inch thick steel plate beneath the tank to add extra rigidity, and the main loading ram raised accordingly.

To allow transfer of instrumentation and other fixtures from the sand-nailing apparatus, the proposed hole diameter for grouting was $100mm$. In particular, this meant that the instrumented nail used by Chang (see section 1.2.3) could be used for the tests in clay with the minimum of modification. In a typical soil nailing design for clay soils, the hole diameter is $150mm$ and the nail spacing approximately 1 to $1.5m$ in both horizontal and vertical directions. The required design spacing may be assumed to be proportional to the bond provided by the nails. In other words, more nails will be needed if the bond is less. The bond is proportional to nail circumference, and so to nail diameter (for a given length). The nail spacing is therefore proportional to nail diameter. Also, if it is assumed that lines of symmetry between nail heads may be modelled by rigid boundaries (zero-displacement lines), the height and width of a pull-out box correspond to vertical and horizontal nail spacings respectively. Hence a $1m$ cube tank holding a nail of grout diameter $100mm$ is in scale with a typical design. However, to reduce sample preparation time the height of the sample was set to $0.6m$, which was the same height as the sand tank used by Chang. This corresponded to a vertical nail spacing of $0.9m$, around the lower limit for spacings in clay. An advantage of this height was that the problem of creating a large hole at the midplane of the LDSA was avoided. Creating such a hole would have been difficult due to the join between the two halves of the tank at this level; it would have been necessary to fabricate four new panels instead of only two. To set the depth, a false bottom was installed at a height of $0.4m$ from the bottom of the tank, leaving a $0.6m$ depth

available for the sample. The false bottom consisted of a $5mm$ thick steel plate resting on dense sand.

A consequence of this was that the mid-height of the sample was raised by $0.2m$, leaving the loading ram too low. Previously, when the concrete slab had been installed below the tank, the ram had been raised $0.25m$ to compensate using steel blocks. A further $0.2m$ of packing would have been untidy and possibly dangerous, so the blocks were removed and replaced with open steel sections to bring the ram up to the correct level. At all points, the original bolt holes were preserved to facilitate reconstruction of the rig as a shear box.

The main tank comprised eight steel panels, fabricated from $25mm$ thick steel plate and $75mm$ by $25mm$ steel webbing. Two of the panels were constructed from Perspex plate backed by steel webbing to allow observation of material movements within the tank. The installation of the false bottom meant that the mid-plane of the sample and hence the level of the hole axis was now in the top half of the box. To enable nail installation, clearance holes were required at both ends of the tank, in opposite panels. The layout of the webbing and previously drilled holes in the existing panels meant that these would be unsuitable without major modification, so two new panels were designed using similar steel components. These were fabricated in the Department of Engineering Science workshops. Additional bolt holes had also to be drilled in some of the existing panels to allow for rigid connection of the two tank halves.

In an attempt to measure the horizontal stresses in the soil sample, two $300mm$ diameter total stress cells were built into the two side walls of the tank parallel to the nail axis. These two panels were removed, and a recess $10mm$ deep was machined into the face of each to house the cells. Holes were also drilled to allow the transducers from these cells to locate outside the tank for connection to the mobile reading unit (see section 2.6.5). The units were sealed in place using silicone sealant, then securely bolted into the side panels.

The original top platen of the tank had been replaced by a $50mm$ thick steel plate weighing over $300kg$. This was cumbersome and excessively thick for the purpose of containing soil at a maximum vertical stress of $200kPa$. The old bottom plate for the tank had been retained, so it was decided to use this as the new top for the tank. This had the

advantage of having holes drilled in the right places, including holes to feed the vertical pressure bag to be housed on the underside. The original top plate with pressure bag had also been retained, but this was unsuitable because it relied on an overhead reaction structure and did not bolt directly on to the top of the box. The pressure bag frame and attachments were transferred from the original top plate to the original bottom plate to make the new top plate. The pressure bag rubber membrane was replaced due to repositioning of access holes and decay of the old rubber.

2.4. Vertical loading system

Vertical stresses were applied to samples using a pressurised water bag fixed to the underside of the top plate of the box. The water was pressurised from the laboratory compressed air line through an air-water interface. A control system was designed and constructed which allowed all routine emptying, filling and pressurising tasks to be controlled from one board. A schematic diagram of the pressurising system is shown in figure 2.3.

2.5. Nail loading system

The hydraulic circuits used to load the nail during testing are shown in figure 2.4 During the test series, the nail was required to be subjected to two different types of load, depending on whether pull-out or sustained loading conditions were to be applied. The jack employed was the same in both cases - a $378kN$ *Enerpac* unit with a stroke of $166mm$. The capacity of this unit far exceeded anticipated maximum nail head loads (around $20kN$). It was, however, necessary to have excess jacking capacity available to facilitate constant rate of displacement tests. When performing pull-out tests, it was desirable to keep the pull rate as constant as possible, so the pump had to keep hydraulic fluid flowing at a constant rate. This was made easier by using a jack and pump operating near the bottom of their range where the pump was not significantly loaded by the system.

During pull-out tests, the jack was powered using a $700bar$ *Enerpac* electric pump as originally supplied with the jack. Control over the pull-rate was afforded by a dump

valve and a flow valve inserted into the appropriate side of the hydraulic circuit. The dump valve acted as a pressure regulator, and hence controlled the force at the nail head. The flow valve, as the name suggests, controlled the amount of hydraulic fluid flowing from the pump.

It might have been possible to use the same system during sustained loading tests, but it was considered undesirable to leave the pump running continuously for up to two weeks at a time, and it was unclear how constant a pressure it would be able to provide. A different apparatus was therefore devised to power the jack for these tests. The pressure was provided by a nitrogen gas bottle, regulated down in the pressure range 2 to 43*bar*. The hydraulic oil was pressurised through an accumulator, which then fed into the jack input. This resulted in available loads within the range 1 to 23*kN*, which was thought to be sufficient. The pressure from the regulator remained constant, and continually topped up pressure in the accumulator when oil flow from the bottom caused it to drop, hence keeping the force at the nail head constant. When a new load increment was to be imposed on the nail, the regulator was adjusted accordingly.

All valves and gauges associated with both hydraulic circuits were mounted on a board attached to the side of the main apparatus. In this way it was possible to remain close to the rig and instrumentation output on the PC when changing loads or pull rates.

2.6. Instrumentation

2.6.1. Introduction

The main quantities to be measured during testing were the load at the nail head and the axial displacement of the nail. Also, the pressure of the vertical and nail loading systems were monitored during sustained loading tests to ensure stable ground conditions and steady loads respectively. During the initial stages of this research, it was hoped that nail-soil interface instrumentation similar to that employed by Chang would be used. The *Cambridge In-Situ* 'dog bone' load cells were to be deployed in housings modified to include mountings for miniature pore water pressure transducers. This instrumentation

package was not developed and employed for two reasons. Firstly, there were inevitable delays in waiting for Chang to finish testing. It was intended to use the same stress cells, and indeed the same housings in a modified form. Chang's experimental work was originally scheduled to finish by early 1997, but due to difficulties with this instrumentation was not complete until early 1998. Secondly, the large quantity of data from Chang's work proved difficult to interpret. Problems were encountered with asymmetrical readings, and other questions were raised regarding the validity of the data. Preparation of the instruments prior to testing was both complex and time consuming, requiring an experienced technician. Further to this, there were doubts as to whether major modifications would be needed to modify the transducer mountings for use in the clay tank, and attempts at measuring pore water pressure separately had already proven unsatisfactory.

Separate ideas were also considered for measuring the normal stress on the nail by means of miniature stress cells. Two $200kPa$ units manufactured by Kyowa with an active face diameter of $6mm$ had previously been used by Chang on his instrumented nail to check on stress distributions across the active face of the main stress cells. However, it was decided that the data obtained would be highly susceptible to local variations along the nail (due to the small active face), and would be of little use without corresponding pore water pressure data.

The remainder of this section describes the instrumentation used during testing, and also includes a section on the attempted measurement of pore water pressure. It also describes the stress cells used to measure the horizontal total stress before testing.

2.6.2. Nail head load cell & nail displacement transducer

The total axial load at the head of the nail was measured by a $50kN$ load cell manufactured by Maywood Instruments Ltd. This was connected to the end of the jack by a coupling which allowed rotation, figure 2.5. This was necessary to allow easy assembly of the threaded components. The load cell was connected to the nail head using a short length of chain, in an attempt to reduce the effects of any small misalignments between the

two. The chain used was of substantial cross section to keep the strain energy stored at maximum load at a safe value. Calibration was carried out at regular intervals during testing using the *Instron* testing machine in the Department of Engineering Science.

The displacement of the nail under load was measured at the far end of the nail using a DC powered LVDT manufactured by RDP. The unit had a stroke of $\pm 75mm$ and was of high linearity throughout this range. This was mounted in line with the nail using a vertical channel whose main purpose was to support the cutting guides during drilling. An advantage of using this was the high stiffness of the support provided, ensuring minimal fluctuation in readings due to vibration or the LVDT spring force. The unit was calibrated at regular intervals by clamping rigidly onto a bench against an accurate steel rule. A parallel was then moved along the rule flush against the LVDT armature, and corresponding readings taken. The unit was found to be highly linear and of very stable calibration coefficient.

2.6.3. Loading systems pressure transducers

During sustained loading tests, the pressure in the hydraulic loading systems was logged to ensure that major fluctuations did not occur. The pressure in the loading jack hydraulic system was monitored using a *Maywood* oil pressure transducer which was teed off the input line to the jack. This unit was calibrated against an analogue gauge of known accuracy. The pressure in the vertical loading system was measured using a *Druck PCDR81* miniature pressure transducer mounted in a brass housing. This was similarly connected to the input of the water pressure bag, and was calibrated against a digital pressure indicator which itself had been recently calibrated.

2.6.4. Pore water pressure measurement

Attempts were made to measure the pore water pressure developed at the interface between soil and nail during loading. A *Druck* pressure transducer as described in section 2.6.3 was used to measure remotely the pore pressure by means of a collection module connected to the transducer by a length of tube filled with glycerol. The collection

module consisted of a 6*mm* diameter *Vyon* filter mounted in a small brass housing which could be pressed against the wall of the nail hole before grouting. Glycerol was used to prevent the filter from drying out rapidly before installation. A disadvantage of this was that the system proved extremely difficult to de-air, as there were many places for bubbles to lodge, and it was difficult to make the rather viscous glycerol flow through. However, after 5 days of forward and reversed flow through, it was possible to de-air the system to a satisfactory level.

In this way it was hoped that the pressure might be measured without the need for submersing these rather sensitive transducers in liquid grout during curing. Unfortunately, the output from this instrument was confusing. Large variations in signal occurred over time. These variations were possibly caused by changes in ambient temperature and pressure, although fluctuations were larger than those predicted as a result of normal changes in atmospheric conditions. One transducer was used during the preliminary sustained loading test P5. Some useful data were obtained from the instrument during this test, in that general trends in the fluctuation of pore water pressure during nail loading were observed. The absolute values of pressures recorded must be treated as suspect, owing to the large amount of drift recorded under ambient conditions described above. The output from the transducer during this test is described in section 4.3.1.

After some discussion, it was decided to abandon pore water pressure measurements at the nail-soil interface due to the difficult nature both of satisfactorily installing instruments, and of interpreting the data obtained. The process of de-airing transducers before testing would have consumed an unacceptable amount of time limiting the already short experimental testing programme. The validity of absolute values measured would always be uncertain, and as such would make estimates of effective stress values extremely unreliable.

2.6.5. Horizontal stress measurement

Two 300*mm* diameter total stress cells manufactured by Soil Instruments Ltd were installed into the side panels of the tank as described in section 2.2. These operated on a

pressure balance system, whereby a readout unit applied a ramp air pressure to the back of a thin steel plate, the other side of which formed the active face of the instrument in contact with the soil. As soon as there was a return flow to the readout unit, the pressure in the air was assumed to be the same as the total stress in the soil. The units were calibrated by the manufacturer using a dead weight tester before delivery.

2.7. Data acquisition

The data acquisition system employed a 16 channel logging module connected by serial link to a standard PC running *Labtech Notebook XE* Windows-based control software. The logging module was fully contained within a steel box which was located near the soil tank during testing, but could be easily disconnected and removed during filling and drilling. This box also contained a stabilised DC power supply board for all the instrumentation and appropriate transformers to allow the box to be powered from $240V$ AC mains supply. The power supply for both computer and logging box was protected by a 15 minute uninterruptible power supply unit during testing to reduce the risk of data loss. The *Datascan 7220* unit was manufactured by Measurement Systems. Only four channels were used for most of the tests. The logging interval and resolution were set by the software.

The Labtech software used ran on a standard 486 PC. It allowed continuous graphical and numerical display of all channels as the tests progressed. It was also possible to log nail displacement and simultaneously provide graphical display of pull rate during pull-out tests. This was necessary due to the manual control of the nail loading system. The data was stored in ASCII text files before importing into spreadsheets for analysis.

2.8. Drilling equipment

A $100mm$ diameter hole was required to run through the length of the soil sample in line with the loading jack. This was achieved by forming the hole in two stages. The first stage involved pushing a $50mm$ diameter sharpened stainless steel tube through the sample,

effectively coring out a hole. The tube was pushed in using a bracing arrangement powered by an air wrench, figure 2.6. The second stage employed a rotary cutter running along a guide rail running through the stage one hole and rigidly fixed at each end of the tank, figure 2.7. In this way, alignment of the hole with the jack was ensured.

Two cutting heads of the same design were used, with diameters $90mm$ and $100mm$ respectively. This allowed the drilling to be divided into two stages when forming the final $100mm$ diameter hole, reducing the amount of power required to turn the cutter. A stainless steel cutting blade was welded into a steel disc at a suitable cutting angle to the soil, figure 2.8. This cut away the 'tunnel' face, and the spoil was propelled backward in a continuous helix, allowing for easy removal. The second stage drilling rig was powered by a hand brace. Support for the drilling components was provided at the far end by a length of steel channel mounted on what was the old LDSA loading boss. Support for the guide rail at the jack end was provided by a steel cup fitting inserted in the hole in the tank side panel.

2.9. Grouting equipment

It was initially intended to investigate the effects of pressurising the grout around the nail during curing. Several abortive attempts were made to seal the ends of the hole so as to confine the grout under pressure. The final system used two tapered plugs pushed into the soil and sealed against the tank using O-rings. The north plug of this pair is shown in figure 2.9 (refer to figure 2.2 for orientation). The south plug was of the same design, except that the tapered length was made shorter. The north plug had to be long enough to ensure that the end of the nail grout nearest the jack was a suitable distance from the tank wall, to minimise the effect of this wall on the stress state in the soil surrounding the nail. At the far (south) end of the nail, the nail was to move away from the tank wall, so any restraining effects of the tank were considered less significant. The taper meant that the plugs had to be forced into the hole, and a tight fit against the soil was achieved, so that under low pressures the liquid grout would not reach the O-ring at the tank wall.

This system worked extremely well in that grout was unable to leak either between plug and tank or between plug and nail. However, once this had been achieved after many iterations, it became clear that the sample itself was unable to withstand a pressure of more than a few kPa before rupturing, presumably along the rather weak lines provided by the clay blocks. When a pressure of $50kPa$ was applied to a sample experiencing the same overburden pressure, the grout made its way to the top of the sample. Since only limited extra grout was available in the supply tubes, the level of grout in the hole eventually dropped to an unacceptable level, and the test had to be abandoned. This effectively precluded the use of high grout pressures during the rest of the test programme, as it was uncertain whether a given sample would be able to hold the desired pressure. The test programme usually operated around a one or two week turnaround; it would have been highly inconvenient to lose more test samples in this way.

The final series of tests employed grout pressures of $10kPa$ and below. No difficulties were experienced at this low pressure limit. The grout was mixed using a small electric mixer, capable of mixing the three batches of grout required in around 5 minutes. The grout was poured into a funnel connected to the far end grout plug by $19mm$ diameter tubing. Similar tubing was attached to the jack end plug, and the grout was poured until the level was approximately 1m above the nail axis in both tubes. Additional lengths of 4mm diameter tubing enclosed within the main grouting tubes allowed easy escape of air from the hole as the grout level rose, figure 2.10. During the high pressure grouting exercise, regulated air pressure was then applied to the end of both grouting tubes.

Chapter 3. TEST PROCEDURES

3.1. Introduction

This chapter describes the procedures followed when preparing for, and performing, the laboratory tests. It also includes tabulated specifications of all the tests whose results are presented in the following chapter. The laboratory tests comprised pull-out, sustained loading and interface tests. The pull-out and sustained loading tests were both performed in the large nailing apparatus, and shared the same methods of sample preparation, drilling and grouting. These topics are therefore presented in sequence, before describing separately specific procedures followed for each type of test. The interface tests were performed in a different apparatus, and are described separately in Chapter 5.

3.2. Pull-out and sustained loading tests

3.2.1. Sample preparation

This section describes the preparation of the sample for testing, starting from the end of the previous test. The pressure in the air-water interface controlling the vertical load was released, and the water drained from the system. The top platen of the loading tank could then be unbolted and removed from the top of the sample. The nail was then removed from the sample by pushing out from the loading end. The diameter of the nail was then measured at several locations along its length and an average value taken.

Following the first test after commissioning of the apparatus, all of the clay was removed from the sample tank. The size of the tank was $1m \times 1m \times 0.6m$ high, containing approximately 1.5 *tonnes* of material when full. Owing to the considerable amount of effort involved in completely refilling the tank, and also the large amount of new material that would have been required for each test, the decision was made to remove only a trench of material most likely to have been affected by the nail during the previous test. Marks

were made across the top of the sample to indicate the position of the cuts to be made, and a trench approximately $0.3m$ wide and $0.5m$ deep was excavated along the line of the nail axis. This entirely removed any clay cut by the previous drilling process, allowing a margin of $0.1m$ on each side and below the sides of the hole formed.

The trench was filled with fresh clay blocks (Plate 2) which had been stored in damp conditions under polythene in the laboratory. Careful trimming of the side walls of the trench was required to ensure the blocks were a tight fit – a spade and a small hand trowel were used for this purpose. The blocks were arranged so that a minimum number of joints would be encountered along the length of the nail hole, figure 3.1. To ensure that the blocks were firmly seated into the bottom of the trench, they were then tapped down using a $1m$ long piece of large section timber; this technique proved very effective. The next layer of blocks was then laid horizontally on top, before cutting the final layer of blocks to size to bring the surface of the sample level with the top of the tank. A heavy duty 'cheese wire' arrangement was used to cut the bricks, figure 3.2. This allowed the blocks to be cut to a tolerance of approximately $1mm$.

The sample was then inundated by supplying water to the top face over a period of about 30 minutes and allowing it to soak in, especially around the newly installed trench of fresh material. A sheet of permeable *Vyon* was then placed on top of the sample. The purpose of this was to protect the rubber membrane underneath the top platen of the tank. The top platen was then manoeuvred into place using the overhead crane, and lightly bolted into place in 28 locations. It was important not to over-tighten these bolts, as otherwise the pressure bag beneath would have insufficient space to fill with water and function correctly. The pressure bag was first filled using the mains supply, until it started to overflow from the second vent, (refer to figure 2.3). This vent was then closed, and the required pressure applied through the air-water interface. The sample was then left for 2 days before drilling.

3.2.2. Drilling

The hole for the nail was drilled in three stages: pilot, rough cut and final cut. The pilot drill consisted of a 50*mm* diameter thin walled stainless steel tube which was driven through the sample, guided by a frame at the south end of the tank. The end of the tube was sharpened to allow easier progress through the soil. In the early tests, it was hammered through the clay by hand, a lengthy and tiring process. During the later tests, a bracing system was devised which allowed the tube to be propelled forward using an air wrench. This greatly reduced the amount of effort expended in making the hole, but did not save a great deal of time, since the tube still had to be periodically removed by hand and cores of material removed from the centre. These cores were conveniently taken as moisture content samples.

Once this central core was removed, a guide rail was then inserted along the length of the hole for the next two drills to follow. This ensured the best possible line was achieved through the sample, minimising any possible misalignment between loading ram and nail. The guide rail was supported at each end of the hole so as to allow complete removal of the cutter at the south end during drilling. This was necessary to allow periodic removal of the spoil. Both the second and third stage cutters were powered by hand using a small hand brace situated at the end of the mounting tube as described in section 2.8. The first (rough) cutter opened up the hole from 50*mm* to 90*mm* in one run. The final cutter took a small additional cut to leave the desired final hole diameter of 100*mm*. Plates 3 and 4 show the second stage cutter in use. The surface of the hole created was quite smooth and very straight, no deviation from line or level being detectable by eye. It is worth pointing out that this is the worst scenario for the development of bond resistance; in the field, bore holes generally deviate significantly from line and level, and the surface formed is unlikely to be completely smooth.

3.2.3. Grouting

When the drilling was complete, the nail was placed in the hole and located in the centre by two aluminium plugs designed to hold the nail in place during curing and also to

prevent leakage of liquid grout. These 'grouting plugs' are described in section 2.9. The north plug was installed first, having been thoroughly coated in silicone grease to allow easier removal. The 31.75*mm* diameter plain mild steel nail was then inserted into the hole and fed through the grouting plug at the north end. The second grouting plug (similarly greased) was then installed at the south end, and the nail carefully tapped into place so as to be the correct distance from the loading ram. Hoses were then connected to tubes running through the grouting plugs and the ends secured approximately 1*m* above the axis of the hole. A funnel was attached to the hose at the south end to allow easy pouring of the grout into the hose (Plate 5). In this way a low grout pressure of around 10*kPa* was ensured at nail axis level in each test, provided the level of the grout in the hoses was maintained.

The grout was mixed in three batches using a small electric mixer. 1.6*l* of water was added to 2.5*kg* of ordinary Portland cement for each batch, resulting in a relatively high water content of around 40% by weight. The grout needed to be of low viscosity to aid complete filling of the void between the nail and the hole surface. In industry, holes are typically aligned downwards at an angle of 10° to alleviate this problem. Once the required level of grout was attained in both tubes, it was left to set for four hours, by which time it had hardened sufficiently for the hoses to be removed, but was still sufficiently malleable for the hoses to be completely cleaned out. The grout was left to cure for 2 days before testing.

3.2.4. Test procedure – pull-out tests

After the grout had cured, the grouting plugs were removed from the ends of the tank. This was a difficult task, since the grout always stuck to the front face of the plug in spite of it having been well greased before assembly. There was also some soil suction, although this was broken fairly quickly since the plugs were tapered. It was usually necessary to remove the north plug using the loading ram. The south end plug was more easily removed once eye bolts had been screwed into it to provide an adequate handhold. The loading ram was then connected to the nail head via the coupling, the load cell and a

short length of chain. All these shared a common M16 thread allowing easy connection. The LVDT used to measure the horizontal displacement of the nail was mounted at the south end of the rig. The leads from all transducers were then connected to the data collection module, which was in turn connected to the PC. The instruments were tested for positive signal, and the data acquisition software settings checked. The horizontal total stress was measured using the cells built into the side of the tank.

The computer monitor displayed three main quantities during testing. Two plots showed the output from the load cell and the LVDT, and another window indicated the current pull rate. By watching the latter plot, the pull rate was controlled by hand, adjusting the hydraulic dump valve as necessary in small increments as the test proceeded. This was not an ideal method, and some fluctuation of the rate was observed, although it was possible to keep it within ±25% of the desired rate most of the time. The test was considered to be finished once the loading ram had run out of travel, which corresponded to a final pull-out of between 100 and 130*mm*. Plates 6 and 7 show typical nails removed from the tank after testing.

3.2.5. Test procedure – sustained loading tests

Preparation for the sustained loading tests followed the same procedure as that described for pull-out tests above. The data-acquisition software settings were different, however, to allow for the longer logging periods required during these tests. Changes in recorded readings took place over a much longer time scale, so the sampling rate was reduced to one reading every few minutes. This prevented the generation of excessive amounts of data which would have been awkward to handle. The output displayed during the tests was the same as for the pull-out tests, with the exception of the pull-rate window, which was replaced by a window displaying the pressure of the oil in the hydraulic loading system. This was useful since a time lag was sometimes observed between changes in the pneumatic pressure applied to the accumulator, and the hydraulic pressure at the input port of the loading ram.

The loading was applied in increments, the size of which depended on the anticipated pull-out capacity of the nail. For example, if the pull-out capacity of a similar nail in similar stress conditions was known to be $12kN$, the loading would be applied in $2kN$ increments during the early stages of the test. These load increments were left in place until the rate of change of displacement had dropped below a nominal value. The next loading increment was then applied, and the same procedure followed. As the load on the nails increased, it took longer for the displacements to settle. When it was clear that the capacity of the nail was close to being reached, the size of the following load increment was reduced to approach the failure load as closely as possible. The nail was assumed to be failed once the ram had reached its full stroke, corresponding to a nail displacement of over $100mm$.

3.2.6. Testing programme

The two series of tests undertaken are summarised in Table 3.1. A total of eleven tests were performed in the large nailing apparatus. Of these, three were sustained loading (constant load) tests, and eight were pull-out (constant rate of displacement) tests. Five preliminary tests were performed to test the loading apparatus and instrumentation, and to establish general trends in the behaviour of the nails. The test numbers for this series are prefixed by 'P'. During these tests, the pull-out displacement rate was not fixed at a specific value, but attempts were made to keep the rate constant through the test (with limited success).

The final series of six tests formed a set of test conditions intended to uncover specific trends in behaviour. The test numbers for this series are prefixed by 'F'. The parameters varied were: pull rate, vertical total stress and type of loading (sustained loading or pull-out). Tighter control over the displacement rate was achieved than during the preliminary series, and with the exception of F5, the target values tabulated here were achieved within a reasonable tolerance.

Test P4 was planned to investigate the effect of leaving the grout to cure for 28 days before pulling out, but insufficient time was available within the research period to

study this. The six final tests were considered to be the best use of the time available, forming a basic study of the effects of different ways of loading the nail under different in-situ stress conditions. The interface tests took less time to prepare and perform.

Test	Pull rate *mm/min*	Surcharge *kPa*	Comments
P1-A	-	100	First test performed under controlled conditions.
P1-B	-	50	Set as base test to compare with other preliminary tests.
P2	-	200	High surcharge test.
P3	-	50	Several attempts made to use high-pressure grouting.
P5	SL	50	Preliminary sustained loading test. Attempt made to use pore pressure instrumentation.
F1	20	50	Base test for the final series.
F2	SL	50	Sustained loading comparison with F1.
F3	20	100	F1 repeated at higher surcharge.
F4	SL	100	Higher surcharge sustained loading to compare with F2 & F3.
F5	100	50	Pull-rate investigation.
F6	4	50	Pull-rate investigation.

Table 3.1 - Test programme: Pull-out and sustained loading tests

Chapter 4. TEST RESULTS

4.1. Introduction

This chapter presents the results from the pull-out and sustained loading tests performed in the laboratory. The pull-out and sustained loading test results fall into two categories: those from the preliminary test series performed to test equipment and establish general trends; and those from the final test series which aimed to compare specific trends in behaviour. In the following sections, the presentation of preliminary test results is accompanied by analysis of the observed behaviour. Results from the final series of tests are then presented, and some basic comparisons between the data from each test are made. More detailed analysis and discussion of the laboratory test data are presented in Chapter 9, where they are compared with trends in behaviour observed from the finite element analyses, and also with the interface test results. The latter are presented separately in section 5.4.

4.2. Pull-out tests

The important quantities logged during pull-out tests were the axial force, P_a, measured at the head of the nail, and the nail displacement, δ. Conventionally, pull-out test results are presented in the form of a plot of P_a against δ. In the graphical results presented in this chapter, the average shear stress acting over the grout surface in contact with soil, τ, is also shown. The area of contact was not constant during testing. The plugs used to contain the liquid grout during setting had tapered diameters, from $108mm$ at the tank wall down to $100mm$ at the face in contact with the grout, figure 2.9. This meant that once the nail was displaced axially the contact area reduced, so the average shear stress on the surface increased for a given load. Therefore, for all tests in the nailing apparatus, τ

was calculated using (15.), where l_{nail} and d_{nail} are the nail length and diameter respectively.

$$\tau = \frac{P_a}{\pi d_{nail}(l_{nail} - \delta)} \qquad (15.)$$

A summary of the pull-out results is given in Table 4.1. Two values of τ for each test are shown in the table. τ_{max} is the value of shear stress corresponding to the maximum nail axial load, and τ_{pp} is the average value of τ calculated over the range $80mm < \delta < 90mm$. The latter is intended to provide a means for comparing the post-peak shear stress measured for the different tests.

It should be noted that accurate measurements of nail diameter were not made following the first two tests P1-A and P1-B. d_{nail} has been approximated as $100mm$ (indicated * in the table), and this figure was used to calculate τ_{max} and τ_{pp}.

4.2.1. Preliminary tests P1-A to P3

The results from test P1-A are shown in figure 4.1. The quantities shown are P_a in kN (left-hand y-axis) and τ in kPa (right-hand y-axis), plotted against δ in mm. The results show a small, sharp peak in P_a near the start of the test, followed by a gradual decline. The value of τ was approximately constant for $55mm \geq \delta \geq 70mm$, but it started to decrease again towards the end of the test. The sharp peak might be due to a high pull-out displacement rate at the start of the test, but this cannot be confirmed since reliable time data were not recorded.

The results from test P1-B are shown in figure 4.2. This test did not exhibit the peak behaviour that was observed in P1-A. A slight reduction in P_a was recorded after $\delta = 20mm$, but this is seen to correspond to a constant value of τ. A similar curve is shown for test P2 in figure 4.3. P_a fell after reaching a slight peak, but the rate of reduction again corresponds to an approximately constant value of τ. The displacement before the development of maximum bond resistance was considerably greater for P1-B and P2 than for P1-A.

Test	σ_v	σ_h	m_{avg}	l_{nail}	d_{nail}	R_{po}	τ_{max}	$\delta(\tau_{max})$	τ_{pp}
	kPa	*kPa*	%	*mm*	*mm*	*mm/min*	*kPa*	*mm*	*kPa*
P1-A	100	-	17.9	860	100*	16	44	1.5	29
P1-B	50	63	-	800	100*	60	30	23	30
P2	200	166	-	890	87.5	8	66	29	65
P3	50	58	-	725	98.5	33	40	3.5	21
F1	50	69	19.4	755	100.5	20	36	10	27
F3	100	101	19.5	755	100.5	22	50	17	41
F5	50	69	17.9	752	100.5	54	50	5.8	27
F6	50	70	19.2	752	100.5	3.2	36	8.6	30

Notes to Table 4.1

σ_v Vertical total stress applied to sample

σ_h Horizontal total stress measured at the tank walls before testing

m_{avg} Average moisture content of the soil samples taken during drilling

l_{nail} Completed length of the grouted nail

d_{nail} Completed diameter of the grouted nail (* approximate)

R_{po} Average pull-out displacement rate recorded during testing

τ_{max} Maximum shear stress (bond resistance) during testing, calculated from (15)

$\delta(\tau_{max})$ Nail displacement at which the above maximum was reached

τ_{pp} Average shear stress, $80mm < \delta < 90mm$

Table 4.1 – Summary of pull-out test results

The main difference between P1-B and P2 was the vertical surcharge applied to the sample: $50kPa$ for P1-B, $200kPa$ for P2. The average total stress at the boundaries of the sample during P2 was approximately 3.2 times that during P1-B. These differences in boundary stress have the effect of raising the bond resistance by a factor of approximately 2.2. In contrast, the final bond resistance measured during P1-A (surcharge $100kPa$) was very similar to that measured during P1-B, in spite of the difference in surcharge.

It was expected that higher pull-out resistances would be recorded at higher in-situ total stresses, since this implied the effective stresses in the soil around the nail would be

higher, allowing the mobilisation of higher shear stresses. Hence the observed trend of τ_{max} increasing with in-situ stress seemed reasonable. The contribution of dilation to soil strength was expected to reduce with increasing in-situ stress, so the factor of 2.2 increase in bond resistance for a factor of 3.2 increase in in-situ stress between tests P1-B and P2 could also be accounted for.

However, the values of τ_{pp} for the three tests did not follow the same pattern. $\tau_{pp} = 65kPa$ for P2 seemed reasonable in comparison to $\tau_{pp} = 30kPa$ for P1-B, but $\tau_{pp} = 29kPa$ for P1-A fell below both of these values when it would have been expected to fall somewhere in between. Two possible reasons for this were: that the pull rate used for the tests was different and that this could affect the measured strength (see below); or that the grout surface area in contact with the soil was different for each test due to incomplete grouting of the annular space between nail and soil. The stiffer response shown by P1-A compared to P1-B and P2 is not easily explained.

Throughout the preliminary series, difficulties were encountered in completely filling the nail borehole with grout. The horizontality of the borehole meant that air was liable to become trapped in a large bubble along the top of the grout, figure 4.4. It was not possible to discover whether this had happened before testing, since the grout section appeared complete at each end of the hole. The defect only became apparent once the nail had been exhumed at the end of the test. The non-circular nails formed in this way made the calculation of bond stresses difficult (it was unclear exactly how much of the grout surface was in contact with the soil), and may also have significantly reduced the normal stresses acting on the nail surface. This problem was eliminated before the final test series by the use of extra breather tubes installed before grouting (see section 2.9).

Sudden jumps in P_a are seen in the results for P1-B and P2. The full data acquisition system was used for these tests, allowing the calculation of instantaneous displacement rate during pull-out. These data were recorded, and are shown with the pull-out shear stress curve for both tests in figure 4.5. The jumps in P_a both correspond to sudden unplanned increases in pull rate. Testing at a constant rate of displacement was difficult to achieve, since control of the hydraulic loading system was carried out by hand (see section 3.2.4). However, the displacement rate was held within a smaller tolerance

during later tests, when the Author had more experience of using the equipment. It was clear from these tests that the strength measured during pull-out tests depended critically on the rate used, and this was therefore identified as a potential area of investigation for the final test series.

The purpose of test P3 was to investigate whether or not applying a pressure to the grout during setting would affect the pull-out resistance. In the event, the pressurising system failed many times. During the setting of the grout, substantial leakage occurred, and the nail borehole was therefore incompletely filled. The resultant loss of bond with the soil made interpretation of the results impossible.

4.2.2. Final tests F1, F3, F5 & F6

The pull-out curve from the first test in the final series, F1, to which the other results will be compared is shown in figure 4.6. It is emphasised that the nails formed during the final test series were all of cylindrical section, the grout bubble problem having been eliminated at this stage. A rounded peak in the shear stress curve over roughly the first half of the test is seen, with the maximum value being reached early in the test. After a pull-out displacement of around $50mm$, τ drops off to approach 70% of peak towards the end of the test. The pull rate during the test is shown in figure 4.10(a). It is seen that the target value of around $20mm/min$ was held within a reasonable tolerance for most of the test, with no large discontinuities in rate having occurred.

The other pull-out tests in the final series each differed from F1 in one respect only. F3 was performed under a higher surcharge, F5 was performed at a faster pull rate, and F6 at a slower pull-rate. The result of F3, figure 4.7, shows very similar behaviour to that seen in F1. Both peak and post-peak values of shear stress are $14kPa$ higher for F3. The peak of the shear stress curve is more rounded than that for F1, and occurs at a slightly greater displacement. The sudden drop in shear stress shown at a pull-out displacement of $4mm$ is certainly due to a sudden drop in pull-rate following a large initial value, figure 4.10(b). (The pull rate was especially difficult to control smoothly during the first moments of the test as is clearly demonstrated here.) Initially, a pull-out rate of over

70*mm/min* was recorded, followed by a value of zero. The pull rate was more stable at around the target value of 20*mm/min* for the remainder of the test.

The result of the faster pull-out test F5 is shown in figure 4.8. The response is seen to be quite different to that observed in F1 and F3. The shear stress reaches a peak value 30% higher than that observed during F1, at a pull-out displacement of only 5*mm*. This is followed by a rapid reduction in shear stress to a steady value identical to τ_{pp} for F1, which remains approximately constant for the remaining 70% of the test. The pull-rate during the test is shown in figure 4.10(c). The target pull-rate for this test was 100*mm/min*, but it emerged that the hydraulic pump was unable to supply fluid at a sufficient rate. The average achieved rate of 54*mm/min* represents the maximum possible value attainable with the apparatus used. An unexpected advantage of this was that the rate was relatively constant since no user intervention was required during the test – all valves were left fully open.

Finally, figure 4.9 shows the result from the slower pull-out test F6. The shear stress curve is extremely similar to that from test F1, with the exception of the last 30*mm* of pull-out displacement, where the shear stress unexpectedly increases slightly. The reason for this is unclear, as no abnormal behaviour was noted during the later stages of the test. The pull rate recorded during the test is plotted in figure 4.10(d). The plot shows that the pull-rate was held reasonably constant for the duration of the test at close to the target value of 4*mm/min*.

The main features of behaviour observed during the final series of pull-out tests may be summarised as follows:

- Both the peak and post-peak bond resistance of nails increased with in-situ stress
- At a given in-situ stress, the bond resistance recorded towards the end of tests was similar regardless of pull-out displacement rate
- High initial values of bond resistance were recorded at the highest pull-out displacement rate
- The shear stress curves recorded during the medium and slow pull-out rate tests were very similar in terms of their shape and also in terms of the values of τ_{max} and τ_{pp}

Further discussion of the pull-out test results described in this section is presented in Chapter 9, following on from the advances in understanding that were made during the numerical analyses described in the next three chapters.

4.3. Sustained loading tests

A summary of the sustained loading test results is given in Table 4.2. The quantity τ_f is not shown for test P5 - the surface area of grout in contact with the soil during this test was not clear, preventing the calculation of shear stress. This was due to the grouting air-bubble problem described in section 4.2.1.

Test	σ_v	σ_h	m_{avg}	l_{nail}	d_{nail}	τ_{stable}	τ_f	t_{final}
	kPa	*kPa*	*%*	*mm*	*mm*	*kPa*	*kPa*	*hours*
P5	50	64	19.4	850	98	-	-	25
F2	50	69	19.5	755	102	26	30	456
F4	100	102	18.5	755	101	34	39	280

Notes to Table 4.2 (refer to the notes to Table 4.1 for other definitions)

τ_{stable} Shear stress corresponding to the maximum stable applied load

τ_f Shear stress corresponding to the applied load that caused the nail to fail

t_{final} Duration of test

Table 4.2 – Summary of sustained loading test results

4.3.1. Preliminary test P5

The behaviour observed during test P5 is shown in figure 4.11. This test was performed from similar conditions to the pull-out test P1-B. The graph shows the displacement of the nail on the left-hand y-axis and the nail axial force plotted against time. The main objective of this test was to determine the maximum bond resistance that could be mobilised under conditions of constant load. In this respect, P5 was not successful, since the nail failed after the application of the first load increment. The increment was

intended to be equivalent to half the pull-out load measured during test P1-B. It was considered unlikely that the nail would fail at this level, since previous researchers had found that results from the two types of test were broadly comparable, Clouterre (1991).

After the test, it was discovered that the nail had been incompletely formed in the bore hole, so that insufficient surface area was available for interface stress mobilisation. In addition, the normal stresses acting on the bottom half of nail were probably significantly reduced, since there were no earth pressures bearing down on the top half. It is therefore unsurprising that the nail failed at such a low load. Displacement of the nail stopped at around $140mm$ when the loading ram reached the extent of available travel.

It is interesting to note that the load applied at the nail head fell during the test as the nail was displaced towards the loading ram. This was due to the pressure falling in the hydraulic system as the ram piston moved backwards and drew fluid from the accumulator. It is seen, however, that the nail kept on accelerating even though the applied load was dropping. This might be due to the shear stress staying relatively high due to the reduction in available grout surface area with nail displacement (see section 4.1).

P5 was the only test performed which was instrumented with pore water pressure transducers at the grout-soil interface. The instrumentation used is described in section 2.6.4. The data recorded by the transducer during the test are plotted in figure 4.12. Since all the measurements were negative compared to atmospheric pressure, they have been plotted as positive suctions on the left-hand y-axis. It is seen that once the suction indicated by the transducer reached a maximum value just after the application of the load increment, it slowly dissipated for a few hours, before increasing again until the nail came to a stop as the loading ram reached its maximum movement. Then the reading dropped suddenly, only to start increasing again shortly thereafter.

It was unclear whether the fluctuation in the readings described above represented real phenomena which had occurred within the soil, or were caused by drift of the signal from the transducer. Prior to installation of the instrument, drifts in output signal equivalent to $5kPa$ over a few hours had been recorded under laboratory ambient conditions. However, it was reasonable to deduce that the soil was generally in a state of

capillary suction during and before loading, and that that suction increased significantly when the load was applied.

In fact, the pore pressure response in figure 4.12 was found to be consistent with the results of the finite element modelling described in section 8.4.5. This suggests that the signal drift of the transducer might have been reduced after it was installed in the nailing apparatus, and that the output, therefore, corresponded closely to the suctions present at the grout-soil interface. It is probable that the temperature within the apparatus was relatively unaffected by daily fluctuations of laboratory temperature; this may have contributed to a more stable transducer response.

Also shown in figure 4.12 is the axial velocity of the nail in *mm*/hour, derived from the displacement data plotted in figure 4.11. It is interesting to note that the shape of this plot bears a resemblance to the suction plot at times greater than ten hours. This is particularly noticeable around t = 15 hours when the velocity of the nail suddenly dropped, then increased again. This occurred at the same time as a small fluctuation in the applied load. The reason for the fluctuation in load is not clear.

This test will not be considered further in relation to the final test series for the same reasons as were stated in section 4.2.1 above. It did however, supply some interesting data regarding the state of pore water pressures around the nail during loading. It also served to test the hydraulic loading system, which had been substantially modified to accommodate the sustained load testing of nails.

4.3.2. Final tests F2 and F4

The results of test F2 are shown in figure 4.13. The 'Shear stress' shown in this plot, on the right-hand y-axis, is calculated in the same way as was described in section 4.1 earlier. The implication is that although a given force applied at the head of a nail may remain constant, the shear force acting over the surface area of the grout will not, since this area will decrease as the nail displaces.

During test F2 the shear load was initially applied in three approximately equal increments. After the application of the first two increments, the nail had not moved

significantly - whatever movements occurred stabilised quickly. Following the application of the third increment at 54*h* the displacement increased more substantially, and the nail was left for one day to stabilise. On returning, it was noted that the load had dropped by a few Newtons. The pressure in the hydraulic system was raised slightly to compensate, and the apparatus again left for 24*h*. A similar drop in load was noted, and the compensatory action repeated. In both cases the load was ultimately increased to a level slightly above that at the start of the third load increment. This was due to a time lag in the system between the setting of the regulator and the subsequent increase in load. The effect of this on the nail displacement is apparent if the curve is examined carefully between t = 54*h* and 126*h*. The line in this region actually consists of three curves, all levelling off to some extent before the load was again fractionally increased.

At t = 126*hr* the load was increased suddenly due to an operator error. The velocity of the nail again increased in response to this. After 24*h* it was decided that the nail movement was unlikely to stabilise within the displacement capacity of the loading ram, and the load was reduced to the level of the second increment. This caused the nail to stop moving completely, so after a 24*h* period the load was increased slightly. This process was repeated until the load was increased just beyond the value at which it had previously been considered unstable. Displacement of the nail then restarted, but at a relatively low rate, and after 8 days of approximately constant load the nail velocity had dropped below 0.1*mm*/day and was still dropping, and the nail was considered stable. The final load increment caused the nail to displace very rapidly towards a limit of 160*mm* when the loading ram ran out of travel.

It will have been noted that control over the load increments during this test was rather poor. This was mostly due to the difficulty of adjusting the air pressure regulator connected to the accumulator with sufficient accuracy. Adjustment of the regulator unit was afforded by a coarsely threaded tap which was unpredictable to use, in that a given rotation of the tap sometimes doubled the output pressure immediately, and sometimes increased the pressure by a smaller amount over a period of approximately 30 minutes. The peculiarities of this device were better understood by the end of F2, and the load increments during F4 were more tightly controlled.

The results of test F4 are shown in figure 4.14. The procedure followed during this test was more precisely defined than during F2. Instead of maintaining loads until the nail appeared to have stopped moving by any significant amount, the velocity was taken as a critical measure of whether or not the nail was stable. The critical velocity was set at the value deduced from the displacement curve at 288*h* during F2. The gradient at this point was approximately $0.05mm/h$. During F4, the nail loading was incremented once the velocity of the nail (calculated daily) dropped below this value.

The first four loading increments applied during F4 were intended to correspond to 20, 40, 60 and 70% of the maximum value of P_a recorded during pull-out test F3 performed from the same initial conditions. The achieved load ratios (in terms of τ) were 21, 46, 64 and 73% respectively, due to the time lag associated with the pressure regulator. The nail velocity dropped below the critical value within one or two days following the application of all three of the initial loading increments, but started to increase more significantly following the fourth. Following the application of this increment, the pressure in the hydraulic system was held constant, so keeping the axial load constant. The shear stress acting over the nail thus increased as the nail displaced, but the nail still reached a stable position after 7 days. A further increase in load of similar size to the fourth increment was then applied, causing the nail to fail completely in that the loading ram once more reached the extent of available travel.

The main features of behaviour observed during the final series of sustained loading tests may be summarised as follows:

- The bond resistance of nails increased with in-situ stress.
- Time dependent movements of the nail were observed even at low loads.
- After the application of larger loads - equivalent to greater than approximately 80% of τ_{pp} measured during an equivalent pull-out test – the nail was able to reach a stable position, but only after a substantial axial displacement of the nail had occurred.
- The results from F2 suggest that it might be able to limit the above displacement by subjecting the nail to an unload-reload cycle.

The sustained loading test results are discussed further in section 9.3.3.

Chapter 5. INTERFACE TESTS

5.1. Introduction

A series of interface tests were undertaken to measure directly the friction between the clay and grout used during the nailing tests. Seven tests were performed at different displacement rates and vertical stresses. A simple numerical model of the test was developed, based on a finite difference solution scheme. This was able to predict qualitatively the trends observed during the laboratory interface tests.

5.2. Interface test equipment

The tests were carried out in a standard 60×60*mm* Casagrande direct shear box. Samples were prepared by pouring grout onto a clay sample cut to fit the bottom half of the shear box. To allow grout to be placed on top of the clay half of the sample, a mould was devised in which to prepare the sample before placing in the shear box for testing. The mould was constructed from Dural, held together by a combination of bolts and dowels, figure 5.1. It was constructed slightly undersize (59.9*mm* square) to facilitate transfer of the sample to the shear box. The bottom half of the mould also served as a sample cutter. The mould could be completely disassembled around the sample to avoid damage or disturbance before testing. Upon reassembly, dowels were inserted vertically through the side panels of the mould to ensure the exact size and shape were retained.

The shear box was powered using an electric motor operating through a five speed gearbox and worm drive through to the loading ram. Part of the gear train ran outside of the body of the gearbox, to allow the use of different gears and obtain drive speeds outside the normal range. By reversing the position of the two standard gears, the maximum driving rate was increased by a factor of 4 to 1.2*mm*/minute. The horizontal load on the shear plane was measured using a proving ring. Vertical and horizontal movement of the

shear box was measured using dial gauges. It was not considered worthwhile setting up electronic data acquisition due to the small number of tests performed.

5.3. Interface test procedure

5.3.1. Sample preparation

The samples used in the interface tests were cut from single clay blocks of the same type as those used in the pull-out and sustained loading tests. The Casagrande shear box would have been difficult to seal when placing the grout on top of the clay. The interface sample was therefore first prepared in a separate sealed mould, capable of containing the liquid grout, under pressure if desired. Initially, the bottom half of the mould was filled with clay. This was achieved by first roughly cutting the clay sample to size by hand, then pressing the bottom half of the sample mould down over the clay. Excess clay was trimmed from the top and bottom face. The two halves of the mould were then joined and connected to the base.

When the mould was assembled, the grout was mixed by hand and poured on top of the clay. The grout water content was the same as that used in the pull-out tests (40%), typical quantities being 120*g* ordinary Portland cement, 72*g* water. The grout was left to set for 1 day; the mould was then carefully disassembled around the sample by first knocking out the dowels, then completely unbolting all fasteners. In this way, the sample was recovered with minimal disturbance. It was then transferred to the shear box, which was then placed in the direct shear apparatus, figure 5.2. Strips of shim were placed under the loose base, to ensure that the top of the clay remained slightly proud of the lower half of the shear box. A small gap was created between the two halves of the shear box by inserting there 1*mm* thick spacers, shaped to allow easy removal upon application of the vertical load. The top platen was placed on top of the interface sample, and the vertical load applied. In accordance with recommendations made by Jewell (1987), the top platen was locked to the top half of the box, improving the symmetry of the boundary conditions at the top and bottom of the sample. The spacers between the shear box halves were removed, and water poured into the bath surrounding the sample, which was then left

under the specified vertical load for one day. During this period, a dial gauge was placed in contact with the top of the loading hanger, to record the vertical consolidation deformation. After one day had elapsed, this reading had always settled to a constant value within the accuracy of the gauge ($0.01mm$ divisions), and the sample was considered stable and ready for testing.

5.3.2. Test procedure

Dial gauges reading the horizontal shear displacement, vertical displacement and load (via the proving ring) were moved into place and zeroed. The required displacement rate was obtained by selecting gears on the drive unit, and also by switching two of the gear train wheels mounted externally in the case of the fastest test. When the test started, readings were taken at predetermined intervals until the bottom half of the box had travelled through approximately $5mm$. This was the extent of travel allowed by the safety cut out, which was essential in case the rig was left unattended.

Once the test was complete, the sample was immediately withdrawn from the shear box and a moisture content sample taken from the sheared interface. The bottom (clay) half of the sample was also taken as a bulk moisture content sample, to investigate whether water had been drawn to the interface during shearing. The next interface sample could then be placed in the rig to consolidate ready for testing the following day.

5.3.3. Testing programme

The test programme for the interface tests is shown in Table 5.1. Tests I1 and I2 were preliminary tests undertaken while still establishing a standard test procedure. The remainder were all prepared and carried out under the same conditions.

Test	Shearing rate *mm/min*	Surcharge *kPa*	Comments
I3	0.3	50	Set as base test to compare with other tests
I4	1.2	50	Fast test
I5	0.01	50	Slow test
I6	0.3	100	Medium surcharge
I7	0.3	200	High surcharge

Table 5.1 - Test programme: Interface tests

5.4. Interface test results

The results from the interface tests I3 to I7 are summarised in Table 5.2. The first two columns of output data in the table are best referred to along with the graphical results, which are described later in this section. The last three columns, however, may be discussed independently. The readings, m_i and m_b show that large local increases in moisture content occurred at the interface between soil and grout in all tests compared to the bulk of the clay. Typically the difference was measured at around 10%, and was even higher for I4. Moisture content readings were not taken during I3. These readings are probably due in part to the infiltration of water from the grout before it set, but they might also be explained by the existence of a thin shear zone in the clay adjacent to the grout-soil interface. Here, dilation of the soil associated with large plastic strains would cause capillary suctions, drawing pore fluid inwards from the bulk of the clay sample and locally raising the water content.

Values for y_0 are similar for all tests with the exception of I7 which was performed at the vertical stress of $200kPa$. The settlement of this sample was so much bigger than the others that the test had to be repeated. During the first attempt, the grout block moved down into the bottom half of the shear box. This was only discovered when the test was complete, and an extremely high sample strength had been recorded. The results of this

test were abandoned; the results presented here are for the rerun I7. To prevent the same problem occurring, thicker strips of shim were placed beneath the base of the shear box, so that the interface lay at the usual height after the sample had consolidated.

Test	*Load rate* *mm/min*	σ_v *kPa*	$\left(\frac{\tau}{\sigma_v}\right)_{max}$	x_1 *mm*	m_i *%*	m_b *%*	y_0 *mm*
I3	0.3	50	1.28	1.38	-	-	0.05
I4	1.2	50	1.33	1.35	37.3	20.9	0.05
I5	0.01	50	1.01	0.58	29.9	21.8	0.06
I6	0.3	100	0.93	1.27	29.9	21.3	0.05
I7	0.3	200	0.74	1.73	31.0	20.1	0.28

Notes to Table 4.3

σ_v Vertical total stress applied to sample

τ Shear stress on interface measured during test

x_1 Shear displacement at which maximum shear stress was recorded

m_i Moisture content of clay trimmings taken from the interface following testing

m_b Moisture content of the bulk of the clay sample

y_0 Settlement of the top platen under the vertical load before the start of shearing.

Table 5.2 – Summary of interface test results

The results from I3 to I7 are shown in figures 5.3 to 5.7 respectively. The upper curve in each plot shows the ratio of the interface shear stress, τ, to the vertical stress, σ_v, imposed on the sample during testing. The area over which shearing takes place actually changes during any direct shear test, but this effect may be disregarded if the ratio τ / σ_v is considered. Also shown, by the lower plot, is the vertical movement of the top platen, and hence the top half of the shear box. Both quantities are conventionally plotted against the relative horizontal displacement between the two box halves.

The general behaviour seen during the tests was as follows. The shear load first increased quickly, then less quickly towards a peak value attained before the shear

displacement reached $2mm$. In the same period, the top half of the box first dropped, then started to rise. Under the influence of higher vertical stresses (I6 and I7), the size of the load peak reduced, while the end points remained similar. The strength measured towards the end of the test was very similar for all except the fast test I4.

The results shown in figure 5.3 for I3 are very similar in appearance to those obtained from a drained shear box test on dense sand. The main difference is that the vertical displacements measured during the interface tests are much smaller, suggesting that the dilation angle of the clay is quite small. However, the peak in τ/σ_v is large, a feature normally associated with soils having a large dilation angle. This can be explained by an increase in effective stress in the zone of soil under shear, due to pore water suctions generated as the clay dilates. The suctions do not have time to dissipate, because of the low permeability of the soil. When the soil stops dilating (at critical state), the suctions dissipate, and both effective and shear stresses decrease.

This explanation of behaviour is consistent with the other interface test results. Test I4, carried out at a faster load rate, showed a larger peak in τ/σ_v since the suctions had less time to dissipate. The slower test, I5, showed a smaller peak suggesting that greater drainage occurred. Tests I6 and I7 were both performed at the same load rate as I3, but at higher vertical stress levels. The increases in vertical stress from $50kPa$ in I3, to $100kPa$ in I6, and $200kPa$ in I7 caused corresponding decreases in the amount of dilation and consequently, corresponding decreases in the size of the τ/σ_v peak.

The main features of behaviour observed during the interface tests were:

- The interface resistance increased with load rate,
- The interface resistance increased with applied vertical load.

The trends observed from the results can be explained by considering the interaction between soil dilation, pore water flow and effective stress. The interface test results are discussed further, and in relation to the nailing tests, in section 9.3.4.

5.5. Numerical modelling of interface tests

A simple numerical model based on a finite difference solution scheme was developed to investigate trends observed during the laboratory interface tests. The interface between the clay and the grout was modelled as a discrete shear zone, using standard interface element modelling (see for example Burd and Brocklehurst, 1992). The shear zone provided the boundary conditions for the finite difference analysis of elastic one-dimensional consolidation in the clay, using the standard theory developed by Terzaghi. The formulation and results are presented here in a self contained section, since this formed a small part of the numerical work performed, and does not closely relate to the finite element analysis.

5.5.1. Finite difference formulation

(a) Shear zone behaviour

A schematic of the model is shown in figure 5.8. The problem is characterised by a constant vertical total stress σ_v, imposed by the loading hanger, and a shear displacement u imposed on the surface of the clay at the interface. The effective stresses within the interface shear zone are shown in figure 5.9. For elastic deformation in the shear zone, the stiffness of the interface in the shear and vertical directions may be calculated in terms of the normal drained elastic parameters assuming plane strain conditions apply ($\varepsilon_h = 0$):

$$K_x = \frac{\tau}{u} == \frac{E'}{2h(1+\nu')} \tag{16.}$$

$$K_y = \frac{\sigma'_v}{v} = \frac{E'(1-\nu')}{(1-2\nu')(1+\nu')h} \tag{17.}$$

where v is the normal displacement of the top surface of the interface and h is the interface thickness. Note that for the purpose of this analysis, compressive stresses and strains are taken as positive. When the interface becomes plastic, behaviour may be modelled using an approach based on classical plasticity theory as described below. (This analysis follows

closely the approach used to model elastic-plastic interface behaviour in finite element analysis). Displacement increments (rates) may be divided into elastic and plastic components:

$$\dot{u} = \dot{u}^e + \dot{u}^p$$
$$\dot{v} = \dot{v}^e + \dot{v}^p \qquad (18.)$$

Stress rates are related to elastic displacement rates by:

$$\dot{\sigma}' = [D]^e \dot{\mathbf{u}}^e \qquad (19.)$$

where

$$[D]^e = \begin{pmatrix} K_x & 0 \\ 0 & K_y \end{pmatrix}, \ \dot{\mathbf{u}}^e = \begin{pmatrix} \dot{u}^e \\ \dot{v}^e \end{pmatrix} \text{ and } \dot{\sigma}' = \begin{pmatrix} \dot{\tau} \\ \dot{\sigma}' \end{pmatrix}$$

The plastic behaviour was represented by a Mohr-Coulomb material model. Yield function and plastic potential, f and g, were defined in terms of the friction and dilation angles respectively,

$$f = \tau - \sigma'_v \tan\phi \qquad (20.)$$

$$g = \tau - \sigma'_v \tan\psi \qquad (21.)$$

A simple dilation cut-off algorithm was adopted, whereby the dilation angle was set to zero once the volumetric strain exceeded a certain value. Ideally, a variable dilation angle model would have been used, such as the Wroth model described in section 7.6.1. This would not have been straightforward, however, since the mean effective stress in the interface during plastic shear is not easily deduced.

Stress rates are related to general elasto-plastic displacement rates by:

$$\dot{\sigma}' = [D]^{ep} \dot{\mathbf{u}} \qquad (22.)$$

where the plastic stiffness matrix for stresses lying on the Mohr-Coulomb yield surface is taken from e.g. Brocklehurst (1993) as

$$[D]^{ep} = \frac{K_x K_y}{K_x + K_y \tan\phi \tan\psi} \begin{bmatrix} \tan\phi \tan\psi & \tan\phi \\ \tan\psi & 1 \end{bmatrix} \qquad (23.)$$

(b) Elastic consolidation in the clay

The next step is to consider consolidation behaviour. Terzaghi's expression for one-dimensional consolidation is ,

$$\frac{\partial u_w}{\partial t} = C_v \frac{\partial^2 u_w}{\partial y^2} \tag{24.}$$

where u_w is the pore water pressure, t is time and y is the vertical displacement downwards from the interface into the clay. For an elastic material, C_v may be shown to be given by

$$C_v = \frac{kE'(1-\nu')}{\gamma_w(1-2\nu')(1+\nu')} \tag{25.}$$

Writing (24.) in finite difference form,

$$\frac{u_w(y+\Delta y,t)-2u_w(y,t)+u_w(y-\Delta y,t)}{(\Delta y)^2} = \frac{1}{C_v \Delta t}\left(u_w(y,t+\Delta t)-u_w(y,t)\right) \tag{26.}$$

which may be rearranged thus

$$u_w(y,t+\Delta t) = u_w(y,t)+\frac{C_v \Delta t}{(\Delta y)^2}\left\{u_w(y+\Delta y,t)-2u_w(y,t)+u_w(y-\Delta y,t)\right\} \tag{27.}$$

This is an 'explicit scheme' which is stable provided that (see for example Gerald and Wheatley, 1989):

$$\frac{C_v \Delta t}{(\Delta y)^2} < \frac{1}{2} \tag{28.}$$

(c) Combining shear zone and consolidation behaviour

Consolidation and constitutive model are now combined through continuity and the principle of effective stress. Any movement of the interface in the positive y-direction is given by the flow out of the interface:

$$\dot{v} = -\frac{k}{\gamma_w}\frac{\partial u_w}{\partial y} \tag{29.}$$

Since the vertical total stress remains constant, changes in vertical effective stress are given by

$$\dot{\sigma}'_v = -\dot{u}_w \tag{30.}$$

Substituting (29.) and (30.) into (22.) leads to

$$\begin{Bmatrix} \dot{\tau} \\ -\dot{u}_w \end{Bmatrix} = [D]^{EP} \begin{Bmatrix} \dot{u} \\ -\frac{k}{\gamma_w}\frac{\partial u_w}{\partial y} \end{Bmatrix} \tag{31.}$$

From the above, the following are derived in terms of finite differences

$$\tau(t+\Delta t) = \tau(t) + K_{xy}\Delta t\left[\dot{u}\tan\phi\tan\psi - \frac{k}{\gamma_w}\frac{u_w(\Delta y,t)-u_w(0,t)}{\Delta y}\tan\phi\right] \tag{32.}$$

$$u_w(0,t+\Delta t) = u_w(0,t) + K_{xy}\Delta t\left[-\dot{u}\tan\psi + \frac{k}{\gamma_w}\frac{u_w(\Delta y,t)-u_w(0,t)}{\Delta y}\right] \tag{33.}$$

where

$$K_{xy} = \frac{K_x K_y}{K_x + K_y\tan\phi\tan\psi} \tag{34.}$$

(d) Solution procedure

1. Apply vertical stress, set $u_w = 0$ throughout.
2. Find u to just cause yield in the shear zone (Note: this assumes zero dilation).
3. Apply further increments of u in the following loop:
   i. find $\tau(t+\Delta t)$
   ii. find $u_w(0,t+\Delta t)$, then $u_w(y,t+\Delta t)$ for all y
   iii. impose values of u_w as new boundary condition for next calculation step.

5.5.2. Results

The finite difference scheme was implemented in the MATLAB programming language. The effects of shearing rate and vertical stress were investigated during five analyses, assuming typical material properties for a dense, low permeability soil. The dilation angle was assumed to be constant until a volumetric strain of 0.05%, when it was reduced to zero.

The results from three analyses performed at shear rates, R_{shear} corresponding to R_{shear}/k values of 500, 5 000 and 50 000 are shown in figure 5.10. Greater shear resistance is mobilised at the higher displacement rates due to the higher effective stress in the shear zone, caused by suctions induced in the dilating soil. This trend in behaviour corresponds well to that shown during the laboratory interface tests. Clearly the shape of the computed shear stress curve could be improved by the use of a more complex dilation model.

The effect of increasing the vertical total stress on finite difference predictions for the case R_{shear}/k = 5 000 is shown in figure 5.11. Note that the vertical scale is different to that in figure 5.10. As would be expected, a higher shear resistance is mobilised at the higher stress levels, but the increase in resistance is not in proportion to the increase in stress. This is because the plastic behaviour described by the model is not dependent on the initial stress, so that the magnitude of the extra shear strength due to dilation is the same in all cases. The results are plotted in terms of τ/σ_v, and so the relative effect on strength is seen to decrease with increasing vertical total stress. Qualitatively, this behaviour is similar to that observed during the laboratory tests

Chapter 6. NUMERICAL MODELLING OF GROUTED NAILS

6.1. Introduction

At the beginning of the research project, the main emphasis was placed on experimental work. It was assumed that this would be the best way of investigating the mechanism of bond between nail grout and soil, especially after the measurements successfully obtained by Chang (Milligan et al.,1997). Numerical modelling of the problem was planned as a relatively small, separate exercise to take place near the end of the experiments, using previously developed software to check how well the experimental results agreed with theory.

After it became clear that the detailed instrumentation planned for use at the grout-soil interface was not going to be employed during the main test series, the decision was taken to place more emphasis on theoretical and numerical examination of the pull-out and sustained loading processes. Two pieces of finite element analysis software were considered: *Plaxis V7.0* is a commercially available package for rock and soil analyses, developed by Plaxis BV, based in the Netherlands; *Cavexp* was originally formulated as a one-dimensional axisymmetric program for cavity expansion analyses - it has been developed by several past and present members of the Oxford Soil Mechanics Group.

This chapter specifies the problem to be analysed, and compares *Cavexp* and *Plaxis* in terms of their ability to model this problem. *Cavexp* was ultimately selected as the most suitable program; the second half of this chapter describes the theory behind the program, and its capabilities at the start of the project. The extensive development required before it could be used to model the problem specified is the subject of the next chapter.

6.2. Specification of analysis

The aim of this stage of the work was to predict the type of behaviour observed during pull-out and sustained loading from standard directly measurable material properties. This required detailed models of: the loading imposed on the soil by the nail; the boundary conditions some distance away from the nail; and the material behaviour of the soil itself. The models are presented in this order since the loading encountered dictates the type of mesh required to model the soil. Before proceeding to more detailed descriptions of these models, it is first necessary to describe the general assumptions made in modelling the nailed soil.

The first and most important assumption of all the analyses performed was that axisymmetrical conditions applied around the nail (i.e. no variation of internal forces or displacements was expected in a circumferential direction around the nail axis). In the pull-out apparatus, conditions around the nail were clearly not axisymmetric. The boundary stresses were different in the vertical and horizontal directions, and the boundaries themselves were square. Nonetheless, provided that the boundary stresses in the horizontal and vertical directions are approximately equal, the stresses in the soil immediately surrounding the nail may well be very nearly axisymmetrical, since the stress field here is dominated by the effect of the circular hole driven through the medium. Laboratory tests on model piles in clay, Martins (1983), indicated that the majority of soil plastic deformation around a loaded cylindrical inclusion occurs within a narrow band or annulus close to the surface of the inclusion, so it is reasonable to assume that it is this region which largely governs the load-displacement behaviour.

Typical geometries of soil nails and piles are compared in figure 6.1. The obvious difference is that of orientation. Piles are generally installed vertically, whereas soil nails are installed approximately horizontally. This has implications regarding the boundary stresses assumed during numerical or theoretical analyses. To aid comparison between the two cases, the following effective stresses are defined in relation to the nail or pile axis: radial σ'_r, circumferential σ'_θ, axial σ'_z and shear τ_{rz}. In addition, the following total

stresses are defined at the boundaries: vertical σ_v and horizontal σ_h. In the case of a pile, the z-axis is vertical, whereas in the case of a soil nail, it is horizontal.

In general, salient conditions at a point below the surface in real undisturbed ground are well described by a vertical total stress, a horizontal total stress and the position of the water table to define pore pressures and hence effective stress values. The horizontal stress σ'_h is often found to be approximately constant in all directions on a given horizontal plane, so assumptions of axisymmetry around piles are likely to be accurate. This is not the case in the soil nailing geometry where the boundary stresses in the z-plane will vary between σ_v and σ_h. The program *Cavexp*, which was conceived to model the effects of cavity expansion in relation to pile driving and pressuremeter testing, allows different boundary stresses in the vertical and horizontal directions in relation to a pile geometry. In using the program to analyse soil nailing problems, these boundary stresses were set to be equal, since both z- and r-axes were in this case horizontal. The effects of different boundary stresses in the vertical and horizontal directions on soil nail behaviour was therefore not modelled since this would preclude the assumption of axisymmetry.

The second major assumption was that conditions of plane strain existed in the axial direction, i.e. $\Delta\varepsilon_z = 0$. This implied that all deformations were confined either to the r-θ plane radially towards or away from the nail, or to shear deformations in the direction of the z-axis, leading to shear strains $\Delta\gamma_{rz}$. At some distance from the nail, the total radial and circumferential stresses tend to some constant value (ignoring any small shear forces this far from the nail), as prescribed by overall equilibrium. The condition here is therefore more akin to plane stress, and strains $\Delta\varepsilon_z$ will occur. However, the assumption of plane strain is reasonable close to the nail, and this was the main area of interest for the analyses.

6.2.1. Inner boundary conditions

The type of loading encountered by the soil changes through the sequence of construction. The construction sequence was split up into the distinct stages listed below:

i. **Starting condition of the soil.** The soil is assumed to be homogeneous and isotropic, with an initial isotropic total stress and uniform pore water pressure throughout the sample.

ii. **Drilling**. To simulate the effect of drilling a hole through the sample, the total radial stress on the inner radius is reduced to zero over a short time period.

iii. **Waiting**. From the laboratory tests, it had been noticed that significant radial movement of the soil might be expected during the short interval between drilling and grouting, especially at high in-situ stress levels.

iv. **Grouting.** Over a short time period, the pressure acting on the inner radius is increased to simulate the effect of introducing grout. Since the water content of grouts used is generally high, the pore water pressure on the inner boundary is also increased to the same pressure.

v. **Setting.** The time that a grout takes to reach *final set* depends on several factors including: cement type, water content and ambient temperature. During this time, it is assumed that the grout pressure and the pore water pressure on the inner boundary are constant.

vi. **Curing.** The loading on the inner boundary then undergoes a transition from pressure to displacement control. During the days between the final set and nail loading, the grout might expand, contract or stay constant. The effect of the soil stresses on the grout movement are negligible, so this is best described as a displacement controlled process. The inner boundary is assumed to be impermeable from this point; little flow is expected into or out of the hardened grout.

vii. **Loading.** The inner radius is then subjected to an out of plane shear loading in the direction of the z-axis, controlled either by displacement to simulate a pull-out test, or by load to simulate a sustained loading test.

A summary of the proposed nail loading regime is shown in Table 6.1. The values chosen for the magnitudes of the loads and stage durations are discussed in more detail in section 8.3, which describes the analyses performed in the finite element parametric study.

Stage	Description	Inner boundary conditions		
		Radial	*Axial*	*Flow*
i.	Initial conditions	Cavity pressure equal to the in-situ radial stress.	Displacement fixed at zero.	Permeable. Pore water pressure set to initial condition.
ii.	Drilling	Cavity pressure reduced to atmospheric.		Impermeable.
iii.	Waiting			
iv.	Grouting	Cavity pressure increased to grouting pressure.		Permeable. Pore water pressure brought up to grouting pressure.
v.	Setting			
vi.	Curing	Switch to displacement control. Imposed displacement either positive (expansion), negative or zero.		Impermeable.
vii.	Loading	Displacement fixed at value from previous stage.	Displacement or shear force applied as appropriate.	

Table 6.1 – Change of inner boundary conditions through simulated test sequence

6.2.2. Soil modelling

The soil model used had to be two-phase. In other words, full allowance had to be made for the separation of total stress into effective stress and pore water pressure components, and for time dependent consolidation. The material model would then be applied to computed strains to deduce effective stresses. The choice of material model was

not initially clear, although it was thought that the highly overconsolidated plastic clays under consideration would probably best be simulated by a frictional soil model.

6.3. Available FE analysis packages

Two packages available within the Soil Mechanics Group at Oxford were considered. Before *Cavexp* could be used, it had to be extended to include additional degrees of freedom for axial displacement and pore water pressure. *Plaxis* possessed the necessary capabilities, but the scope for modification to suit individual problems was limited because the source code could not be altered. The features of each program are now described and compared.

6.3.1. *Plaxis*

Plaxis is a two-dimensional analysis package developed for use by practising engineers. The geometry of analyses is input graphically – i.e. the user essentially sketches the boundaries using a CAD-type interface, and assigns material models to closed blocks. Boundary conditions are applied to the edges of these blocks, those for displacement and stress being applied separately to those for flow of water. The program was able to model in two dimensions some of the boundary constraints imposed by the laboratory nailing apparatus - in particular the rigid, impermeable walls at the ends of the soil tank. However, since the program was used in axisymmetry mode, the geometry was assumed to be that of a thick cylinder of soil surrounding a $1m$ length of nail. The top, bottom and sides (running parallel to the nail) of the tank were therefore modelled as a single continuous boundary.

The program includes a range of simple material models and a more complex model based on Cam Clay. Initially, an elastic model was used to investigate basic behaviour, and to facilitate interpretation of the results obtained. A consequence of using this model was that incorporating of nail installation stages in the analysis had little effect

on the final pull-out response of the nail, since the material behaviour was unaffected by its stress history.

In fact, the nail loading stage proved to be the most difficult to model accurately. The soil adjacent to the nail was locally subjected to large shear strains during loading. When examining the calculated effective stresses within a typical element at the inner boundary, large variations were found in the states of adjacent stress points. The total stresses within an element were constrained to be in equilibrium, so the pore pressures fluctuated in opposite phase to the effective stresses. (It is possible that this behaviour was due to a local instability of the type described in section 7.6.8.) These variations, which occurred regardless of the type and density of elements used, led to doubts as to whether the program would be able to realistically model pull-out response. As a result, attention was switched to the development of *Cavexp*.

6.3.2. *Cavexp*

Cavexp as it was originally designed is described by Yu and Houlsby (1990) and Yu (1990). The novel feature of the program at the time was that the displacement interpolation functions (shape functions) were chosen so as to minimise the kinematic constraints imposed on the nodal velocities by the constant volume condition. The authors were particularly concerned with undrained cavity expansion associated with pressuremeter loading. During this process, the material was assumed to be nearly incompressible, with Poisson's ratio of very nearly ½ - typically a value of 0.49 was assumed. Yu and Houlsby (*loc. cit.*) observed that the displacements around a cylindrical cavity in an infinite medium under this loading become of the form:

$$u = C / r \tag{35.}$$

where C is a constant and r is the radius. Conventional linear displacement interpolation functions are unable to capture this type of behaviour, whereas the new function:

$$u = C_0 / r + C_1 r \tag{36.}$$

was able to model it exactly, and furthermore was able to exactly match the elasticity solution for cavity expansion in compressible and non-compressible materials (see section

A1.1, Appendix A). The results from the program confirmed that the new displacement interpolation was preferable to the conventional linear type for the types of problem outlined above.

At the start of the project, *Cavexp* was still a one-dimensional analysis tool, capable of modelling the displacement- or pressure-controlled expansion of cylindrical and spherical cavities formed in one-phase materials. The program used a mesh of two-node linear elements, each element having only one (radial) degree of freedom. Consolidation behaviour was not modelled. The global stiffness matrix formed was diagonal, and of bandwidth equal to three. The solver routine was written specifically for this simple matrix, and was not able to cope with matrices of higher bandwidth.

A recent improvement of the program had been the separation of material models from the main code, so that new models could more easily be developed and incorporated. Existing material models included: elastic, Von Mises and Matsuoka (with constant dilation angle). Implementation of the latter two models is described by Yu (1990).

This section has summarised the capabilities of *Cavexp* at the start of the project. The following chapter describes the modifications that were performed to enable the program to be used for the analysis of stress conditions around a loaded nail.

Chapter 7. FINITE ELEMENT FORMULATION

7.1. Introduction

This chapter describes the developments in the formulation of *Cavexp* carried out prior to performing the parametric study described in Chapter 8. The main stages of this development were:

- Inclusion of nodal axial degrees of freedom
- Implementation of coupled consolidation
- Development of a new material model incorporating variable dilation

The old code was written in FORTRAN 77, so the first task involved updating to the more versatile and user-friendly FORTAN 90. The particular case of cylindrical geometry was then expanded to allow nodes an extra degree of freedom in the axial direction. This allowed the movement of soil in response to nail loading to be captured. The resulting global stiffness matrix formed was diagonally banded as before, but the bandwidth was increased from 3 to 7. In anticipation of further increases in bandwidth, the solver routine was rewritten to handle matrices of general bandwidth.

The 'coupled consolidation' model derived by Houlsby (1998) adopted was different to many such formulations, e.g. Britto and Gunn (1987), in that the pore pressure nodes were deployed such that displacements and pore pressures (rather than strains and pore pressures) had the same order of variation across an element. This led to the coincidence of pore pressure and displacement nodes, a considerable simplification. The stiffness matrix for each element contained new terms, bringing the bandwidth of the global stiffness matrix up to 11. Non-linear shape functions for pore pressure were implemented, matching the steady state distribution of pore fluid pressures under a constant fluid pressure at the cavity wall.

The program was checked and validated using an elastic material model, before emphasis was transferred to the development of an existing Matsuoka (1976) material model to model the overconsolidated clays typically encountered in the field. The existing model, originally implemented in OXFEM* by Burd (1986) used a constant value of dilation angle. When modelling nail pull-out, this caused the normal stress and hence the shear stress to increase indefinitely as the soil around the nail expanded, as described by Houlsby (1991) in relation to pile behaviour. This was rectified by introducing a variable dilation angle whose magnitude was determined by a simple equation put forward by the late Professor Wroth, described by Houlsby (1991).

The final period of development involved extensive testing of the new program's capabilities, and the incorporation of a relatively simple automated procedure for varying the size of calculation steps according to the global error as the calculation proceeded. All analyses were performed on a twin 300*MHz* processor Sun Microsystems SPARC workstation belonging to the Oxford University Soil Mechanics Research Group. The code was compiled on the same platform using a standard FORTRAN 90 compiler supplied by Sun.

7.2. Shape functions

When formulating finite elements, it is usual to use interpolation or shape functions to describe the behaviour of displacements between the nodes, where the displacements are known. It is convenient to specify shape functions in terms of a local element co-ordinate, which typically spans a whole element in the range 0 to 1 or in some cases –1 to +1. This simplifies calculation procedures, as the same local co-ordinate system may be used for all elements in the mesh.

The form of the shape functions likely to be used depends on several factors including: mesh geometry, material behaviour and available processor power. When modelling materials exhibiting elastic or near elastic behaviour, the displacement

* Oxford Finite Element program - the main three-dimensional FE package used for the analysis of geotechnical problems at Oxford.

distribution for simple loading is often known in the form of a closed form analytical solution. These solutions are sometimes linear, therefore it is advantageous to use linear interpolation functions of the same order as the analytical solution, so that any elastic behaviour is modelled exactly. A common way of doing this is to use Lagrangian shape functions. These are essentially set algorithms for obtaining suitable linear interpolation polynomials of the desired order.

Elastic solutions for the stresses and displacements in axisymmetry contain non-linear terms of the type $1/r$ and $1/r^2$. These can never be fitted exactly using the linear interpolation polynomials described above. The shape functions used in *Cavexp* are non-linear, and are designed to match the form of the elastic solution. These are described in more detail in the next two sub-sections. A disadvantage of using these shape functions is that the Jacobian term relating the local to global co-ordinates now depends on the particular global co-ordinate, r, at which the shape function is being evaluated. This is not the case when using linear interpolation polynomials, where any point and its space differential may be specified exactly given only the element nodal co-ordinates and the local co-ordinate.

The shape functions used for radial displacement were the same as those described by Yu and Houlsby (1990); the derivation is given in Appendix A. The axial and pore pressure shape functions have not previously been described elsewhere; therefore their derivation is outlined here.

7.2.1. Shape functions for axial displacement

The elastic solution for shear stresses within a thick walled cylinder under a shear load along the z-axis at the inner boundary may be derived as follows. The geometry is shown in figure 7.1. Considering axial equilibrium of the element shown,

$$\left(\tau_{rz} + \frac{\partial \tau_{rz}}{\partial r}\delta r\right)2\pi(r+\delta r)t = \tau_{rz}.2\pi rt \qquad (37.)$$

where t is the thickness of the element. Rearranging, and neglecting second order terms,

$$r\frac{\partial \tau_{rz}}{\partial r} + \tau_{rz} = 0 \qquad (38.)$$

Since τ_{rz} is a function of r only, the partial differentials may be written as total differentials. Integrating,

$$\int \frac{d\tau_{rz}}{\tau_{rz}} = \int \frac{dr}{r} \tag{39.}$$

so

$$\tau_{rz} = \frac{C_1}{r} \quad \text{where } C_1 \text{ is a constant of integration.} \tag{40.}$$

The first boundary condition specifies the loading on the inner surface of the cylinder

$$F_0 = 2\pi r_i t.\tau_{rz}(r = r_i) \tag{41.}$$

Substituting this into (40.) we obtain

$$C_1 = \frac{F_0}{2\pi t} \tag{42.}$$

To obtain an expression for the axial displacements, $w(r)$, we must first examine the equation for the relevant shear strain in term of small displacements:

$$\gamma_{rz} = \frac{\partial w}{\partial r} + \frac{\partial u}{\partial z} \tag{43.}$$

The second term in the above equation disappears under the plane strain assumption, and the first term may be written as a total differential. Then, applying Hooke's Law

$$\frac{dw}{dr} = \frac{\tau_{rz}}{G} = \frac{F_0}{2\pi t G}\frac{1}{r} \tag{44.}$$

Integrating again,

$$\int dw = \frac{F_0}{2\pi t G}\int \frac{dr}{r} \tag{45.}$$

$$w = \frac{F_0}{2\pi t G}\ln(C_2 r) \quad \text{where } C_2 \text{ is another constant of integration.} \tag{46.}$$

The second boundary condition sets w to be zero on the outer boundary. Hence $C_2 = 1/r_0$ and

$$w = \frac{F_0}{2\pi t G}\ln\left(\frac{r}{r_0}\right) \tag{47.}$$

which may be written

$$w = A_2 + B_2 \ln r \tag{48.}$$

where A_2 and B_2 are constants. This is the form used for the axial displacement interpolation functions. Considering a two-node element using this type of interpolation function

$$\begin{aligned} W_1 &= A_2 + B_2 \ln(R_1) \\ W_2 &= A_2 + B_2 \ln(R_2) \end{aligned} \tag{49.}$$

where W_1 and W_2 are the axial displacements at the nodes. Solving simultaneously,

$$\begin{aligned} A_2 &= \frac{W_1 \ln R_2 - W_2 \ln R_1}{\ln(R_2 / R_1)} \\ B_2 &= \frac{W_2 - W_1}{\ln(R_2 / R_1)} \end{aligned} \tag{50.}$$

The displacement at any point within the element is described in terms of the displacement at the nodes and the shape functions.

$$w = N_{a1} W_1 + N_{a2} W_2 \tag{51.}$$

or, in matrix notation

$$w = \mathbf{N}_a \mathbf{W} \tag{52.}$$

where $\mathbf{N}_a$ is the matrix of shape functions for axial displacements, given by

$$\mathbf{N}_a = \mathbf{N}_a(r) = \begin{bmatrix} N_{a1} \\ N_{a2} \end{bmatrix} = \begin{bmatrix} \dfrac{\ln(R_2 / r)}{\ln(R_2 / R_1)} \\ \dfrac{\ln(r / R_1)}{\ln(R_2 / R_1)} \end{bmatrix} \tag{53.}$$

7.2.2. Pore pressure shape functions

The pore pressures also vary continuously within the elements, and a similar method was used to model this variation. The shape functions were chosen to match the steady-state seepage equation for the axisymmetrical case of a thick walled cylinder, with a fixed pore pressure difference between inner and outer permeable boundaries.

The total flow at any radius, Q must remain constant, but the artificial velocity, v_a, varies thus:

$$v_a = \frac{Q}{A_{cylinder}(r)} = \frac{Q}{2\pi rt} \tag{54.}$$

Darcy's law may be written

$$v_a = -\frac{k}{\gamma_w}\frac{du_w}{dr} \tag{55.}$$

where k is the soil permeability, γ_w is the unit weight of pore fluid, and u_w is the pore pressure. Combining these two equations gives

$$\int \frac{dr}{r} = -\frac{2\pi kt}{Q\gamma_w}\int du_w \tag{56.}$$

and it can be seen that the solution for pore pressures has the form

$$u_w = A_3 + B_3 \ln r \tag{57.}$$

This solution is of the same form as that derived in section 7.2.1 above for the axial displacements, allowing the same form of shape function to be used. The following are noted here for completeness:

$$u_w = N_{w1}U_{w1} + N_{w2}U_{w2} \tag{58.}$$

or, in matrix notation

$$u_w = \mathbf{N}_w\mathbf{U}_w \tag{59.}$$

where $\mathbf{N}_w$ is the matrix of shape functions for pore pressures, given by

$$\mathbf{N}_w = \mathbf{N}_w(r) = \begin{bmatrix} N_{w1} \\ N_{w2} \end{bmatrix} = \begin{bmatrix} \dfrac{\ln(R_2/r)}{\ln(R_2/R_1)} \\ \dfrac{\ln(r/R_1)}{\ln(R_2/R_1)} \end{bmatrix} \tag{60.}$$

7.3. Finite element equations

The derivation of the finite element equations for coupled consolidation using virtual work is given in Appendix A, Houlsby (1998). The equations to be solved are:

$$\dot{\mathbf{F}} = \mathbf{K}\dot{\mathbf{U}} - \mathbf{L}\dot{\mathbf{U}}_w \tag{61.}$$

$$\mathbf{Q} = -\mathbf{L}^T\dot{\mathbf{U}} - \mathbf{M}\mathbf{U}_w \tag{62.}$$

The vectors $\dot{\mathbf{F}}$ and $\mathbf{Q}$ are the nodal force rates and flows; the vectors $\dot{\mathbf{U}}$ and $\mathbf{U}_w$ are the nodal displacement rates and pore water pressures. The matrix $\mathbf{K}$ is the stiffness of the soil skeleton; $\mathbf{M}$ is the matrix of flow terms. These are both derived from statements of equilibrium and compatibility, the former of forces, the latter of flows. The cross linking between nodal forces and flows is given by the matrix $\mathbf{L}$ which combines a statement of compatibility (relating volumetric strain of soil to flow of pore water) with the principle of effective stress, itself an equilibrium statement. These equations have also been derived by Britto and Gunn (1987) but different nomenclature was used, and the sign convention for stress was compressive-positive.

7.4. Solution procedure for coupled consolidation

The equations (61.) and (62.) would be difficult to use in their current form, since pore pressure increments appear in the first equation, but not in the second. This may be resolved by expressing the current pore pressure in terms of that during the previous step:

$$\mathbf{U}_w = \mathbf{U}_w^{t-\Delta T} + \dot{\mathbf{U}}_w \Delta T \tag{63.}$$

substituting into (62.),

$$\mathbf{Q} + \mathbf{M}\mathbf{U}_w^{t-\Delta T} = -\mathbf{L}^{\mathrm{T}}\dot{\mathbf{U}} - \mathbf{M}\Delta T\dot{\mathbf{U}}_w \tag{64.}$$

The equations are now written in incremental form as they appear in the analysis.

$$\begin{aligned} \frac{\Delta \mathbf{F}}{\Delta \mathrm{T}} &= \mathbf{K}\frac{\Delta \mathbf{U}}{\Delta \mathrm{T}} - \mathbf{L}\frac{\Delta \mathbf{U}_w}{\Delta T} \\ \mathbf{Q} + \mathbf{M}\mathbf{U}_w^{t-\Delta T} &= -\mathbf{L}^{\mathrm{T}}\frac{\Delta \mathbf{U}}{\Delta T} - \mathbf{M}\Delta T\frac{\Delta \mathbf{U}_w}{\Delta T} \end{aligned} \tag{65.}$$

multiplying through by ΔT,

$$\begin{aligned} \Delta \mathbf{F} &= \mathbf{K}\Delta \mathbf{U} - \mathbf{L}\Delta \mathbf{U}_w \\ (\mathbf{Q} + \mathbf{M}\mathbf{U}_w^{t-\Delta T})\Delta T &= -\mathbf{L}^{\mathrm{T}}\Delta \mathbf{U} - \mathbf{M}\Delta T\Delta \mathbf{U}_w \end{aligned} \tag{66.}$$

which may be written in the form

$$\begin{Bmatrix} \Delta \mathbf{F} \\ (\mathbf{Q} + \mathbf{M}\mathbf{U}_w^{t-\Delta T})\Delta T \end{Bmatrix} = \begin{bmatrix} \mathbf{K} & -\mathbf{L} \\ -\mathbf{L}^{\mathrm{T}} & -\mathbf{M}\Delta T \end{bmatrix} \begin{Bmatrix} \Delta \mathbf{U} \\ \Delta \mathbf{U}_w \end{Bmatrix} \tag{67.}$$

This now represents a soluble set of simultaneous equations, with unknowns $\Delta\mathbf{U}$ and $\Delta\mathbf{U}_u$. The matrix relating the 'force-like' and 'displacement-like' vectors shall henceforth be referred to as the **KLM** matrix.

7.5. Material models

Two material models were used: a linear elastic model, used to validate the FE formulation against standard elastic solutions; and a Matsuoka (1976) model similar to that used by Burd (1986) and Yu (1990). The Matsuoka model is usually applied to the analysis of granular material; Cam-Clay type models being more commonly used when modelling clays. However, the clays under consideration as possible nailing materials are usually overconsolidated, and as such are on the dry side of critical. Failure on this side is generally governed by a Hvorslev failure surface; in other words frictional soil behaviour is exhibited. The most common constitutive law used to model frictional soil is the Mohr-Coulomb model. This model has a discontinuous yield surface, making differentiation of the yield function difficult at certain 'locations'. Sloan (1981) notes that these singularities are infrequently approached under plane strain conditions except under axisymmetrical loading, when stresses may be located almost exclusively in these regions. This problem is avoided when using the Matsuoka model, which is differentiable everywhere except at the origin.

The Matsuoka yield function was coupled with the non-associated flow rule described by Yu (1990), where the plastic potential function is of a similar form to the yield function, but the dilation angle replaces the friction angle, and the apex of the surface is moved from the origin to the point $\sigma_1 = \sigma_2 = \sigma_3 = M$ in principal stress space*. A two-dimensional representation is shown in figure 7.2. M was calculated on the basis that the plastic potential and yield function must coincide at the current stress state. This condition was used to derive a cubic equation in M from which the required root was selected.

---

* Yu (1990) uses the notation $-k$ for M, but this symbol has been reserved for permeability in this dissertation. The omission of the minus sign indicates that the apex of the plastic potential surface lies in tensile stress space; therefore M may be considered a positive quantity.

Previously, this constitutive model had been used with constant friction and dilation angles. This is inconsistent with the observed behaviour of dense soil under shear whereby dilation decreases as specific volume and normal stress increase. The latter is particularly relevant to geometries where dilation is constrained, for example the axial loading of piles or soil nails. If dilation continues with shearing, the soil around a circular inclusion will expand, pushing against the soil outside the shearing zone. The normal stress acting on the inclusion will increase, causing the shear stress to increase indefinitely with axial displacement. Any attempt to numerically model pull-out realistically had to take this into account.

Houlsby (1991) presents a simple model for calculating dilation angle suggested by the late Professor Wroth, whereby the dilation rate is related to the vertical distance of the current stress point to the critical state line on a V-ln p' plot, figure 7.3. This concept was originally suggested by Wroth and Basset (1965), and most famously proposed by Been and Jefferies (1985) in their use of the 'state parameter'. The model suggested by Wroth is $\sin\psi = \xi(\Gamma - V_\lambda)$ where ξ is constant for a given material*. The choice of ξ for a particular soil should be made on the basis of experimental measurements. The simple shear tests performed by Stroud (1974) were convenient for this, and Wroth found that a value of ξ=1.15 fitted these data well. Wroth (unpublished notes, circa 1990) also analysed the simple shear tests performed on kaolin by Borin (1973), and suggested a value of ξ=1.79, although he never confirmed this in any published work.

The effect of different values of ξ on results obtained from finite element analyses was investigated; the results are presented in section 8.2.4.

7.5.1. Elastic model

The behaviour of an elastic material may be described by any two of the four parameters G, K', E' and ν'. The first two of these were used as input parameters, and the other two

* Wroth, and Houlsby (1991), used the symbol α instead of ξ, but α is reserved for the relation between pile shaft friction and undrained shear strength in this thesis.

calculated using the standard relationships. In the finite element model, material behaviour is described by the **D**-matrix:

$$\dot{\sigma}' = \mathbf{D}\dot{\varepsilon} \tag{68.}$$

where the stress and strain rate vectors are given by

$$\begin{aligned} \dot{\sigma}' &= \left[\dot{\sigma}'_r \quad \dot{\sigma}'_z \quad \dot{\sigma}'_\theta \quad \dot{\tau}_{rz}\right]^T \\ \dot{\varepsilon} &= \left[\dot{\varepsilon}_r \quad \dot{\varepsilon}_z \quad \dot{\varepsilon}_\theta \quad \dot{\gamma}_{rz}\right]^T \end{aligned} \tag{69.}$$

In this case, **D** is simply derived from Hooke's laws, yielding:

$$\mathbf{D}^e = \begin{bmatrix} E' & -\nu' E' & -\nu' E' & 0 \\ -\nu' E' & E' & -\nu' E' & 0 \\ -\nu' E' & -\nu' E' & E' & 0 \\ 0 & 0 & 0 & G \end{bmatrix} \tag{70.}$$

7.5.2. Extended Matsuoka model

The new material model is based on the Matsuoka (1976) model, in the form proposed by Yu (1990). The proposed 'extension' to this model is the incorporation of a variable dilation angle. The stiffness matrix for an elastic - perfectly plastic material (see Appendix A for derivation) is given by

$$\mathbf{D}^{ep} = \frac{\mathbf{D}^e \left[\frac{\partial g}{\partial \sigma}\right]\left[\frac{\partial f}{\partial \sigma}\right]^T \mathbf{D}^e}{\left[\frac{\partial f}{\partial \sigma}\right]^T \mathbf{D}^e \left[\frac{\partial g}{\partial \sigma}\right]} \tag{71.}$$

For Matsuoka, define yield function, f, and plastic potential, g.

$$f = I_1 I_2 - I_3\left(9 + 8\tan^2\phi\right) \tag{72.}$$

$$g = I_1^* I_2^* - I_3^*\left(9 + 8\tan^2\psi\right) \tag{73.}$$

Stress invariants:

$$\begin{aligned} I_1 &= \sigma_r + \sigma_z + \sigma_\theta \\ I_2 &= \sigma_r\sigma_z + \sigma_z\sigma_\theta + \sigma_\theta\sigma_r - \tau_{rz}^2 \\ I_3 &= \sigma_\theta\left(\sigma_r\sigma_z - \tau_{rz}^2\right) \end{aligned} \tag{74.}$$

and define $I_i^* = I_i(\sigma + M, \tau)$ so that

$$I_1^* = I_1 + 3M$$
$$I_2^* = I_2 + 2MI_1 + 3M^2 \qquad (75.)$$
$$I_3^* = I_3 + MI_2 + M^2 I_1 + M^3$$

Where M is the offset of the plastic potential envelope set so that a plastic stress point at the start of a calculation increment lies on the surface of both f and g (see figure 7.2). The flow rule is then associated in the π–plane.

Using Wroth's expression for dilation angle, (Houlsby, 1991)

$$\sin\psi = \xi(\Gamma - V_\lambda) \qquad (76.)$$

where

$$V_\lambda = V - \lambda\ln(-p') = V + \lambda\ln\left(-\frac{I_1}{3}\right) \qquad (77.)$$

noting tension positive sign convention. V_λ in the above equation is determined from the equation of a 'λ-line' on a $v - \ln(-p')$ plot running parallel to the CSL, figure 7.4.

$$\sin\psi = \xi\left(\Gamma - V - \lambda\ln\left(-\frac{I_1}{3}\right)\right) \qquad (78.)$$

The instantaneous friction angle is related to the critical state value and the current angle of dilation by Bolton's (1986) empirical relation

$$\phi = \phi_{cv} + 0.8\psi \qquad (79.)$$

Having defined the material, the terms in (71.) may be calculated, but the dependence of friction and dilation angles on mean effective stress (due to the Wroth formulation), and hence on I_1 must be remembered when calculating differentials.

7.6. Notes on implementation

7.6.1. Wroth dilation model

To calculate V_λ during a time step, the current values of $V, (-p')$ must be calculated. The mean effective stress is calculated as

$$p' = \frac{1}{3}(\sigma_r + \sigma_z + \sigma_\theta) = \frac{I_1}{3} \qquad (80.)$$

If it is assumed that the specific volume is known at the start of the step, at the end of the step, $i = i + 1$, it is given by

$$V_{i+1} = V_i + \delta V \tag{81.}$$

Specific volume is defined:

$$V = \frac{v}{v_s} \tag{82.}$$

so that

$$\delta V = \frac{\delta v}{v_s} \tag{83.}$$

where v is the total volume of a soil element, and v_s the volume of solids. The volumetric strain is given by

$$\dot{\varepsilon}_v = \dot{\varepsilon}_r + \dot{\varepsilon}_z + \dot{\varepsilon}_\theta = \frac{\delta v}{v_i} \tag{84.}$$

inserting (83.) and (84.) into (81.) gives

$$V_{i+1} = V_i + \frac{\delta v}{v_s} = V_i + \frac{v_i \dot{\varepsilon}_v}{v_s} \tag{85.}$$

so

$$V_{i+1} = V_i\left(1 + \dot{\varepsilon}_v\right) \tag{86.}$$

The only problem remaining is the calculation of an initial value of the specific volume of the material, given the initial conditions. Referring to figure 7.4, we obtain

$$V_{initial} - V_0 = \kappa \ln\left(\frac{-p'_c}{-p'_{initial}}\right) = \kappa \ln(OCR) \tag{87.}$$

but

$$V_0 = N - \lambda \ln(-p'_c) \tag{88.}$$

so

$$V_{initial} = \kappa \ln(OCR) + N - \lambda \ln(-p'_c) = \kappa \ln(OCR) + N - \lambda \ln\left[OCR(-p'_{initial})\right] \tag{89.}$$

leading us to our final result

$$V_{initial} = (\kappa - \lambda)\ln(OCR) + N - \lambda \ln(-p'_{initial}) \tag{90.}$$

7.6.2. Pore pressure nodes and matching orders of variation

The normal way of distributing pore pressure nodes around consolidation elements is to place them so as to enforce a lower order (by one) of spatial variation in pore pressure than the order of spatial variation in displacement (see for example Britto and Gunn, 1987). Hence typical linear elements for one-dimensional analyses might look like those in figure 7.5(a). The first has two displacement nodes and one pore pressure node, allowing a linear variation in displacement and hence a constant distribution of strain. The pore pressure distribution along the element is also constant. The second element has three displacement nodes and two pore pressure nodes, thus allowing for linear variations of strain and pore pressure. Typical triangular consolidation elements for modelling linear and cubic strain variations are shown in figure 7.5(b), taken from Britto and Gunn's (*loc. cit.*) description of the *CRISP* finite element analysis package. Again, the variation in pore pressure is of the same order as that of strains.

The thinking behind this idea is that (for a linear material model) the stresses are of the same order as the strains, and since the principle of effective stress must be applied to link pore pressure and displacement behaviour, it makes sense that the algebraic description of stress within an element should be of the same order as that of pore pressure. The principle of effective stress is an equilibrium statement about how forces are shared between soil particles and pore fluid. But compatibility also has to be enforced between pore fluid and soil particle velocities. This is just as important as equilibrium, but if pore pressures are one order lower than displacements, then pore fluid velocities are two orders lower than particle displacements, which are of the same order as particle velocities. Thus the compatibility, or continuity statement is mismatched by two orders.

By allowing pore pressures the same order of variation as displacements, this mismatch is reduced to one order, although a mismatch in equilibrium of one order is now introduced. This compromise is fully justified by the resulting simplification of the elements. Each node is allowed the requisite number of displacement degrees of freedom plus a pore pressure degree of freedom, dispensing with the need for separate displacement

and pore pressure nodes. The 'displacement' vector for the mesh as whole is thus of the form:

$$[u_1 \quad w_1 \quad u_{w1} \quad u_2 \quad w_2 \quad u_{w2} \ldots]^T \tag{91.}$$

where u, w represent displacements and u_w pore pressures. This results in a tightly banded **KLM**-matrix which may be solved quickly and efficiently. In contrast, elements having separate pore pressure nodes lead to a **KLM**-matrix which comprises a central well-populated diagonal band and a pair of sparsely populated outer bands either side. The linear two-node element used by *Cavexp* is shown in figure 7.5(c). Each node has two displacement degrees of freedom, in the r- and z- directions, and one pore pressure degree of freedom.

7.6.3. Mesh geometry

The mesh for each analysis was specified in the input data in terms of inner and outer radii, and number of elements. The elements were laid out evenly in logarithmic space, resulting in a higher density of short elements near the inner boundary, and relatively few, longer elements near the outer boundary. This allowed for the expected greater variation of response in the loading region.

7.6.4. Initial conditions

The effective stresses at the start of analysis were assumed isotropic, and were specified in the input as a total stress and a pore pressure. The effective stress value was assigned to all Gauss points, and the pore pressure value was assigned to the vector of nodal pore pressures. For convenience, the pore pressure and flow vectors were stored separately from the displacement and force vectors until just before inversion of the stiffness matrix.

The initial application of a constant effective stress in all directions at all Gauss points along the mesh should in theory have left the mesh in equilibrium, providing the same stress was also applied at the inner and outer boundaries. However, as good practice,

nodal forces in equilibrium with these stresses for each element were calculated, and any out-of-balance forces incorporated in the forcing vector for the first loading step.

7.6.5. Assembly of stiffness matrix and solution

The stiffness matrix for each element was made up of material stiffness terms, terms cross-linking flow and strain behaviour, and flow terms, contained in the **K**, **L**, and **M** matrices respectively. These matrices were calculated separately, before being combined into a **KLM**-matrix for each element, of the form given in (67.). These elemental matrices were then placed in order in the global stiffness matrix for the mesh. Since this matrix was always banded, it was stored in an array of width equal to the stiffness matrix bandwidth, saving space, and avoiding the storage of large numbers of zero terms.

The boundary conditions for the loading step were applied, then the left-hand side of (67.) was assembled. The solver routine worked by reducing the stiffness matrix to upper triangular form by Gauss elimination, then solving from the bottom upwards. Reduction of the matrix to upper triangular proved less simple for the new larger bandwidths, since not all diagonals were fully populated. This caused problems when attempting to use a standard algorithm which subtracted multiples of adjacent rows to clear terms. A modified algorithm was devised which took account of this, making use of the fact that the leading diagonal was by necessity always fully populated.

Once solution was complete, the global vector of degrees of freedom was disassembled into displacement and pore pressure increment vectors, and the stresses in equilibrium with the new displacements calculated. The latter is now described in more detail.

7.6.6. Stress updating

When using an elastic-perfectly plastic material model, there is always the chance of updated stress points lying outside the current yield surface, i.e. in impossible states. Before the next step of the calculation, these stress points must be corrected back onto the

yield surface by a suitable algorithm. The Matsuoka model was particularly awkward in this respect, since the algebraic formulation leads to the existence of four separate surfaces, only one of which is valid. Points lying on or inside one of the bogus surfaces were identified by one of the principal stresses being tensile (see Burd, 1986). A series of checks performed at certain points during calculations ensured that the correct surface was being considered.

The method of correcting stresses was dictated by the Wroth dilation model. The yield function was dependent on friction angle and hence on dilation angle through equation (79.). Corrections were performed at constant p' ; this prevented the dilation angle from changing during the correction. The correction itself was effected using the method of bisection, a primitive but reliable algorithm for finding the surface.

7.6.7. Automatic step size control

The number of steps required to accurately compute the response to a loading stage depended greatly on the amount of plasticity present within the mesh. Loading which started and ended with all Gauss points elastic could in principle be applied in one step, whereas the highly non-linear material behaviour in the plastic regime typically required hundreds of steps to maintain accuracy. Automatic step size control was therefore necessary to locally increase or decrease the density of calculation steps, keeping the solution accuracy within limits. A measure of the accuracy being obtained during computation was given by the sum of out-of-balance forces calculated at each node. A large out-of-balance indicated that calculation steps were too large, whereas a small out-of-balance indicated that equilibrium was being maintained.

A simple algorithm was implemented to set the step size automatically according to the amount of out-of-balance recorded throughout the mesh in both displacement directions. If the out-of-balance (normalised by the internal nodal force at node 1) was greater than a certain input tolerance, the step size was decreased by a user-controlled factor, and the preceding calculation step cancelled. All quantities were set to their

previous values at the start of the step, and a new calculation performed with the smaller step size.

The normalised out-of-balance terms for previous calculation steps were stored in a buffer of user-controlled length. If the average amount of out-of-balance stored in this buffer dropped below a second tolerance value, the step size for the next calculation step was increased. This meant that the calculation speed increased when possible. Following an increase in step size, the buffer was filled with large numbers so that a number of steps equal to the length of the buffer had to elapse before another increase in step size was allowed, even if the average out-of-balance was small. This was necessary to ensure that step sizes did not get too large too quickly during elastic deformation (see below).

Large increases in out-of-balance typically occurred when the innermost Gauss points first went plastic from previous elastic states. A problem occurring with frustrating regularity was that this step was achieved without significantly increasing the out-of-balance, maintaining the current step size and proceeding to the next calculation step. It then proved impossible to complete this subsequent step within tolerance, regardless of step size. The reason for this is not clearly understood, although it was found possible in most cases to avoid this problem by generally not allowing step sizes to get too big immediately before plastic stresses were encountered. A solution might have been to move back by more than one calculation step when such a halt occurred. This would require the storage and manipulation of all relevant quantities in full for the previous calculation steps, and as such would represent considerable costs in both efficiency and complication of the code.

More sophisticated automatic step size algorithms have been successfully implemented in finite element codes by other authors, e.g. Van Langen and Vermeer (1990) and Abbo and Sloan (1994). These were considered too complicated to implement in the limited time available, but would almost certainly have been of benefit. The primitive scheme adopted was of only limited use in facilitating analyses, but it did ensure that equilibrium was maintained within tolerance throughout solution.

7.6.8. Calculation stability

It has been noted by several authors that the stability of consolidation analyses may be adversely affected when time steps are small. Vermeer and Verruijt (1981) derived an expression for the minimum time step at which stability is maintained. Similar results have also been described by Britto and Gunn (1987) and Pyrah (1980). The expression derived by Vermeer and Verruijt is specific to the analysis of one-dimensional Terzaghi consolidation using linear shape functions for pore pressures. The finite element mesh consists of elements of equal length, and loading takes place at the draining boundary. Under these conditions, a necessary and sufficient condition for stability is demonstrated to be

$$\Delta t \geq \frac{1}{6}\frac{(\Delta h)^2}{\theta c} \tag{92.}$$

where Δh is the element length, c is the one-dimensional coefficient of consolidation and θ represents the type of approximation chosen for the behaviour of the excess pore pressure during the time step, defined by

$$\int_{t^0}^{t^1} u_w \mathrm{d}t = \left(u_w^0 + \theta \Delta u_w\right)\Delta t \tag{93.}$$

The factor of 1/6 is related to the type of shape function used for pore pressures. If quadratic shape functions are used, this factor is reduced to 1/10.

It is not obvious how this accuracy criterion relates to the axisymmetric formulation described earlier in this chapter, which uses logarithmic shape functions and non-evenly distributed elements. However, instabilities in pore pressure were observed when using small time steps under certain loading conditions. It is noted that backward interpolation of pore pressures was performed (63.) implying $\theta = 1$.

A simple investigation into instability effects was performed using the axisymmetric mesh shown in figure 7.6. Both inner and outer boundaries were permeable, and the outer boundary was also rigid. An elastic material model was used to calculate the pore pressure transient response to a radial load applied on the inner boundary.

Two loading cases (a) and (b) were considered. During (a) the load was increased linearly in 5 steps until T = 0.00418, then held constant over 30 steps until T = 12.5. During (b) the load was increased 10 times more slowly in 5 steps to the same level, (until T = 0.0418), then again held constant over 30 steps until T = 12.5. Thus the effect of shortening the loading time steps on transient response observed over the same period was investigated. The dimensionless time variable T, is given by $T = ct/(\Delta h)^2$, where Δh is the length of the largest element used, t is the real time elapsed in seconds and c is the coefficient of consolidation in m^2/s. The latter takes the same value as that for one-dimensional consolidation (Randolph and Wroth, 1979), given by (97.)

The results from the two loading cases are shown in figure 7.7(a) and (b) respectively. The pore pressure axis is normalised with respect to the radial stress imposed on the inner boundary, and the radial axis is normalised with respect to the inner radius. Distributions of dimensionless pore pressure are shown at four different times after application of the load. Unfortunately it was not possible to compare results with theory, owing to the difficulties encountered in analysing the problem (see section 7.7.4), but a comparison of distributions at T = 0.0418 and 0.418 for load case (a) and (b) respectively clearly indicates the dependence of instability on time step duration. Following loading, the fluctuations quickly die away, and similar distributions are observed in both load cases.

It is interesting to note that fluctuations are greatest in the elements near the outer boundary. This may be explained by the fact that the elements are longer on this side of the mesh, so the minimum time step for accurate consolidation modelling in this region is greater than that in the region near the inner boundary, according to the trend indicated by (92.)

In practice, the loading regimes dictated by the modelling requirements of the finite element study programme meant that instability problems were seldom encountered. The problem described above only occurs when elements at high pore pressure lie close to a free draining boundary, and the limit of the 'draining front' from the boundary after one time step has not reached the first internal pore pressure node. This causes the finite element algorithm to over predict the pore pressure at this node, in turn causing under

prediction of the pore pressure at the second internal node by way of compensation, and so on.

Axial shearing (pull-out) was analysed using a rigid impermeable inner boundary. Dilation of the shearing soil generated suctions, but these were confined to the elements in the near vicinity of the boundary. When analysing the effects of high grout pressures, however, significant cavity expansions occurred and care was taken to ensure that elements were sufficiently small to prevent instability.

7.7. Test problems

The four analytical solutions outlined below were used to check the model. The first two are solutions from elastic theory, following from the simple assumptions of the mechanics of continuous media. The third is a closed form analytical solution relating to the process of cavity expansion in a linear elastic-perfectly plastic material obeying the Mohr-Coulomb yield function. The fourth is another closed-form analytical solution which describes the consolidation around a driven pile, given simple assumptions about the stress and pore pressure conditions around the pile immediately after driving,

Other checks on the code were carried out using *Plaxis* as new features were implemented. In particular, *Plaxis* was particularly useful when checking the effects of boundary conditions on simple coupled consolidation behaviour, where no closed form solutions were available. These checks were performed to confirm broad trends in behaviour, and are not described in detail here.

It was not possible to check the extended Matsuoka material model against an analytical solution, as none were available. Two analyses investigating the response of the model in single element tests are described in Appendix B. The results from these analyses demonstrate the basic stress-strain response of the material model in drained and undrained shear.

7.7.1. Elastic thick cylinder analysis

The basis of the solution for displacements and stresses within a thick cylinder of elastic isotropic material under plane strain conditions is described in Appendix A. Given that the soil was to be loaded at the inner radius, the relationship between cavity pressure and cavity expansion was determined according to the outer boundary conditions. The elastic solutions for stresses and displacements are of the form:

$$\begin{aligned}
\frac{\sigma'_r}{p_i} &= f_1\left(\frac{r_o}{r_i}, \frac{r}{r_o}, \nu'\right) \\
\frac{\sigma'_z}{p_i} &= f_2\left(\frac{r_o}{r_i}, \nu'\right) \\
\frac{\sigma'_\theta}{p_i} &= f_3\left(\frac{r_o}{r_i}, \frac{r}{r_o}, \nu'\right) \\
\frac{u}{r_o} &= f_4\left(\frac{r_o}{r_i}, \frac{r}{r_o}, \nu', \frac{p_i}{E'}\right)
\end{aligned} \qquad (94.)$$

where p_i is the difference between the cavity pressure and the negative stress at $r = \infty$ (compressive stresses negative). r_i and r_o represent the inner and outer radii respectively. Three types of outer boundary were modelled: flexible, rigid and infinite, implying the following: Flexible – radial stress equal to in-situ undisturbed stress at outer boundary; Rigid – zero displacement on outer boundary; Infinite – radial stress on outer boundary set so that all stresses would approach zero at infinite radius.

Stress-radius and displacement-radius curves for each of these cases are presented in non-dimensional form in figures 7.8 and 7.9 respectively. The values of the non-dimensional parameters used for the analyses were: $p_i / E' = 0.01$, $r_o / r_i = 10$, $\nu' = 0.25$. The finite element analyses used non-linear shape functions with 10 elements, and 2 Gauss points per element. From the graphs it is clear that the agreement with theory is excellent; accuracy is better than one part in a thousand for stresses and displacements.

7.7.2. Elastic pull-out analysis

The elastic solution for the shear stress and axial displacement distributions in a thick cylinder subjected to an internal shear force in the axial direction is laid out in section

7.2.1. If the applied shear force corresponds to a shear stress on the inner boundary of $\tau_{rz}(r_i)$, then from global equilibrium of the cylinder, a shear force $\tau_{rz}(r_o)$ must also be applied in the opposite direction at the outer boundary, where

$$\tau_{rz}(r_o) = \tau_{rz}(r_i).\frac{r_i}{r_o} \tag{95.}$$

distributions of shear stress and displacement with radius are then given by:

$$\begin{aligned} &\frac{\tau_{rz}(r)}{\tau_{rz}(r_o)} = \frac{r_o}{r} \\ &\frac{w}{r_o} = \frac{\tau_{rz}(r_o)}{G}\ln\left(\frac{r}{r_o}\right) \end{aligned} \tag{96.}$$

Stress-radius and displacement-radius curves are presented in non-dimensional form in figures 7.10 and 7.11 respectively. The values of the non-dimensional parameters used for the analyses were: $\tau_{rz}(r_i)/G = 0.1$, $r_o/r_i = 10$. The finite element analyses again used non-linear shape functions with 10 elements, and 2 Gauss points per element. Accuracy is better than one part in a hundred thousand for stresses and displacements – this corresponds to the rounding errors incurred during output.

7.7.3. Cavity expansion

Closed form solutions for the stress and displacement distributions in the soil surrounding a cylindrical cavity in an infinite dilatant elastic-plastic soil have been developed by Carter *et al.* (1986)* and Yu and Houlsby (1991). The former solution is based on small strain theory, the latter on large strain theory. Both use a non-associated Mohr-Coulomb yield criterion. *Cavexp* was designed to be able to predict large strain behaviour, since large strains are always encountered in pressuremeter and pile driving modelling. The strains expected during the analyses performed during this research were small (with the exception of shear strains). Hence very little accuracy was lost in performing exclusively small strain analyses, with a small benefit in computing time.

* The final solution presented by Carter, Booker and Yeung (1986) is for large strains, but the small strain solution is also developed. The large strain solution was later criticised by Yu and Houlsby (1991) for making 'certain unjustified assumptions'.

The two analytical solutions were compared with finite element analyses using the Matsuoka yield criterion. This was possible providing account was taken of the different friction and dilation angles needed when comparing Matsuoka and Mohr-Coulomb criteria. The former is based on triaxial angles, whereas the latter is based on plane strain angles. The relationship between the two is discussed by Burd (1986) and Yao (1996). Analyses at two combinations of angles were performed; $\phi_{ps} = 33.00^{\circ}$, $\psi_{ps} = 0.00^{\circ}$ and $\phi_{ps} = 38.00^{\circ}$, $\psi_{ps} = 5.31^{\circ}$. The corresponding Matsuoka angles are $\phi_{mat} = 29.35^{\circ}$, $\psi_{mat} = 0.00^{\circ}$ and $\phi_{mat} = 33.94^{\circ}$, $\psi_{mat} = 5.31^{\circ}$ respectively, taken from Yao (1996).

Results from the comparison are shown in figure 7.12. The first point to note is that, the range of pressure ratios p_i / p_{i0} is large, to show how the large and small strain solutions diverge at large strains. The pressure ratios envisaged for the modelling of pressurised grout for soil nails during this research were in the range 0.5 – 2.0 (half to double the overburden stress). In this range, the solutions give very similar results. Large and small strain solutions only differ significantly at pressure ratios greater than 3 or 4. It is seen that the finite element curve at all times lies within 0.1% of the value determined from the small strain solution, predicting slightly higher displacements at high pressure ratios.

7.7.4. Drainage around a driven pile in clay

The consolidation behaviour of the model was checked against the analytical solution presented by Randolph and Wroth (1979) for the dissipation of pore pressures around a driven pile. Implementation of the solution presented is not straightforward (details are given by Randolph 1977), so an attempt was made to model the problem presented in the paper. Figure 7.13 shows the variation of radial distribution of excess pore pressure with time after pile driving, taken directly from Randolph and Wroth (1979) for a material with $G / s_u = 50$. Here, c is the coefficient of consolidation, given by

$$c = \frac{k}{\gamma_w} \frac{2G(1-\nu')}{(1-2\nu')} \qquad (97.)$$

In order to directly match the form of the output, a finite element analysis was performed with the following material properties: $s_u = 1$, $r_i = 1$, $c = 1, G = 50$. Other property values were then determined from (97.) above. Fifty elements were used in conjunction with non-linear shape functions. Results are presented in figure 7.14 in the same form as the original. Agreement with the analytical solution is excellent, suggesting that consolidation behaviour is correctly modelled.

Chapter 8. FINITE ELEMENT PARAMETRIC STUDY

8.1. Introduction

The aim of the finite element study was to examine qualitatively the effects of changing certain parameters on nail bond resistance. The study consisted of three analysis series, A, B and C, concerned with pull-out test behaviour, sustained loading behaviour and installation effects respectively. Before these could be carried out, however, it was necessary to investigate the capabilities of the finite element model, and establish a standard methodology for all the analyses. Certain input specifications had a significant effect on results, but the relationships between these specifications and the physical problem being modelled were not simply defined. Examples of these are mesh geometry, types of element, material models and methods of distributing calculation steps. A series of preliminary analyses investigated the effects of these specifications, and established a general analysis specification within which the parametric study could be performed.

One further purpose of the preliminary analysis series was the establishment of a standard analysis, A1, to which the other analyses in the study could be compared. A1 simulated a pull-out test from undisturbed initial soil conditions, i.e. the installation process was not modelled. The problems of selecting both general and A1 specifications were linked; hence they are discussed together in section 8.2

8.2. Preliminary analysis series

The large number of analyses performed during development of the program confirmed that behaviour similar to that observed in practice could be modelled reasonably well. All analyses used the non-linear shape functions (section 7.2) because of the greater accuracy with which these capture elastic behaviour. The soil was modelled using the elastic-perfectly plastic formulation (section 7.3) coupled with the extended Matsuoka

material model* (section 7.5.2.). During calculations, checks were continuously made on the out-of-balance forces through the mesh to ensure these did not become too large in relation to the external loading. Where this was not possible using a fixed step size, the automatic step size algorithm was used to locally increase the density of calculation steps as needed (section 7.6.7). Other general features of the analyses are now discussed in more detail.

8.2.1. Element mesh

A one-dimensional mesh might normally be specified in terms of its size, and the number of elements it contains. There was, however, an additional complication when modelling axial shear loading. The shear stress in the soil surrounding a loaded nail is inversely proportional to distance from the nail through equilibrium. This meant that the first element in the mesh (at the inner radius) was always the first to reach the elastic limit, providing that the soil was all initially in the same state. Once this element went plastic, it was found that the majority of soil shear displacements occurred between the two nodes of this element. Hence the first element acted like an interface element where all plastic deformation was concentrated; the rest of the mesh normally remained elastic. The first element may therefore physically be interpreted as a shear zone.

First element

The response of the mesh to pull-out loading is critically dependent on the length of this element. For a given shear displacement between the nodes, shear strain is inversely proportional to the length. Assuming that the volumetric strain is approximately proportional to the shear strain, the specific volume increases more quickly (with displacement) for a shorter element than for a longer element. The dilation angle reduces as specific volume increases (78.). The dilation angle therefore decreases to zero more quickly for a shorter element, so that dilation stops earlier. A consequence of this is that

* No further use was made of the elastic material model – all results presented in this and later chapters were obtained using the extended Matsuoka model.

the mean effective stress in a shorter element does not increase as much during shearing, and a lower shear stress is mobilised on the inner boundary. A shorter element also drains more quickly, so temporary increases in p' due to suctions are shorter in duration, and the peak in shear stress is less rounded.

Martins (1983) observed that displacement discontinuities appeared around axially loaded model piles at large displacements. Around the $15mm$ diameter piles used, the discontinuity was measured to be approximately $0.01mm$ thick, and situated $0.5mm$ from the pile surface. Assuming that such a discontinuity would form in the middle of a shear zone, it was proposed in the current research that the first element should straddle the position of such a discontinuity evenly, thus confining plastic deformations within a similar region*. This raised the question of how the distance to such a discontinuity would scale with pile/nail radius. Two possibilities were considered: (a) that the distance remained constant at $0.5mm$, and (b) that it scaled linearly with radius to $3.33mm$ for a $100mm$ diameter nail. Unfortunately, direct measurement of the thickness of clay remaining around the $100mm$ diameter nails during the experimental tests had not been carried out, but it was certainly within this range.

Figure 8.1 shows the results from two analyses identical save for the lengths of the first element, l_1. Other input parameters were the same as for the proposed standard analysis. The results are presented in non-dimensional form; shear stresses and pore water pressures, both measured at the inner boundary are normalised with respect to the initial mean effective stress, the axial displacement of the inner boundary (and hence of the nail), δ, is normalised with respect to nail radius. The small amount of dilation afforded by the smaller element, case (a), is clearly shown by the small displacement during which the suction at the inner boundary increases. The sudden cessation of dilation allows the suctions to dissipate quickly. In comparison the longer element, case (b), dilates for a greater displacement, permanently and significantly increasing p', and the shear stress mobilised is greater.

---

* Several authors have examined the relationship between shear band thickness, h and mean grain diameter d_{50} in coarse-grained soils (see for example Mühlhaus and Vardoulakis, 1987). Typical values quoted for h are 10 to 20 d_{50}. For CMS, $d_{50} = 0.005mm$ approx. The observations by Martins (1983) suggest that this type of relationship may not be directly applicable in fine-grained soils.

The mesh using the shorter interface element (a) proved difficult to work with; the large shear strain increments caused by the small element required large numbers of calculation steps to ensure that the solution remained close to equilibrium. Furthermore, the shape of the pull-out curve did not correspond well with experimental results, which showed more rounded peaks in strength. l_i was hence set at $6.67mm$ for all subsequent analyses, or 0.133 times the inner radius.

Inner boundary

The inner boundary was situated at $0.05m$ for all analyses, simulating a $100mm$ diameter nail.

Outer boundary

The position of the outer boundary was important when modelling pull-out behaviour, when axial displacements were necessarily set to zero on the outer boundary. To model deformations in an infinite soil mass realistically, it is necessary to consider the extent to which deformation of the soil is likely to occur following loading. It is not possible to take the boundary to infinity, since this would imply an infinite shear deformation at the inner boundary. Field measurements around a vertically loaded pile reported by Cooke (1974) indicated that (vertical) deformations were confined within a radius of 10 pile diameters. Later finite element analyses reported by Randolph and Wroth (1978) and Potts and Martins (1982) placed the outer boundary at 50 and 46 pile radii respectively. The former authors also note that the radius at which shear stresses become negligible is likely to increase with pile length. Taking the above points into account, the outer boundary in these finite element analyses was placed at 50 nail radii.

When modelling cavity expansion during nail installation it was found that the simulation of an infinite outer boundary in the radial direction caused problems with stability. The boundary was modelled by linking the external force applied to the last node to its radial displacement by a spring of stiffness $2\pi \times 2G$, emulating the elastic solution. This was equivalent to placing an element of infinite length at the outer boundary, invoking the instability associated with large elements described in 7.6.8, and requiring

time steps of infinite duration for calculation stability. To allow for finite time steps, the boundary was in these cases considered to be stress controlled; the force on the outer boundary at all times corresponded to the initial in-situ stress regardless of displacements.

Number of elements

When modelling pull-out behaviour, plastic deformations were confined to the first element as described above. Due to the ability of the non-linear shape functions to capture elastic behaviour exactly, the number of elements beyond the first had little impact on the accuracy of solution obtained. The number of elements was thus dictated by the number of sampling points required to obtain reasonable output curves. Figure 8.2 shows the radial distribution of effective stresses at the end of loading for two analyses performed with 10 and 100 elements respectively. The pull-out curves for the two cases are not shown, since they were identical within the resolution afforded by a typical plot (see, for example figure 8.7 for analysis A1, 10 elements). It is clear that 10 elements are able to provide a suitable distribution of data points, the stress distributions for 10 and 100 elements being identical within the accuracy shown. Note that two Gauss points per element were used, so that 10 elements produced 20 stress data points.

When modelling cavity expansion behaviour, the size of the largest element was crucial to the stability of the calculation (see section 7.6.8). To allow time steps of suitable length to maintain accuracy, this and all elements had to be kept small, necessitating the use of a finer mesh. By using 150 elements, the critical time step was reduced to a level which allowed the application of loads over a realistic time scale.

8.2.2. Gauss points

The number of stress, or 'Gauss' points per element was a variable input parameter. These points are positions within the elements at which the stress is computed and stored. Stresses are calculated to correspond to the strain distribution in the element (which in turn is calculated from nodal displacements via the **B**-matrix), and to be in equilibrium with the external loads on the mesh. It has been noted by Yu and Houlsby (1990) that the accuracy

obtained when using the non-linear Matsuoka material model is not necessarily improved by increasing the number of Gauss points. The reason for this is that the distribution of stresses within an element is non-linear, and therefore an infinite number of Gauss points would be required in order to exactly integrate the stresses over the element.

Results from the standard pull-out analyses using 1,2 and 4 Gauss points per element are shown in figure 8.3. The pull-out curves are not shown, as they were identical within visual accuracy. The graph shows the distribution of effective stresses at the end of the analyses. The same distribution of stress is shown by all three analyses. It was therefore assumed that the number of Gauss points used was unlikely to be crucial. When modelling axial loading using 10 elements, 2 Gauss points per element were used, allowing the output of reasonable stress distribution curves if desired. However, when analysing radial loading using 150 elements, one Gauss point per element was used to reduce calculation time, since plenty of data points were provided by the large number of elements. The standard analysis A1 was also repeated with 150 elements to allow more resolution in examining stress distributions (see section 8.4).

8.2.3. Materials

The material parameters used for all analyses except A6 and A7 were based on data previously obtained for Speswhite Kaolin. The critical state parameters N, Γ, λ, κ and M were taken from Steenfelt et al (1981). Using standard critical state theory, and assuming isotropic consolidation, these parameters were used to calculate a value for undrained shear strength via the expression

$$s_u = \frac{M p'_{initial}}{2}\left(\frac{OCR}{r}\right)^{\Lambda} \qquad (98.)$$

where r is the spacing ratio and Λ is defined by

$$\Lambda = \frac{\lambda - \kappa}{\lambda} \qquad (99.)$$

The ratio E_u / s_u for a plasticity index of 31% (Kaolin) was taken from the correlation presented by Duncan and Buchignani (1976), shown in figure 8.4. This value was used to calculate the shear modulus since

$$G' = G_u = \frac{E_u}{2(1+\nu_u)} = \frac{E_u}{3} \qquad (100.)$$

Poisson's ratio ν' was taken as 0.2, allowing calculation of the drained bulk modulus K' from G.

During the first series of analyses (A), an investigation into the effect of using different critical state parameters was performed. This was not intended as a comparison of the likely pull-out behaviour in different clays, but as an investigation into how a different set of these parameters might affect the dilation behaviour through the Wroth model (section 7.5.2). Data sets for Weald Clay and London Clay were taken from Schofield and Wroth (1968). The corresponding G and K' values were calculated in the same way as described above, again assuming ν' = 0.2. Fixed material properties of the three clays are given in Table 8.1.

Soil	N	Γ	λ	κ	ϕ'_{cv}	I_p
Kaolin†	3.65	3.44	0.250	0.050	23.0	31%
Weald clay◊	2.10	2.06	0.093	0.035	24.2	25%
London clay◊	2.83	2.76	0.161	0.062	22.8	52%

Table 8.1 – Material properties

† Values from Steenfelt, Randolph and Wroth (1981)
◊ Values from Schofield and Wroth (1968)

8.2.4. Wroth dilation coefficient, ξ

The variation in pull-out response caused by changing the ξ value for the Kaolin data set is shown in figure 8.5. The results from five analyses are shown, for α = 0, 0.1, 1, 1.8 and 3. The increase in pull-out strength observed is due to the increases in effective stress around the nail caused by dilation. Dilation is greater for larger ξ, but is sustained for a shorter displacement, since the increases in specific volume cause the dilation angle to decrease. All curves approach the same value at large displacements, except for the curve for ξ = 0. When ξ = 0, the sample does not dilate, and as such would only reach a true critical state at infinite shear displacement. Thus although ξ is a material property, it only affects the rate at which the soil approaches critical state. The value of ξ = 1.8 for Kaolin suggested by Wroth was used in subsequent analyses. It is noted that it is unclear at this stage how this parameter is likely to vary for different soils.

8.2.5. Calculation step size and stability

The pull-out analyses in series A were modelled in one calculation stage, divided into the required number of steps using the automatic step size algorithm. The sustained loading analyses in series B were performed in several stages. During these analyses, the load was increased to the required level at the same speed, but the number of steps required depended on whether or not this load induced plasticity in the soil. Thus the first loading stage would increase the load up to the elastic limit in relatively few steps, while the second might use many more steps to increase the load to the final level required. The load was then held constant, again using multiple loading stages (with output at the end of each) until the point of failure. The plastic stress updating routine could not cope with the large strains at failure, causing the program to terminate. Hence the process of finding the exact time to failure was iterative, but by splitting the period of constant loading into stages and noting in which stage the soil had failed, it was possible to adjust the duration and number of stages to capture the onset of unstable displacements.

During series C, direct loading in the radial direction was introduced during the modelling of nail installation and grouting. It was hoped to be able to model the effect of

opening a borehole, which would have the effect of reducing the cavity pressure, and hence the total radial stress, to zero. However, it proved impossible to complete such analyses with the Matsuoka material model within the programme set for the finite element study. Subsequent development of the code allowed cavity unloading to be investigated – this work is described in Appendix C.

It did prove possible to model the effects of grouting at different pressures, provided that this process was considered to start from homogeneous isotropic soil conditions. During loading the instability associated with consolidation using finite elements arose as described in section 7.6.8. It was found that stability and accuracy were maintained by using smaller elements which in turn allowed suitably small loading steps to be applied. A flexible outer boundary was also used (see section 8.2.1 above).

8.3. Specification of study

The parametric study consisted of three analysis series A, B and C. Series A compared the pull-out response of nails under different conditions. The soil was considered as undisturbed and homogeneous, hence installation effects were not considered. Nine analyses were performed, investigating the effects on pull-out response of the following: pull rate (R_{po}), overconsolidation ratio (OCR), material type and initial mean effective stress ($p'_{initial}$). A1 was taken as the standard analysis to which the others were to be compared.

Different pull rates are expressed in terms of the dimensionless group R_{po}/k since the effects of increased pull rate were entirely due to the prevention of flow in areas of volume change due to low permeability. It might have been assumed that $p'_{initial}/G$ would also be a simple controlling parameter, but the dependence of dilation angle on p' through the Wroth equation (76.) complicates matters. Since Γ in this equation represents the critical state specific volume at atmospheric pressure, the group $p'_{initial}/p_{atm}$ also influences results. Both $p'_{initial}$ and OCR affected the elastic parameters G and K' as described in section 8.2.3. Input specifications for the A-series analyses are given in Table 8.2.

	R_{po}/k	*Material*	*OCR*	$\frac{p'_{initial}}{p_{atm}}$	Notes
A1	**10^3**	**Kaolin**	**5**	**1**	standard analysis
A2	**10^{-1}**	Kaolin	5	1	slow pull-out
A3	**10^7**	Kaolin	5	1	fast pull-out
A4	10^3	Kaolin	**1**	1	normally consolidated
A5	10^3	Kaolin	**10**	1	heavily overconsolidated
A6	10^3	**Weald clay**	5	1	different material
A7	10^3	**London clay**	5	1	parameters
A8	10^3	Kaolin	5	**0.5**	different initial
A9	10^3	Kaolin	5	**1.5**	stresses

Table 8.2 – Finite element study series A

Series B investigated the performance of nails subjected to constant loads, with the intention of discovering how this behaviour related to the pull-out results obtained during series A. Each of the analyses in series B started from the same initial conditions as A1. During the sustained loading test procedure described in *Clouterre* (1991), the load is increased in increments whose size is dependent on the result of previously performed pull-out tests. It was not necessary to analyse this type of test with an elastic-perfectly plastic model, since behaviour up to the point of yield was entirely predictable. Hence series B focussed on determining the time dependence of failure after relatively high constant loads had been applied.

It was found that the transient behaviour of the nail following the application of a constant load was dependent on the rate at which the load was applied. Ideally, a load might have been applied instantaneously, but the finite element formulation did not respond favourably to sudden changes in loading, due to the extremely small time steps required and resulting instability problems (section 7.6.8). Instead, loads had to be ramped over time, to allow the variables to respond. The loading for analysis B1 was applied over

100*s* which was sufficient for equilibrium to be maintained within tolerance. The duration of the loading stage for the other analyses was calculated by imposing the same loading rate.

The results from 4 analyses are presented in section 8.4. The magnitudes of the loads held constant during these analyses are shown in Table 8.3, expressed (a) in terms of the shear stress applied on the inner boundary $\tau(r_i)$ divided by the initial mean effective stress, and (b) in terms of $\tau(r_i)$ divided by the peak value of $\tau(r_i)_{A2}$ during the slow pull-out analysis A2, whose behaviour was considered to be fully drained.

	$\frac{\tau(r_i)}{p'_{initial}}$	$\frac{\tau(r_i)}{\tau(r_i)_{A2}}$
B1	0.65	0.977
B2	0.67	1.008
B3	0.69	1.038
B4	0.70	1.053

Table 8.3 – Finite element study series B

Series C investigated the effects of grout pressure and grout curing movements on the stresses around a nail, and the subsequent changes in pull-out response these might cause. The method of applying the grout pressures and curing movements was the same in all analyses, and is described below (see also figure 8.6):

Stage 1 - Increase cavity pressure and pore water pressure on the inner boundary to p_g over 3600*s*, simulating the pressure from fluid grout.

Stage 2 - Hold both loads for a further 7200*s* (2*hr*).

Stage 3 - Reduce the pore water pressure on the inner boundary to zero over 3600*s* while holding the cavity pressure constant.

Stage 4 - Curing stage, duration 28 days. Change over to displacement control of the inner boundary in the radial direction. During C1, C2 and C3 the boundary was fixed. During C4 and C5, shrinkage and expansive displacements were applied linearly over the stage.

Stage 5 - Pull-out. The pull-out tests were simulated in the same way as A1.

The input specifications for the C-series analyses are given in Table 8.4. The grout pressures applied, p_g, are expressed in terms of the ratio to initial mean effective stress (overburden). The grout movements are expressed in terms of the radial expansion (positive) or contraction divided by the nail radius, r_i. C1 was the standard analysis to which the others were to be compared.

	$\frac{p_g}{p'_{initial}}$	$\frac{\delta_g}{r_i}$
C1	**1.0**	**0.0**
C2	**0.5**	0.0
C3	**2.0**	0.0
C4	1.0	**-0.003**
C5	1.0	**+0.003**

Table 8.4 – Finite element study series C

8.4. Results

The results from the three series of finite element analyses are presented in the next eight subsections, each of which details the effects of changing one aspect of nail loading. Before proceeding to the results of this parametric study, the results from the standard analysis A1 are described in some detail to illustrate the general behaviour predicted by the model.

Figure 8.7(a) shows the 'pull-out test result' of shear stress on the inner boundary (nail surface) against nail axial displacement, δ. Also shown on the plot is the variation in pore water pressure at the inner boundary. Both of these quantities are expressed in dimensionless form. N.B. The sign convention used by the program was tension positive, but the results for all analyses are presented with compressive stresses and pore pressures positive.

From the plot several features of behaviour are apparent. $\tau(r_i)$ initially increases linearly with δ, until yield, when the rate of increase starts to fall until a peak is reached. As soon as yielding starts, the soil around the nail starts to dilate causing suctions to develop. The peak suction occurs just after the $\tau(r_i)$ peak. The increases in stress and specific volume cause the dilation angle to decrease, eventually to zero. This causes a reduction in friction angle ϕ through the Bolton flow rule (79.), shrinking the yield surface, and $\tau(r_i)$ falls off as the suctions dissipate, lowering the mean effective stress.

Figure 8.7(b) shows the effective stress distribution close to the nail at peak, and at the end of the analysis (final). Each dot on the stress curve indicates the stress within an individual element. It is clear from this plot that the stress state in the first element is different to, and largely independent of the others. Equilibrium dictates that the distributions of radial (total) stress and shear stress be continuous, and this is clearly followed, but the out-of-plane and hoop stresses, σ'_z and σ'_θ, undergo a step change from the first to the second element. This is because all of the plastic deformation occurs in the first element (confirmed by flags at each Gauss point set for this purpose), causing dilation and an increase in p' in the other elements. This increase moves the current stress state up the yield surface, where the locus of the yield surface in the deviatoric plane is larger. This allows the other elements to remain elastic. However, at large displacements, the dilation causes the hoop stress to decrease, bringing the mean effective stress down, even though the radial stress remains high. Within the first element, interpreted as the shear zone, the stress distribution is close to hydrostatic at peak, and *is* hydrostatic by the end of the analysis.

Figure 8.7(c) shows the corresponding distributions of radial and axial displacement, and pore pressure. The displacement distributions confirm that almost all shear deformation occurs across the first element. The plot of axial displacements $w(r)$ suggests that the shear zone might not be well established at peak, but should be clearly present at large displacements. The pore pressure curve shows that at peak, the suctions generated by dilation have yet to influence soil beyond one diameter from the nail, but by the end of the analysis, water has been able to flow into the region from outside,

dissipating the suctions. Note that insufficient time has elapsed for these to have dissipated completely.

8.4.1. Pull-out rates

The results from three analyses performed at different pull-rates are shown in figure 8.8. The graph shows that the peak pull-out resistance measured at faster pull rates is greater than that measured at lower pull rates, and that if the pull rate is sufficiently large in relation to k, this peak value may be held for a considerable displacement, as there is insufficient time available for the large suctions generated to dissipate. The increased size of the peak is due to the larger peak friction angle and larger effective stresses (imposed by the suctions) allowing higher shear stress to be mobilised. It is interesting to note that although the fastest pull rate causes large suctions equivalent in magnitude to the overburden stress to be generated at the interface, the shear stress mobilised increases only modestly (10% increase) in relation to the fully drained case. The reason for this is that the suction is extremely localised at the inner boundary and insufficient time is available for it to penetrate significantly the region of soil close to the nail. Hence the effective stresses here are not raised, and the shear capacity is not increased. The shear stress in the shear zone is tied to the shear stress further away from the soil by equilibrium; if the shear stress cannot increase here, it will not increase significantly over the short interface zone.

It should be noted that the range in R_{po}/k covered by the plots is extremely wide. This is not only to illustrate the trend in behaviour observed at different pull-rates, but to cover the wide range of soil permeability encountered in practice. A low permeability clay might be given by $k = 10^{-11} m/s$, in which case a value of $R_{po}/k = 10^{7}$ would correspond to a pull rate of $6mm/min$. For silty clays of permeability greater than $10^{-8} m/s$, the $1mm/min$ pull rate recommended by *Clouterre* (1991) is represented by the middle curve in figure 8.8, suggesting that the peak load measured during such a test would be greater than if it were performed fully drained.

8.4.2. Overconsolidation ratio

The effect of changing the in-situ overconsolidation ratio (*OCR*) of the soil is shown in figure 8.9. As expected, the greater dilation associated with increasing *OCR* raises both the peak and final shear strength predicted by the model. The initial dilation angle of the soil is partly determined from the initial specific volume, which is lower for a soil having high *OCR*, equation (90.). A low initial specific volume implies a large initial value of $(\Gamma - V_\lambda)$ and hence a large initial dilation angle. This not only increases the peak friction angle, but also causes the soil around the nail to expand significantly against the restraining body of soil beyond, generating high effective stresses and allowing the mobilisation of a higher final shear stress.

According to the Wroth dilation model, only soils whose initial state is to the left of the critical state line in $V - \ln(p')$ space will dilate, hence dilation is confined to soils of $OCR > r$, where r is the spacing ratio, calculated from

$$r = \exp\left(\frac{N - \Gamma}{\lambda - \kappa}\right) \qquad (101.)$$

The critical state parameters for Kaolin listed in Table 7.1 imply $r = 2.86$. The value of r deduced from the measured properties of real soils varies considerably. Parameters listed by Atkinson (1993) for London clay, Kaolin and glacial till imply r values of 10.6, 2.3 and 9.5 respectively. This implies that high overconsolidation ratios are necessary for dilation to be observed in certain soils, and the non-dimensional group (OCR / r) may be a controlling parameter.

The dependence of shear modulus on *OCR* is also clearly demonstrated in figure 8.9. Both overconsolidated results show very similar shear stiffness, while the normally consolidated result shows a significantly lower stiffness. The method of calculating G (section 8.2.3) appears to be reasonable, since one might expect that all overconsolidated samples would have broadly similar stiffness, while normally consolidated soil would have a significantly lower stiffness.

8.4.3. Soil type

The influence of different critical state material parameters is illustrated by the results shown in figure 8.10. From the plot it is clear that the influence of these parameters is not great under the conditions studied. It should be noted that the values of N in Table 8.1 for Weald clay and London clay were calculated assuming $r = 2$, whereas for the Kaolin data listed, $r = 2.86$. Since all three analyses were performed at $OCR = 5$, a certain amount of the discrepancy between the curves might be attributed to different values of (OCR / r), which were higher for Weald clay and London clay. However, although this explains the differences in peak strength, the order is reversed at the end of the analysis, with Kaolin showing the highest final shear strength, followed by London clay and Weald clay. Clearly the critical state parameters exert some influence on behaviour regardless of OCR.

8.4.4. Initial in-situ stress

The results of three analyses starting from different in-situ stress levels are shown in figure 8.11. The dependence of dilation angle on the absolute value of mean effective stress is shown by increased shear strength (relative to $p'_{initial}$) at lower stress levels. The effect is, however, small due to the logarithmic dependence on p' indicated by equation (78.)

8.4.5. Sustained loading

The results from the sustained loading analysis B3 are shown in figure 8.12. This is taken as representative of the analyses ending in failure of the nail. The shear loading on the soil increases linearly with time up to the prescribed level, and is then held constant. The displacement response appears elastic until this point. However, the final part of the loading stage is undrained, and suctions are generated near the nail, raising the effective stress. After the load stops increasing, the suction at first starts to dissipate, but the effective stress is kept high because of the expansion of the shear zone soil against the

outer bulk caused by dilation. The soil continues to dilate, causing the suctions to increase again, but the falling dilation angle controlled by the increases in p' and specific volume causes ϕ to decrease, negating any extra strength gained through the rise in p'. The mechanism by which ψ and hence ϕ decrease appears then to dominate, and the nail accelerates towards failure.

The results from all sustained loading analyses are compared in figure 8.13. Also shown in the figure are three shear stress loads from pull-out analyses performed from identical initial conditions. The bottom two lines indicate the peak and final shear stresses recorded during the analysis A2, which simulated a slow pull-out, the behaviour at all points during the analysis being fully drained. The top line corresponds to the peak shear stress taken from a separate pull-out analysis performed at $R_{po}/k = 35269$. This corresponds to the nail displacement rate observed during the (elastic) loading stage of all the sustained loading analyses. In order to show the range of times observed between loading and failure, the time axis is logarithmic, and the linear loading stage appears distorted.

The results show that the nail is stable below a certain loading, but that if larger loads are applied, the nail will eventually fail. It is perhaps unsurprising that the critical load appears to be very close to the peak value measured during the fully drained pull-out analysis. The length of time for which the nail is stable decreases as the magnitude of the load increases. If the load were increased to the equivalent peak pull-out load, the nail would be instantly unstable, so there is a range of loading over which the nail is temporarily stable. The upper end of this range is dependent on the rate at which the load is raised to its steady level, and may be predicted by an equivalent pull-out analysis.

The pore water pressure behaviour observed during the sustained loading test P5 (described in section 4.3.1) agrees well with that observed during the B series numerical analyses. Equivalents to both the initial decrease and subsequent increase in suctions observed as the nail failed, figure 4.1, are seen in the FE behaviour shown in figure 8.12.

8.4.6. Installation sequence

The pull-out response from analyses A1 and C1 are compared in figure 8.14. The analysis for C1 included the effects of grouting to a pressure equivalent in magnitude to the overburden stress, and curing for 28 days. In contrast, the analysis A1 was performed from artificial homogeneous initial conditions. The plot shows that the effect on the observed result is small, with slightly higher shear stresses at peak and final being measured for A1. This difference is observed because the mean effective stress around the nail was permanently slightly lowered as a result of the grouting process (see section 8.4.7), causing a drop in shear strength. The effects of different grout pressures on pull-out response are now discussed in more detail.

8.4.7. Grout pressure

The dependence of pull-out resistance on grouting pressure is shown in figure 8.15. An increase in shear strength is clearly gained from the high pressure process, while the plot suggests that grouting to below the overburden stress results in a significantly lower strength being mobilised. (The irregular pore pressure response shown for analysis C3 is discussed later in this section.) The common practice of grouting nails in place under the pressure of gravity only is not uniquely identified at any position on the plot due to the dependence on $p'_{initial}$. For a nail $10m$ long inclined downwards at $10°$ to the horizontal, the pressure under gravity grouting falls within the range $0 < p_g < 50kPa$ depending on grout density. For most applications, the overburden stress on each nail is likely to lie at the top end of, or beyond this range.

The mechanisms by which higher grout pressures might influence pull-out strength are complex. Although the high cavity pressure might be expected to expand the cavity causing consolidation of the soil around the nail, the pore water pressure is also increased to the same level as p_g by the high water content of the grout, and the radial effective stress at the inner boundary is necessarily reduced to zero. Effective stress distributions for analyses C1,2 and 3 are shown in figures 8.16-8.18 both during grouting and after curing (immediately before pull-out). The first of these shows that the stresses generated during

grouting to overburden change back almost to their original in-situ values once the excess pore water pressures have dissipated during curing. σ'_θ and σ'_z in the first element are permanently lowered by the process, but the rest of the soil has remained elastic. This explains observed small difference in pull-out behaviour exhibited by analyses A1 and C1 (see 8.4.6 above).

In contrast, the permanent changes in effective stress caused by the lower (C2) and higher (C3) grout pressures are large, as illustrated in the second pair of graphs. In both cases, the region of plastic deformation is more extensive than during C1. This may be confirmed by examining the stress states of each element – these were automatically output with the effective stress distributions. The zone of plasticity during grouting extends to $1.27\,r_i$ (6 elements) for C2, and $2.4\,r_i$ (31 elements) for C3.

The ultimate effect of the lower grout pressure is to reduce permanently the mean effective stress in the immediate vicinity of the nail by approximately 30%. At a distance of $0.3r_i$ beyond the nail $p'/p'_{initial}$ is back to unity, although σ'_r and σ'_θ remain low and high respectively. The plastic region extends further under the higher grout pressure, probably because of the greater difference in magnitude between p_g and $p'_{initial}$. The mean effective stress around the nail is increased by only 14%, but the zone of influence extends much further – in the range $1 > r/r_i > 2$, the average value of $p'/p'_{initial}$ is 1.09. This represents the consolidation of a significant volume of soil; the corresponding increase in shear strength is illustrated by the pull-out result.

It is observed from figure 8.15 that suctions were not generated around the nail during C3, the high pressure grouting analysis. This suggests that dilation was suppressed by the increase in $p'/p'_{initial}$, but this alone does not explain how the positive pore water pressures observed could have been generated. Examination of the radial displacement distributions before and after pull-out shows that the soil around the nail (in the region $1 > r/r_i > 10$) moved inwards during pull-out, generating positive pore pressures by compression of the soil at the inner boundary. The reason for this is that the first element was already at critical state before shearing commenced, and hence did not dilate during the pull-out loading stage. Inspection of the next few elements showed that these also deformed plastically during loading and did dilate, pressing inwards on the first element.

Because the innermost node was fixed radially and the inner boundary was impermeable, this caused a positive pore water pressure to be developed, and water flowed outwards away from the nail.

The final diameter of the grouted nail was not significantly affected by the grouting pressure. It was postulated in section 1.2.6 that increases in diameter caused by the use of elevated grout pressures might partly explain the higher values of bond resistance recorded by previous authors. The increase in cavity diameter, and hence grout perimeter, following the grouting stage in analysis C3 ($p_g = 2p'_{initial}$) was less than 1%. Similarly, the reduction in grout diameter in analysis C2 ($p_g = 0.5p'_{initial}$) was 0.5%. These figures suggest that consolidation of the soil around the nail is the predominant mechanism by which bond resistance is affected by grout pressure, and that effects caused by changes in cavity diameter are of only secondary significance.

8.4.8. Grout expansion or contraction during curing

The results from the final pull-out stage of analyses C4 and C5 are compared to those from C1 in figure 8.19. During the curing phase of C4, the inner radius was drawn inwards simulating grout shrinkage, while during C5, the inner radius was drawn outwards by the same amount, simulating grout expansion. The magnitude of the deformation imposed was calculated assuming typical 500 day shrinkage strains for concrete taken from Jackson (1980). Since the imposition of these displacements over a 28 day period constituted fully drained loading, it was considered unnecessary to further prolong the time scale.

It is observed that the effect of these movements on predicted pull-out resistance is small. The reason for this is clearly shown in figure 8.20 which shows the effective stress distributions after curing for the two cases. The radial movements of the inner boundary were insufficient to significantly alter the effective stress regime around the nail. However, if the soil were stiffer, or if it were possible to employ grout with a greater curing expansion, the increases in stress could lead to a significantly improved strength.

Chapter 9. ANALYSIS OF EXPERIMENTAL AND NUMERICAL RESULTS

9.1. Introduction

The finite element analyses have led to a better understanding of the mechanisms by which bond resistance of grouted nails is mobilised under pull-out and sustained loading conditions. The laboratory tests have highlighted some interesting trends in behaviour regarding nail testing methods and nail performance in the medium and long term. In this chapter, data from the experimental and numerical modelling are examined together. Where similar trends are observed from both sources, the implications for nail behaviour in the field may be asserted with greater confidence. Also considered in this chapter are predictions of bond resistance from some of the design methods for soil nailing described in section 1.2.5. Before these topics are considered, it is necessary to make some assumptions regarding the soil used in the laboratory tests, so that comparisons may be made between these tests and the FE analyses.

9.2. Laboratory test soil

The soil used in the laboratory tests was a stiff clay described by the supplier as Coal Measure Shale (CMS). The main advantage of using this material was the short time in which it was possible to create large samples. A disadvantage was the lack of previously obtained engineering data, especially in comparison to kaolin, whose properties have been extensively documented by past researchers. Furthermore, the effective stress state of kaolin samples prepared by consolidation from slurry may be estimated with some accuracy, as the stress history is known. This is not true of the CMS blocks which are produced for a different purpose (brick manufacture), where the stress history is unimportant, and therefore not documented.

The blocks as supplied were in a state of suction, due to the manufacturing process of granulation, saturation and extrusion (see section 2.2.2). It might have been thought that the extrusion process would be undrained, since the process is rapid in relation to the soil permeability. However, the blocks are able to maintain their shape for periods of years before being fired, implying significant shear strength. It is suggested that the pressures applied during extrusion are so great that some (probably highly anisotropic) consolidation occurs very quickly. When the material leaves the extrusion die the soil relaxes, and suctions develop.

In the laboratory, the blocks were stored in low stacks under polythene sheeting, and were periodically wetted to reduce the effect of any evaporation which did occur. It is unlikely that the state of the soil changed significantly during this period, due to its low permeability ($k \approx 10^{-11} m/s$*) and the absence of a high water table. The clay remaining in the nailing tank during the final test series (the material which did not form part of the trench excavated at the start of each test) was not vertically loaded between tests, and so for most of the duration of the series was in a similar state to the unconfined blocks+. The moisture content of samples taken during F4 ($\sigma_v = 100kPa$ for 3 weeks), and F5 ($\sigma_v = 50kPa$, performed immediately after F4) were slightly lower than the values recorded during the other tests, suggesting that some consolidation had occurred under the higher surcharge, but the effects of this on soil properties are difficult to quantify. It is assumed, therefore, that the soil was in a similar state during all the laboratory tests. This is clearly an approximation, but it is necessary to make an assumption regarding soil strength if the results from different tests are to be compared.

Quick undrained triaxial tests gave s_u values of between 100 and $130kPa$; vane tests in the soil during drilling, and in unconfined blocks, indicated slightly lower values. In the following sections, it is assumed that $s_u = 100kPa$. A series of consolidated-drained triaxial tests on CMS samples taken from unconfined blocks were performed by Foundation and Exploration Services in their Basingstoke laboratories. The Mohr circles

---

* Deduced from the results of an oedometer test

+ Water was added to the top of the clay during the preparation for each test, but it is unclear whether the water table actually lay at the top of the tank. The horizontal stresses developed during vertical loading of the sample reduced to approximately zero after the loading was removed and the trench had been excavated.

at failure are shown in figure 9.1; the calculated drained soil parameters are $\phi'_{cv} = 26.4°$, $c' = 11kPa$. NB: Here c' represents the intercept of the straight line fitted through the test results, and should not be assumed to imply significant shear strength at low or zero effective stress. The initial mean effective stress in the soil during the laboratory tests was always greater than $50kPa$, assuming that the soil was generally in a state of capillary suction.

9.3. Trends in behaviour

9.3.1. Pull rates

The FE analyses have shown that an increase in pull-out resistance can be expected at high pull-out rates (section 8.4.1). The strains in the soil around a displacing nail are mostly concentrated in a narrow shear zone, where most of the plastic deformation occurs. As the soil deforms plastically, it dilates, increasing the specific volume and, as a consequence, lowering the pore pressure. The effects of dilation and pore pressure reduction combine to increase the effective stress in the shear zone, therefore increasing shear strength and bond resistance. The increase in specific volume is of permanent benefit to bond strength, but the suctions are only temporary, and dissipate at a rate that depends on k. At higher values of R_{po} / k (greater than ~100), the suctions do not dissipate completely within $\delta \leq r_i / 2$, and high values of bond resistance are mobilised, particularly at the start of plastic deformation when the rate of dilation is greatest. At low values of R_{po} / k (below ~1), significant suctions do not develop.

The results from the pull-out tests F1, F5 and F6 are compared in figure 9.2. The data are here plotted in the same non-dimensional format used for presenting the FE analysis results. These tests were performed at different pull rates but with the same initial conditions. Test F5, performed at the fastest pull rate of $55mm/min$ shows a large peak in resistance. The corresponding peak value of α for F5 is 0.50, compared to 0.36 for both the slower tests. After this peak, the bond resistance decreases to a level below that observed during the slower tests. However, the range of values of α (using equation (98.)

to calculate s_u) from the slowest to the fastest pull-out analysis (R_{po} $k = 10^{-1}$ to 10^{-7}) was only 0.95 to 1.04. The low permeability of the soil used in the laboratory implies R_{po}/k values of the orders 10^6 for the slowest test and 10^8 for the fastest. According to the FE, these laboratory tests would all be classified as 'fast', and substantial suctions probably developed in the soil around the nail.

A feature not predicted by the FE analyses is the rapid decrease in post-peak strength for the fastest test, F5. According to the results shown in figure 8.8, an increase in pull rate should increase both the peak and post-peak strength. A possible explanation for this discrepancy is that the high value of $R_{po}/k = 10^8$ corresponding to F5 places it in a range not explored during the FE analyses. The maximum value of R_{po}/k during the latter was 10^{7*}, and it is possible that different behaviour might be exhibited beyond this value. In particular, the magnitude of the suctions generated for the fastest analysis in figure 8.8 suggest that cavitation might occur during very fast pull-out testing. However, it is unclear whether this could explain the observed behaviour.

9.3.2. Initial stress

The FE analyses suggest that pull-out resistance should increase almost linearly with initial mean effective stress, provided that $p_g / p'_{initial}$ is constant (figure 8.11). The slight decrease in strength predicted at higher in-situ stresses was due to the restriction this placed on the dilatancy of the soil. Upon initial examination of the experimental results, figure 9.3, it might be concluded that this behaviour is not exhibited, with only 40 – 50% increase in bond resistance observed for a 66% increase in in-situ stress. Furthermore, the sustained loading test results (Table 4.2) show only a 30% increase in τ_{stable} for the same increase in in-situ stress. However, the grouting pressure used during all laboratory tests was only $10kPa$, so the ratio $p_g/(p'_{initial})$ was lower for the test performed at the higher surcharge (assuming that $p'_{initial}$ was significantly higher for the greater surcharge). This was demonstrated by the numerical analyses to reduce the pull-out resistance significantly (figure 8.15), and could explain the relatively low values for the higher surcharge tests.

---

* Beyond this value, problems were encountered in the stress updating routines.

9.3.3. Sustained loading tests

Four main features of behaviour are apparent from the results of the sustained loading tests F2 and F4, shown in figure 9.4.

1. The maximum stable loads recorded during sustained loading were lower than the final loads recorded during equivalent pull-out tests.
2. The nail displacement stabilised quickly following the application of the initial load increments, although the response to the loading was not instant. For example, following the application of the second load increment in F2 of just under $15kPa$, the displacement of the nail (although less than $1.5mm$) took approximately 50 hours to stabilise (stability was assumed to have been reached once the displacement rate dropped below a critical value, see section 4.3.2).
3. At higher loads stability was only achieved at the expense of large nail displacements after several days of sustained loading.
4. The results from F2 suggest that it might be possible to limit these large displacements by subjecting the nail to an unload-reload loop -- allowing a short period of deformation at a relatively high load, reducing the load on the nail for a few days, then reapplying the higher load.

Figure 9.4 compares the sustained loads applied during F2 and F4 with the pull-out results from F1 and F3. The mean value of the vertical and horizontal total stress readings before testing, σ_{init}, was $60kPa$ for F1 and F2, and $100kPa$ for F1 and F3. The pull-out test results indicated on the plots are the peak and final (at a pull-out displacement of $100mm$) values of average shear stress. A degree of consistency between the two types of test is seen when comparing the results of F1 and F2. The final stable sustained load applied is very close to the final pull-out result. The subsequent load increment took the load above this value (although initially the load was still below the peak pull-out result), and caused failure of the nail. Comparison of F3 and F4 does not show the same consistency between results. Failure during sustained loading occurred at a level below the loads applied during pull-out testing.

The FE results suggest that the application of a steady load below the peak level observed during a fully drained pull-out test should yield a stable response (figure 8.13). It is unlikely that drained conditions were attained at any point during the laboratory pull-out tests. Assuming that the FE analyses correctly modelled soil behaviour, and that the estimate of soil permeability is correct, both peak and final values taken from the laboratory tests are likely to be high in relation to those measured during a fully drained test. However, almost identical results from the pull-out tests F1 and F6 at pull rates of 20 and 3.2*mm/min* respectively suggest that these might both be fully drained, since a difference in the degree of drainage should influence the peak strength measured. One could conclude from this that the F3 pull-out result should correlate with the F4 sustained loading result. The fact that it does not suggests either that F1 and F6 were both partially drained (and that it is coincidence that the pull-out response was so similar), or that the sustained load nails failed by a different mechanism.

Time dependent deformations observed at low loads during the laboratory sustained load tests confirm that the response of real soil is more complicated than that predicted using simple elastic-plastic models. A detailed discussion of time effects is beyond the scope of this thesis, but two possible explanations for these deformations are briefly discussed here. The first explanation is based on a consolidation model, while the second is based on creep.

Using the elastic-plastic model, no excess pore pressures are developed until the onset of plasticity, so time dependent movements due to consolidation do not occur in the elastic regime. This is because volumetric strains do not occur for the problem of an elastic thick-walled cylinder loaded purely in axial shear. In reality, regions of plasticity probably develop very soon after loading commences, leading to consolidation, an increase of shear strength with time, and the associated transient response. At higher effective stresses (caused by greater loads) these regions become more extensive, until the majority of the soil around the nail is deforming plastically. The absence of any measured elastic recovery following the decrease in load during F2 (figure 9.4) suggests that any elastic strains in the soil are in fact very small in relation to plastic strains, suggesting that plastic deformation commences at small values of nail displacement.

Soil creep may be described as 'deformation resulting from readjustment of particle contacts at essentially constant effective stress', Wood (1990). Consider the application of a small constant load to a nail, such as that applied during the early stages of test F2. Assuming that the strains in the soil are insufficient to induce plastic deformation, and therefore that excess pore pressures do not develop, the effective stress field around the nail should be constant. If creep occurs, however, the nail will move, and the specific volume of the soil will change due of rearrangement of particles under the applied shear stress. Given that the overall effective stress field is compressive, the specific volume will tend to decrease under these rearrangements, and small positive excess pore pressures will be generated as a consequence. As the pore pressures dissipate and the specific volume decreases, the shear strength of the soil increases and the creep rate decreases, so the nail approaches a more stable position.

It is seen therefore, that the process by which the soil reaches stability is similar for both consolidation and creep mechanisms of deformation – reduction in specific volume, resulting in increased shear strength. The only difference is that creep occurs even at constant effective stress; the specific volume decreases by particle rearrangement, which occurs at a rate that is dependent on many factors, not just soil permeability. Recent research into pile settlements at constant load also suggests that the two mechanisms are closely related. England (1999) notes that in saturated soil, the effects of creep on pile settlements are indistinguishable from consolidation effects, and even suggests that the two may actually be one and the same effect.

During F2, the nail was unloaded by approximately 35% because the gradient of the displacement-time curve was so high that failure appeared to be imminent. When it was unloaded, the nail stopped moving completely. No further movements were noted until the load was increased beyond the originally unstable level, whence the nail continued to move, but at a significantly reduced velocity. After 7 days, the nail had stabilised under this load with only $18mm$ further displacement. It seems therefore, that the bond resistance of the nail increased during the 3 days that the load was reduced, without further shear strain. Furthermore, it would appear that large nail deformations could be reduced by first pre-loading above the service level, allowing a small amount of relatively

fast movement, then reducing the load. It is unclear how this result might be explained in terms of traditional soil mechanics models of behaviour.

9.3.4. Interface tests

Results from the five interface tests described in section 5.4 are summarised in figures 9.5 and 9.6. The former shows the results of three tests performed at the same vertical total stress of $50kPa$, but at different shearing rates: 0.01, 0.3 and 1.2 *mm/min*. The latter shows the results of three tests performed at the same shearing rate of $0.3mm/min$ but at different vertical total stresses: 50, 100 and $200kPa$. Clear trends in behaviour are seen in both cases. Higher values of the ratio τ / σ_v are indicated for lower vertical total stresses and for higher shearing rates. These trends have also been observed to apply to results from the finite difference modelling described in section 5.5.

It is noted that the friction angles (based on total vertical stress) calculated from the interface test results (section 5.4) are higher than the drained value obtained from triaxial tests (section 9.2). This is due to the high rate at which the samples were loaded leading to suctions and, as a consequence, increases in σ'_v. The final shear stress during the slowest interface test I5 was $33kPa$; the value predicted from the drained soil parameters, including c' and assuming $\sigma'_v = 50kPa$, is $35.8kPa$. Hence it may be concluded that I5 was the only drained interface test performed.

A point of particular interest is whether laboratory interface test results might be used to predict the bond resistance of soil nails. Comparisons between interface and pull-out tests are often made (for example in HA68/94) in terms of the peak friction angle ϕ'_{max} observed between the maximum shear stress, τ_{max} and the normal effective stress σ'_n acting on the interface. It is recognised that it is the effective stresses which control soil behaviour, but these were not known during either the interface or the pull-out tests because it is thought that these tests were undrained or partially drained. However, the soil is likely to have been in a similar state at the start of all tests, so an attempt is made below to compare the results in terms of total stresses. The most convenient way of doing this is by comparing values of α for nails with the equivalent quantity for interface tests, i.e.

$$\alpha_{it} = \frac{\tau_{max}}{s_u} \qquad (102.)$$

where $s_u = 100kPa$ is again assumed for all tests.

Figure 9.7 shows the distribution of α_{it} and α with the logarithm of displacement rate for interface tests performed at $\sigma_n = 50kPa$ and pull-out tests performed at $\sigma_n = 60kPa$. The trend for both types of test is of increasing values of α with displacement rate, but interface tests are seen to show higher values of α than pull-out tests for equivalent displacement rates. The gradients of the least-squares lines fitted through the results are similar, but the limited data prevent credible quantitative comparisons.

It is possible that the thickness of the shear zone developed was different in the two types of test. The narrow gap between the two halves of the shear box may have imposed a very narrow shear zone during interface testing, whereas the soil around the nails was less confined (note that the ends of the grouted nail were formed $200mm$ away from the tank wall). This would imply that the shear strains were greater for the same displacement during the interface tests, and therefore that the strain rates were greater for a given displacement rate. This might at least partially explain the different level of the lines in figure 9.7.

To compare the results from the different types of test at varying in-situ stresses, it is necessary to define a reference stress quantity. The most obvious quantity is the normal stress acting on the grout-soil interface. For the interface tests, σ_n is defined as the vertical total stress σ_v applied to the sample throughout testing, values of which are given in section 5.3.3. The normal total stress acting on the grout surface at the start of a pull-out test is assumed to be given by the average of the measured vertical and horizontal total stresses. Hence for the pull-out tests,

$$\sigma_n = (\sigma_v + \sigma_h)/2 \qquad (103.)$$

where the values of σ_v and σ_h are given in 0.

Figure 9.8 shows the distribution of α_{it} and α with σ_n for interface tests performed at a displacement rate of $0.3mm/min$ and pull-out tests performed at a displacement rate of $20mm/min$. Ideally, a comparison would have been made at similar shearing rates, but it

was not possible to perform the interface tests sufficiently quickly with the apparatus used. A similar trend in behaviour between the two types of test is again observed.

The FE analyses have shown that the effective radial stress acting on the nail grout is likely to be low when using low pressure grouting (section 8.4.7). According to the observed trends, the fully drained (after 28 days cure) radial effective stress at the soil inner boundary would be equal to the grout pressure applied. During the laboratory pull-out tests, a grout pressure of only $10kPa$ was used. This would suggest that the actual radial stress acting on the grout was as low as 10% of the value of σ_n calculated from (103.).

Assuming that the line through the interface test results in figure 9.8 represents the more accurate relationship between α and σ_n, the actual values of σ_n operating at the nail grout-soil interface may be estimated from the equation of the line to be $7kPa$ and $35\ kPa$ for F1 and F3 respectively. However, these do not correspond directly to the FE results, which would predict a value of approximately $10kPa$ – the grout pressure applied during both tests. It is possible that the stresses around the nail increased after the grout set during F3. This effect was not observed during the FE analyses, but these did not model the close proximity of a stress controlled boundary (the vertical loading system).

9.4. Mechanisms of bond resistance

A general feature of all the pull-out tests performed during the final test series was the development of a peak in bond resistance. After this peak had been reached, the bond resistance decreased, then approached a constant value towards the end of the test. This behaviour may be explained by assuming that dilation of the soil takes place concurrently with plastic deformation, and that the rate of dilation decreases with increasing strain as the soil approaches critical state*. The dilation adds to the strength of the soil, since a shear load has to do work not only in the shear direction, but also in the normal direction as the

* This assumes that deformations occur entirely within the soil – complete bond is maintained between grout and clay at all times. This assumption is supported by the covering of clay found on the grout surface of the laboratory nails after testing.

soil under shear expands against the bulk of indirectly loaded soil. After dilation has stopped, the strength also drops since work is then done in the shear direction only. The dilation does, however, permanently increase the mean effective stress and hence the shear strength of the soil in the vicinity of the nail.

The above explanation is relevant to the FE results, which show a constant bond resistance following the initial peak. The laboratory tests however, show a more gradual decline in resistance, which occurs generally at quite large shear displacements (see for example the results from F1, figure 4.6). A possible explanation for this decrease in bond resistance is that the high shear strains in the shear zone at large displacements lead to rupture of the soil on a cylindrical plane, and the subsequent mobilisation of residual friction angles as the clay particles are aligned by the sliding surfaces. Such failure planes were observed directly by Martins (1983) following model pile loading tests. Examining the axial displacement distribution for FE analysis A1, figure 8.7(c), the 'final' shear strain in the first element is approximately 350%. For a 100*mm* diameter nail, this shear strain is reached at a pull-out displacement of only 25*mm*.

Wood (1990) suggests that clays with significant content of rotund particles mobilise higher residual friction angles, since these particles inhibit the formation of smooth failure surfaces. The CMS clay used in the laboratory has a significant granular content (approximately 20% fine sand to fine gravel), and as such would be expected to exhibit a higher residual friction angle than a soil such as kaolin, which contains little or no sand-sized particles. This would explain why the bond resistance measured during F1 and similar tests decreased only moderately after the maximum was reached.

9.5. Soil nailing design methods and test procedures

9.5.1. Total stress design methods

The most common method of determining the shaft resistance of piles in clay is by the application of a factor α to the undrained shear strength s_u (section 1.2.2). This also forms the basis of simple design methods for soil nails (section 1.2.5). Assuming

$s_u = 100kPa$, the α values calculated for the final laboratory test series are shown in Table 9.1.

Test	$\sigma_v\,(kPa)$	α_1	α_2	*Notes*
F1	50	0.36	0.27	Standard test
F2	50	-	0.30	Sustained load
F3	100	0.50	0.41	
F4	100	-	0.39	Sustained load
F5	50	0.50	0.27	Faster pull-out
F6	50	0.36	0.30	Slower pull-out

Table 9.1 notes

α_1 - calculated from peak value of τ

α_2 - calculated from final value of τ

Table 9.1 – Summary of α-values for F-series tests

Two values of α are given for the pull-out tests – these correspond to peak (α_1) and final (α_2) values of bond resistance measured during the test given in Table 4.1. The values of α_2 for the sustained load tests are calculated from τ_{stable} values given in Table 4.2 (NB these values of bond resistance were only achieved following large nail displacements). Given that ultimate values are usually used for design purposes, α_2 is probably the most appropriate quantity for comparison with existing design methods, particularly since the FE analyses have attributed the majority of additional peak strength to undrained loading effects which are unlikely to be relevant in a typical nailed structure.

The values of α_2 are approximately 0.3 for the tests at $\sigma_v = 50kPa$ and 0.4 for the tests at $\sigma_v = 100kPa$. These values are low compared to the commonly used value of α = 0.45 for London clay quoted in the ground anchorages design code, BS8081 (1989), but compare well with the range 0.25 to 0.75 quoted for clays in the US Federal Highways Administration (1996) document, which suggests values of α at the lower end of this range for stiffer clays. The higher values recorded in the laboratory for $\sigma_v = 100kPa$ are possibly due in part to the sample having higher s_u at this stress level (see section 9.2).

The FE analyses examined the effect that different grouting pressures had on bond resistance. Considering the final values of τ from the analyses, and calculating s_u from (98.), the values of α in Table 9.2 were obtained.

Analysis	$p_g / p'_{initial}$	α
A1	-	0.89
C1	1.0	0.87
C2	0.5	0.73
C3	2.0	1.13

Table 9.2 – Values of α from finite element analyses at different grout pressures

The value of α from A1 is included in the table to show the small difference in behaviour between the analyses which ignored installation effects, and C1 which modelled the effects of using a grout pressure equal in magnitude to the initial mean effective stress. The slightly lower α value for C1 is probably due to softening of the soil around the nail due the water content of the grout. The values of α for C2 and C3, however, show that the bond resistance is strongly dependent on the grout pressure used. The value of $p_g / p'_{initial}$ for the laboratory tests was probably close to 0.2 (assuming $\sigma'_v = 50kPa$ and $p_g \cong 10kPa$), which from the FE would imply values of α of less than 0.7.

Jones and Turner (1980) report values of α of 0.7 to 1.0 for high pressure grouted micro piles in London clay, compared to the normal range of 0.35 to 0.45 for normal bored piles (section 1.2.6). The increase in α from C1 to C3 is only 0.26 in comparison, but the grouting pressures modelled during C3 are low compared to the pressures used for the micro piles. These results confirm that significant increases in bond resistance may be obtained by the use of high pressure grouting techniques.

9.5.2. HA68/94 – An effective stress design method

This design method is described in section 1.2.5. Assuming $\phi'_{dcs} = 26.4$, and $\sigma'_v = 50kPa$, the value of σ'_n from equation (11.) is $46.2kPa$. The term in parentheses in equation (10.), representing the unfactored bond resistance, is then calculated to be $22.9kPa$ (neglecting c' as recommended). This value is low compared to the laboratory values for tests at $\sigma_v = 50kPa$, but it should be noted that the design value would actually be increased due to the high friction angles measured during the interface tests. This is because λ_p in equation (10.) includes a factor $\tan\phi'_{int} / \tan\phi'_{dcs}$, which is equal to 1.33 using the constant volume friction angle measured during the slow interface test I5. Hence the final predicted bond resistance is $30.5kPa$ which is slightly higher than the values of τ_{pp} measured during the pull-out tests (average $28kPa$ for $\sigma_v = 50kPa$) and τ_{stable} measured during the sustained loading tests ($26kPa$ for F2).

The advice note states that in soils with appreciable cohesion, the value of σ'_n may be over predicted by equation (11.) – the value calculated ($46kPa$) certainly appears high compared to the FE predictions for low grout pressures. However, the advice note also recommends the use of high grout pressures or expanding grout to compensate for this. The FE results suggest that high grout pressures are effective in raising σ'_n, but it is doubtful whether an expanding grout would result in a similar increase, unless the grout expansion was significantly greater than that used during analysis C5 (section 8.4.8).

9.5.3. Field testing procedures

It is clear from the laboratory and FE results that higher values of bond resistance are likely to be measured during pull-out tests than during sustained loading tests. Since the latter are more likely to model the loading encountered in a nailed structure, this observation suggests that the use of pull-out tests for predicting or verifying bond resistance may be unsafe for low permeability soils. The design procedure given in *Clouterre* (1991) is unique in recommending the use of sustained loading tests for verifying bond resistance in soils having a plasticity index greater than 20% - other design procedures recommend pull-out testing at unspecified displacement rates. It is suggested,

therefore, that the French approach is more appropriate, and that this should become standard for nails installed in clay soils.

Note that the French method of performing sustained load tests does not require the application of constant loads for periods of days. Instead, proportions of the design nail capacity, T_{LE}, are applied for periods of one hour, apart from one load increment of $0.7\,T_{LE}$ which is maintained for three hours. The displacement – time response is plotted on a logarithmic scale, and is used to predict the final stable displacement for each load. Hence a test need not last more than one day. These tests are still significantly more time consuming than a traditional pull-out test, which can usually be completed within an hour, but the data collected are likely to be of much higher quality in terms of interpretability for design and validation.

9.6. Conclusions

Under partially drained loading, the increases in volumetric strain and hence specific volume due to dilation can cause pore fluid suctions if there is insufficient time for the compensatory inflow of fluid from nearby soil. If the total stress remains constant, the effective stress increases still further under these suctions, allowing higher shear strength to be mobilised. The high permeability of coarse grained soils generally renders this rate effect insignificant under most normal types of loading, but in low permeability soils, even what are generally considered to be very slow loading rates may actually be quick in relation to the response time of the soil. This is shown by the peaks in strength observed during both laboratory tests and FE analyses during displacement controlled loading.

If the purpose of pull-out tests is to be the prediction of stable steady state loads, it is important that the tests should be performed at a sufficiently slow rate to allow complete drainage. It is thought that the pull-out tests carried out during this research were performed too quickly to obtain information about the fully drained bond resistance. The FE results suggest that a pull rate equivalent to $R_{po}/k = 10$ is required to prevent the effects of undrained behaviour significantly influencing pull-out results. This is impractical for low permeability soils such as the coal measure shale ($k \approx 10^{-11} m/s$) used

for the laboratory tests during this research. In such cases it is proposed that sustained loading tests may provide a better method of establishing bond resistance values.

It is the uncertainty regarding creep deformations that has so far prevented extensive use of the nailing technique in clay soils. The laboratory sustained loading tests confirmed that time-dependent deformations in such soils are inevitable under service conditions, and may be expected to increase in magnitude as loads increase towards the ultimate limit state. However, the deformations observed did stabilise within $1.5mm$ provided that the load was kept at or below half the peak value recorded during equivalent pull-out tests. Beyond this loading level, the behaviour was unpredictable. The mechanism by which these time dependent deformations occur is not yet clear; it is probable that both creep and consolidation effects are involved.

It proved difficult to draw any firm conclusions regarding the link between pull-out and interface test behaviour. The boundary conditions are different for each type of test. In particular, σ_n is constant during an interface test, whereas it is likely to increase during a pull-out test due to restrained dilation. In the absence of effective stress data, it is therefore difficult to compare the shearing response obtained from the different apparatus. Furthermore, the thickness of the shear zone during interface tests may be influenced by the physical arrangement of the shear box. An attempt has been made to compare the results in terms of total stresses, and this has succeeded in showing that similar patterns of behaviour are observed during both types of test. However, there is as yet no obvious method of predicting nail bond resistances from the results of interface tests with confidence.

The finite element analyses have shown that the grouting pressure has a significant effect on bond resistance. The method of filling bore holes under gravity pressure only often employed in the field leads to low effective stresses around the nail, and correspondingly low values of soil shear strength. The use of elevated grout pressures increases these effective stresses, resulting in permanently increased bond resistance. The use of high grout pressures might therefore make the use of soil nailing economic in clays, although uncertainty remains regarding long term serviceability.

Chapter 10. CONCLUSIONS

10.1. Laboratory pull-out and sustained load testing.

A large apparatus was developed for the testing of elemental lengths of grouted nail at full scale. Testing procedures for pull-out (constant rate of displacement) and sustained loading were developed, and the effects of varying initial in-situ stress and loading rates were investigated. The test results were compared by measuring the load displacement response of the nail, and using the load data to calculate the shear stress assumed to act uniformly along and around the perimeter of the nail grout.

The magnitude of the peak in bond resistance measured during pull-out testing was found to depend on the rate of loading. The highest peak values were measured during the fastest pull-out test while lower peak values were recorded at lower pull-out rates. The post peak bond resistance measured during pull-out tests at the same vertical surcharge was similar for all pull rates, but these post peak values were higher than the equivalent maximum stable loads applied during sustained load tests.

The effect of loading rate may be explained in terms of the consolidation behaviour of the soil around a nail. Changes in pore water pressure, and hence effective stress, caused by dilation induce the pore water to flow. The magnitude of these flows depends on the relative rates of dilation, which depends (partly) on the loading rate, and pore pressure dissipation, which is a function of soil permeability. If the loading rate is sufficiently high that the suctions caused by dilation do not dissipate, high peak values of bond resistance are mobilised because the soil shear strength is temporarily increased by the raise in effective stress. It is probable that creep also plays a significant role in reducing bond resistance under long term loading conditions – this effect has not been considered in detail in this thesis.

Attempts to use high grout pressures were not successful, due to rupture of the soil sample along the joints of the clay blocks, and subsequent seepage of the grout. This problem could be avoided by the use of soil samples consolidated from slurry. Samples created in this manner would be much less likely to rupture under the action of high grout pressures. However, the time required to produce samples of equivalent size would be great, and there would be room for only a limited number of tests in an equivalent research programme using this technique.

One further aim of the laboratory testing which was not fulfilled during this research due to practical difficulties was the direct measurement of effective stress conditions at the grout-soil interface using instrumentation embedded in the grout. Limited pore pressure data were obtained during one test, but proved difficult to interpret due to drift of the transducer output. Useful data regarding both effective stress behaviour and the action of high grout pressures were, however, obtained during the finite element work.

10.2. Interface testing

A standard Casagrande direct shear apparatus was used to measure directly the shear resistance of a grout-clay interface. The main aim of these tests was to examine whether nail bond resistance might be predicted from this relatively simple small-scale laboratory test. A sample preparation procedure was devised which allowed the grout to set while in direct contact with the soil, simulating grouted nail installation. Tests were performed at varying displacement rates, and at varying vertical total stress levels.

Comparing the results from the interface and pull-out tests performed during this research, similar trends in behaviour are observed in both types of test. However, the values of bond resistance predicted from the interface tests were high compared to measured values. It is suggested that this discrepancy is mostly due to the low stress acting on nails grouted at low pressures. Unless it becomes possible to estimate with some accuracy the normal stress acting on a nail after installation is complete, it is unlikely that this method of predicting bond resistance will have significant advantages over existing methods which are based on soil parameters obtained from standard laboratory tests.

10.3. Finite element modelling

A one-dimensional axisymmetric finite element model was developed to examine trends observed during the laboratory tests, and to investigate further the mechanisms of bond resistance in terms of soil effective stresses. The model incorporated coupled consolidation behaviour, and special shape functions designed to match exactly elastic solutions for displacements and steady state solutions for pore pressures. The material model was frictional to simulate the overconsolidated clays most likely to be used for nailing in the field, and included a variable angle of dilation to simulate more realistically the behaviour of soil under shear.

The dependence of bond resistance on displacement rate during pull-out testing was confirmed by the FE analyses. The output from the FE model also allowed detailed explanations for this behaviour to be developed in terms of the dilation and consolidation characteristics of the soil, and hence the effective stress changes in the soil during nail loading. A limitation of the elastic-plastic model used during these analyses was that time dependent displacements under sustained load conditions were not predicted in the elastic regime. Consequently, the behaviour observed during the early stages of laboratory sustained load tests was not reproduced in the FE results. It is probable that a substantially more complicated material model would be required to capture this type of response.

The pressure applied during grouting was shown to have a significant effect on subsequent bond resistance. The low pressures (gravity only) typically employed in the field are likely to result in low effective stresses around the nail, and hence low soil shear strength. Conversely, higher grout pressures locally increase soil shear strength, while grouting at a pressure equivalent in magnitude to the initial in-situ (isotropic) effective stress results in only a slight decrease in shear strength due to ingress of free water from the liquid grout.

10.4. Recommendations for field testing

The choice of testing method for the verification of bond resistance of soil nails in the field is critical. In low permeability soils, significant suctions are likely to develop during conventional constant rate of displacement pull-out testing. These suctions temporarily increase the effective stress, leading to the measurement of high values of bond resistance which are unlikely to be mobilised at the loading rates encountered in the finished structure. In these soils, it is suggested that some form of sustained load test is more likely to lead to safe estimates of bond resistance.

REFERENCES

Abbo, A.J. and Sloan, S.W. (1994). *An algorithm for controlling load path error in non-linear finite element analysis.* Computer methods and advances in geotechnics, Balkema.

Atkinson, J.H. (1993). *An introduction to the mechanics of soils and foundations.* McGraw-Hill.

BS8006 : 1995 – *Code of practice for strengthened/reinforced earth and other fills.*

BS8081 : 1989 – *Code of practice for ground anchorages.*

Barley, A.D. (1999). *Controlling factor.* Ground Engineering, Feb 1999.

Been, K. and Jefferies, M.G. (1985). *A state parameter for sands.* Géotechnique V.35 No.2.

Bolton, M.D. (1986). *The strength and dilatancy of sands.* Géotechnique V.36 No.1.

Borin, D.L. (1973). *The behaviour of saturated Kaolin in the simple shear apparatus.* PhD thesis, University of Cambridge.

Britto, A.M. and Gunn, M.J. (1987). *Critical state soil mechanics via finite elements.* Ellis Horwood.

Brocklehurst, C.J. (1993). *Finite element studies of reinforced and unreinforced two-layer soil systems.* DPhil thesis, University of Oxford.

Burd, H.J. (1986). *A large displacement finite element analysis of a reinforced unpaved road.* DPhil thesis, University of Oxford.

Burd, H.J. and Brocklehurst, C.J. (1992). *Parametric studies of a soil reinforcement problem using finite element analysis.* Proc. Int. Conf. on Computer Methods and Advances in Geomechanics, Cairns, Australia, pp 1783-1788.

Burland, J.B. (1973). *Shaft friction of piles in clay – a simple fundamental approach.* Ground Engineering V.6 No.3.

Cartier, G., and Gigan, J.P. (1983). *Experiments and observations on soil nailing structures.* Proc. VIII ECSMFE, Helsinki, V.2 pp 473-476.

Carter, J.P., Booker, J.R. and Yeung, S.K. (1986). *Cavity expansion in cohesive frictional soils.* Géotechnique V.36 No.3.

Carter, J.P., Randolph, M.F. and Wroth, C.P. (1979). *Stress and pore pressure changes in clay during and after the expansion of a cylindrical cavity.* Int. Jnl. for Num. and Anal. Methods in Geomechanics V.3 pp 305-322.

Chandler, R.,J. (1968). *The shaft friction of piles in cohesive soils in terms of effective stress.* Civil Engineering and Public Works Review, Jan 1968.

Chandler, R.J. and Martins, J.P. (1982). *An experimental study of skin friction around piles in clay.* Géotechnique V.32 No.2.

Clouterre (1991) – see Presses de l'école nationale des ponts et chaussées (1991).

Cooke, R.W. (1974). *The settlement of friction pile foundations.* Proc. Conf. on Tall Buildings, Kuala Lumpur, Malaysia.

DoT (1994). HA 68/94 – *Design methods for the reinforcement of highway slopes by reinforced soil and soil nailing techniques.* Design manual for roads and bridges, V.4, Sect. 1, Part 4, HMSO.

Duncan, J.P. and Buchignani, A.L. (1976). *An engineering manual for settlement studies.* Geotech. Eng. Report, Dept. of Civil Eng., Univ. of California at Berkley, pp94.

England, M. (1999). *A pile behaviour model.* PhD thesis in preparation, Imperial College of Science and Technology, University of London.

Francescon, M. (1983). *Model pile tests in clay – stresses and displacements due to installation and axial loading.* PhD thesis, Cambridge University.

Gässler, G. (1992). *Full scale test on a nailed wall in consolidated clay.* Proc. Int. Symp. Earth Reinf. Practice, Fukuoka, Japan, pp 475-480.

Gässler, G. (1995). *Stabilisation of a cutting slope along a high-speed railway line using extremely long nails.* The practice of soil reinforcing in Europe, Thomas Telford, London.

Gerald, C.F. and Wheatley, P.O. (1989). *Applied numerical analysis.* 4th Edition, Addison Wesley.

Heymann, G., Rohde, A.W., Schwartz, K. and Friedlaender, E. (1992). *Soil nail pull-out resistance in residual soils.* Proc. Int. Symp. Earth Reinf. Practice, Fukuoka, Japan, pp 487-492.

Houlsby, G.T. (1998). Private communication.

Houlsby, G.T. (1991). *How the dilatancy of soils affects their behaviour.* Proc. 10th Eur. Conf. on Soil Mech. and Found. Eng.

Jackson, N. (Ed.) (1980). *Civil engineering materials.* 2nd edition, Macmillan, London.

Jewell, R.A. (1987). *Direct shear tests on sands.* Report No. OUEL 1719/88. University of Oxford.

Jones, D.A. and Turner, M.J. (1980). *Load tests on post-grouted micro piles in London clay.* Ground Engineering, September 1980.

Martins, J.P. (1983). *Shaft resistance of axially loaded piles in clay.* PhD thesis, Imperial College of Science and Technology, University of London.

Matsuoka, H. (1976). *On the significance of the spatial mobilised plane.* Soils and Foundations V.16 (1) pp 91-100.

Milligan, G.W.E., Chang, K.T. and Morris, J.D. (1997). *Pull-out resistance of soil nails in sand and clay.* Proc. 3rd Int. Conf. Ground Improvement Geosystems, London.

Mühlhaus, H.-B. and Vardoulakis, I. (1987). *The thickness of shear bands in granular materials.* Géotechnique V.37 No.3.

Palmeira, E.M. (1987). *The study of soil-reinforcement interaction by means of large scale laboratory tests.* D.Phil. thesis, University of Oxford.

Pedley, M.J., Jewell, R.A. and Milligan, G.W.E. (1990). *A large scale experimental study of soil-reinforcement interaction.* Ground Engineering, Aug 1990.

Potts, D.M. and Martins, J.P. (1982). *The shaft resistance of axially loaded piles in clay.* Géotechnique V.32 No.4.

Presses de l'école nationale des ponts et chaussées (1991). *Recommandations Clouterre 1991.* English translation, U.S. Federal Highways Administration, 1993.

Pyrah, I.C. (1980). *The solution of two dimensional consolidation problems.* Proc. Symp. on Computer Applications to Geot. Problems in Highway Engineering, P.M. Geotechnical Analysis Ltd, Cambridge.

Randolph, M.F. (1977). *A theoretical study of the performance of piles.* PhD thesis, University of Cambridge.

Randolph, M.F., Carter, J.P. and Wroth, C.P. (1979). *Driven piles in clay – the effects of installation and subsequent consolidation.* Géotechnique V.29 No.4.

Randolph, M.F. and Wroth, C.P. (1978). *Analysis of deformation of vertically loaded piles.* Jnl. of the Geot. Eng. Division ASCE V.104 No.GT12.

Randolph, M.F. and Wroth, C.P. (1979). *An analytical solution for the consolidation around a driven pile.* Int. Jnl. for Num. and Anal. Methods in Geomechanics V.3 pp 217-229.

Randolph, M.F. and Wroth, C.P. (1981). *Application of the failure state in undrained simple shear to the shaft capacity of piles.* Géotechnique V.31 No.1.

Randolph, M.F. and Wroth, C.P. (1982). *Recent developments in understanding the axial capacity of piles in clay.* Ground Engineering, October 1982.

Rogers, C.D.F. (1985). *The response of uPVC pipes to surface loading.* PhD thesis, University of Nottingham.

Schofield, A.N. and Wroth, C.P. (1968). *Critical state soil mechanics.* McGraw Hill.

Skempton, A.W. (1959). *Cast in-situ bored piles in London clay.* Géotechnique V.9 No.4.

Sloan, S.W. (1981). *Numerical analysis of incompressible and plastic solids using finite elements.* PhD thesis, University of Cambridge.

Standing, J.R. (1997). *Studies of the interface resistance of soil nails.* PhD thesis, Imperial College of Science and Technology, University of London.

Steenfelt, J.S., Randolph, M.F. and Wroth, C.P. (1981). *Instrumented model piles jacked into clay.* Proc. X ICSMFE, Stockholm.

Stroud, M.A. (1971). *The behaviour of sand at low stress levels in the simple shear apparatus.* PhD thesis, University of Cambridge.

Tei, K. (1993). *A study of soil nailing in sand.* DPhil thesis, University of Oxford.

U.S. Federal Highways Administration (1996) – *Manual for design and construction of soil nailed walls*

Unterreiner, P., Benhamida, B. and Schlosser, F. (1997). *Finite element modelling of a full-scale experimental soil-nailed wall. French National Research Project Clouterre.* Ground Improvement V.1 No.1.

Van Langen, H. and Vermeer, P.A. (1990). *Automatic step size correction for non-associated plasticity problems.* Int. Jnl. for Num. Methods in Eng. V.29, pp 579-598.

Vermeer, P.A. and Verruijt, A. (1981). *An accuracy condition for consolidation by finite elements.* Int. Jnl. for Num. and Anal. Methods in Geomechanics V.5 pp 1-14.

Wood, D.M. (1990). *Soil behaviour and critical state soil mechanics.* Cambridge University Press.

Wroth, C.P. and Basset, R.H. (1965). *A stress-strain relationship for the shearing behaviour of sand.* Géotechnique V.15 No.1.

Yao, M. (1996). *A study of the effect of length to diameter ratio on the results of pressuremeter tests.* MSc thesis, University of Oxford.

Yu, H.S. (1990). *A new finite element formulation for one-dimensional analysis of elastic-plastic materials.* Computers and Geotechnics V.9 241-256.

Yu, H.S. and Houlsby, G.T. (1990). *A new finite element formulation for one-dimensional analysis of elastic-plastic materials.* Computers and Geotechnics V.9 241-256.

Yu, H.S. and Houlsby, G.T. (1991). *Finite cavity expansion in dilatant soils: loading analysis.* Géotechnique V.41 No.2.

APPENDIX A – FINITE ELEMENT EQUATION DERIVATIONS

A1.1. Shape functions for radial displacement

The elastic solution for stresses within a thick walled cylinder is of the form:

$$\sigma_r = A + \frac{B}{r^2}$$
$$\sigma_\theta = A - \frac{B}{r^2} \qquad \text{(A1.1.)}$$

Where the constants A and B depend on the boundary conditions at the inner and outer surface. Assuming plane strain conditions apply,

$$\varepsilon_z = 0 \qquad \text{(A1.2.)}$$

The solution for radial displacements $u(r)$ is most easily obtained by examining the equation for circumferential stress.

$$\varepsilon_\theta = \frac{u}{r} = \frac{1}{E}\left[\sigma_\theta - \nu(\sigma_r + \sigma_z)\right] \qquad \text{(A1.3.)}$$

Also, from the plane strain assumption,

$$\varepsilon_z = 0 = \frac{1}{E}\left[\sigma_z - \nu(\sigma_r + \sigma_\theta)\right]$$
$$\therefore \sigma_z = \nu(\sigma_r + \sigma_\theta) = \nu(2A) \qquad \text{(A1.4.)}$$

inserting this into (A1.1.) we obtain

$$u = \frac{r}{E}\left[A - \frac{B}{r^2} - \nu\left(A + \frac{B}{r^2} + 2\nu A\right)\right] \qquad \text{(A1.5.)}$$

rearranging,

$$u = \frac{1+\nu}{E}\left[A(1-2\nu).r - \frac{B}{r}\right] \qquad \text{(A1.6.)}$$

or more simply,

$$u = A_1 r + \frac{B_1}{r} \qquad \text{(A1.7.)}$$

where A_1 and B_1 are two new constants. This is the form used for the displacement interpolation function. Now, considering a two-node element using this type of interpolation function we see that

$$U_1 = A_1 R_1 + \frac{B_1}{R_1}$$
$$U_2 = A_1 R_2 + \frac{B_1}{R_2} \qquad \text{(A1.8.)}$$

where U_1 and U_2 are the radial displacements at the nodes. Solving simultaneously,

$$A_1 = \frac{R_1 U_1 - R_2 U_2}{R_1^2 - R_2^2}$$
$$B_1 = \frac{R_1 R_2 (R_1 U_1 - R_2 U_2)}{R_1^2 - R_2^2} \qquad \text{(A1.9.)}$$

In general, the displacement at any point within the element is described in terms of the displacement at the nodes and the shape functions.

$$u = N_{r1} U_1 + N_{r2} U_2 \qquad \text{(A1.10.)}$$

or, in matrix notation

$$u = \mathbf{N}_r \mathbf{U} \qquad \text{(A1.11.)}$$

where $\mathbf{N}_r$ is the matrix of shape functions for radial displacements, given by

$$\mathbf{N}_r = \mathbf{N}_r(r) = \begin{bmatrix} N_{r1} \\ N_{r2} \end{bmatrix} = \begin{bmatrix} \left(\frac{-R_1}{R_2^2 - R_1^2} \right) r + \left(\frac{R_1 R_2^2}{R_2^2 - R_1^2} \right) \frac{1}{r} \\ \left(\frac{R_2}{R_2^2 - R_1^2} \right) r + \left(\frac{-R_1^2 R_2}{R_2^2 - R_1^2} \right) \frac{1}{r} \end{bmatrix} \qquad \text{(A1.12.)}$$

A1.2. Finite element equations

Note: The formulation described in sections A1.2.1 & A1.2.2 was originally derived by Professor G.T. Houlsby.

A1.2.1. Without consolidation

Define global co-ordinates x in terms of nodal global co-ordinates X:

$$\mathbf{x} = \mathbf{N}\mathbf{X} \qquad \text{(A1.13.)}$$

where $\mathbf{N}$ are shape functions of the local co-ordinates $\mathbf{N} = \mathbf{N}(\alpha)$.

Define similarly global displacements $\mathbf{u}$ in terms of the nodal global displacements $\mathbf{U}$:

$$\mathbf{u} = \mathbf{N}\mathbf{U} \tag{A1.14.}$$

Define the strains ε in terms of the nodal global displacements:

$$\varepsilon = \mathbf{B}\mathbf{U} \tag{A1.15.}$$

It follows from the above that:

$$\dot{\mathbf{u}} = \mathbf{N}\dot{\mathbf{U}} \tag{A1.16.}$$

$$\dot{\varepsilon} = \mathbf{B}\dot{\mathbf{U}} \tag{A1.17.}$$

$$\dot{u}^{\mathrm{T}} = \dot{\mathbf{U}}^{\mathrm{T}}\mathbf{N}^{\mathrm{T}} \tag{A1.18.}$$

$$\dot{\varepsilon}^{\mathrm{T}} = \dot{\mathbf{U}}^{\mathrm{T}}\mathbf{B}^{\mathrm{T}} \tag{A1.19.}$$

Define the stress rate $\dot{\sigma}$ in terms of the strain rate $\dot{\varepsilon}$:

$$\dot{\sigma} = \mathbf{D}\dot{\varepsilon} \tag{A1.20.}$$

The equilibrium equation is expressed as:

$$\sigma_{ij,j} - \mathbf{w}_i = 0 \tag{A1.21.}$$

where the subscript after the comma indicates differentiation with respect to that subscript, and $\mathbf{w}_i$ are the body forces per unit volume. This is replaced by an integral form:

$$\int_V \dot{\mathbf{u}}_i^* \left(\sigma_{ij,j} - \mathbf{w}_i\right) \mathrm{d}V = 0 \tag{A1.22.}$$

where $\dot{\mathbf{u}}_i^*$ are a set of weighting functions, in fact identified with virtual velocities.

Applying Green's theorem to the above we obtain:

$$\begin{aligned} \int_V \dot{\mathbf{u}}_i^* \sigma_{ij,j}\, \mathrm{d}V - \int_V \dot{\mathbf{u}}_i^* \mathbf{w}_i\, \mathrm{d}V &= \int_V \left(\dot{\mathbf{u}}_i^* \sigma_{ij}\right)_{,j} \mathrm{d}V - \int_V \dot{\mathbf{u}}_{i,j}^* \sigma_{ij}\, \mathrm{d}V - \int_V \dot{\mathbf{u}}_i^* \mathbf{w}_i\, \mathrm{d}V \\ &= \int_A \dot{\mathbf{u}}_i^* \sigma_{ij} \mathbf{n}_j\, \mathrm{d}A + \int_V \dot{\varepsilon}_{ij}^* \sigma_{ij}\, \mathrm{d}V - \int_V \dot{\mathbf{u}}_i^* \mathbf{w}_i\, \mathrm{d}V = 0 \end{aligned} \tag{A1.23.}$$

we identify $-\int_A \dot{\mathbf{u}}_i^* \sigma_{ij} \mathbf{n}_j\, \mathrm{d}A$ as the virtual work done by external forces on the element, so that we can write for the element:

$$\dot{\mathbf{U}}^{*\mathrm{T}}\mathbf{F} = \int_V \dot{\varepsilon}^{*\mathrm{T}} \sigma\, \mathrm{d}V - \int_V \dot{\mathbf{u}}^{*\mathrm{T}} \mathbf{w}_i\, \mathrm{d}V = \int_V \dot{\mathbf{U}}^{*\mathrm{T}} \mathbf{B}^{\mathrm{T}} \sigma\, \mathrm{d}V - \int_V \dot{\mathbf{U}}^{*\mathrm{T}} \mathbf{N}^{\mathrm{T}} \mathbf{w}_i\, \mathrm{d}V \tag{A1.24.}$$

so that:

$$\mathbf{F} = \int_V \mathbf{B}^T \sigma \, dV - \int_V \mathbf{N}^T \mathbf{w} \, dV \tag{A1.25.}$$

and further that:

$$\dot{\mathbf{F}} = \int_V \mathbf{B}^T \dot{\sigma} \, dV = \int_V \mathbf{B}^T \mathbf{D} \dot{\varepsilon} \, dV = \int_V \mathbf{B}^T \mathbf{D} \mathbf{B} \dot{\mathbf{U}} \, dV = \int_V \mathbf{B}^T \mathbf{D} \mathbf{B} \, dV \, \dot{\mathbf{U}} = \mathbf{K} \dot{\mathbf{U}} \tag{A1.26.}$$

where

$$\mathbf{K} = \int_V \mathbf{B}^T \mathbf{D} \mathbf{B} \, dV \tag{A1.27.}$$

A1.2.2. With coupled consolidation

The preliminaries are as above, except that in addition we define the pore pressure in terms of the nodal pore pressure:

$$\mathbf{u}_w = \mathbf{N}_w \mathbf{U}_w \tag{A1.28.}$$

and the pore pressure gradients:

$$\mathbf{u}_{w,} = \mathbf{E} \mathbf{U}_w \tag{A1.29.}$$

The material stiffness equation is now in terms of effective stresses:

$$\dot{\sigma}' = \mathbf{D} \dot{\varepsilon} \tag{A1.30.}$$

And it is necessary to define the effective stress:

$$\sigma = \sigma' - \delta \mathbf{u}_w \tag{A1.31.}$$

where δ is the vectorial form of the Kronecker delta.

It also follows that the volumetric strain is given by:

$$\dot{\varepsilon}_v = \delta \dot{\varepsilon} \tag{A1.32.}$$

The nodal force rates are given by:

$$\begin{aligned} \dot{\mathbf{F}} &= \int_V \mathbf{B}^T \dot{\sigma} \, dV = \int_V \mathbf{B}^T \dot{\sigma}' - \mathbf{B}^T \delta \dot{\mathbf{u}}_w \, dV = \int_V \mathbf{B}^T \mathbf{D} \dot{\varepsilon} - \mathbf{B}^T \delta \mathbf{N}_w \dot{\mathbf{U}}_w \, dV \\ &= \int_V \mathbf{B}^T \mathbf{D} \mathbf{B} \dot{\mathbf{U}} - \mathbf{B}^T \delta \mathbf{N}_w \dot{\mathbf{U}}_w \, dV = \int_V \mathbf{B}^T \mathbf{D} \mathbf{B} \, dV \, \dot{\mathbf{U}} - \int_V \mathbf{B}^T \delta \mathbf{N}_w \, dV \, \dot{\mathbf{U}}_w = \mathbf{K} \dot{\mathbf{U}} - \mathbf{L} \dot{\mathbf{U}}_w \end{aligned} \tag{A1.33.}$$

where

$$\mathbf{L} = \int_V \mathbf{B}^T \delta \mathbf{N}_w \, dV \tag{A1.34.}$$

It is next necessary to impose the continuity condition, which can be written:

$$\mathbf{v}_{ai,i} + \dot{\varepsilon}_v = 0 \qquad \text{(tensile strain positive)} \tag{A1.35.}$$

Again this is done in an approximate integrated form, multiplying by weighting factors which we identify with a set of virtual pore pressures:

$$\int_V \mathbf{u}_w^* \left(\mathbf{v}_{ai,i} + \dot{\varepsilon}_v \right) = 0 \tag{A1.36.}$$

Applying Green's theorem to the above leads to:

$$\begin{aligned} \int_V \mathbf{u}_w^* \left(\mathbf{v}_{ai,i} + \dot{\varepsilon}_v \right) &= \int_V \mathbf{u}_w^* \mathbf{v}_{ai,i} \, dV + \int_V \mathbf{u}_w^* \dot{\varepsilon}_v \, dV = \int_V \left(\mathbf{u}_w^* \mathbf{v}_{ai} \right)_{,i} dV - \int_V \mathbf{u}_{w,i}^* \mathbf{v}_{ai} \, dV + \int_V \mathbf{u}_w^* \dot{\varepsilon}_v \, dV \\ &= \int_A \mathbf{u}_w^* \mathbf{v}_{ai} \mathbf{n}_i \, dA - \int_V \mathbf{u}_{w,i}^* \mathbf{v}_{ai} \, dV + \int_V \mathbf{u}_w^* \dot{\varepsilon}_v \, dV = 0 \end{aligned} \tag{A1.37.}$$

rearranging,

$$\int_A \mathbf{u}_w^* \mathbf{v}_{ai} \mathbf{n}_i \, dA = - \int_V \mathbf{u}_w^* \dot{\varepsilon}_v \, dV + \int_V \mathbf{u}_{w,i}^* \mathbf{v}_{ai} \, dV \tag{A1.38.}$$

The negative first term we identify with the external virtual work done in supplying water to the element. Defining nodal outflows as $\mathbf{Q}$, it follows that the above equation can be written as:

$$\mathbf{U}_w^{*T} \mathbf{Q} = - \int_V \mathbf{u}_w^* \dot{\varepsilon}_v \, dV + \int_V \mathbf{u}_{w,i}^{*T} \mathbf{v}_{ai} \, dV = - \int_V \mathbf{U}_w^{*T} \mathbf{N}^T \dot{\varepsilon}_v \, dV + \int_V \mathbf{U}_w^{*T} \mathbf{E}^T \mathbf{v}_a \, dV \tag{A1.39.}$$

from which it follows that:

$$\begin{aligned} \mathbf{Q} &= - \int_V \mathbf{N}^T \dot{\varepsilon}_v \, dV + \int_V \mathbf{E}^T \mathbf{v}_a \, dV = - \int_V \mathbf{N}^T \delta \dot{\varepsilon} \, dV - \frac{1}{\gamma_w} \int_V \mathbf{E}^T \mathbf{k} \mathbf{u}_w \, dV \\ &= - \int_V \mathbf{N}^T \delta \mathbf{B} \dot{\mathbf{U}} \, dV - \frac{1}{\gamma_w} \int_V \mathbf{E}^T \mathbf{k} \mathbf{E} \mathbf{U}_w \, dV = - \mathbf{L}^T \dot{\mathbf{U}} - \mathbf{M} \mathbf{U}_w \end{aligned} \tag{A1.40.}$$

where

$$\mathbf{M} = \frac{1}{\gamma_w} \int_V \mathbf{E}^T \mathbf{k} \mathbf{E} \, dV \tag{A1.41.}$$

So equations to be solved are:

$$\dot{\mathbf{F}} = \mathbf{K} \dot{\mathbf{U}} - \mathbf{L} \dot{\mathbf{U}}_w \tag{A1.42.}$$

$$\mathbf{Q} = -\mathbf{L}^T \dot{\mathbf{U}} - \mathbf{M} \mathbf{U}_w \tag{A1.43.}$$

A1.3. General elastic-plastic material model

The strain increment for each step is divided into elastic and plastic components.

$$\dot{\varepsilon} = \dot{\varepsilon}^{e} + \dot{\varepsilon}^{p} \tag{A1.44.}$$

The stress increment may be written

$$\dot{\sigma} = \mathbf{D}^{e}\dot{\varepsilon}^{e} \tag{A1.45.}$$

where $\sigma = \left[\sigma_{r} \quad \sigma_{z} \quad \sigma_{\theta} \quad \tau_{rz}\right]^{T}$.

The plastic strain vector is assumed to be perpendicular to the plastic potential, g, and of magnitude μ.

$$\dot{\varepsilon}^{p} = \mu\frac{\partial g}{\partial \sigma} \tag{A1.46.}$$

The yield function is given by

$$f(\sigma) = 0 \tag{A1.47.}$$

so that

$$\left[\frac{\partial f}{\partial \sigma}\right]^{T}\dot{\sigma} = 0 \tag{A1.48.}$$

Substituting equations (A1.44.), (A1.45.) & (A1.46.) into (A1.48.) we obtain

$$\left[\frac{\partial f}{\partial \sigma}\right]^{T}\left[\mathbf{D}^{e}\left\{\dot{\varepsilon} - \mu\frac{\partial g}{\partial \sigma}\right\}\right] = 0 \tag{A1.49.}$$

rearranging,

$$\mu = \frac{\left[\frac{\partial f}{\partial \sigma}\right]^{T}\mathbf{D}^{e}\dot{\varepsilon}}{\left[\frac{\partial f}{\partial \sigma}\right]^{T}\mathbf{D}^{e}\left[\frac{\partial g}{\partial \sigma}\right]} \tag{A1.50.}$$

from (A1.44.) & (A1.45.)

$$\dot{\sigma} = \mathbf{D}^{e}\left[\dot{\varepsilon} - \dot{\varepsilon}^{p}\right] = \mathbf{D}^{e}\dot{\varepsilon} - \mathbf{D}^{e}\mu\frac{\partial g}{\partial \sigma} \tag{A1.51.}$$

substitute in μ from (A1.50.)

$$\dot{\sigma} = \mathbf{D}^e\dot{\varepsilon} - \frac{\mathbf{D}^e\left[\frac{\partial g}{\partial \sigma}\right]\left[\frac{\partial f}{\partial \sigma}\right]^T\mathbf{D}^e\dot{\varepsilon}}{\left[\frac{\partial f}{\partial \sigma}\right]^T\mathbf{D}^e\left[\frac{\partial g}{\partial \sigma}\right]} = \left(\mathbf{D}^e - \frac{\mathbf{D}^e\left[\frac{\partial g}{\partial \sigma}\right]\left[\frac{\partial f}{\partial \sigma}\right]^T\mathbf{D}^e}{\left[\frac{\partial f}{\partial \sigma}\right]^T\mathbf{D}^e\left[\frac{\partial g}{\partial \sigma}\right]}\right)\dot{\varepsilon} \qquad \text{(A1.52.)}$$

which may be written as

$$\begin{aligned}\dot{\sigma} &= \left(\mathbf{D}^e + \mathbf{D}^p\right)\dot{\varepsilon} \\ &= \mathbf{D}^{ep}\dot{\varepsilon}\end{aligned} \qquad \text{(A1.53.)}$$

where the plastic stiffness matrix is given by

$$\mathbf{D}^{ep} = \frac{\mathbf{D}^e\left[\frac{\partial g}{\partial \sigma}\right]\left[\frac{\partial f}{\partial \sigma}\right]^T\mathbf{D}^e}{\left[\frac{\partial f}{\partial \sigma}\right]^T\mathbf{D}^e\left[\frac{\partial g}{\partial \sigma}\right]} \qquad \text{(A1.54.)}$$

APPENDIX B
RESPONSE OF EXTENDED MATSUOKA MATERIAL MODEL IN SINGLE ELEMENT TESTS

This appendix briefly illustrates the behaviour of the extended Matsuoka material model incorporating variable dilation. This was the material model used for the main series of FE analyses. The specification for these analyses is shown in Table B1. A mesh of one thin element was subjected to shear stress loading, and the response of the material model examined in terms of the material parameters ϕ' and ψ, and the stress and strain quantities τ_{rz} and ε_{y}. The variation of these quantities with shear displacement is shown in figure B1.

	Undrained	*Drained*
Inner and Outer boundaries	stress controlled, impermeable	stress controlled, permeable
Both boundaries, shear direction	displacement controlled	
Material	kaolin, OCR = 5	
$r_i\,(m)$	0.05	
$r_o\,(m)$	0.0505 (=1.01 r_i)	
$p'_0\ (kPa)$	100	
Gauss points per element	1	
$k\ (m/s)$	10	
Duration of shearing (s)	1000	
Shear displacement (mm)	1.0	

Table B1 – Specification for single element analyses

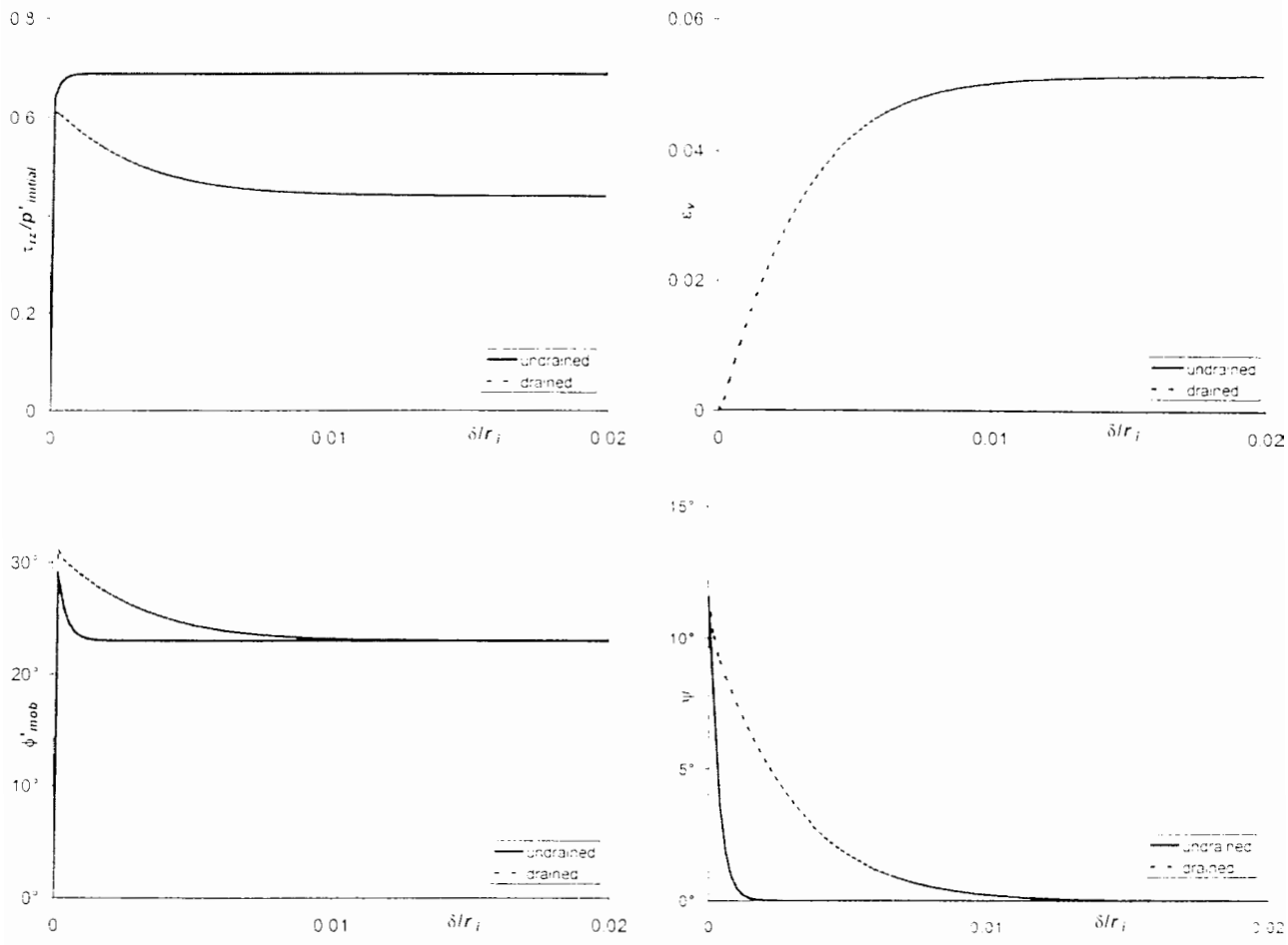

Figure B1 – Results from single element analyses

Clockwise from top left: Normalised shear stress, volumetric strain, dilation angle, mobilised effective friction angle. All quantities plotted against normalised shear displacement.

The graphs show the two extremes of behaviour: undrained (no drainage allowed at mesh boundaries), and fully drained (drainage allowed and shear displacement rate small in relation to permeability). During both analyses, the dilation angle ψ is initially high since the initial stress point is below the critical state line (refer to section 7.6.1 and figure 7.4). During shearing, dilation causes an increase in the total stress in order to maintain the plane strain condition. As the current stress point reaches critical state, ψ decreases to zero, and the total stress returns to its initial value. Following the onset of yield, the mobilised friction angle ϕ'_{mob} is directly related to ψ through Bolton's equation (79).

It is interesting to note that during the undrained analysis when there is no change in volumetric strain, dilation is contributing to shear strength, though by definition it

cannot physically be occurring. The 'potential' of the soil to dilate causes suction and hence an increase in effective stress. This in turn quickly causes ψ to decrease as critical state is approached. However, there is no mechanism for the suctions to dissipate, and the high mean effective stress allows a higher shear stress to be mobilised than during the drained analysis. This mechanism of increasing shear strength is a peculiarity of the material model, but the resulting trend in behaviour seems reasonable.

During the drained analysis, a peak in shear stress is observed due to dilation, which also causes a temporary increase in total stress, and hence in effective stress. However, no suctions are generated to maintain the effective stress level because the volumetric strain rate is low compared to the permeability of the soil, and pore fluid is able to flow into the dilating region. The soil expands against the constant pressure boundary, but once critical state is reached and dilation stops, the mean effective stress returns to its initial value, and the final shear stress level is relatively low. Drained and undrained stress paths are shown in figure B2.

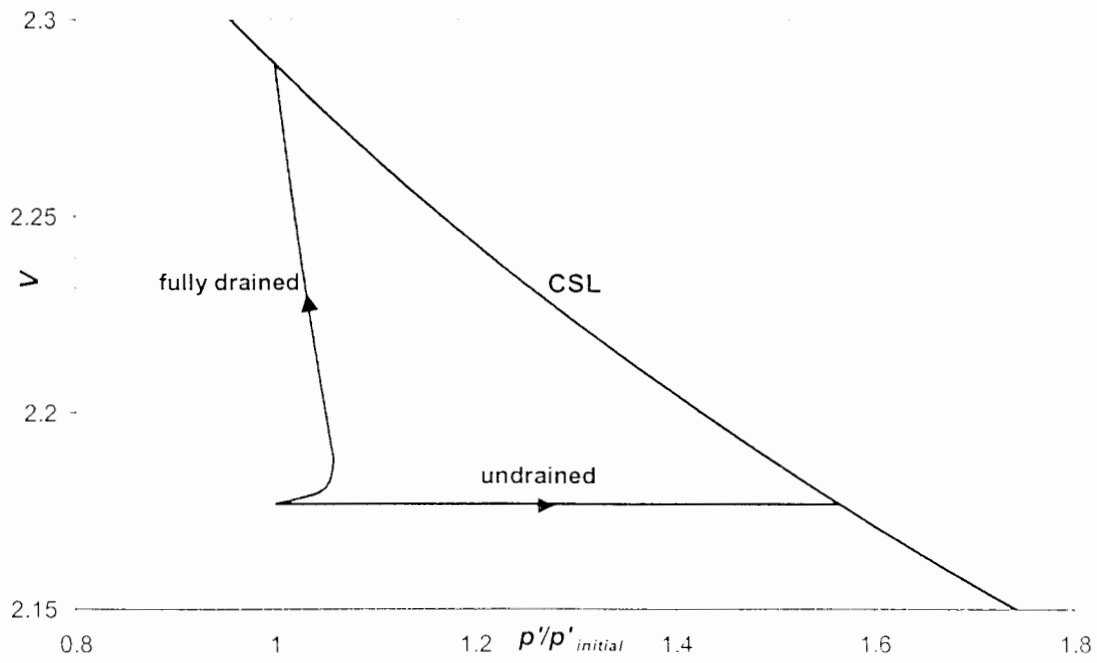

Figure B2 – Stress paths for single element analyses

APPENDIX C
FINITE ELEMENT ANALYSIS OF THE UNLOADING OF A CYLINDRICAL CAVITY

This appendix describes the modelling of the unloading of a cylindrical cavity, as was attempted during the C-series of finite element analyses. During installation of a grouted nail, a hole is drilled in soil, and if the hole is not supported by drill casing before grouting, the soil is temporarily unloaded so that $\sigma_r = 0$ at the inner boundary. This unloading process originally caused problems within stress updating routines relating to the modified Matsuoka material model. Refinements to these routines later in the development of the program have now allowed this problem to be analysed, and results from four analyses are presented here.

Inner and Outer boundaries	pressure controlled
Material	kaolin, OCR = 5
$r_i\ (m)$	0.05
$r_o\ (m)$	2.5 (= 50 r_i)
$p'_0\ (kPa)$	100
Initial cavity pressure (kPa)	100
Final cavity pressure (kPa)	0.1
Number of elements	150
Gauss points per element	1
$k\ (m/s)$	10^{-3}, 5×10^{-6}, 5×10^{-8}, 5×10^{-10}
Duration of unloading stage, $t_{drill}\ (s)$	1000
$k.t_{drill} / r_i$	10^{-7}, 10^{-4}, 10^{-3}, 10^{-5}

Table C1 – Specification for cavity unloading analyses

The specifications for the analyses are shown in Table C1. The effect of the relative rate of unloading was investigated by varying the dimensionless parameter $k.t_{drill} / r_i$. This was achieved by varying the soil permeability. Assuming the same values of t_{drill} and r_i, the chosen range represents the clay used in the laboratory tests (10^{-5}) through to a coarse sand (10^{-7}). During the analyses, the cavity pressure was reduced from the in-situ stress level to $0.1kPa$ over the period t_{drill}. It was not possible to reduce the cavity pressure to exactly zero, because of difficulties with the material model at very low stresses*.

Figure C1 shows the variation in the hoop total stress σ_θ (normalised by initial mean effective stress $p'_{initial}$), as cavity pressure and hence radial total stress σ_r is reduced. Stresses have been measured at the Gauss point of the first element in this and subsequent figures, at a radius of $r = 1.03r_i$. Until σ_r drops to below approximately $0.4\ p'_{initial}$ the relationship between σ_r and σ_θ is linear, and lies very close to the elastic solution which gives $\Delta\sigma_\theta = -\Delta\sigma_r$ at $r = r_i$. Beyond first yield, the response is dependent on the rate of unloading, but all plots thereafter show a decrease in hoop stress with unloading.

Figure C2 shows the variation in normalised radial effective stress σ'_r with σ_r. The quantities are equal until yield is reached, whereupon they differ according to the local pore pressure as expected. The variation in pore pressure (at the same Gauss point) is shown in Figure C3. Greater pore pressure suctions are generated for faster unloading rates. No positive or negative suctions are generated before yield since the theoretical volumetric strain at $r = r_i$ is zero for an elastic material.

Figure C4 shows the extent of plasticity within the mesh as the cavity is unloaded. This has been measured by locating the first elastic Gauss point from the inner radius at each calculation step. The zone of plasticity extends further (at the end of unloading) for the slower unloading rates. This is because less pore pressure suction is generated, which at faster rates raises the effective stress level and hence yield strength.

---

* The Matsuoka material model yield surface converges to a point at zero effective stress – it is thought that proximity of the current stress point to this discontinuity causes problems.

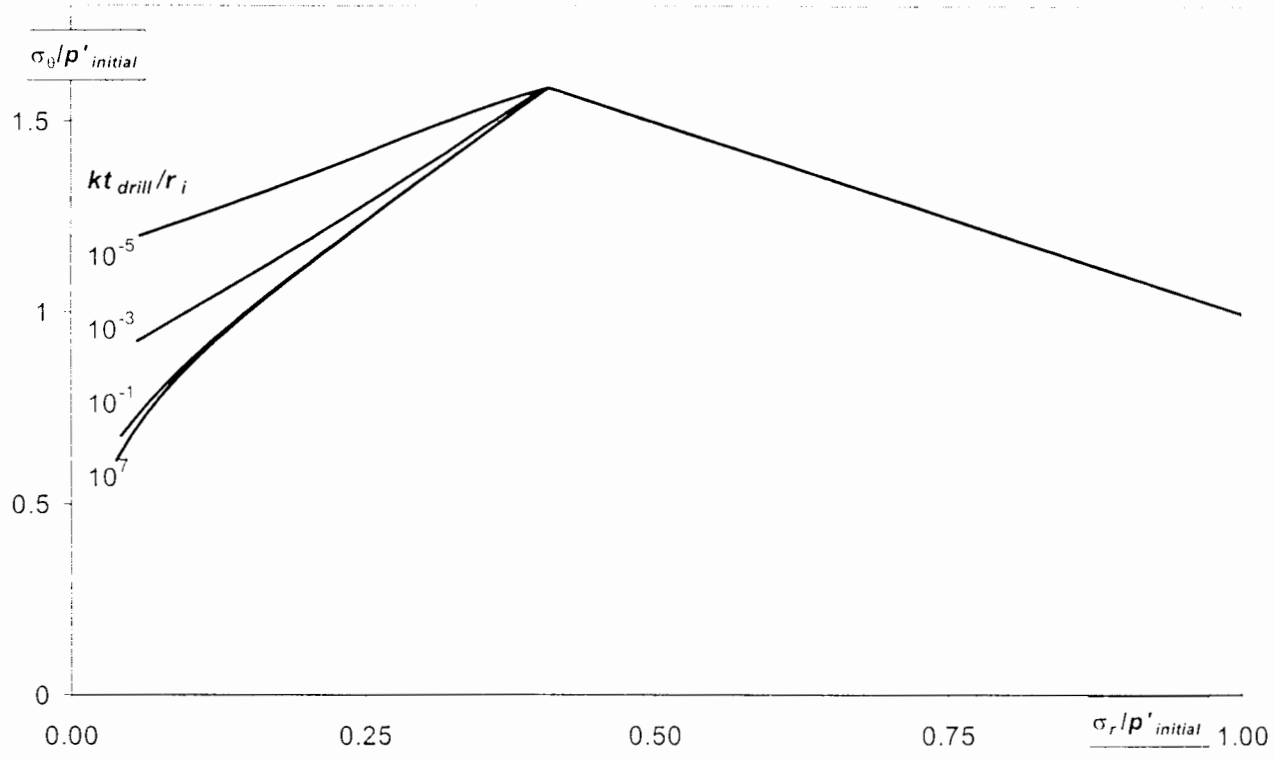

Figure C1 – Variation in 1st element total hoop stress during cavity opening

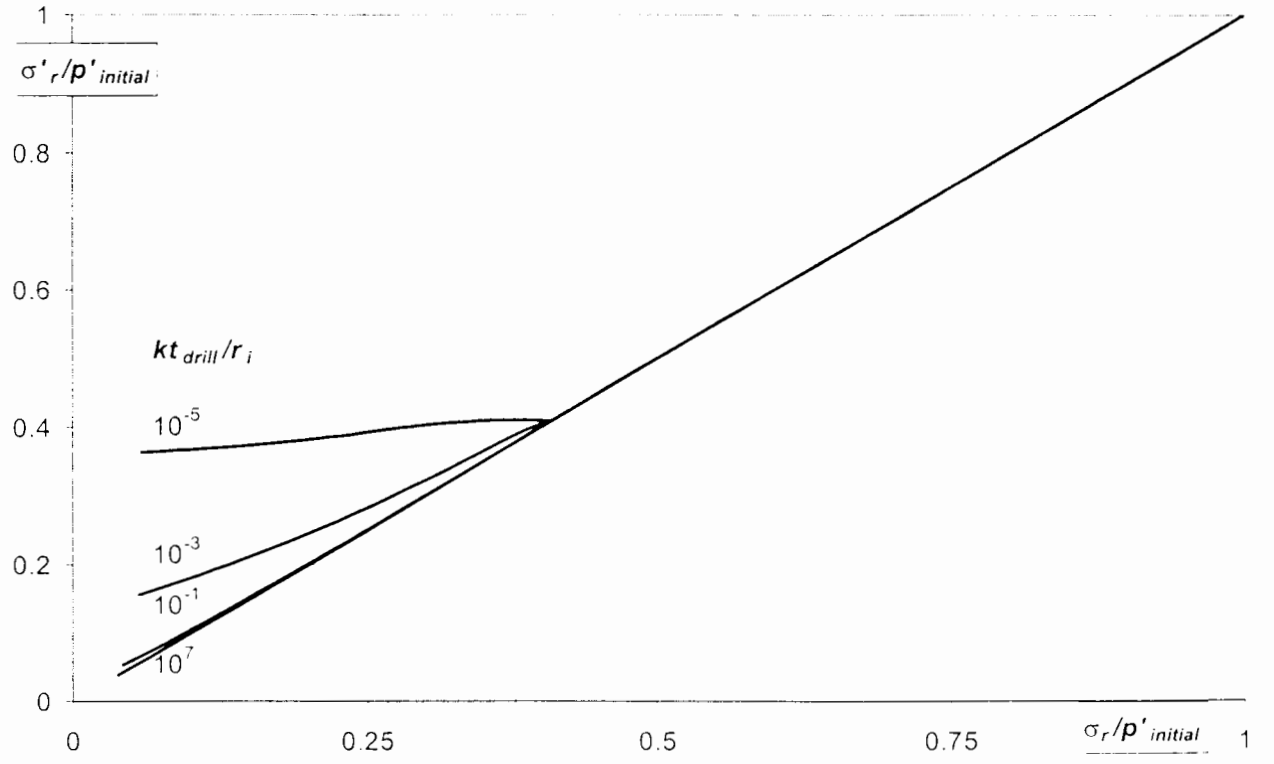

Figure C2 – Variation in 1st element radial effective stress during cavity opening

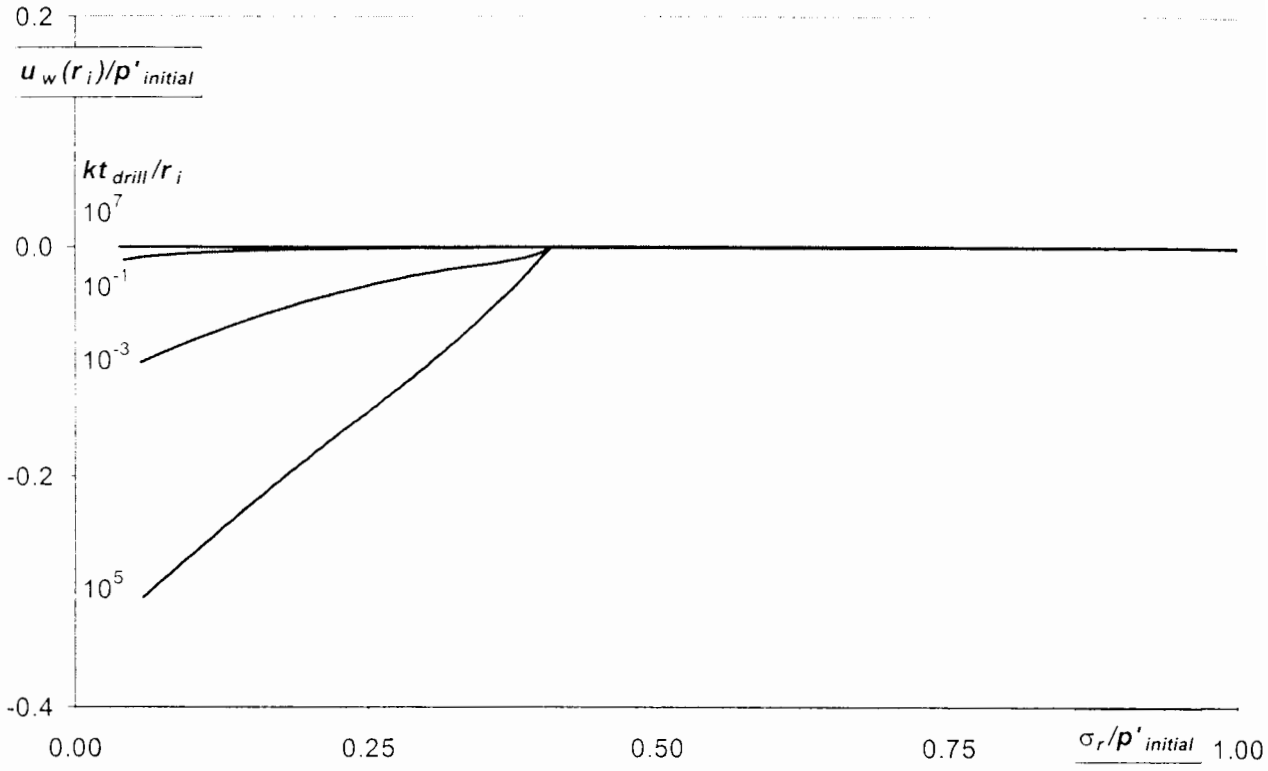

Figure C3 – Variation in 1st element pore water pressure during cavity opening

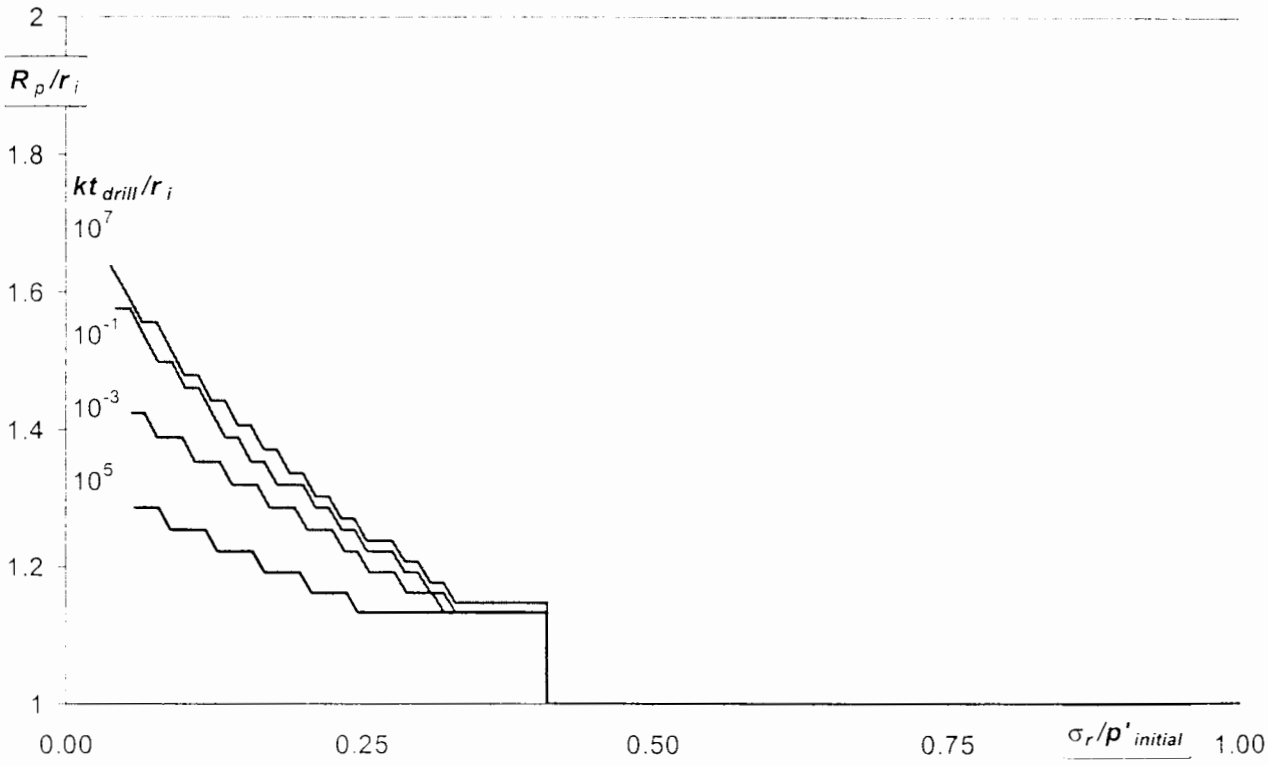

Figure C4 – Variation in plastic radius during cavity opening

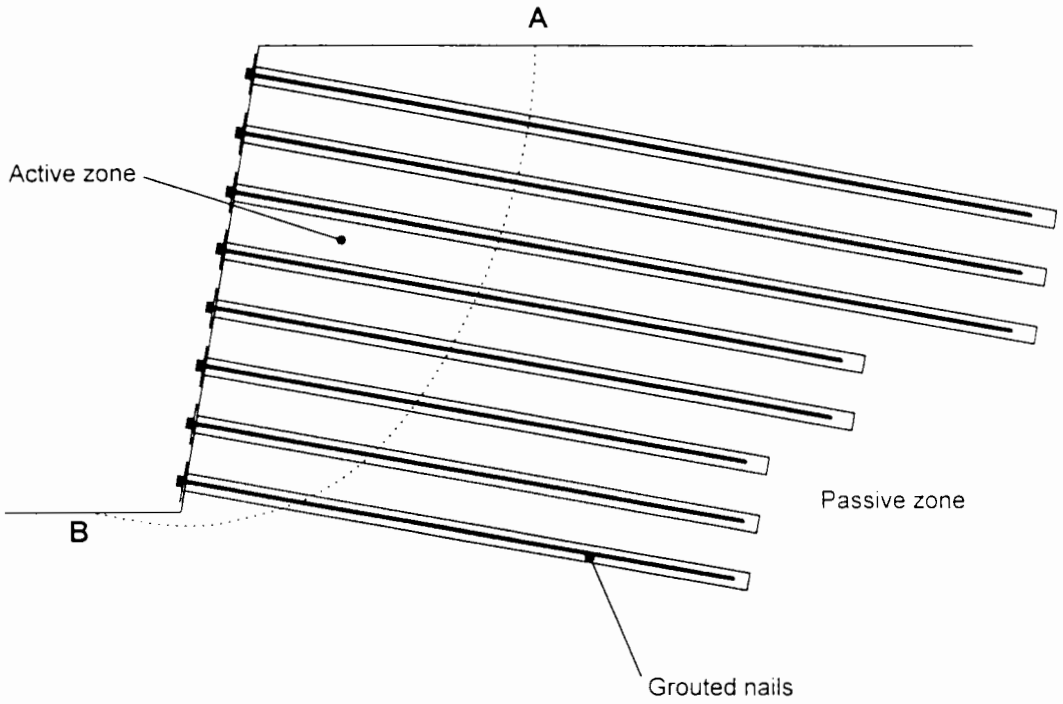

Figure 1.1 – Typical soil nailed slope

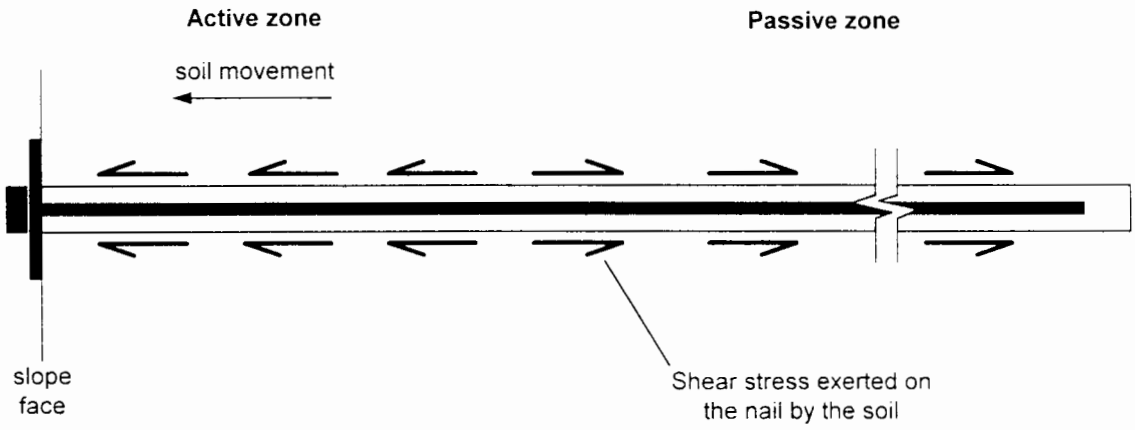

Figure 1.2 – Shear stresses along a typical nail

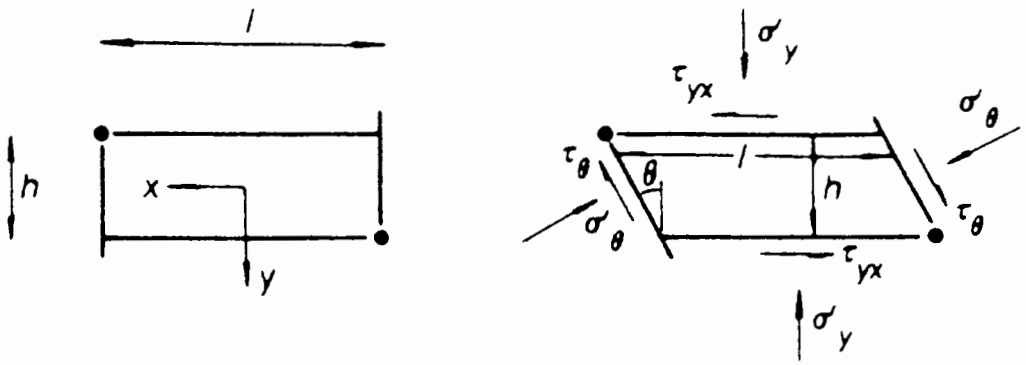

(a)

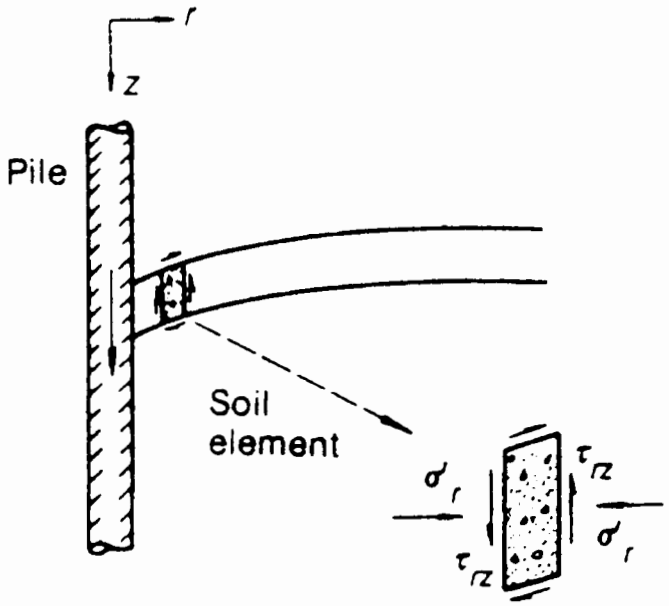

(b)

Figure 1.3 – Comparison of soil behaviour in simple shear to that imposed by pile loading (after Randolph and Wroth, 1981)

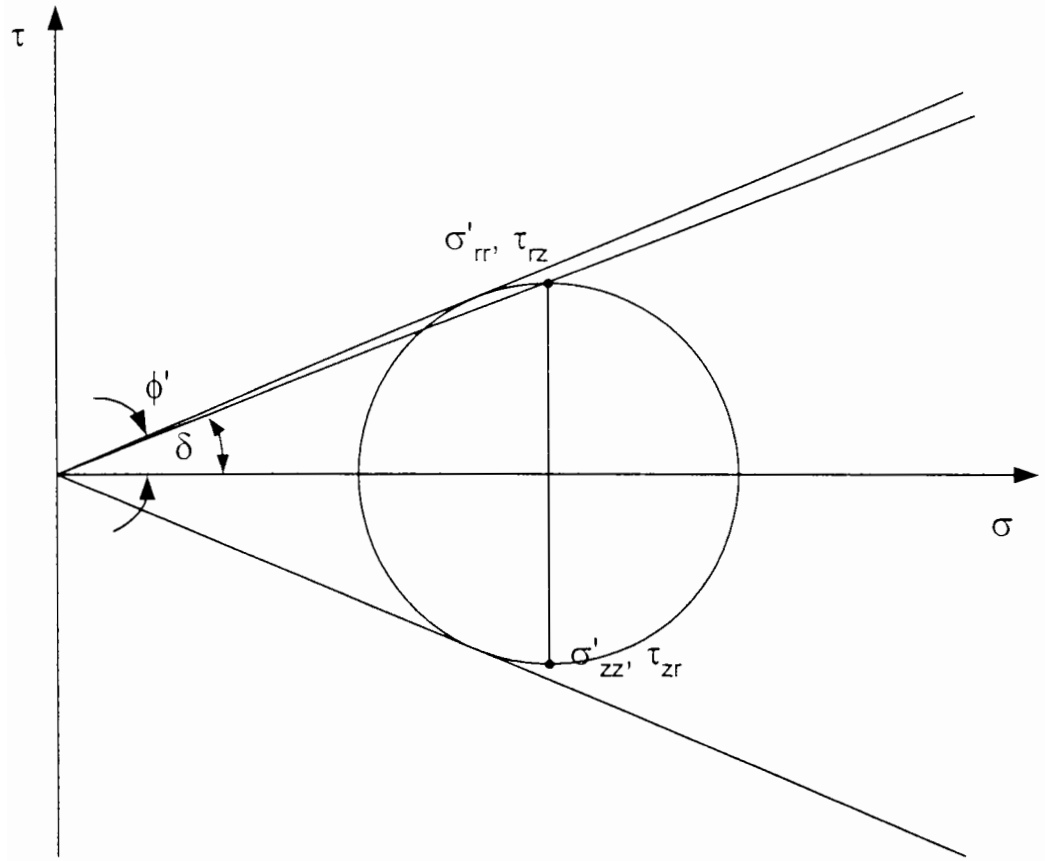

Figure 1.6 – Failure condition indicated by Potts and Martins (1982)

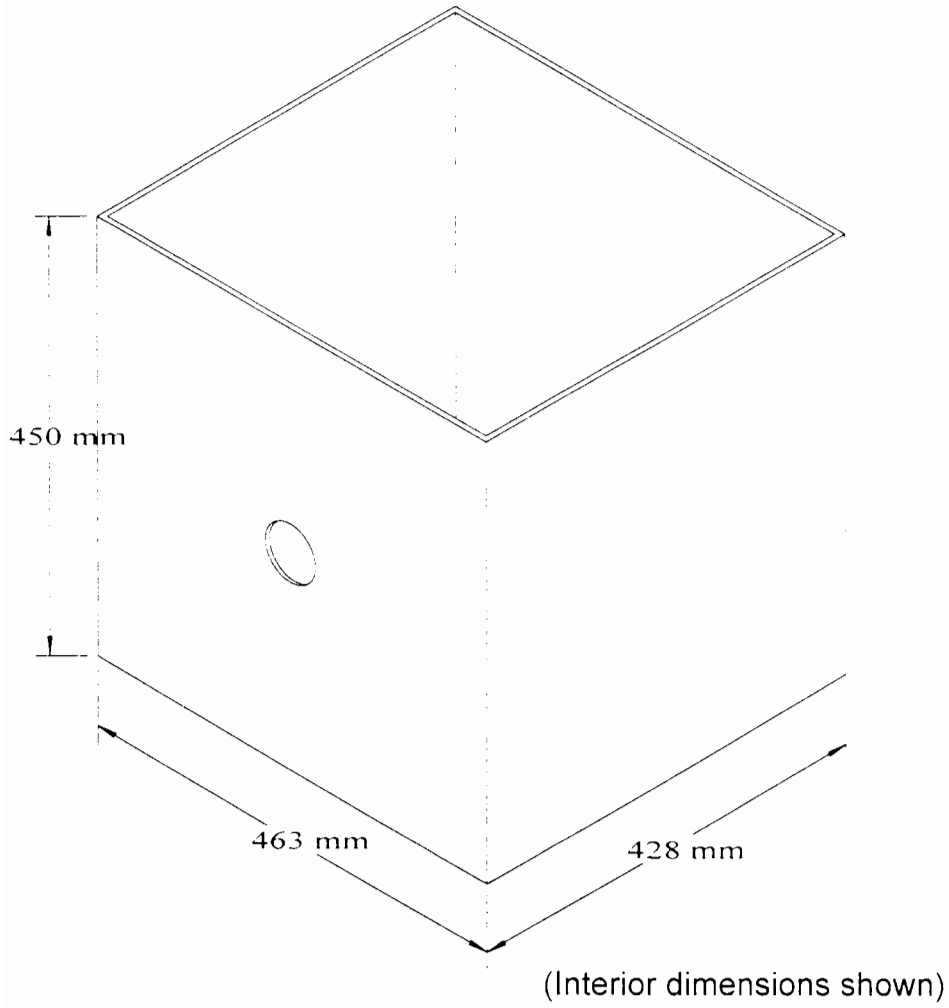

Figure 2.1 – Small test tank

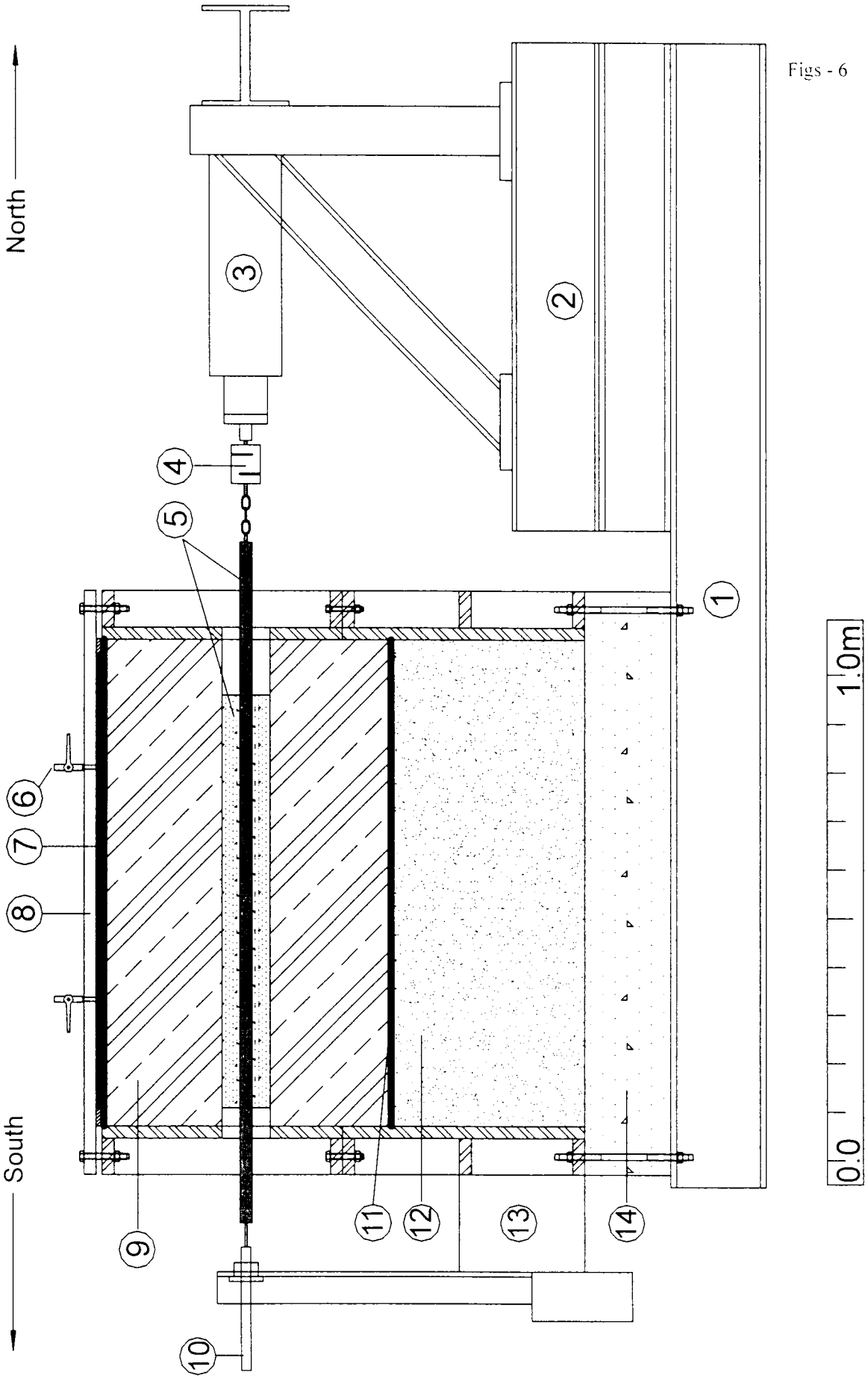

Figure 2.2 – Laboratory nailing apparatus

(for key see following page)

Key to Figure 2.2

1. Main base beams (2 No.)
2. 'Packing' beams to raise loading ram to nail axis level.
3. *Enerpac* 60*t* loading ram.
4. Nail axial force load transducer, capacity 5*t*.
5. Grouted soil nail.
6. Inlet valve for vertical stress membrane.
7. Vertical stress membrane.
8. Top platen of soil tank.
9. Soil sample.
10. Nail axial displacement transducer (LVDT, 150*mm* stroke).
11. False bottom of soil tank (6*mm* thick mild steel plate).
12. Dense sand to support false bottom.
13. Old LDSA loading boss, used to mount drilling attachments and LVDT.
14. Reinforced concrete base.

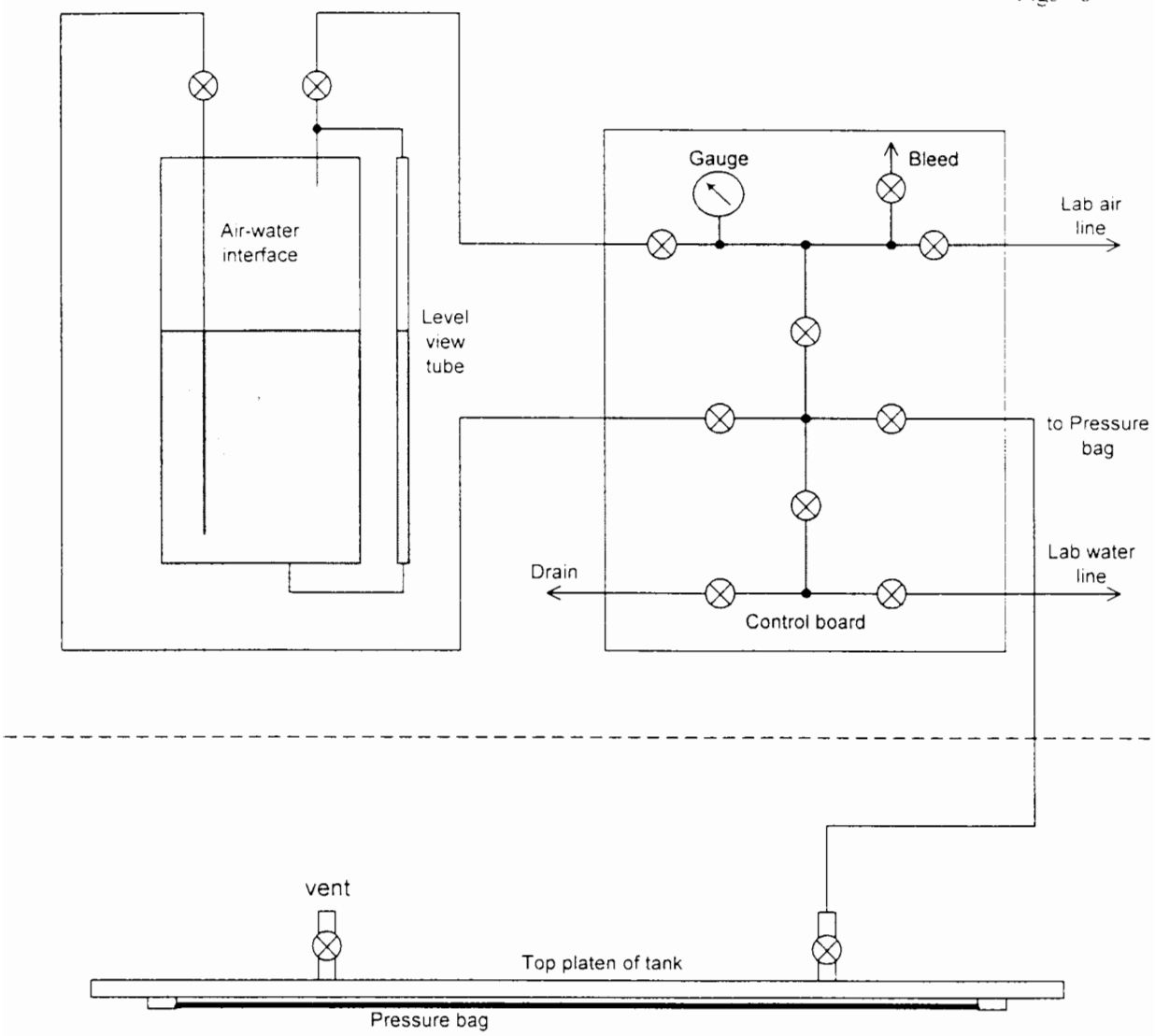

Figure 2.3 – Vertical loading system

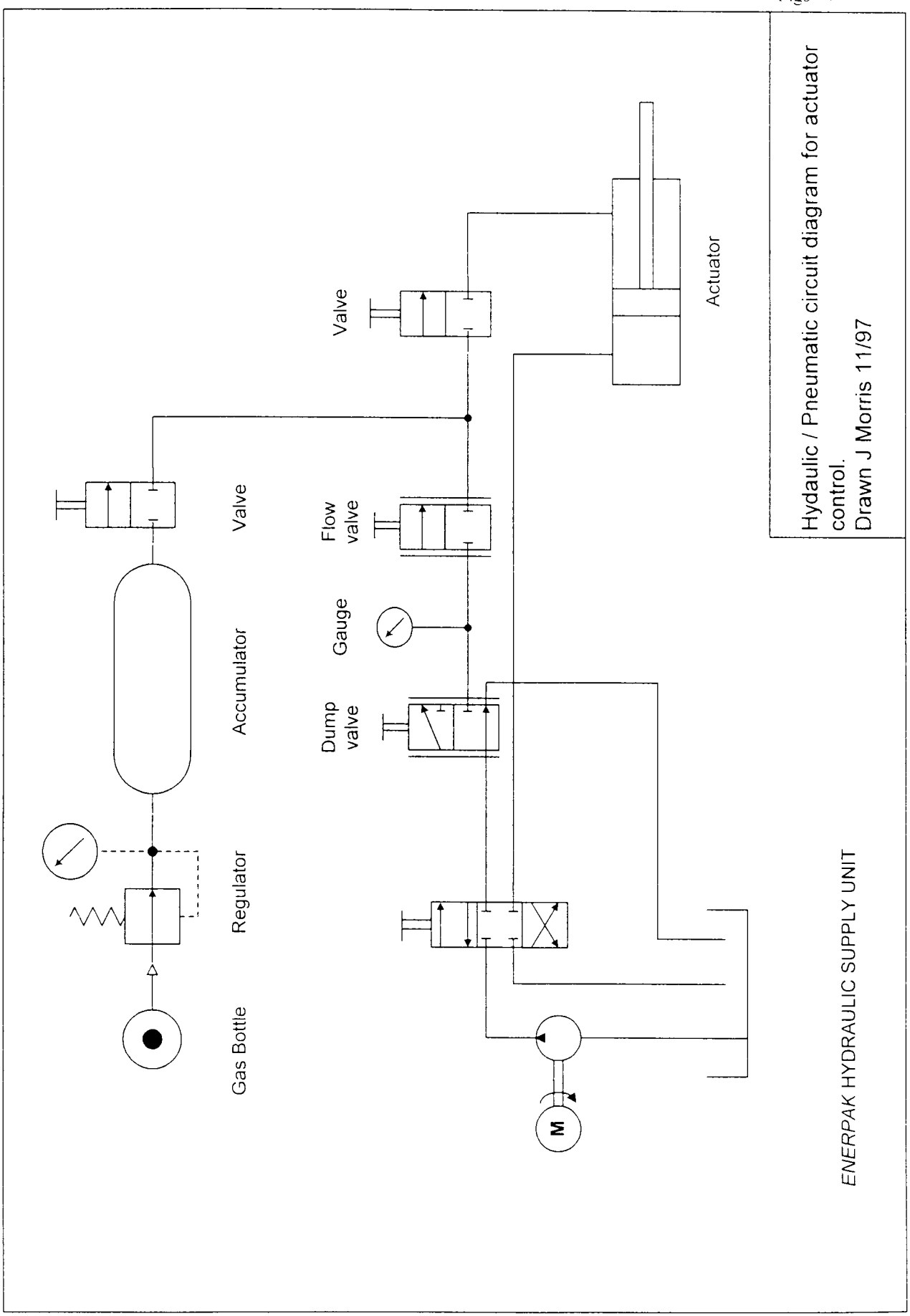

Figure 2.4 – Hydraulic system for nail loading

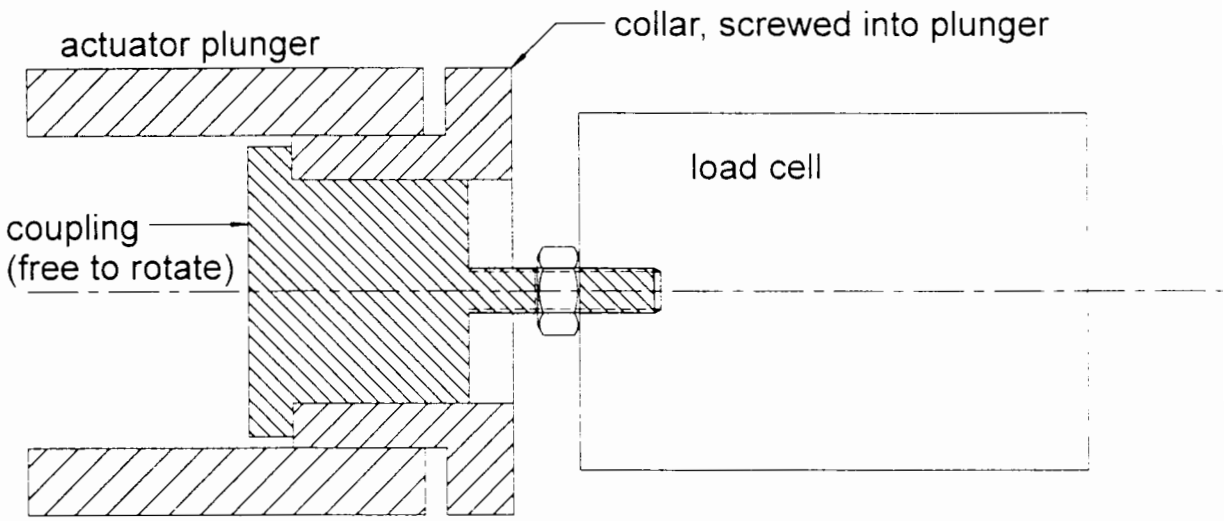

Figure 2.5 – Loading ram / load cell coupling

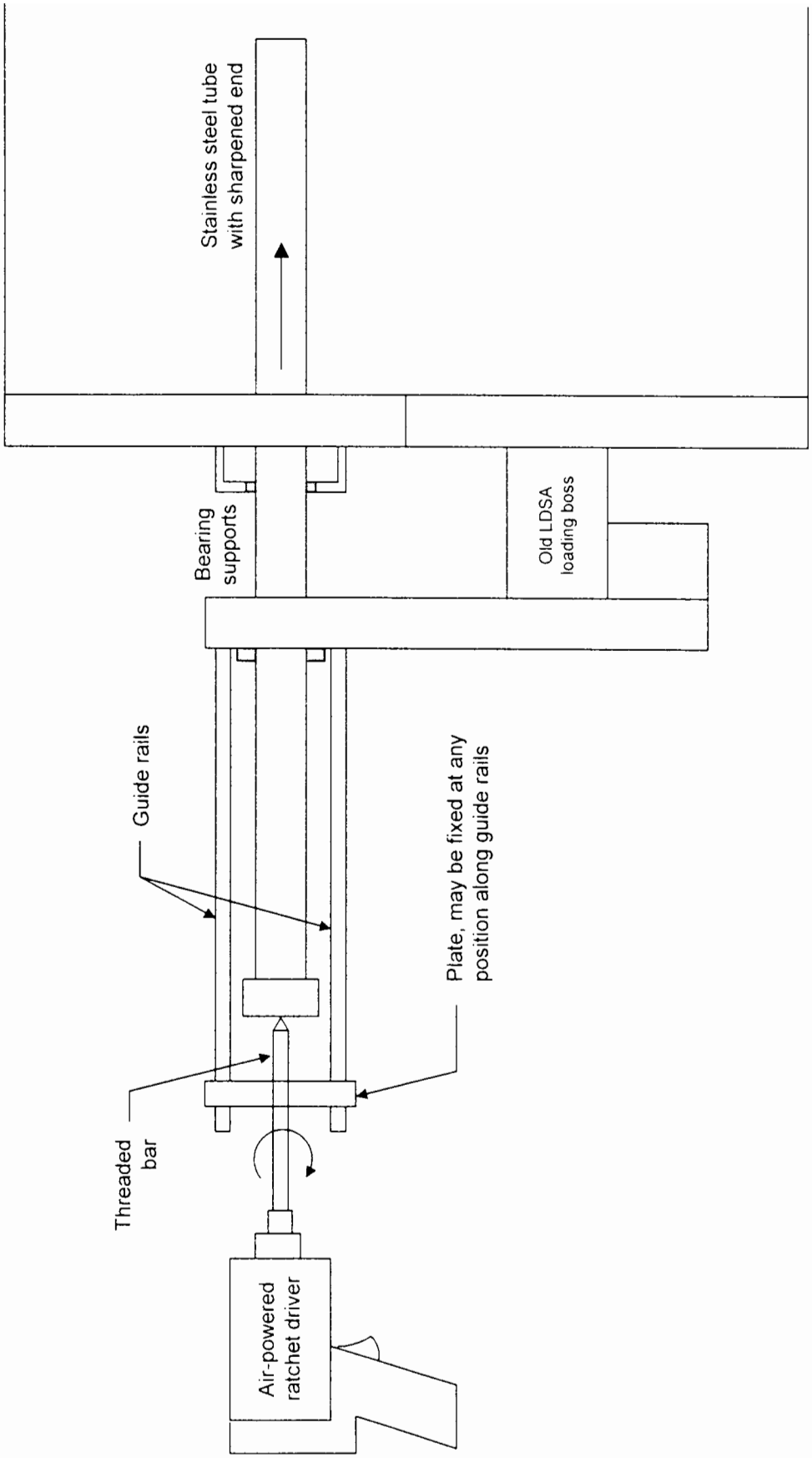

Figure 2.6 – First stage drilling arrangement

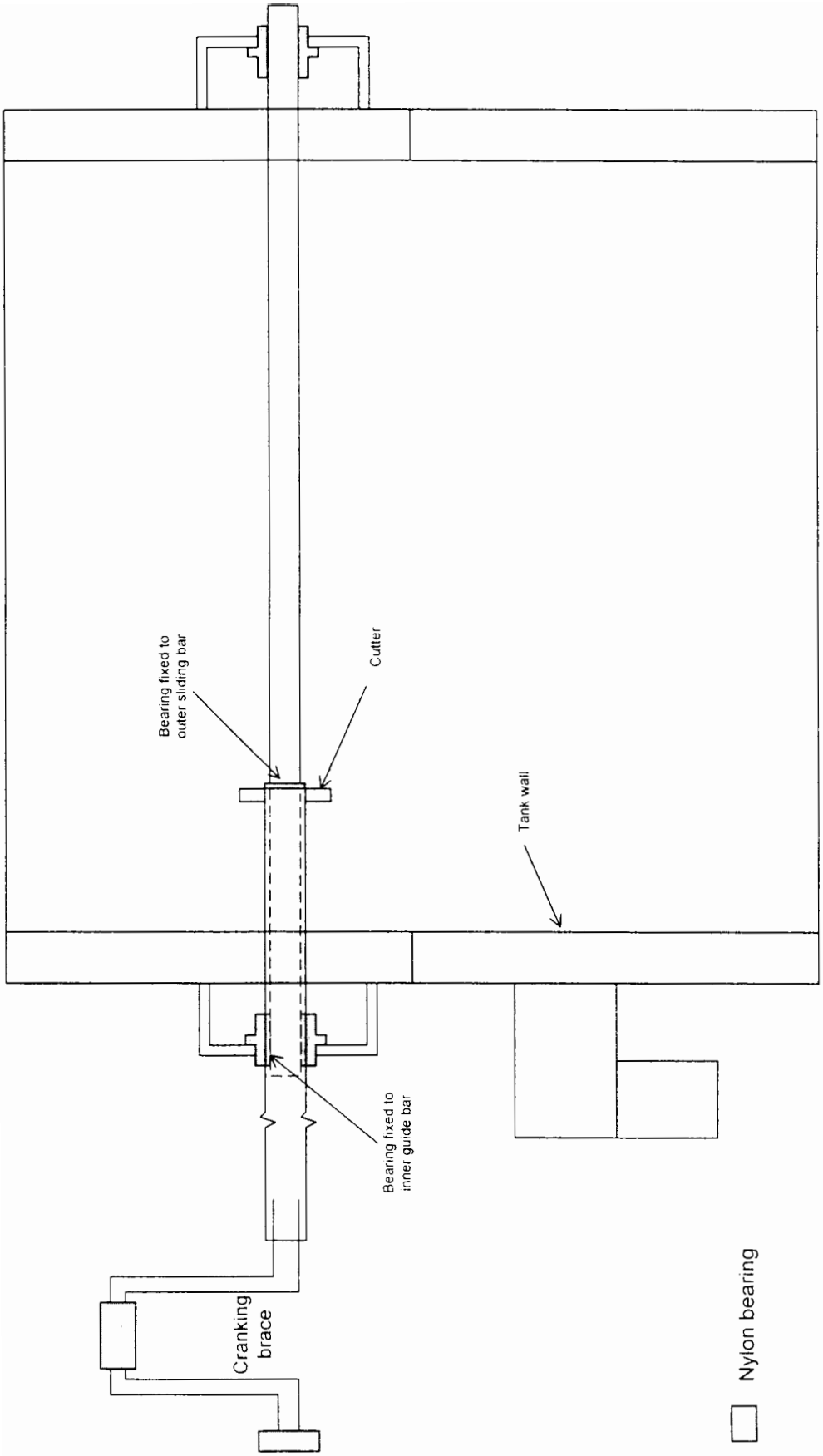

Figure 2.7 – Final stage drilling arrangement

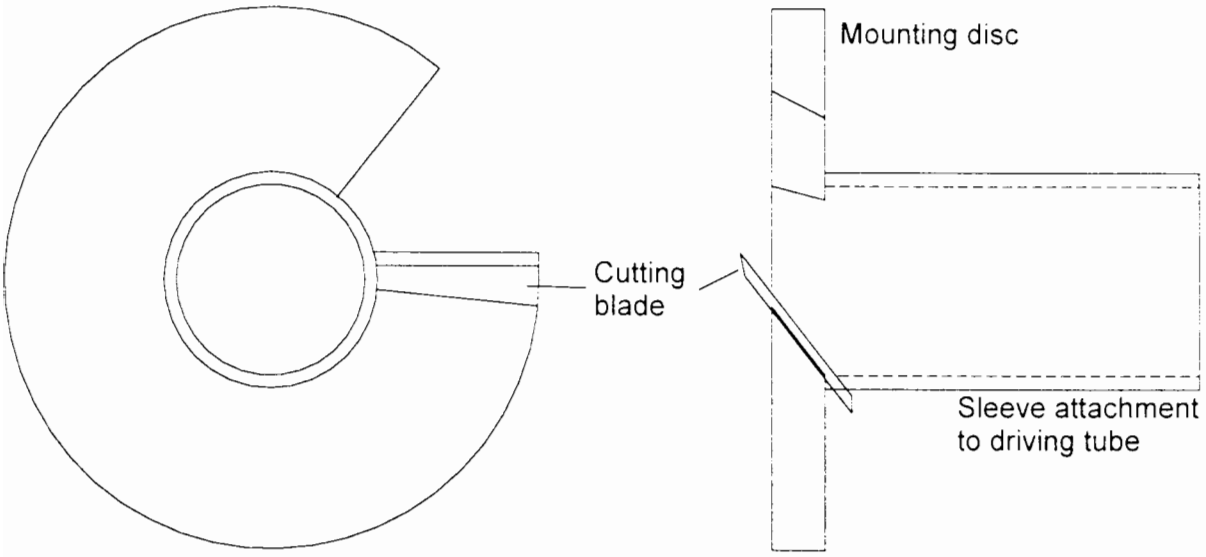

Figure 2.8 – Final stage hole cutter

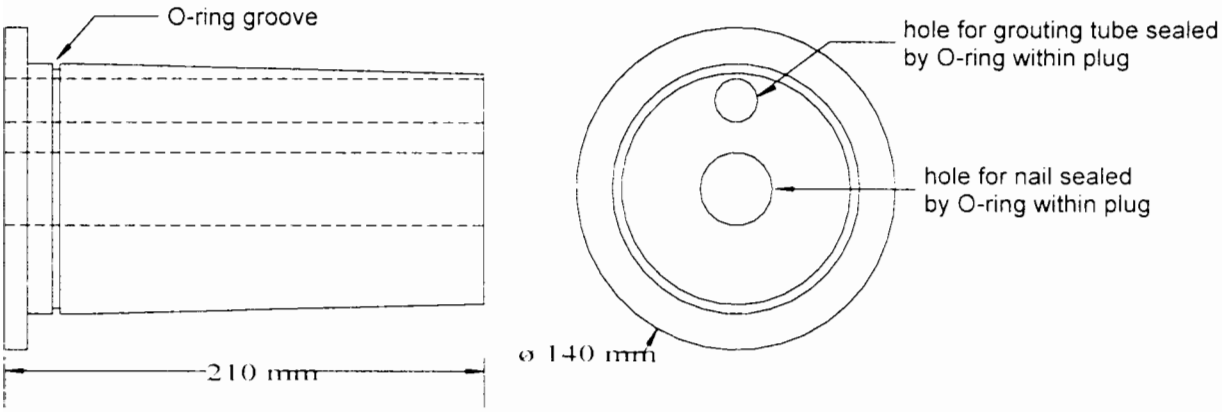

Figure 2.9 – Grouting plug (North end shown)

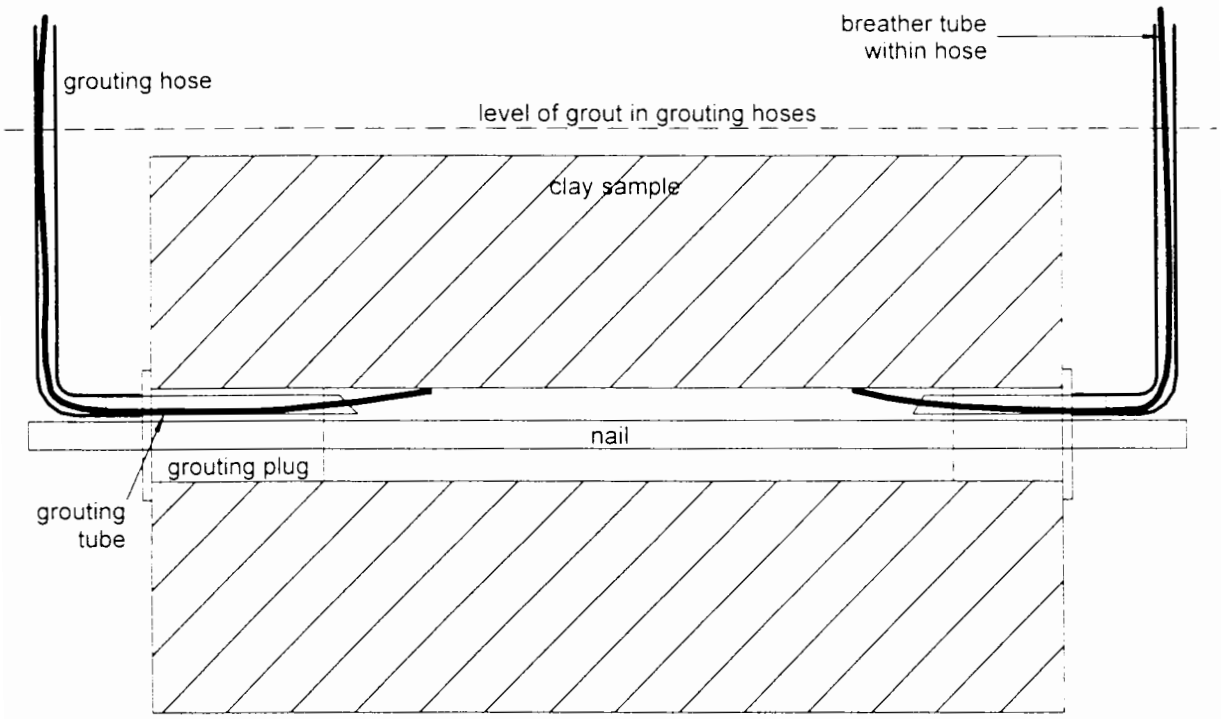

Figure 2.10 – Grouting arrangement showing breather tubes

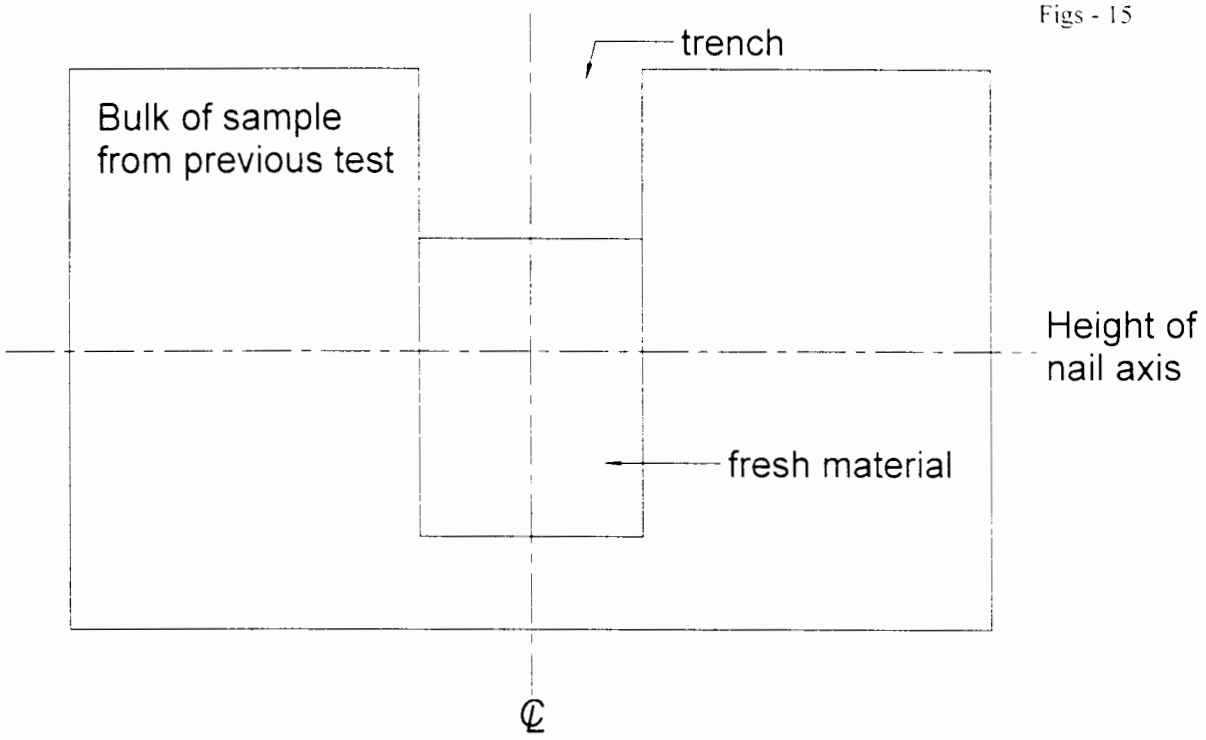

Figure 3.1 – Extent of excavations for each test

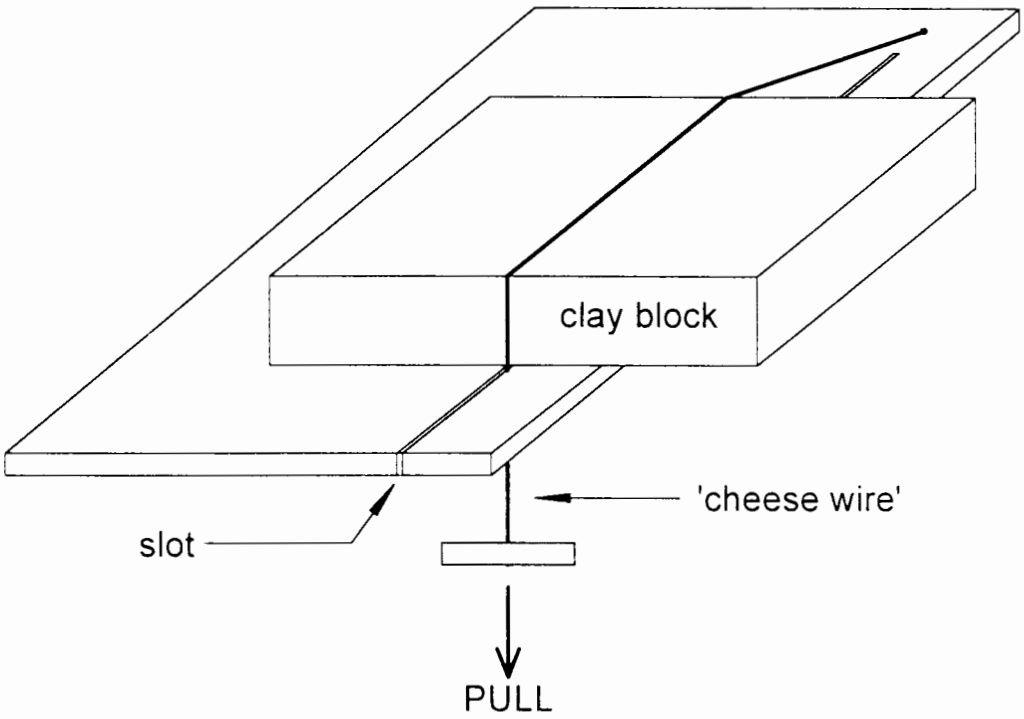

Figure 3.2 – 'Cheese wire' cutter for clay blocks

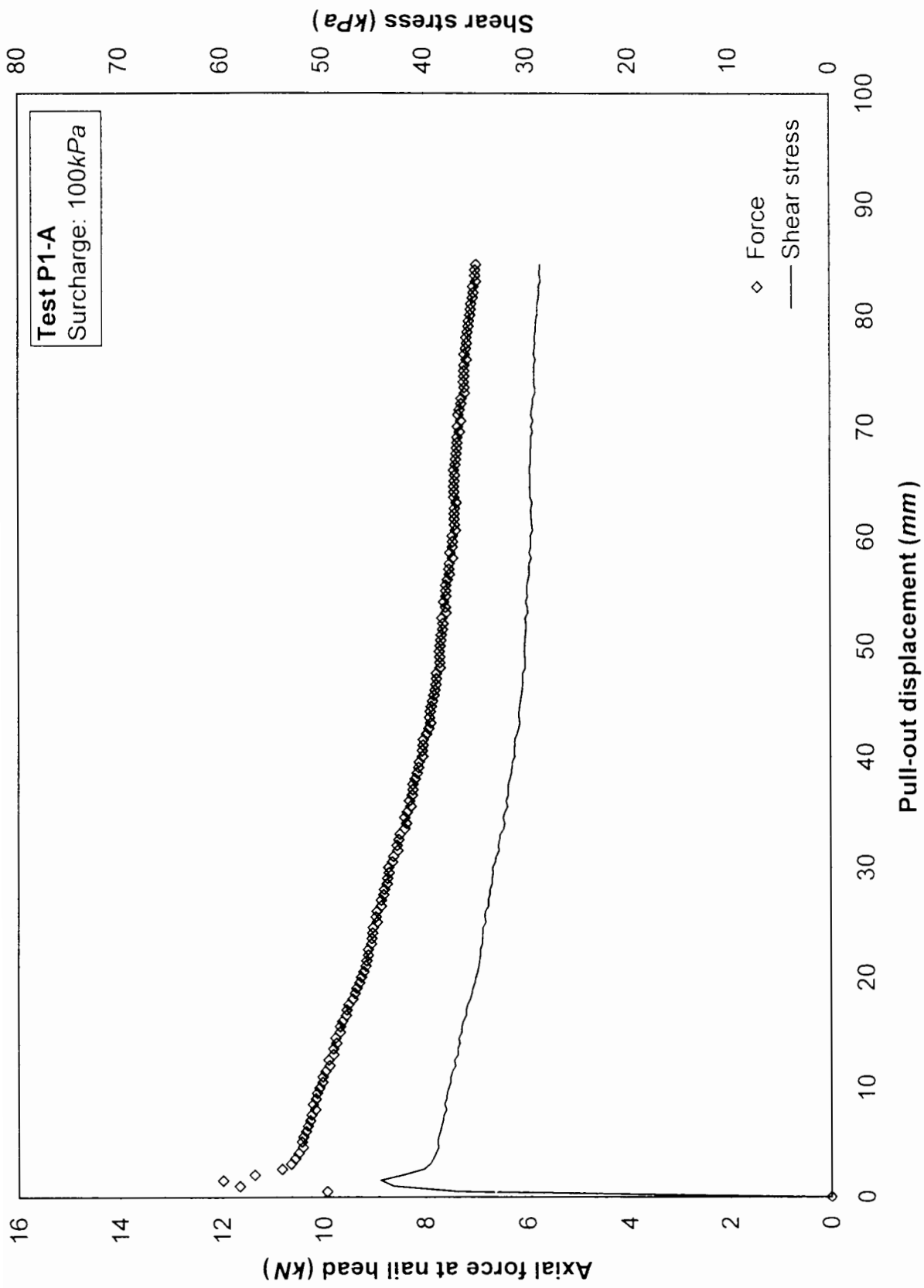

Figure 4.1 - Pull-out test P1-A

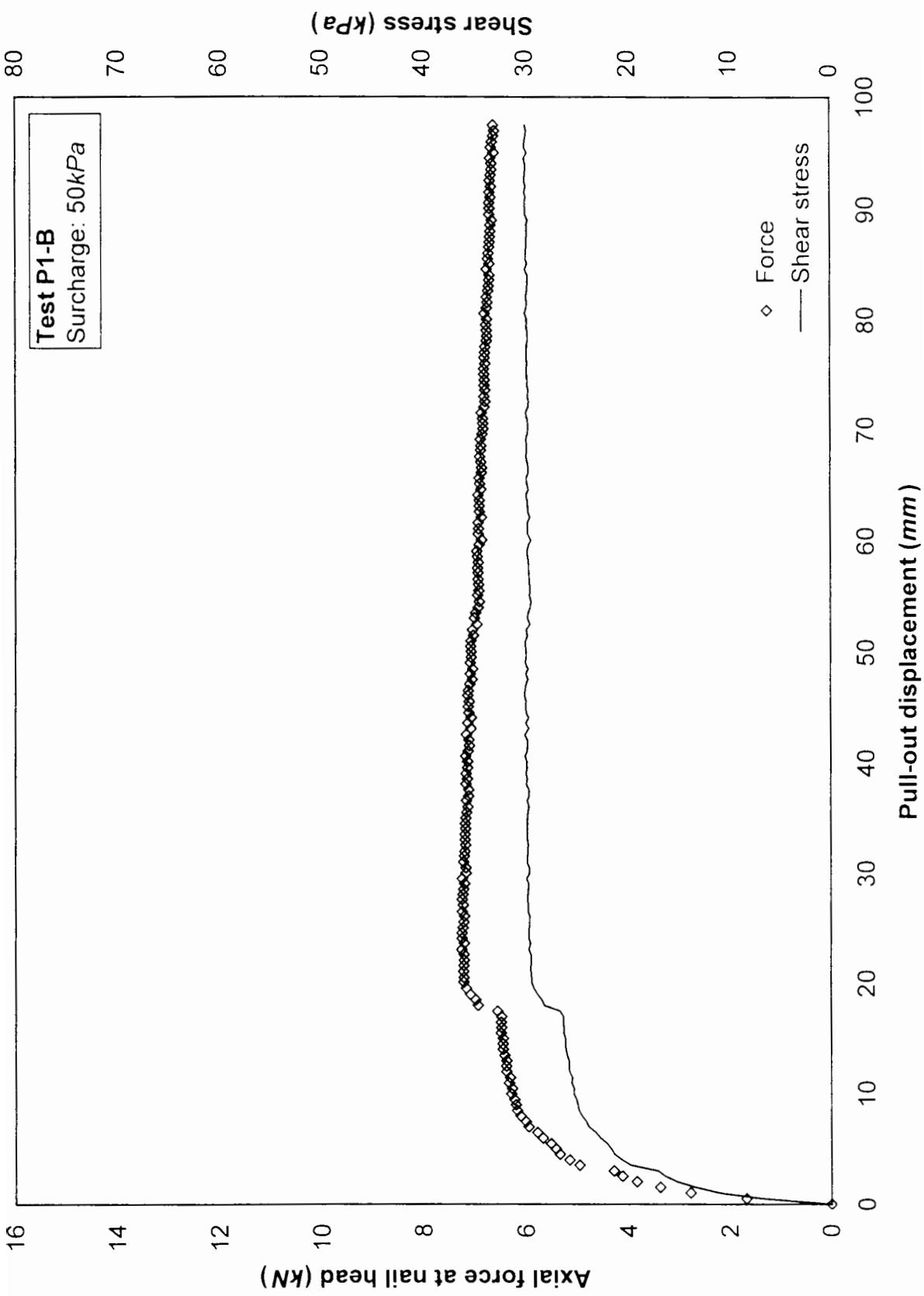

Figure 4.2 - Pull-out test P1-B

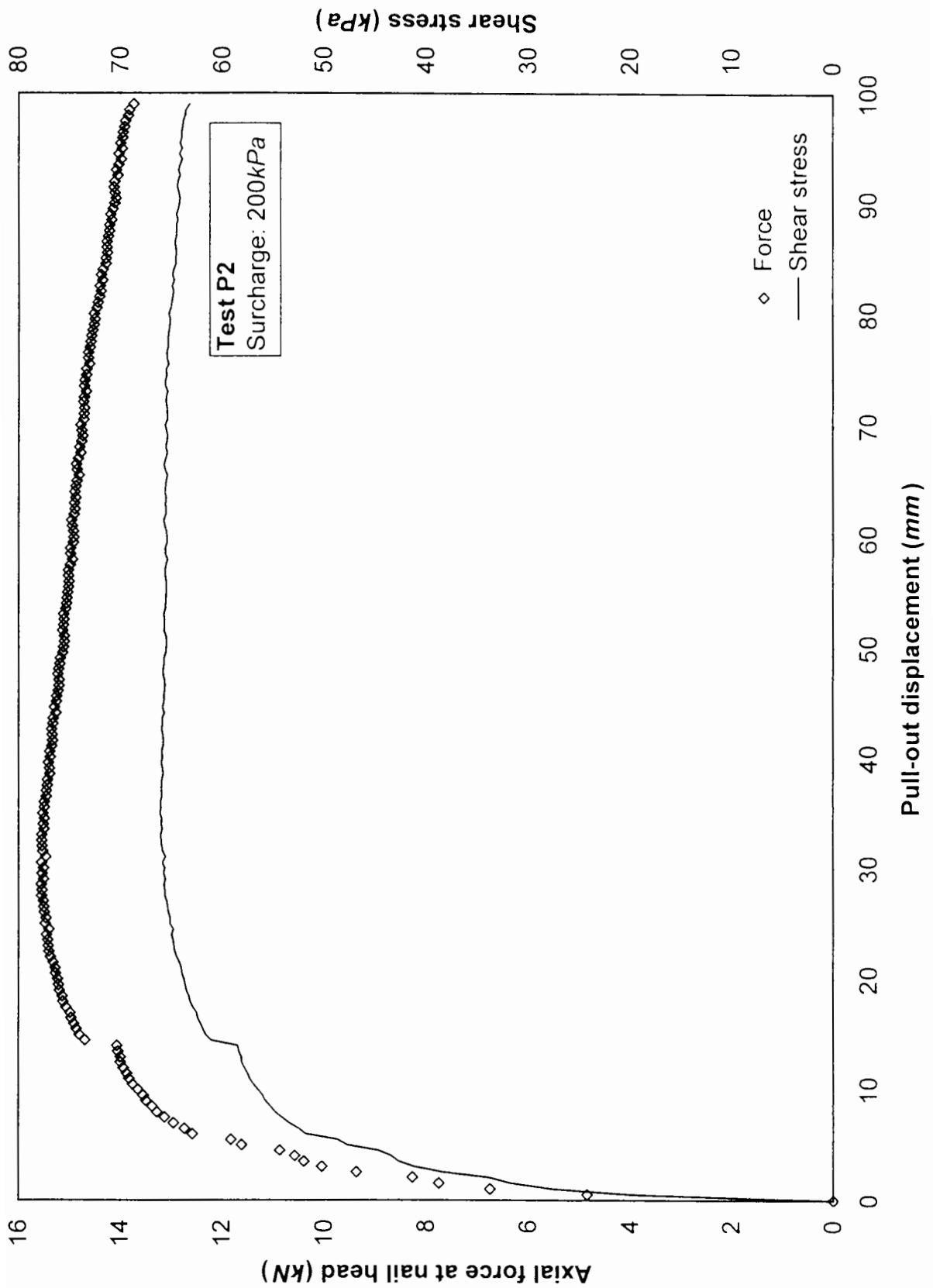

Figure 4.3 - Pull-out test P2

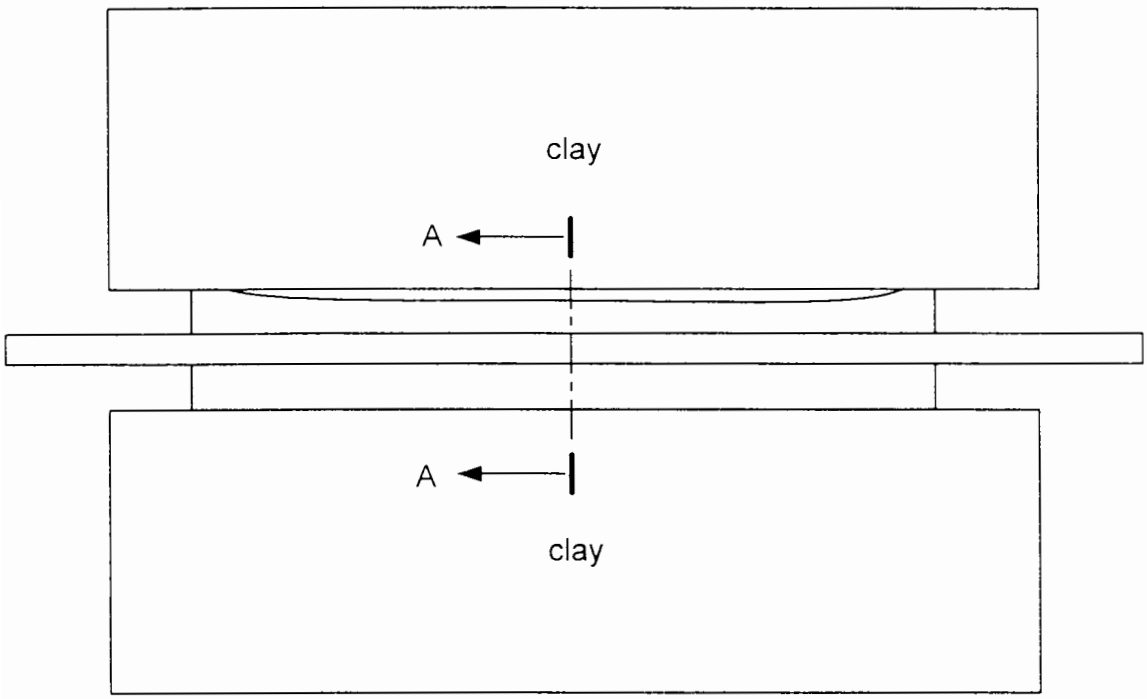

Enlarged section on A-A

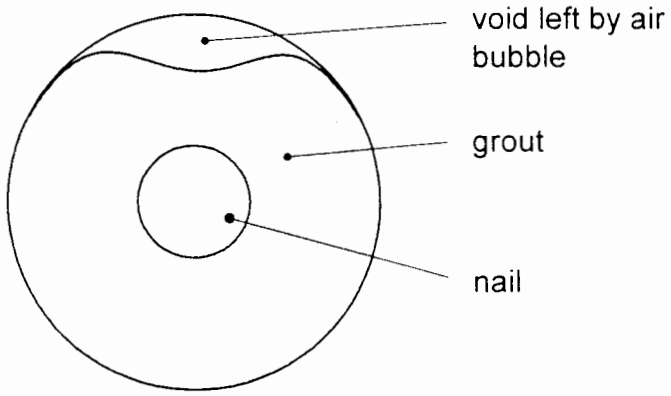

Figure 4.4 – Bubble liable to form when grouting

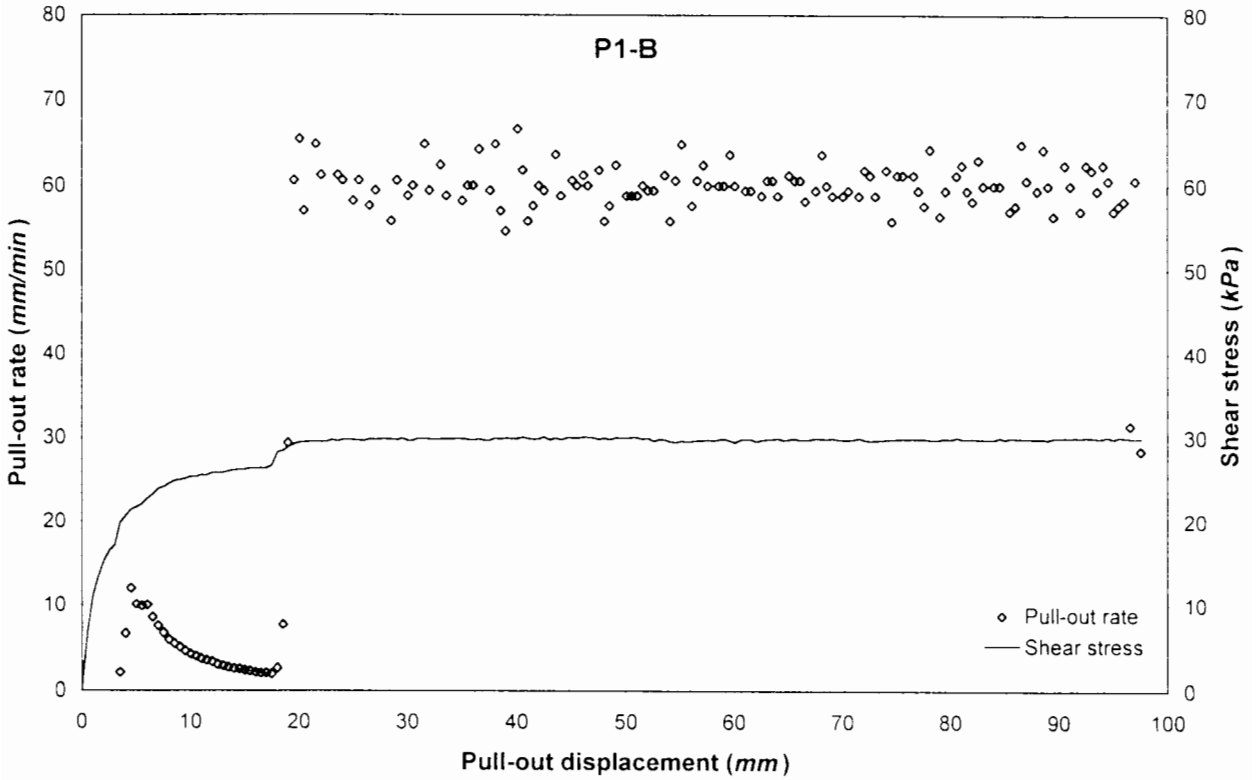

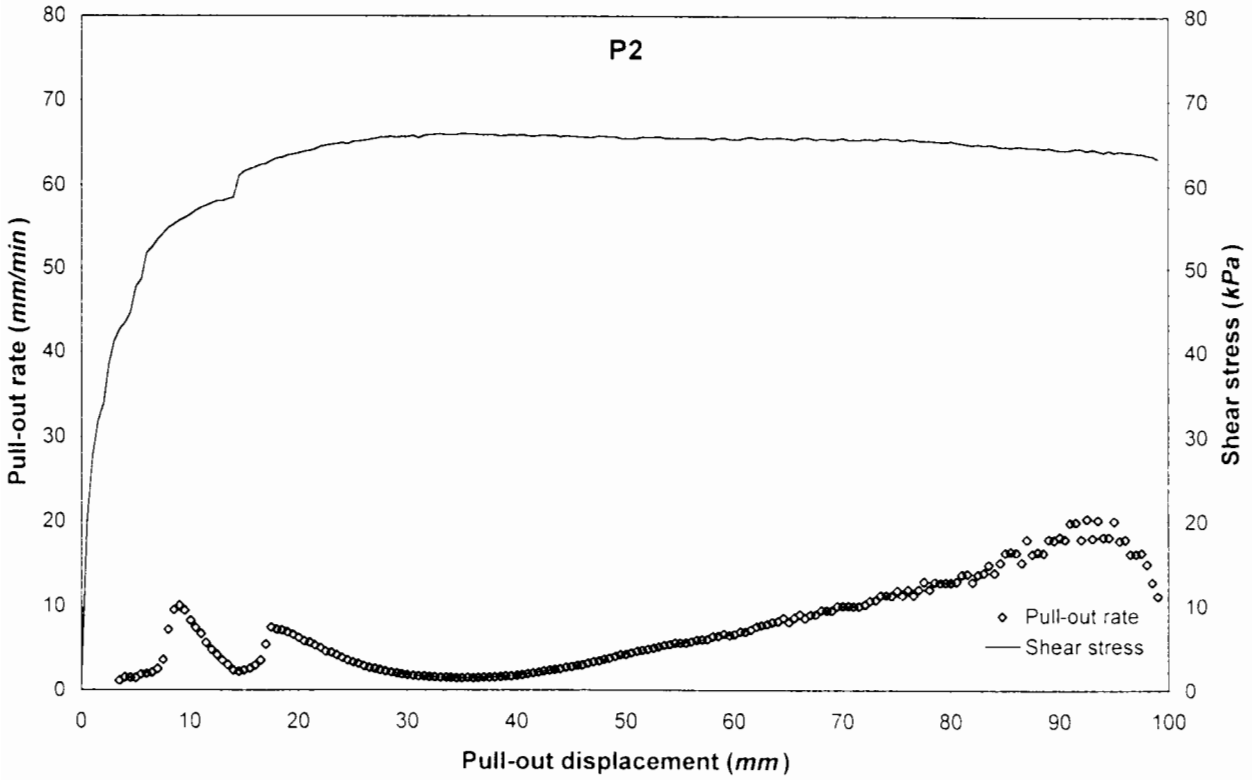

Figure 4.5 - Displacement rate during pull-out tests P1-B and P2

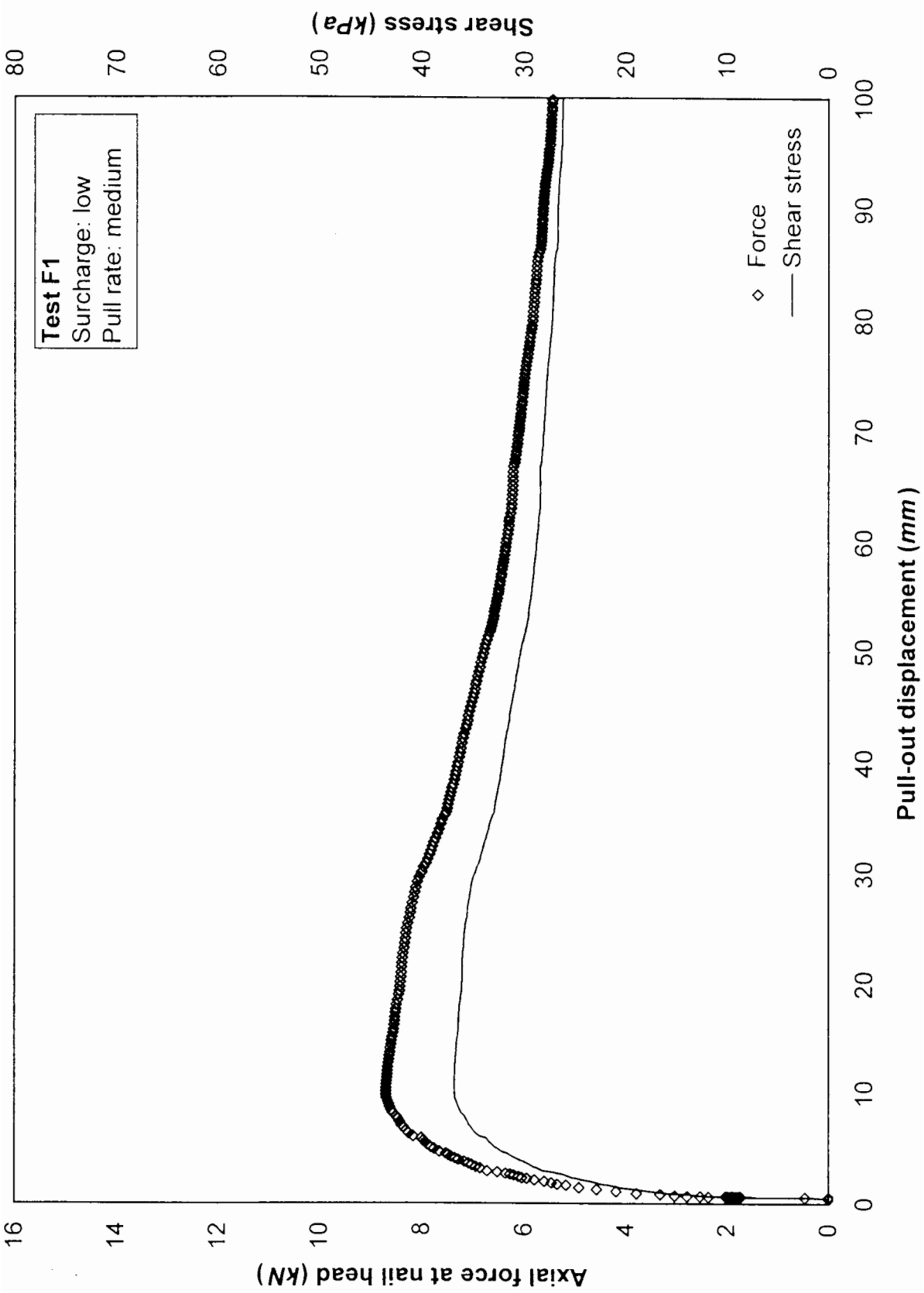

Figure 4.6 - Pull-out test F1

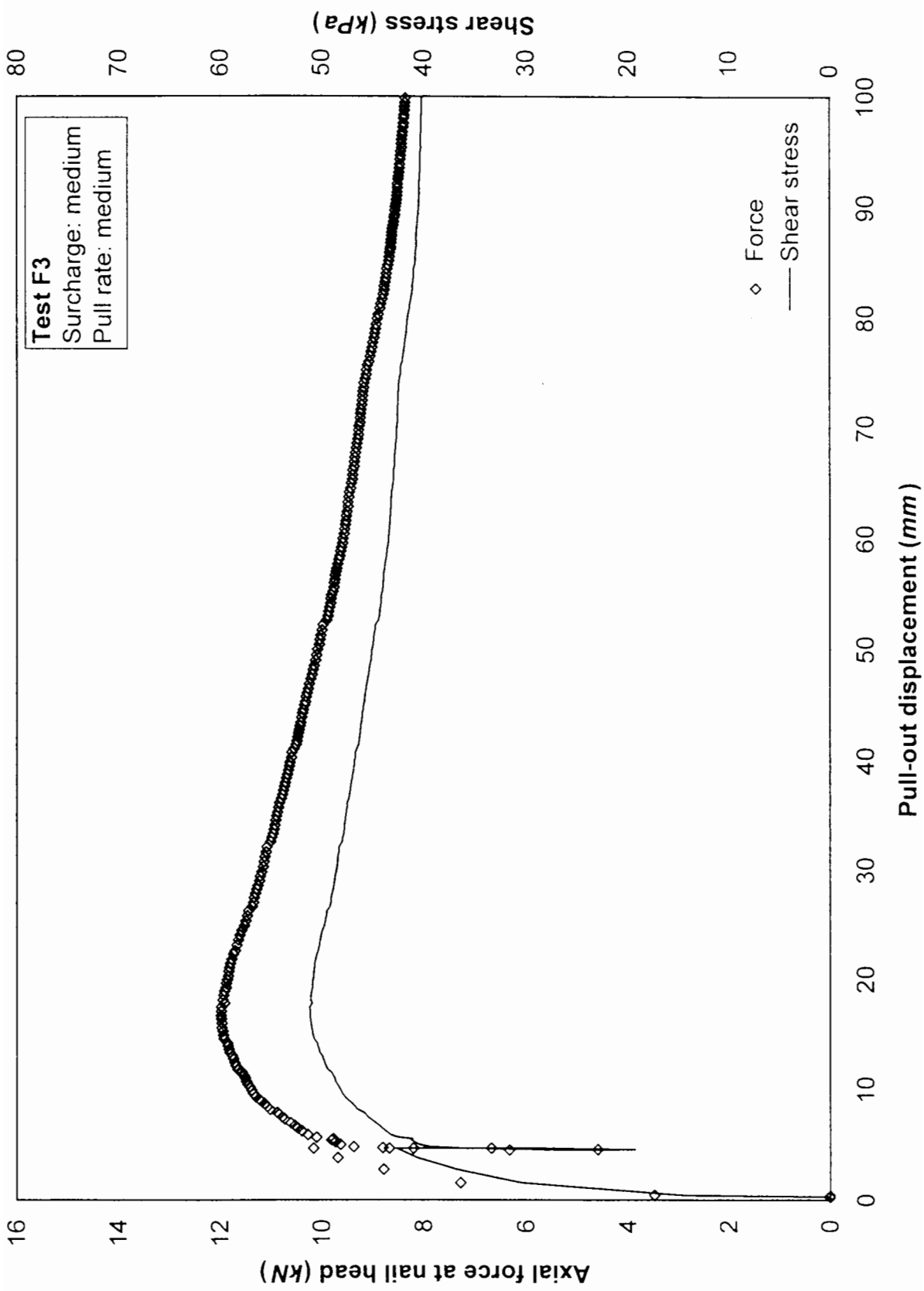

Figure 4.7 - Pull-out test F3

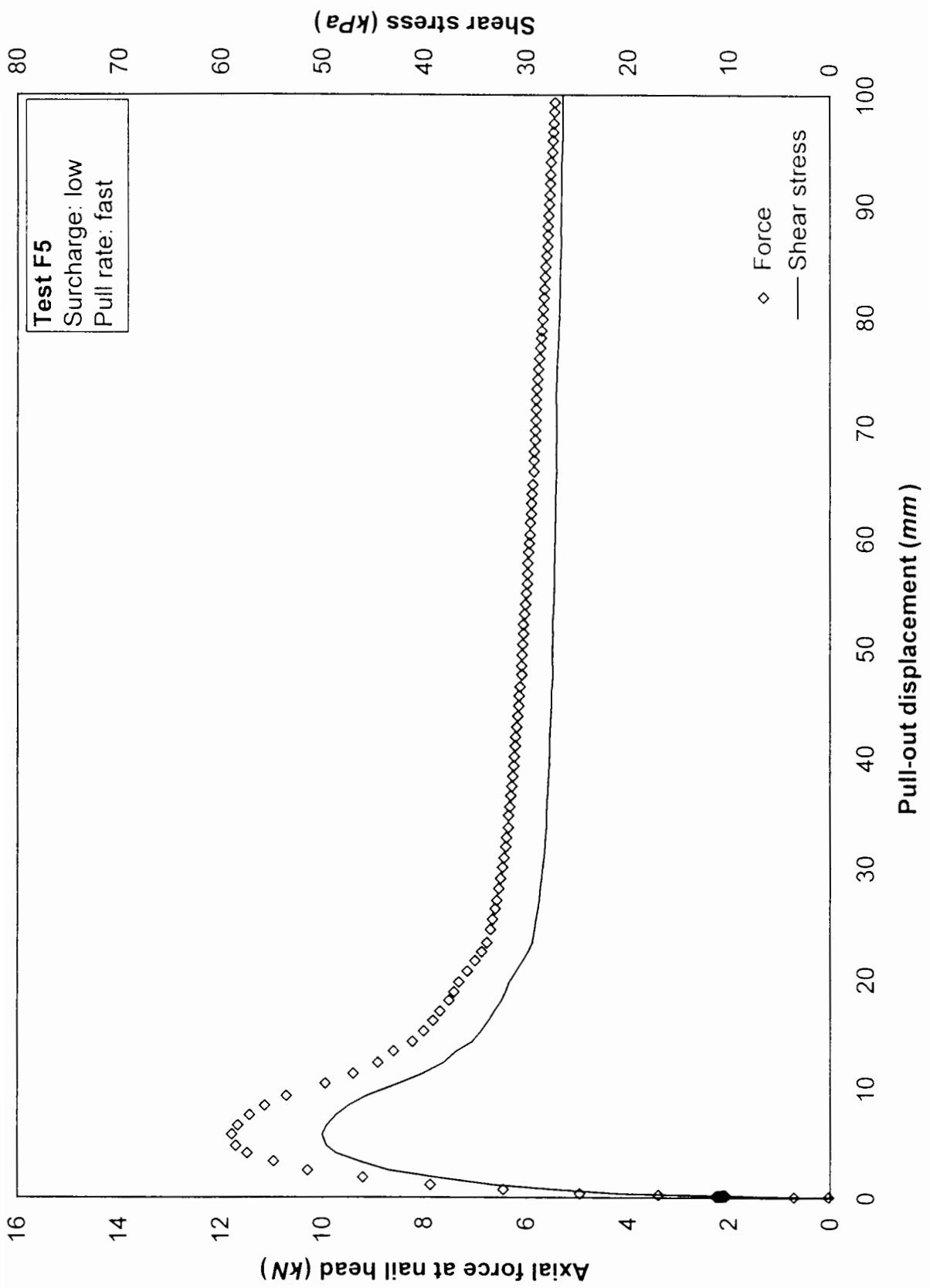

Figure 4.8 - Pull-out test F5

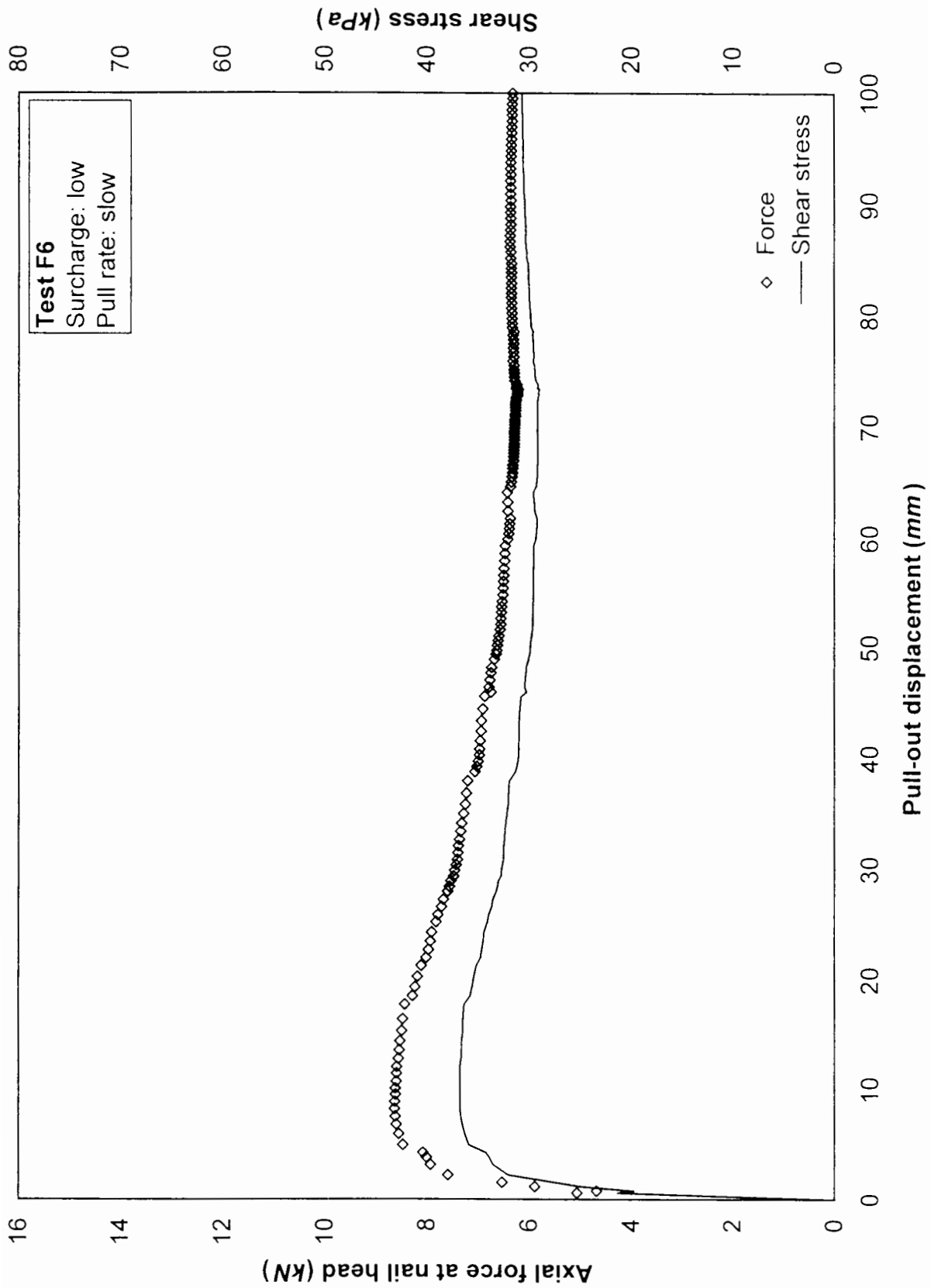

Figure 4.9 - Pull-out test F6

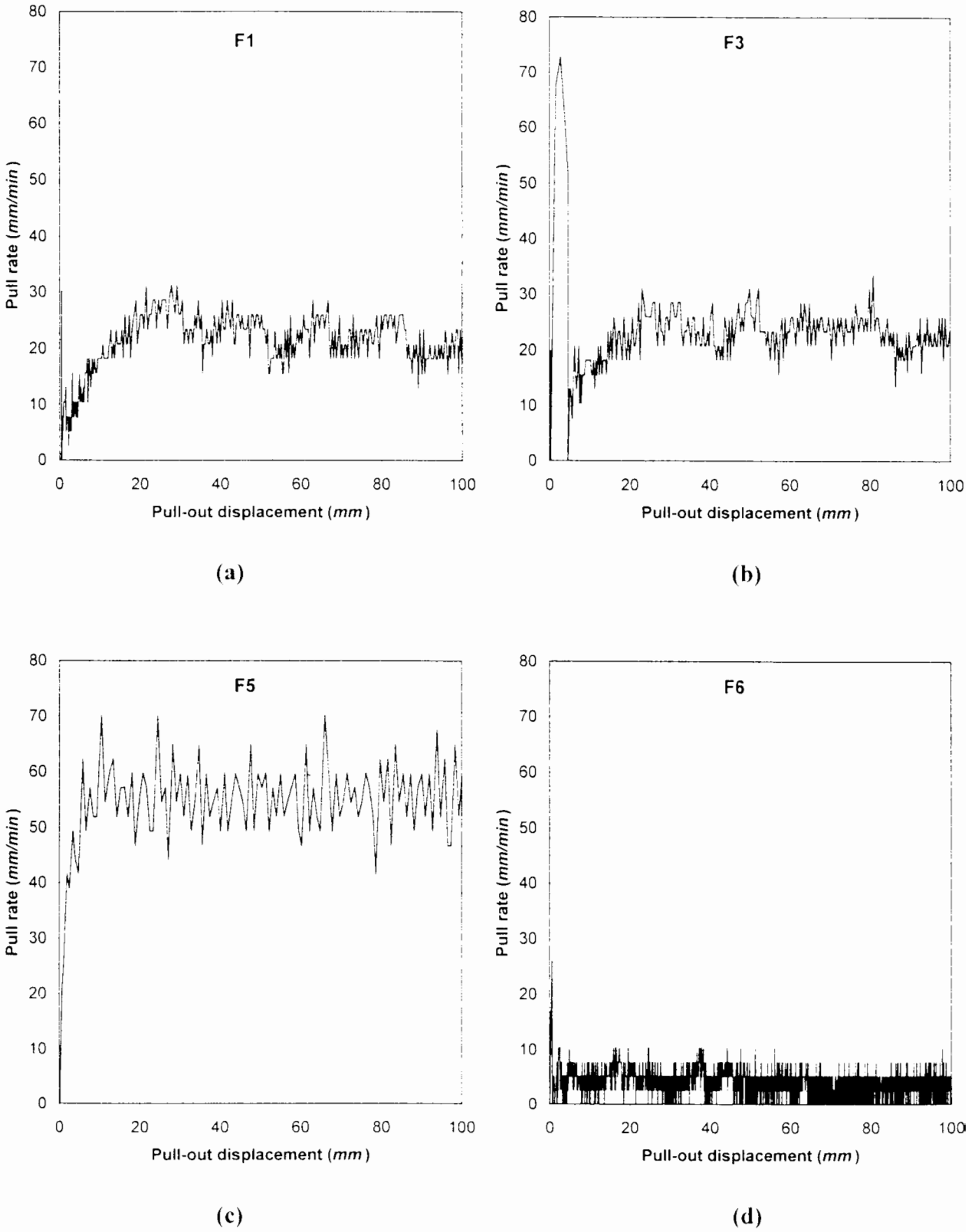

Figure 4.10 – Displacement rates for final series pull-out tests

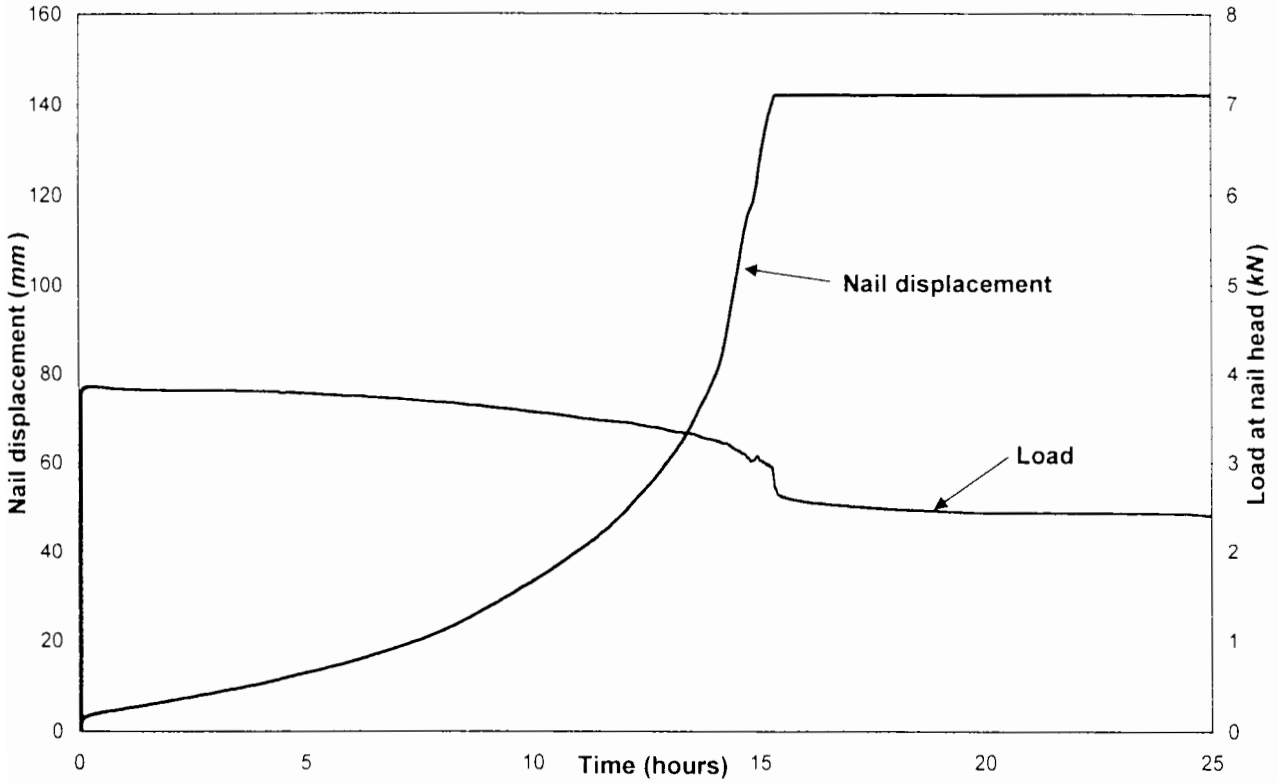

Figure 4.11 – Sustained loading test P5: displacements and loads

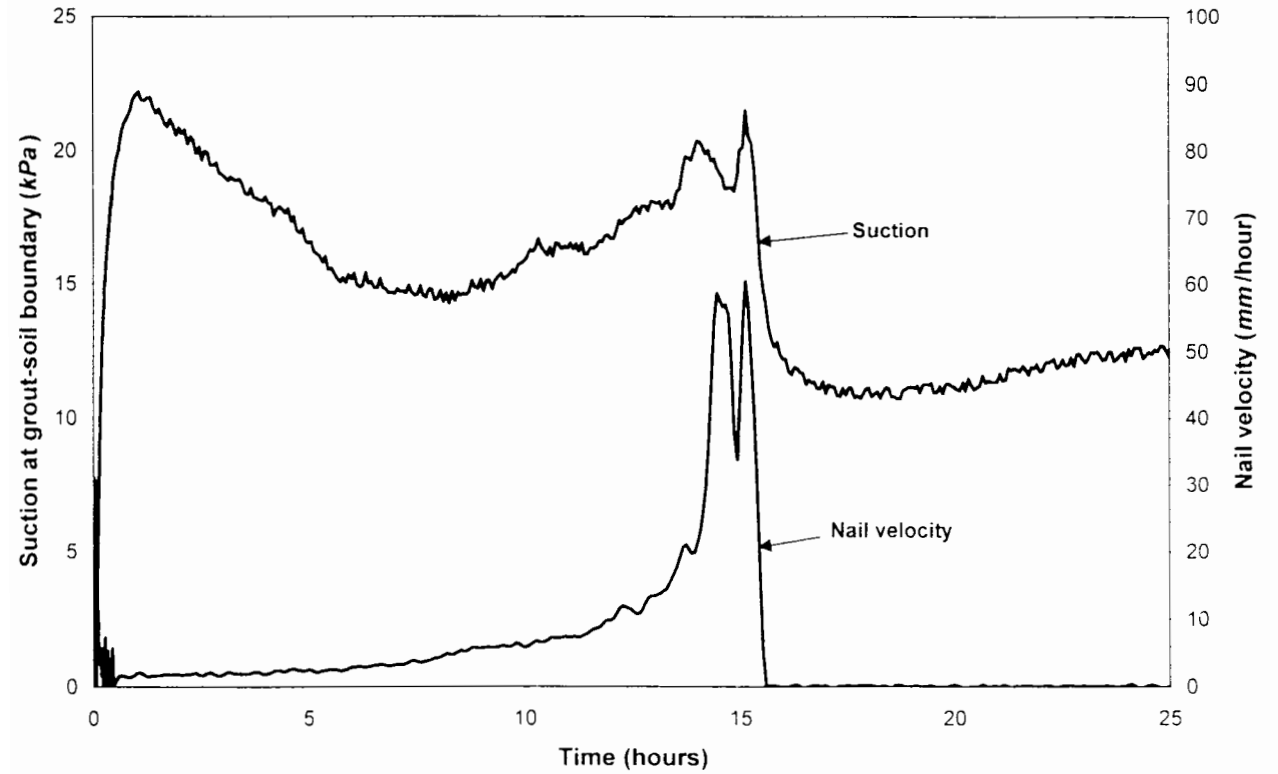

Figure 4.12 – Sustained loading test P5: pore water suctions and nail velocity

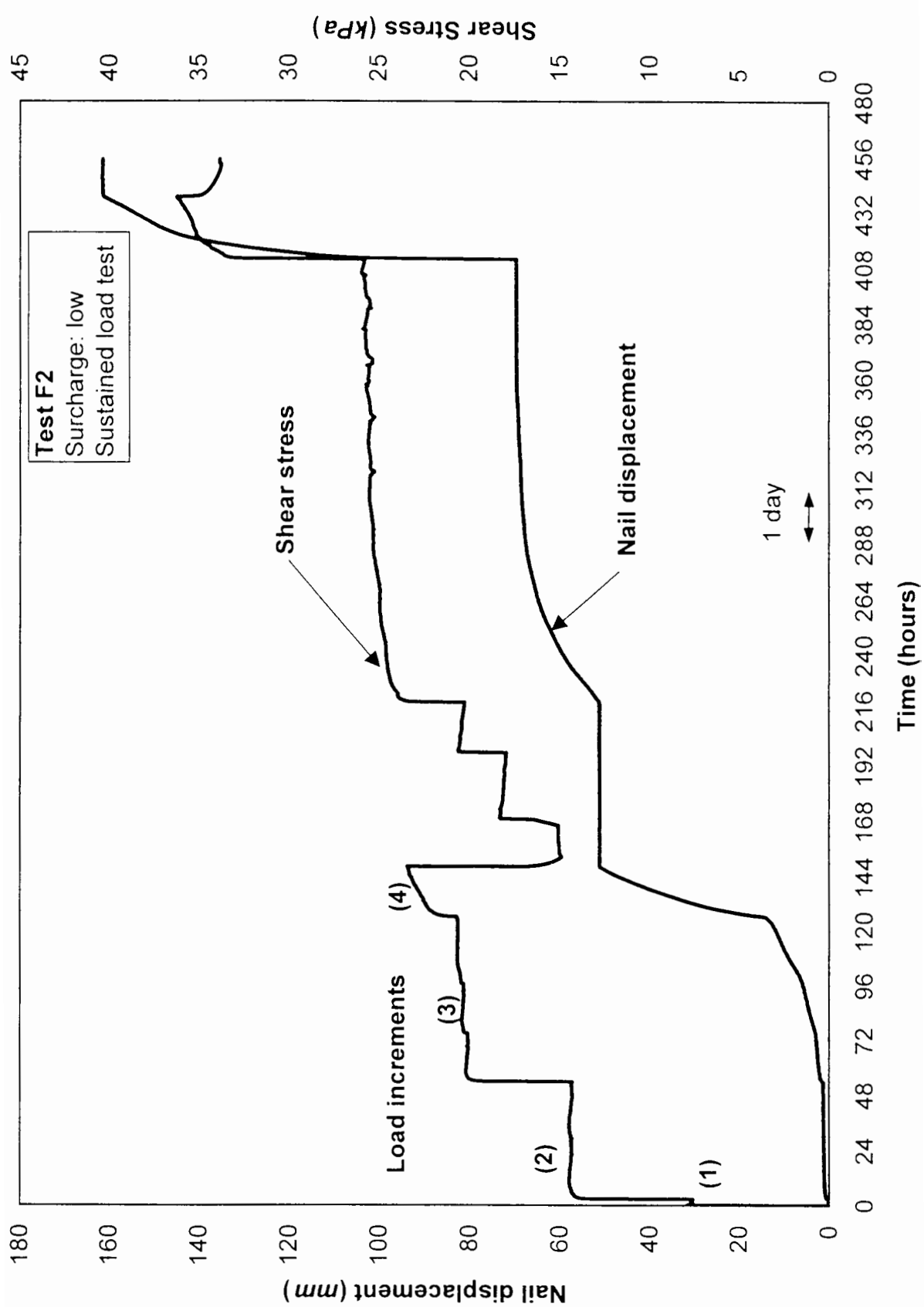

Figure 4.13 – Sustained loading test F2

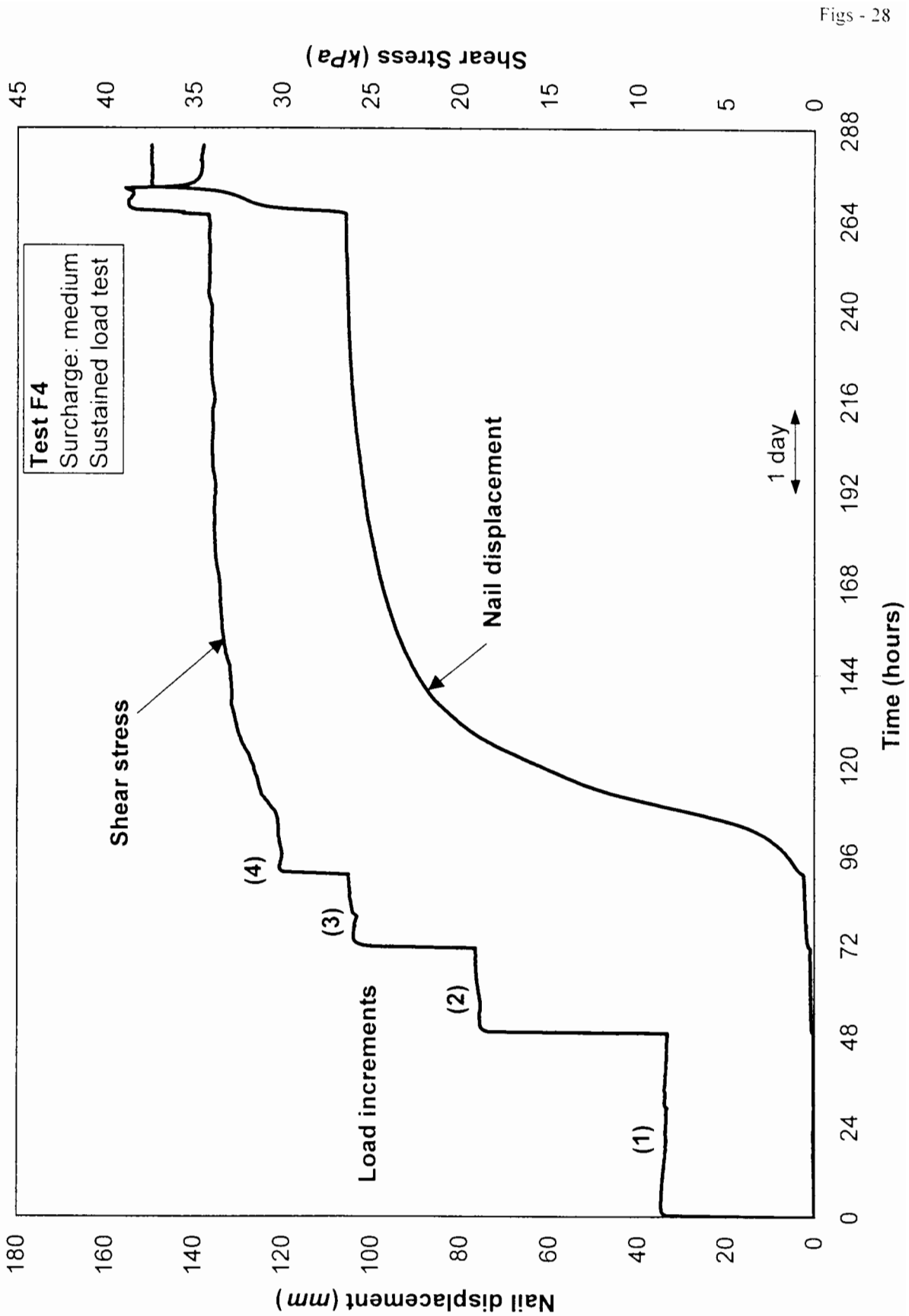

Figure 4.14 – Sustained loading test F4

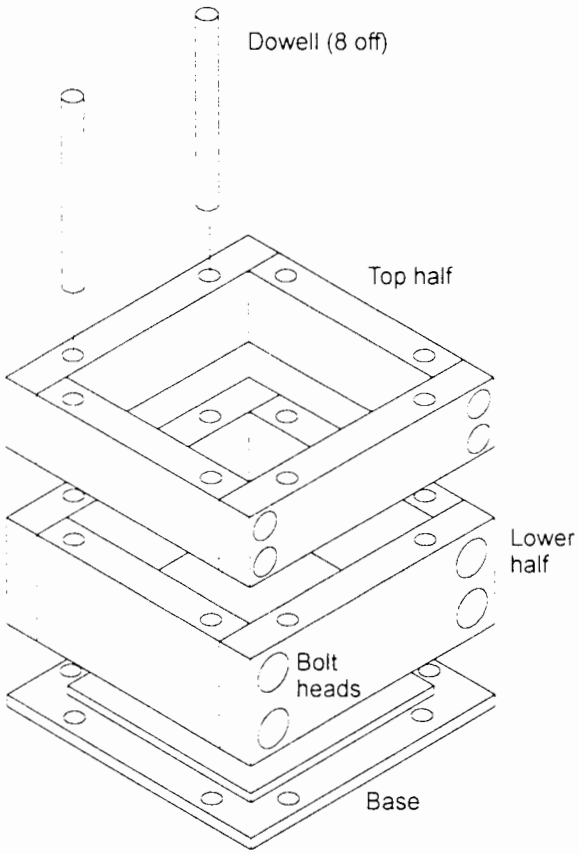

Figure 5.1 – Interface test sample preparation mould

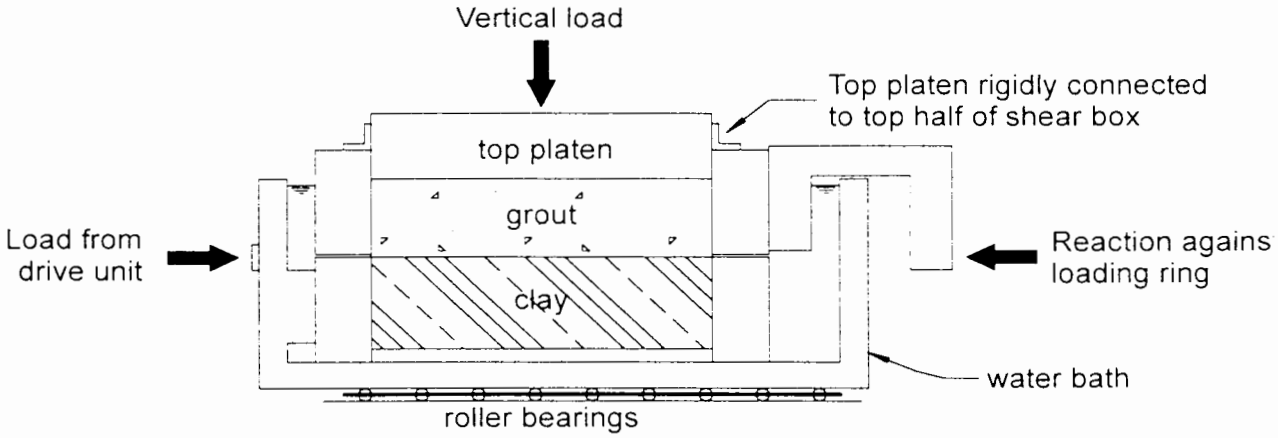

Figure 5.2 – Interface test arrangement

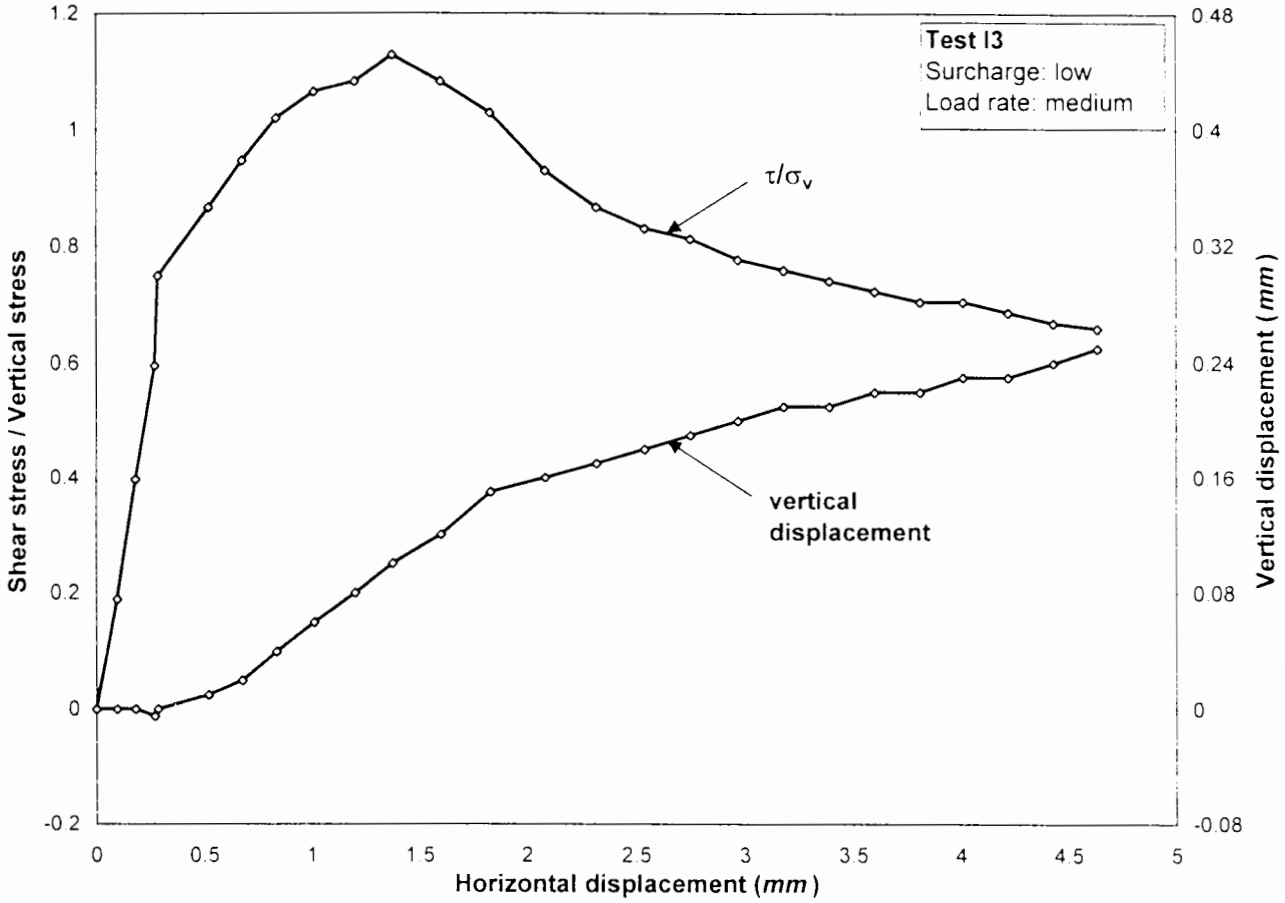

Figure 5.3 – Interface test I3

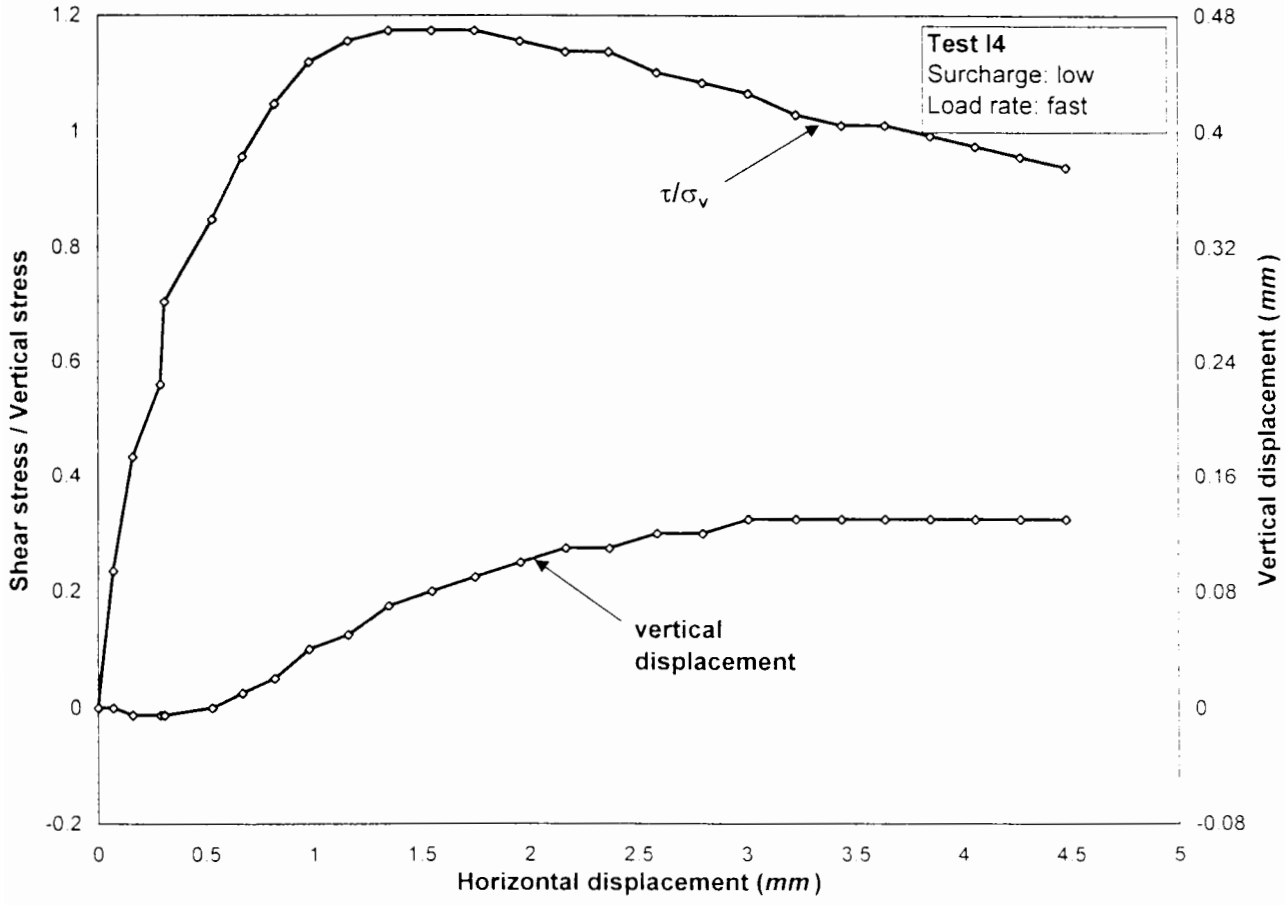

Figure 5.4 – Interface test I4

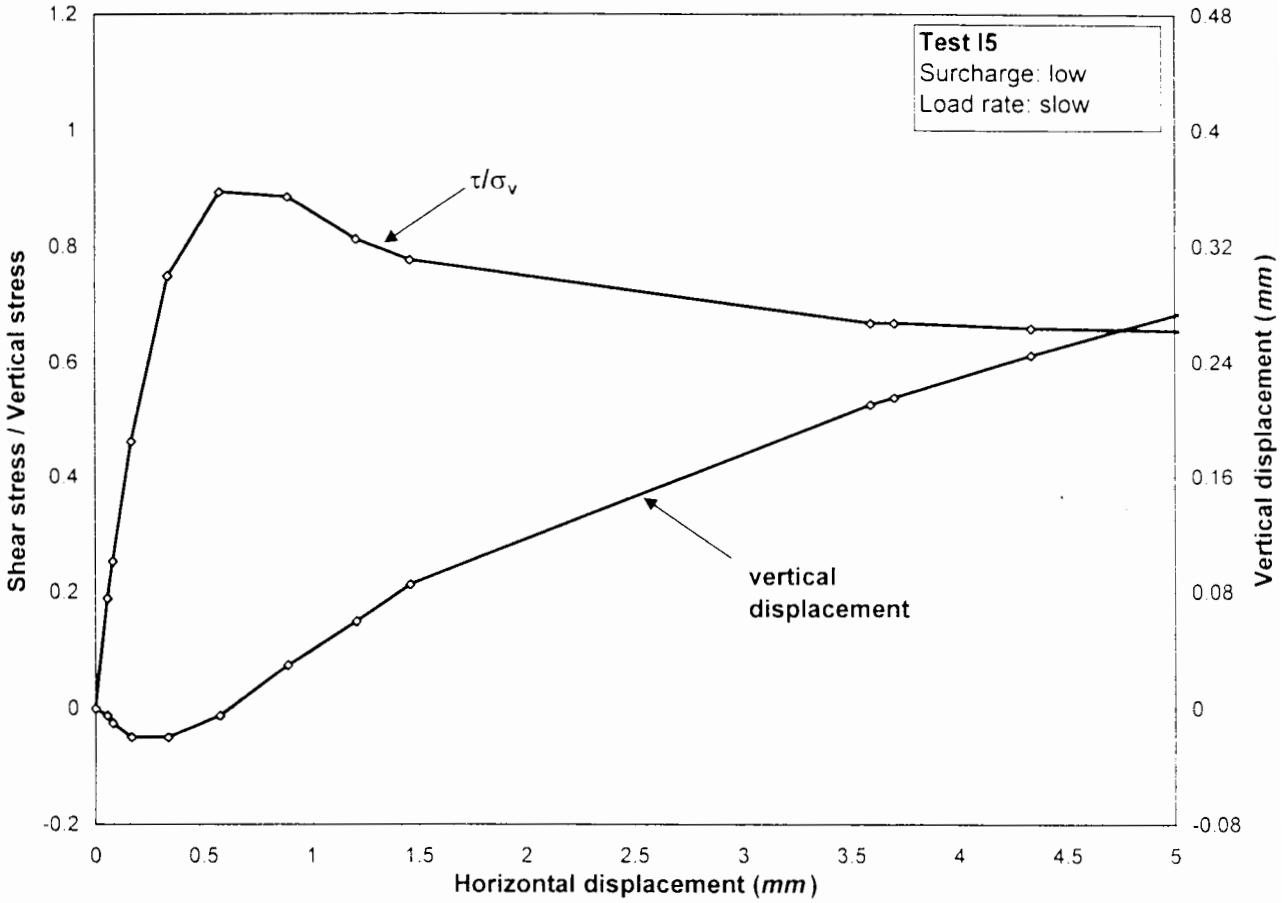

Figure 5.5 - Interface test I5

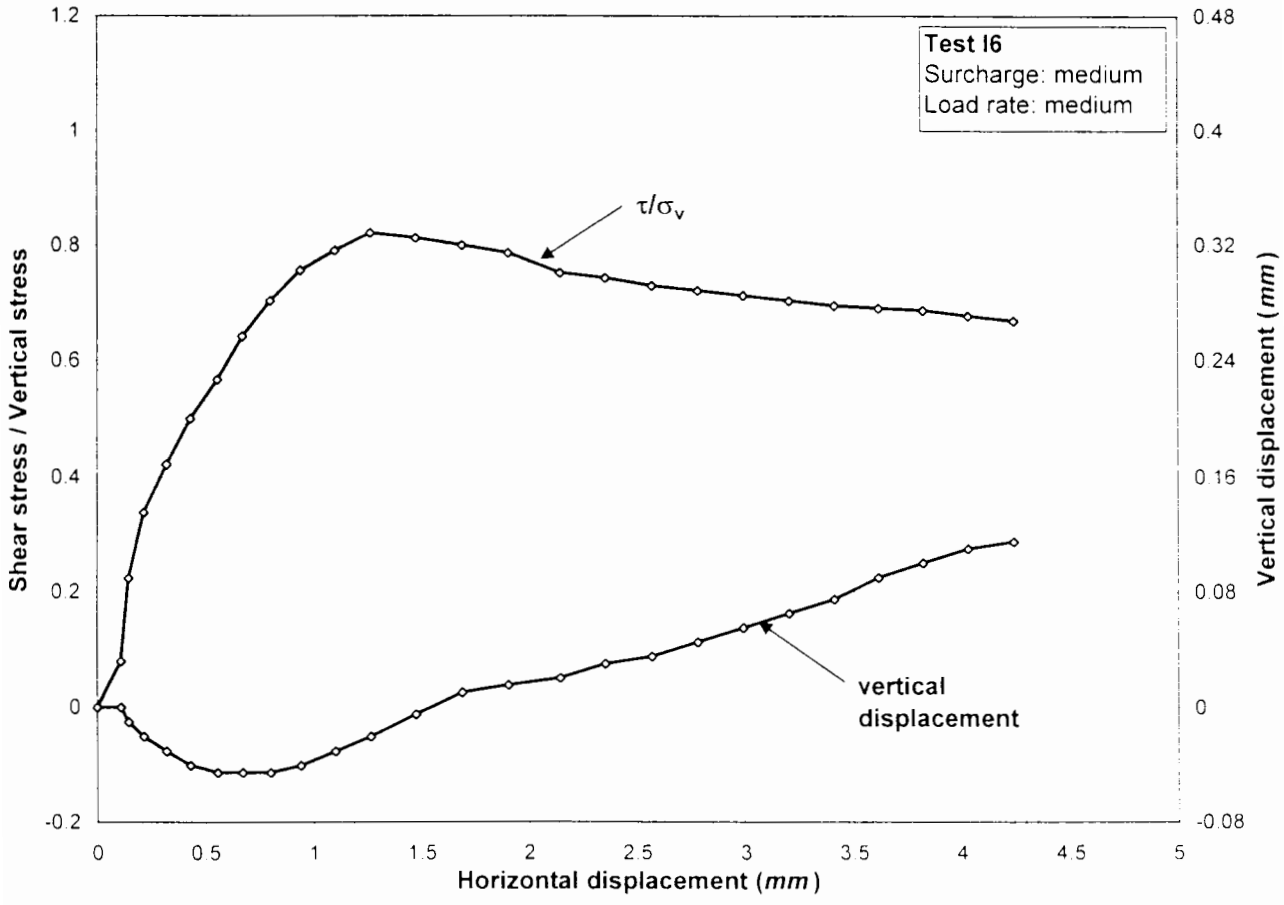

Figure 5.6 – Interface test I6

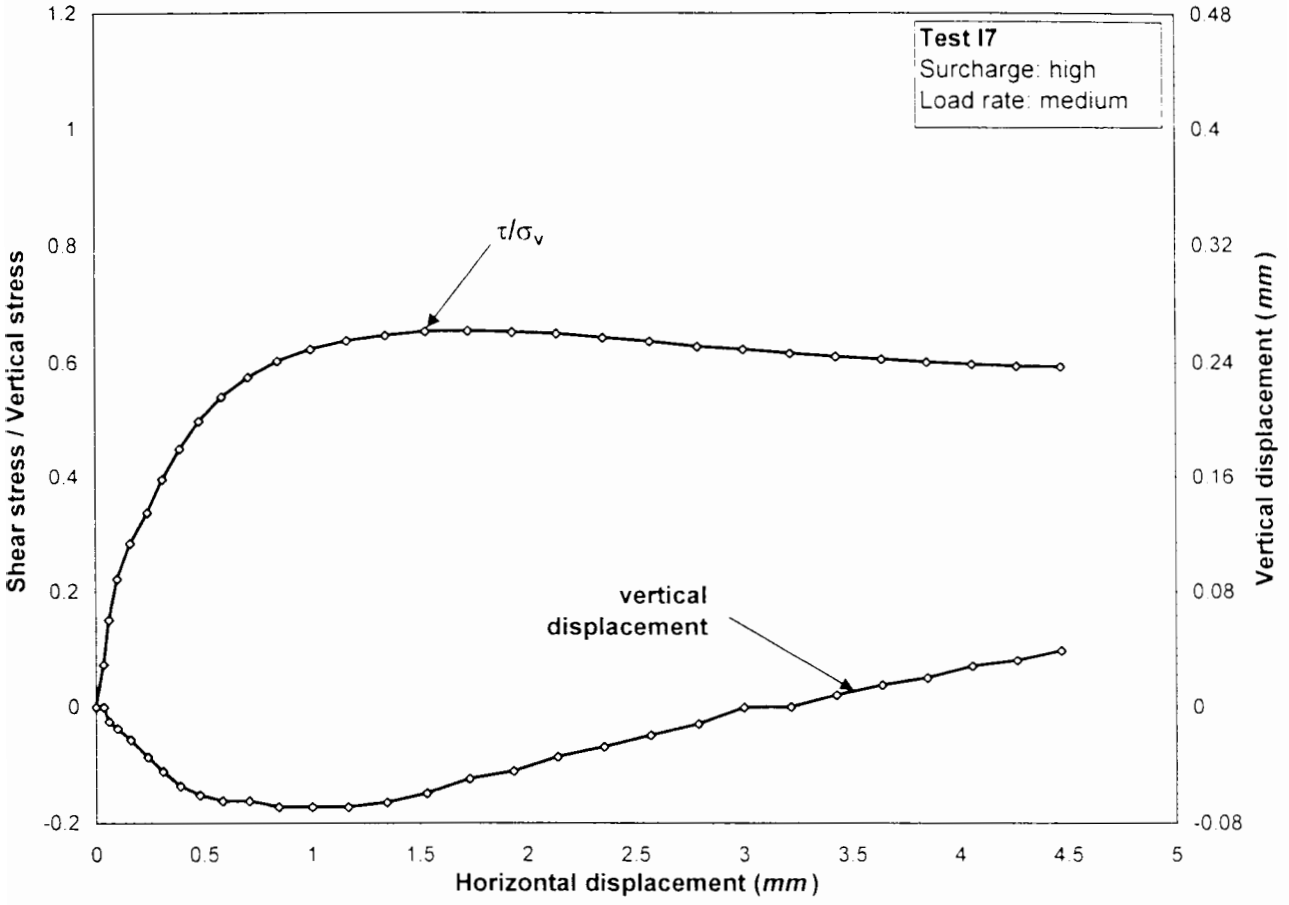

Figure 5.7 – Interface test I7

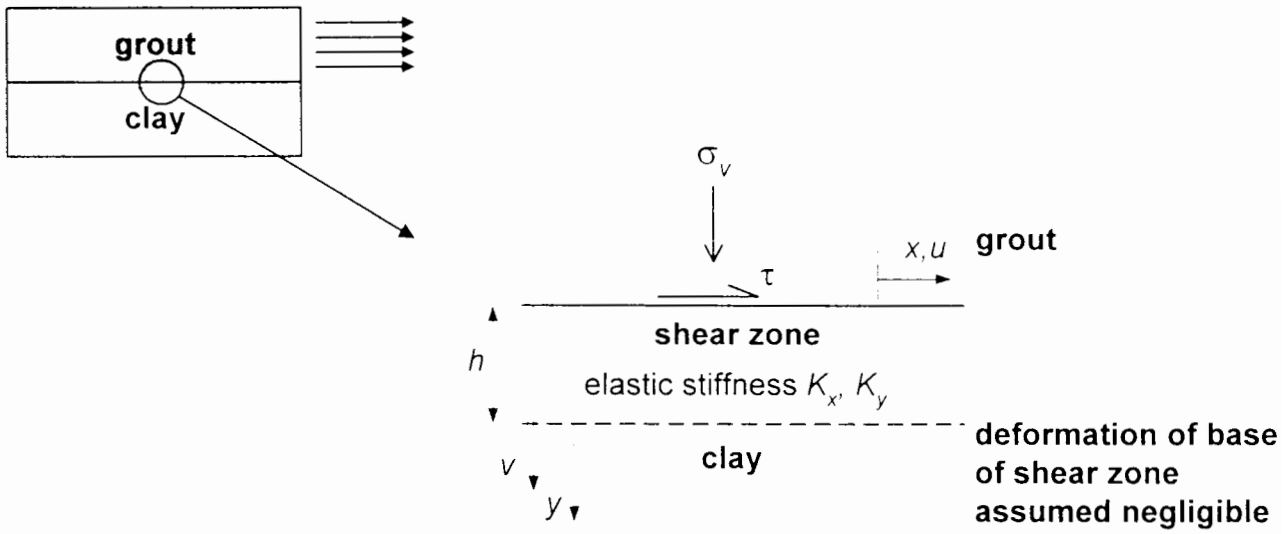

Figure 5.8 – Numerical model of interface test

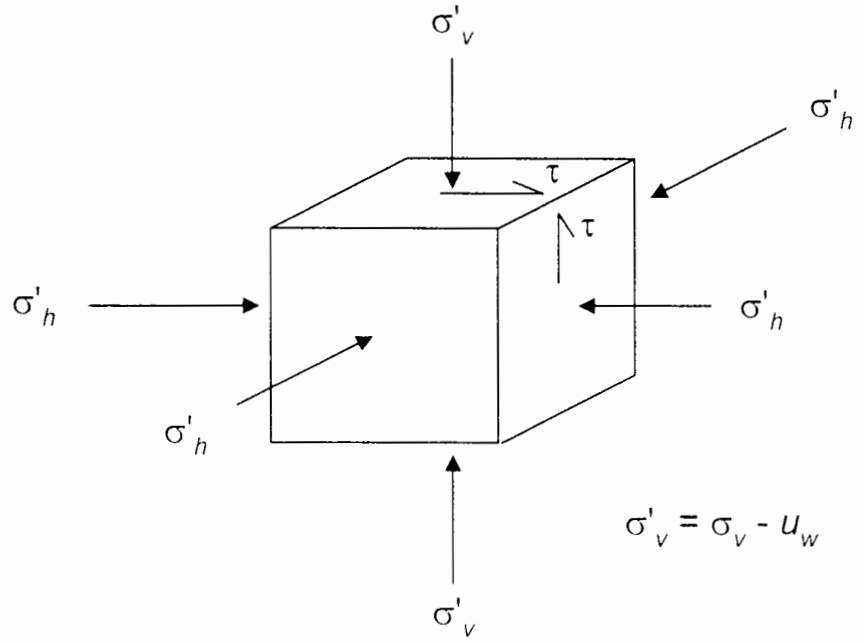

Figure 5.9 – Effective stresses within the interface shear zone

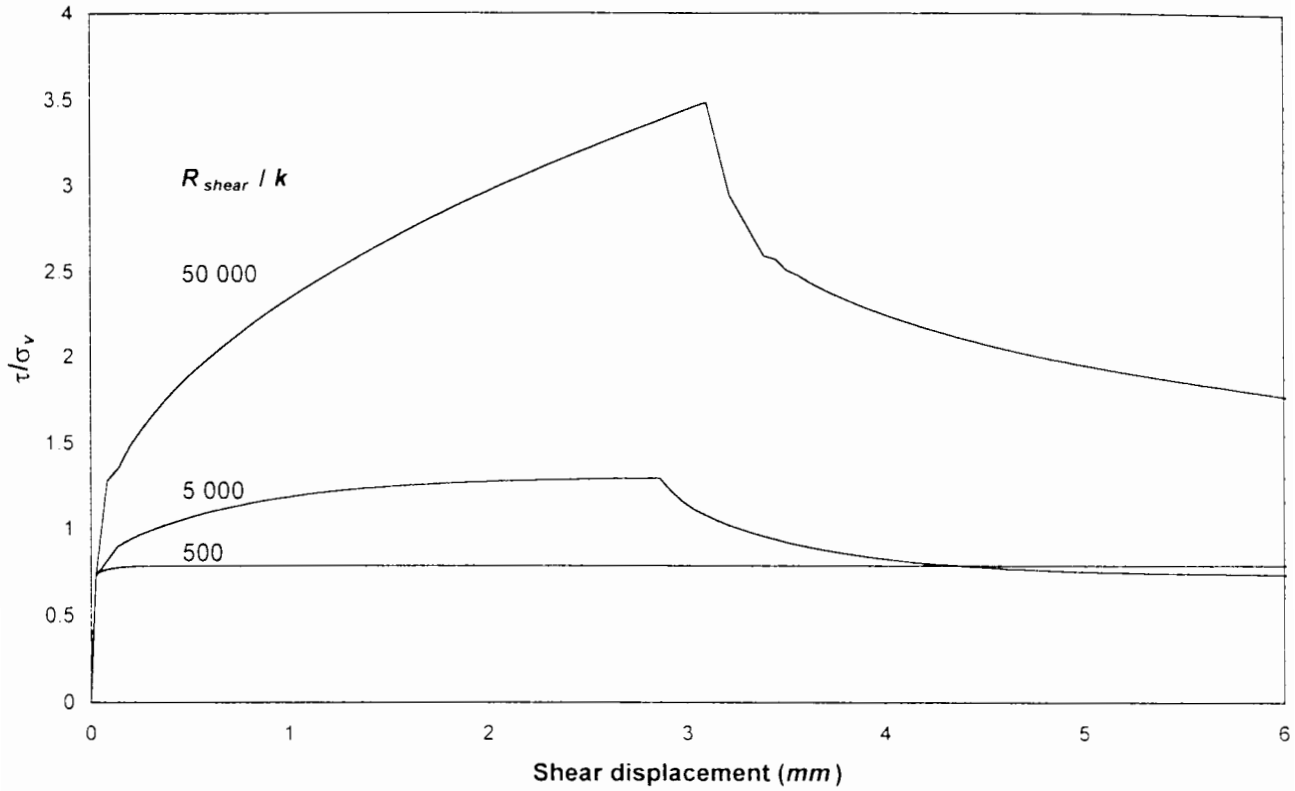

Figure 5.10 – Numerical model of interface tests.
Results from analyses performed at different shear displacement rates

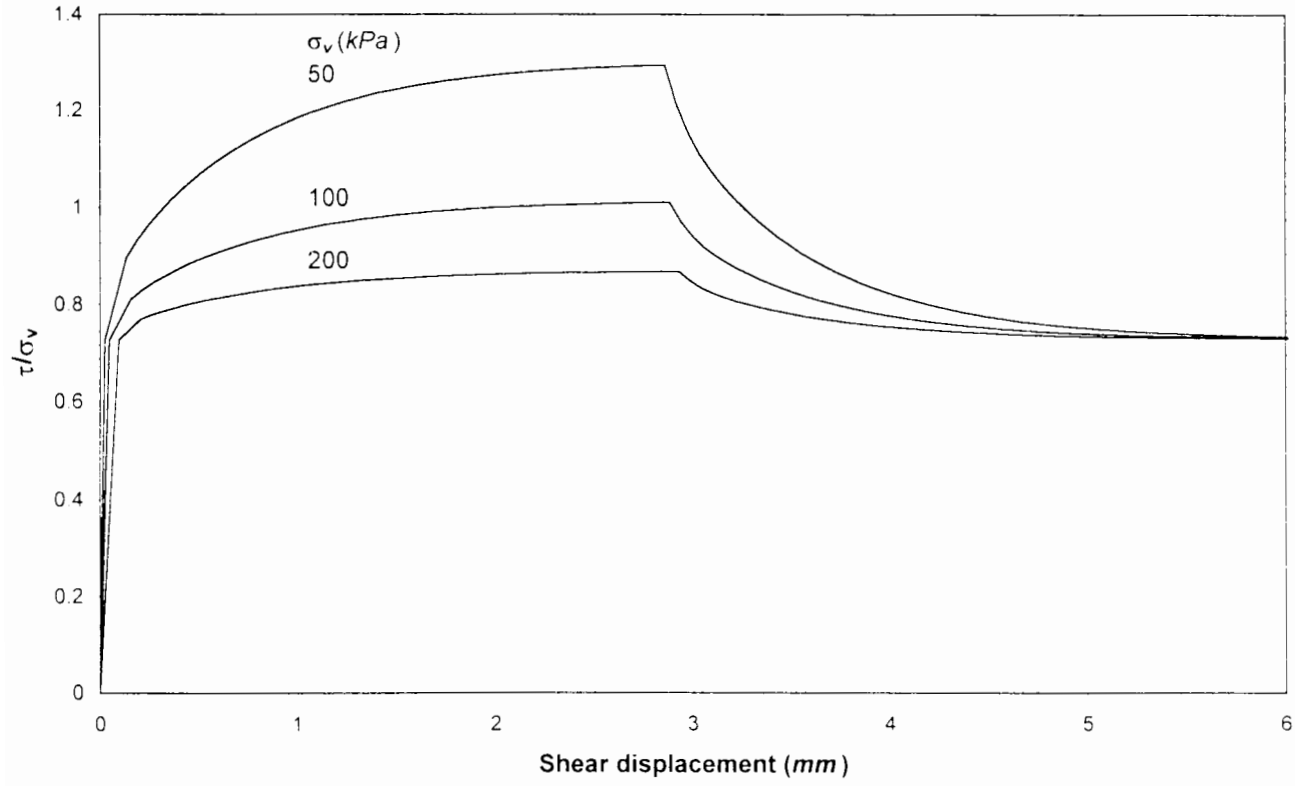

Figure 5.11 – Numerical model of interface tests.
Results from analyses performed at different vertical stress

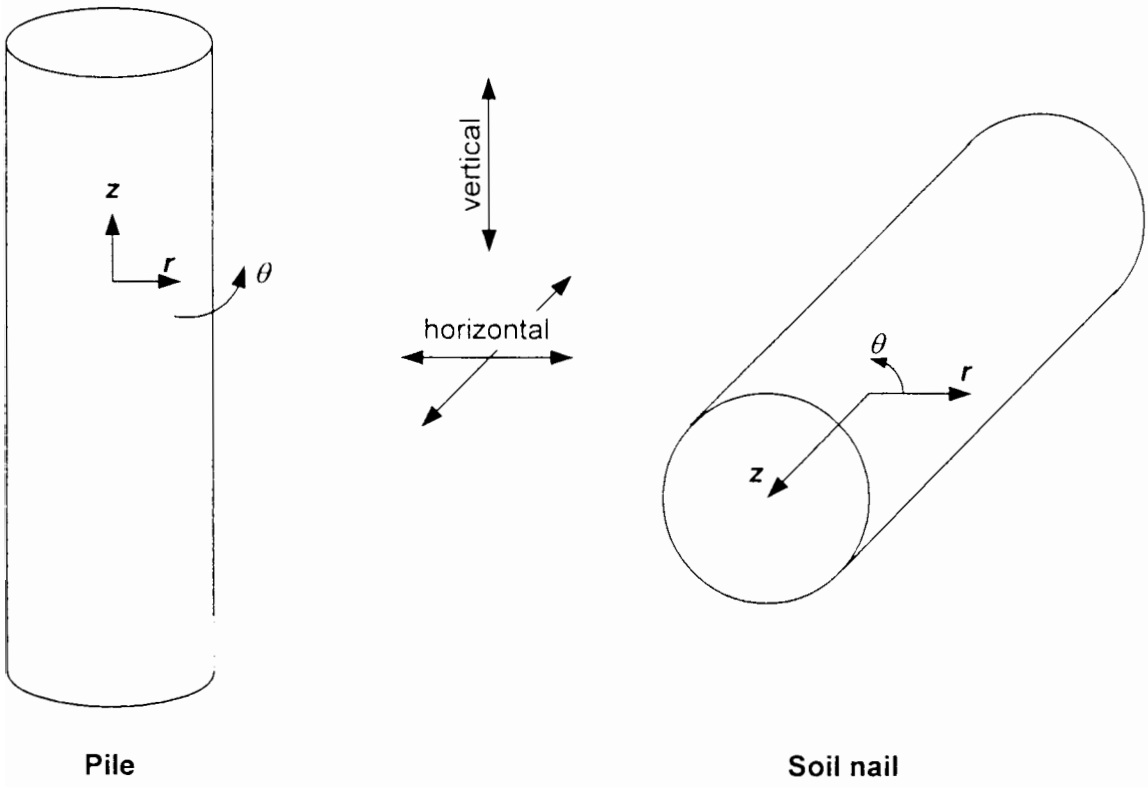

Figure 6.1 – Comparison of the geometries of piles and soil nails

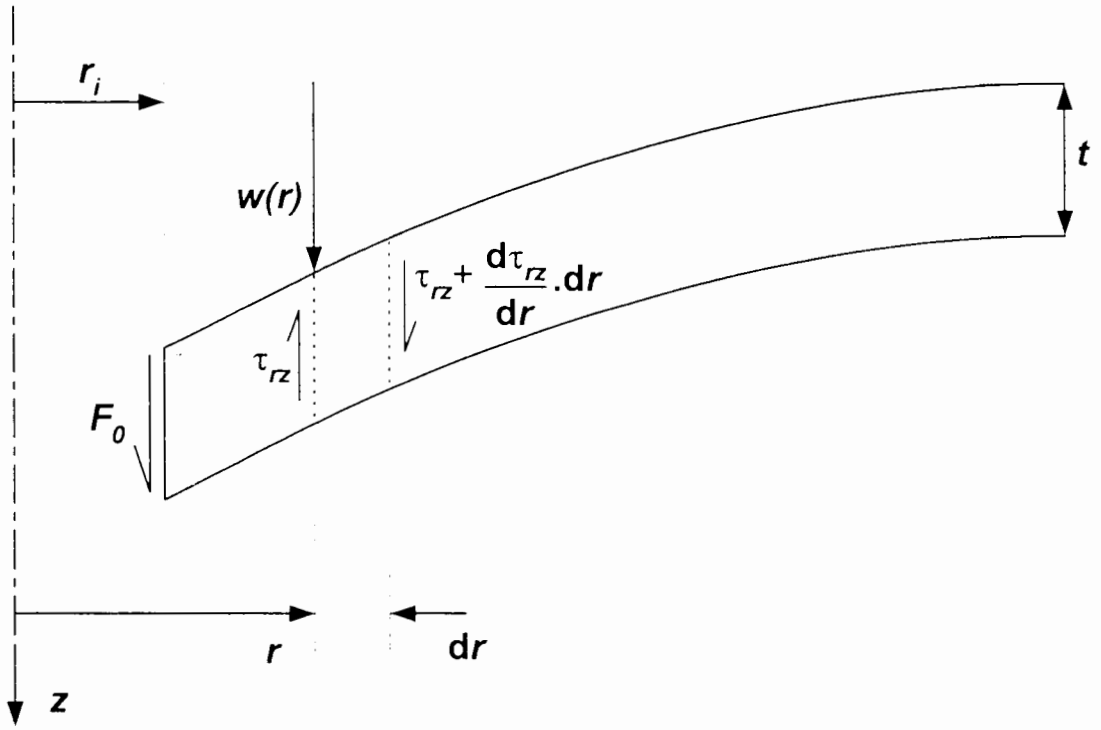

Figure 7.1 – Shear deformation geometry

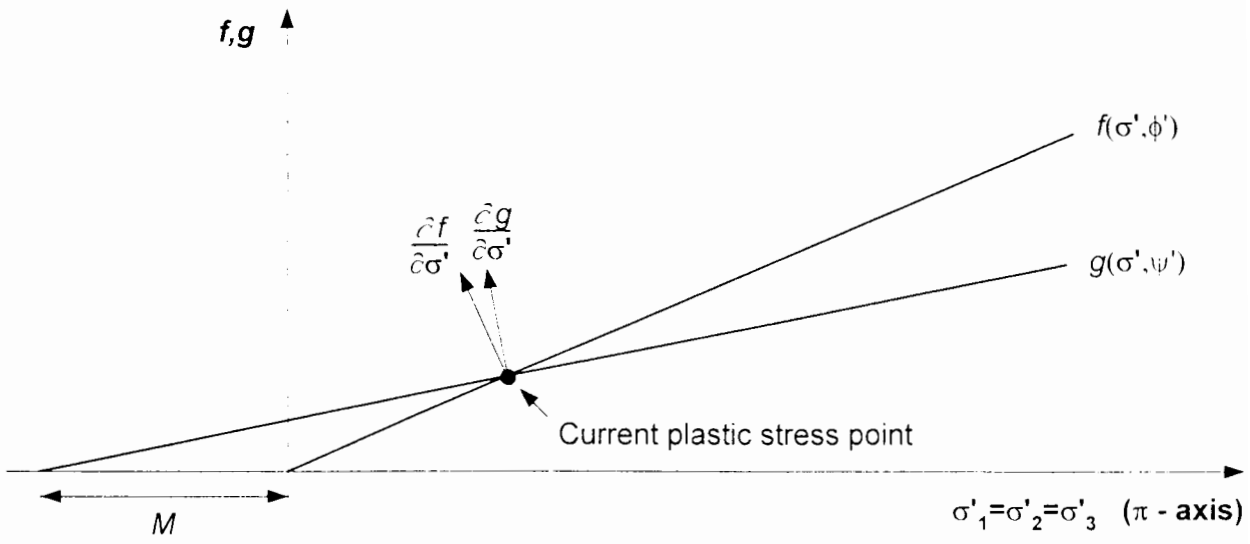

Figure 7.2 – Two-dimensional representation of yield and plastic potential surfaces

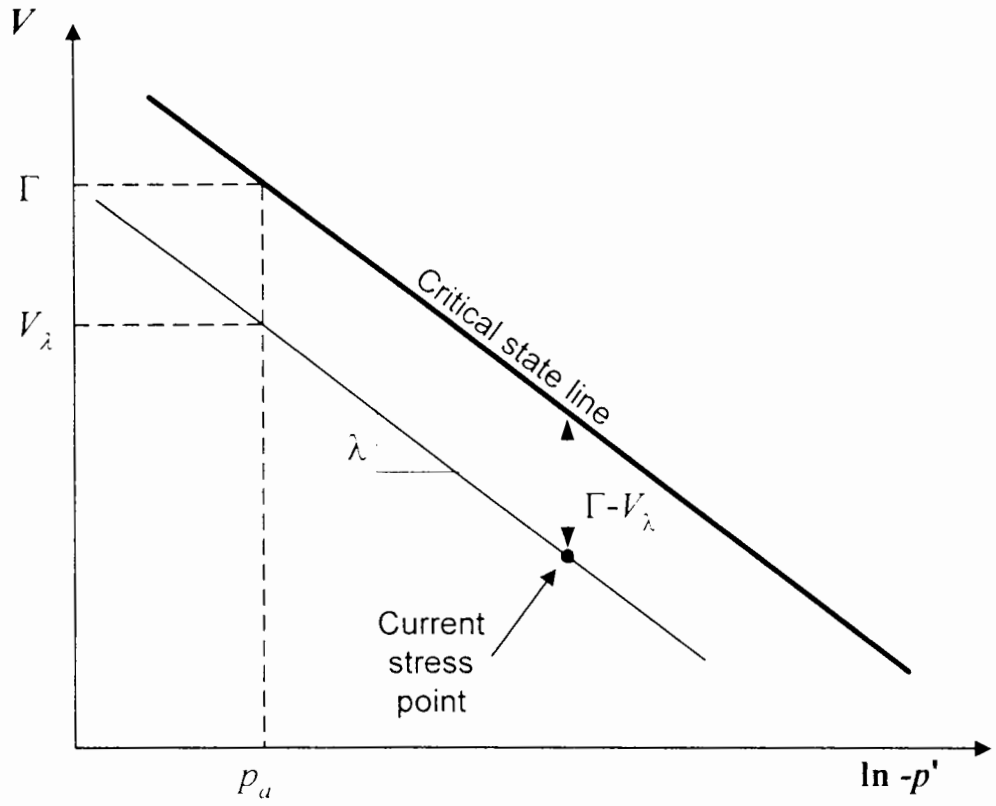

Figure 7.3 – Wroth dilation model

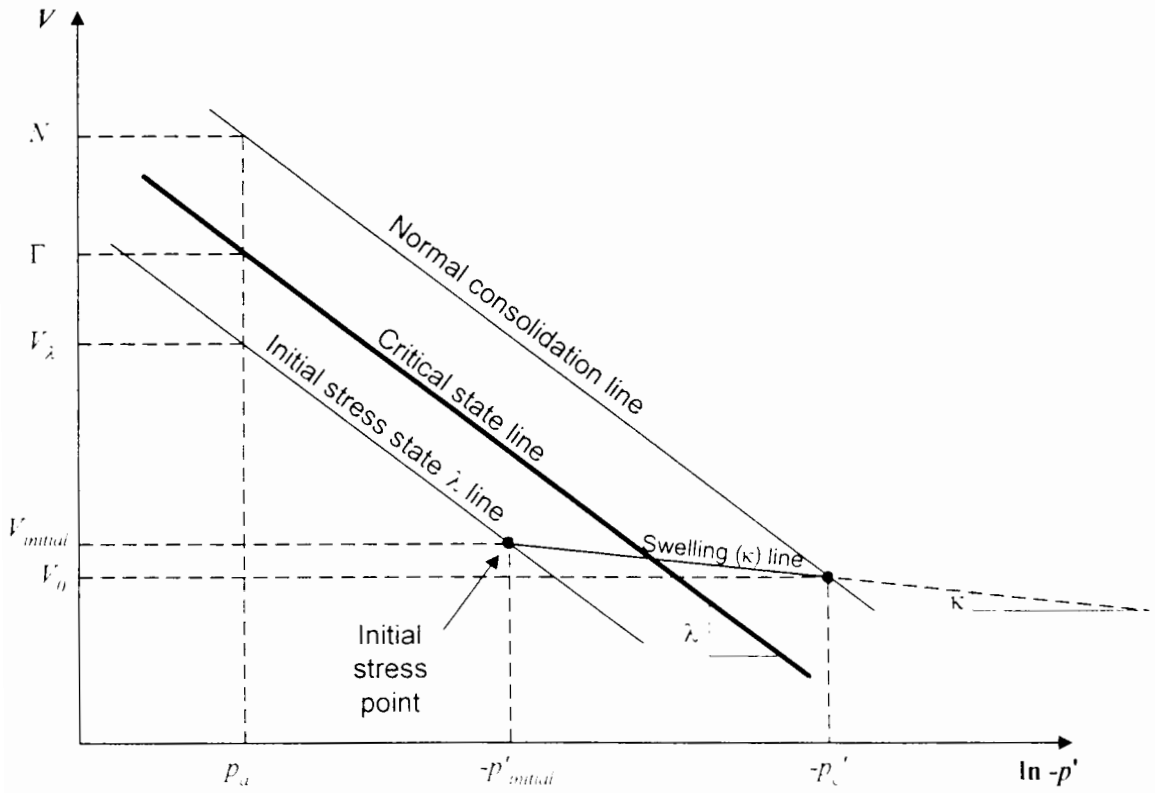

Figure 7.4 – Wroth dilation model – initial conditions

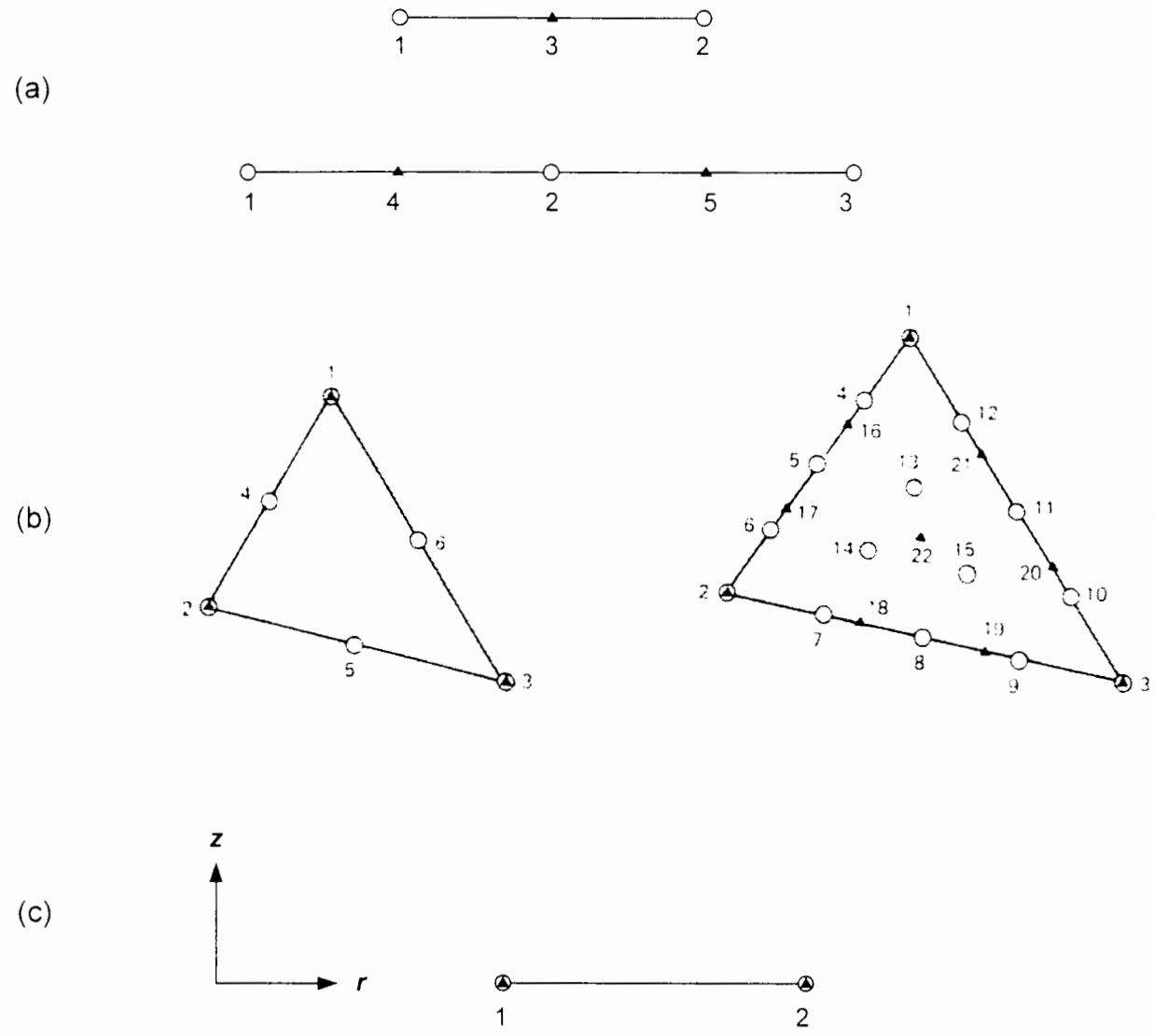

Figure 7.5 – Different types of finite element

(a) – One dimensional element with non-coincident pore pressure and displacement nodes
(b) – Two dimensional elements used in CRISP, after Britto and Gunn (1987)
(c) – One dimensional elements used in *Cavexp* with coincidental pore pressure and displacement nodes

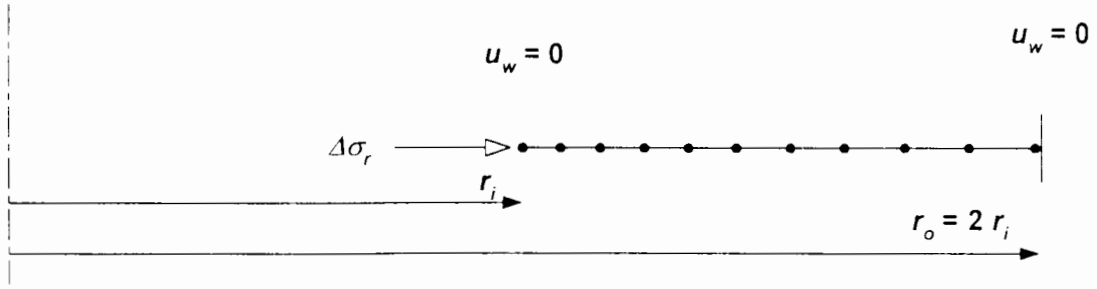

Figure 7.6 – Simple FE mesh used for stability test calculation

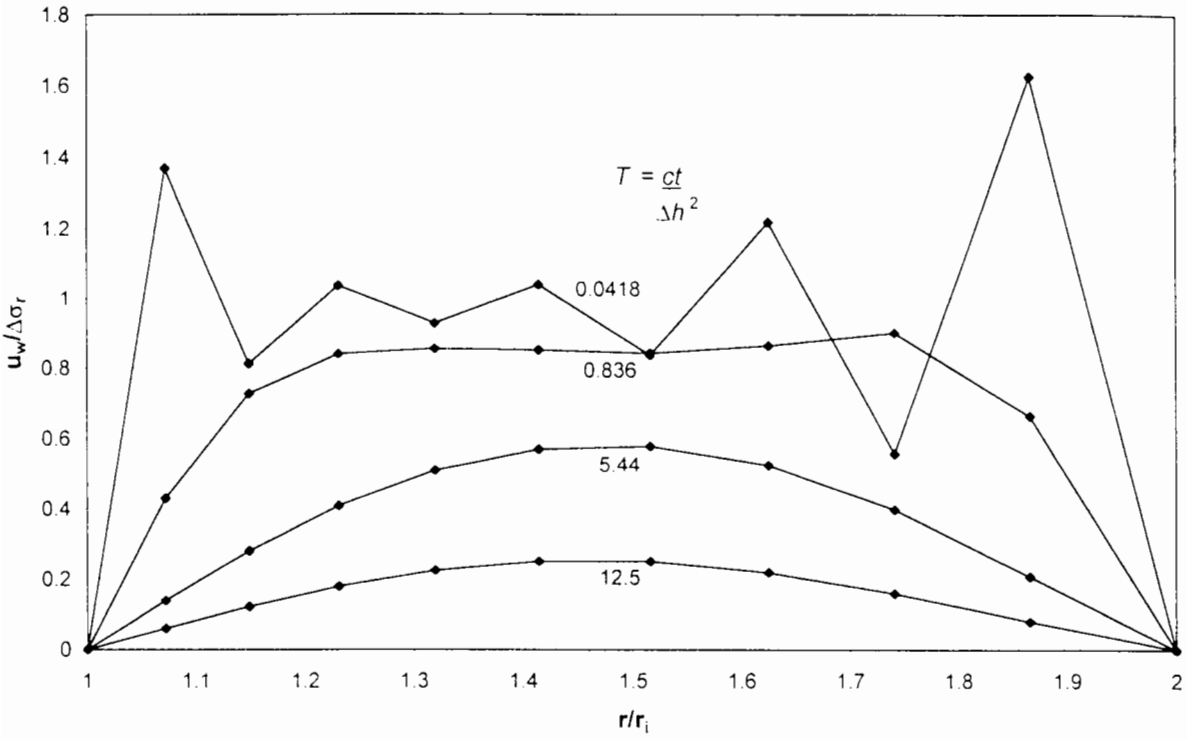

Figure 7.7(a) – Stability test problem, shorter time steps

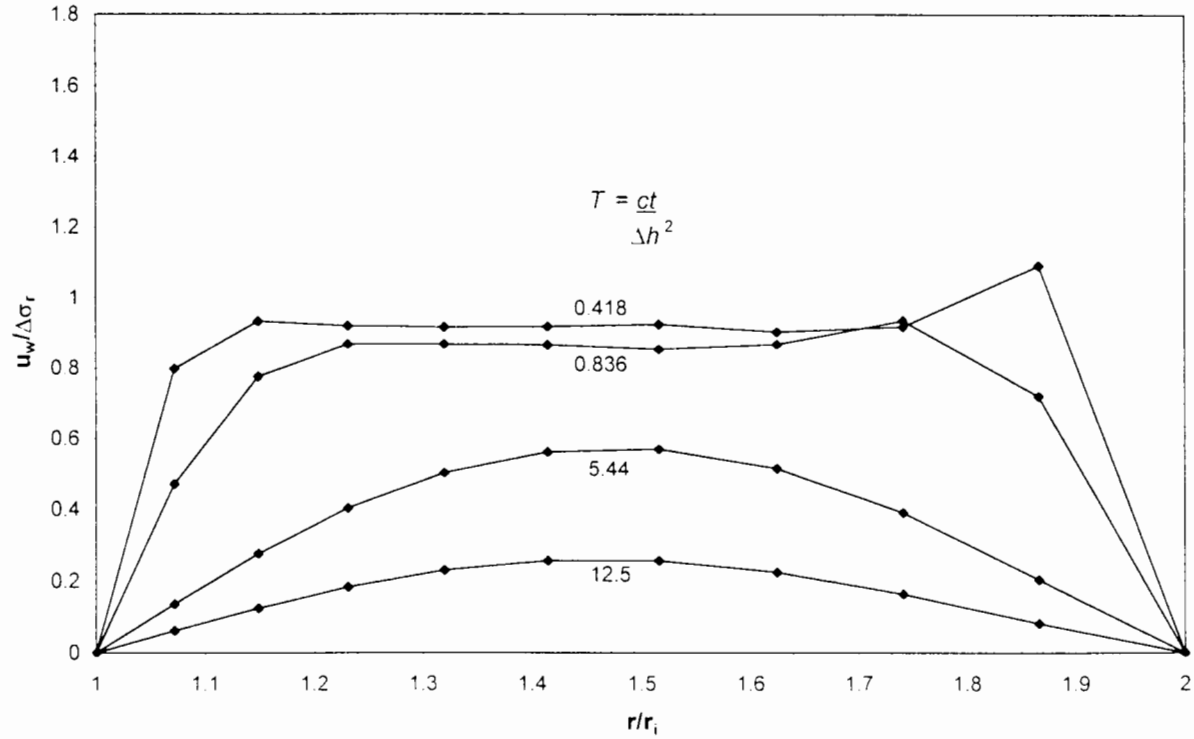

Figure 7.7(b) – Stability test problem, longer time steps

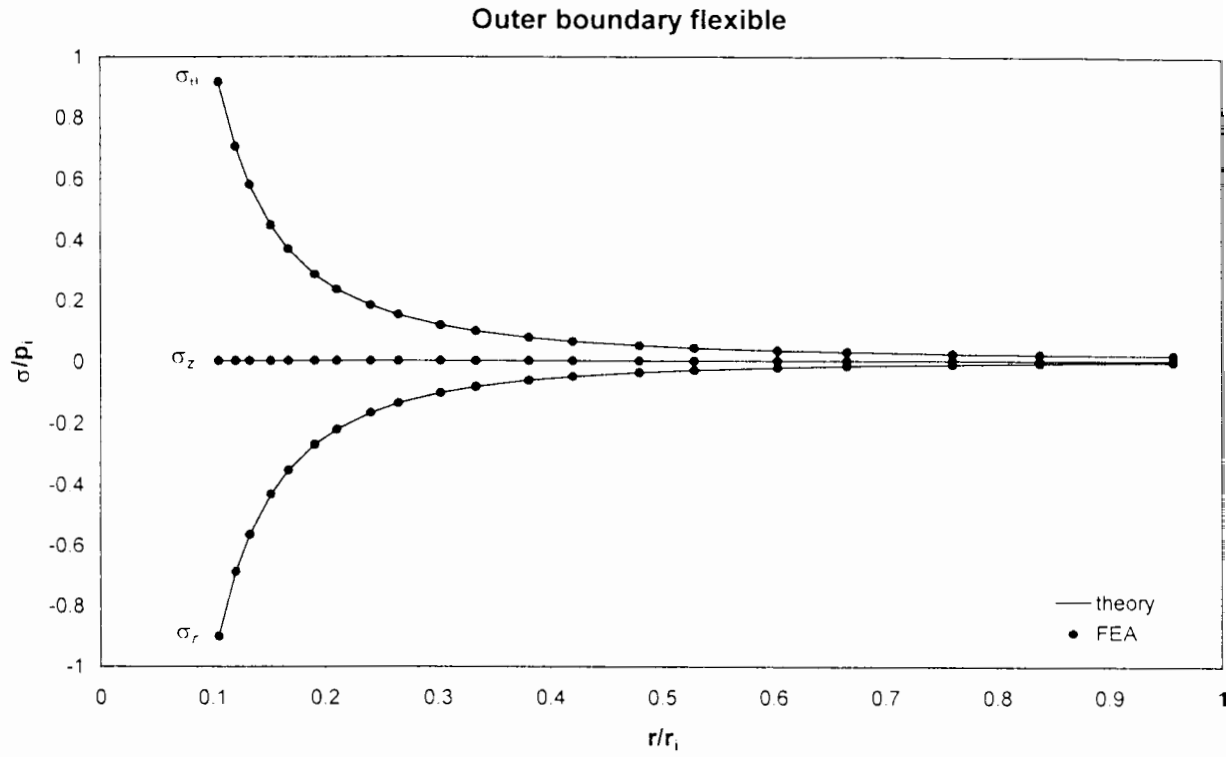

Figure 7.8(a) – Effective stress variation with radius for elastic cavity expansion with stress-controlled outer boundary

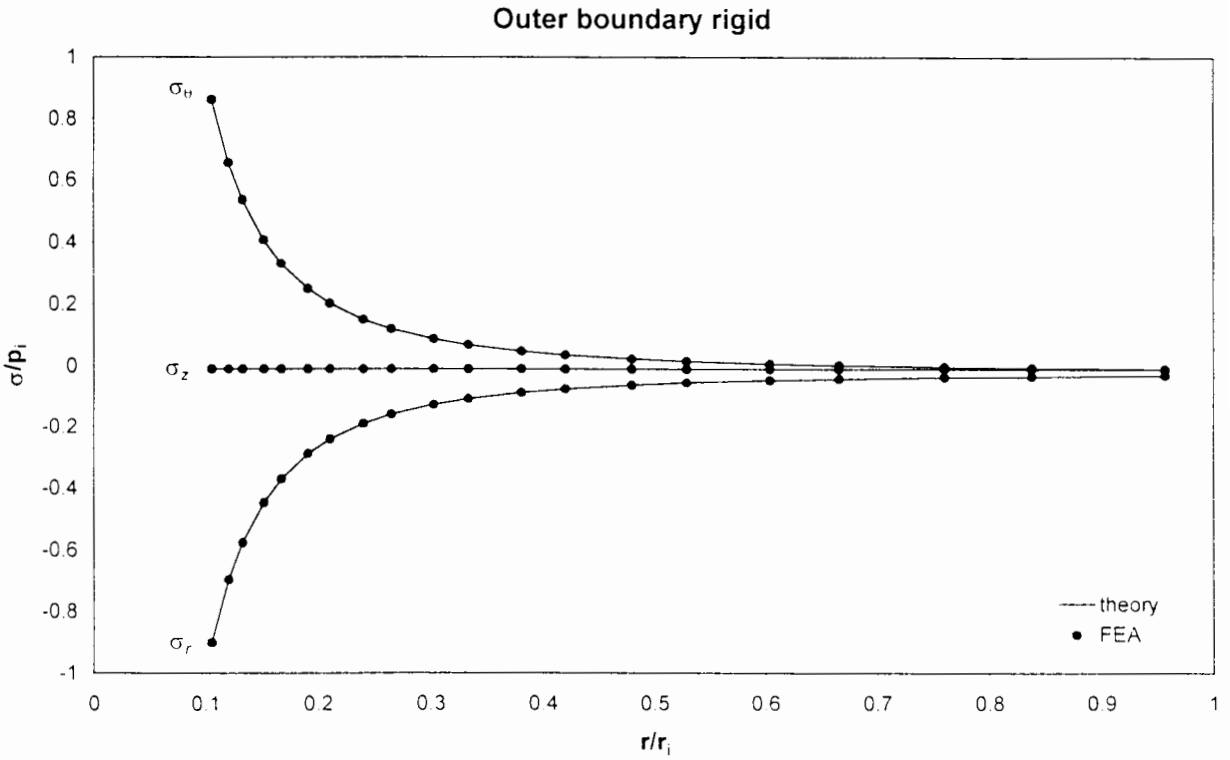

Figure 7.8(b) - Effective stress variation with radius for elastic cavity expansion with rigid outer boundary (displacement-controlled)

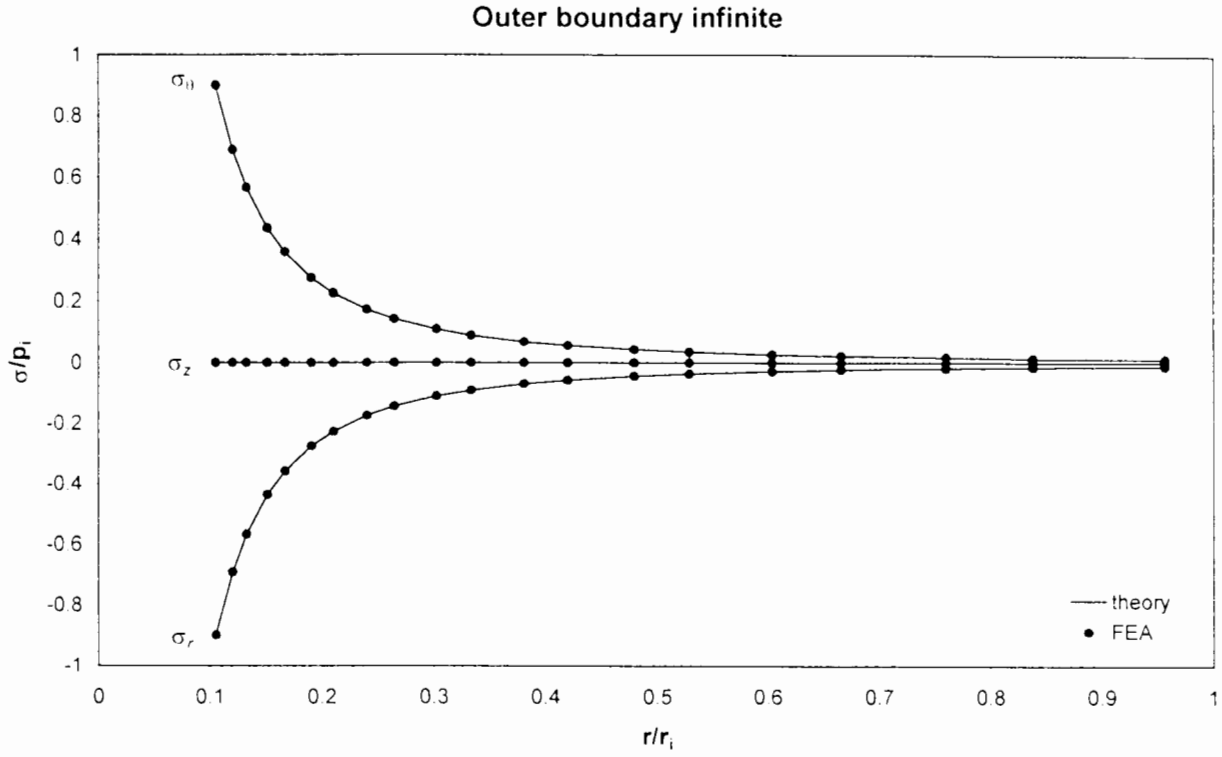

Figure 7.8(c) – Effective stress variation with radius for elastic cavity expansion with infinite outer boundary (stiffness-controlled)

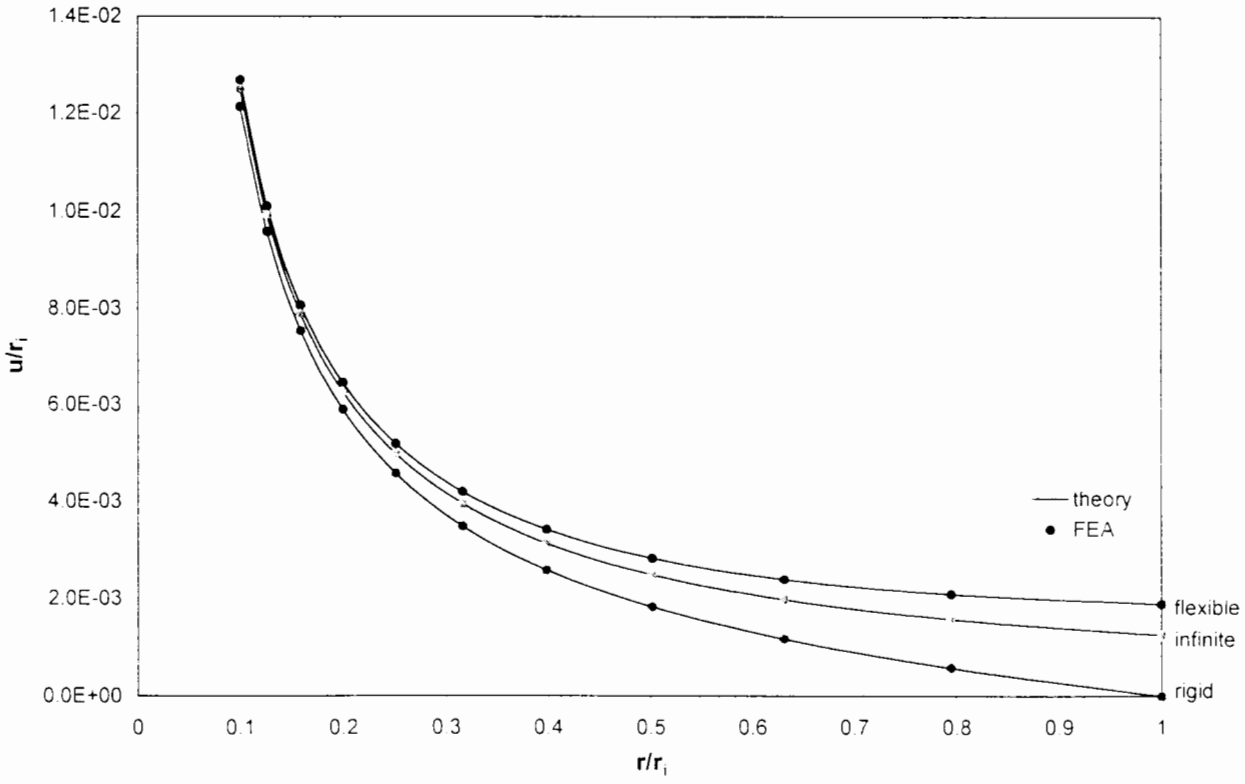

Figure 7.9 – Axial displacement variation with radius for all three outer boundary conditions

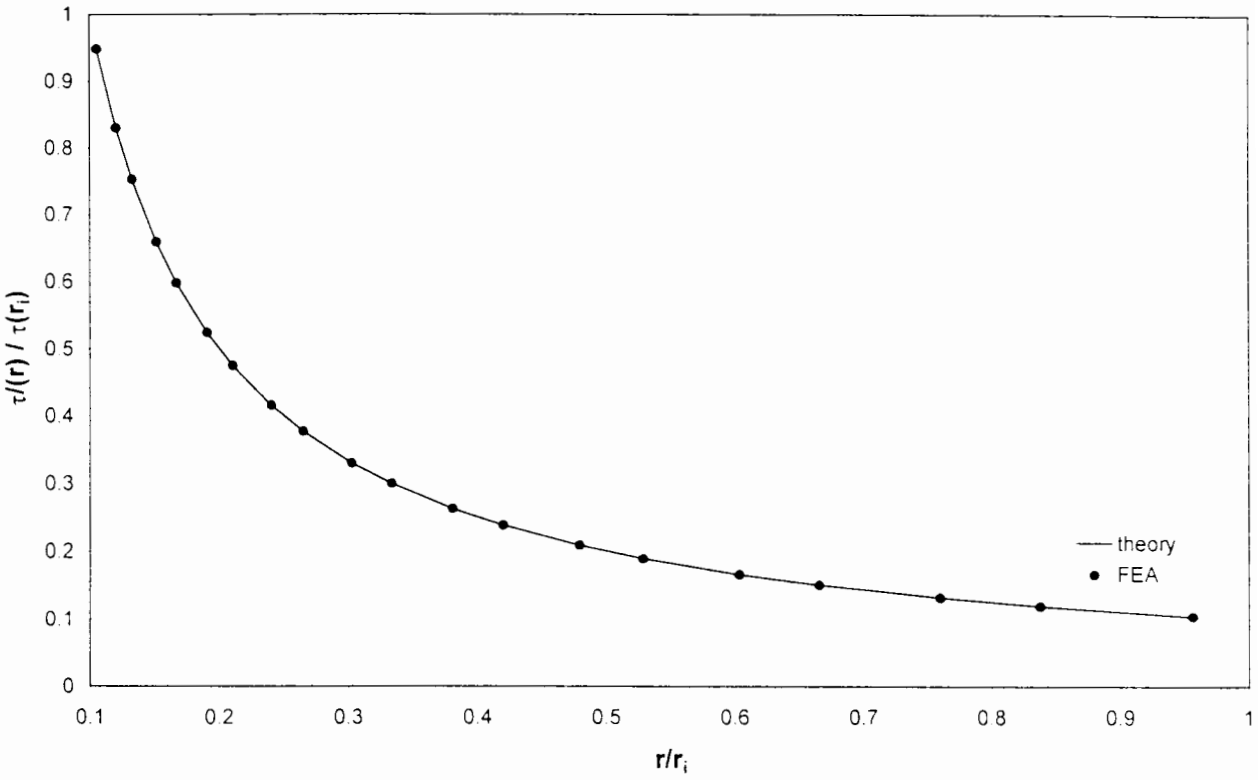

Figure 7.10 – FE elastic pull-out shear stress variation with radius compared with theory

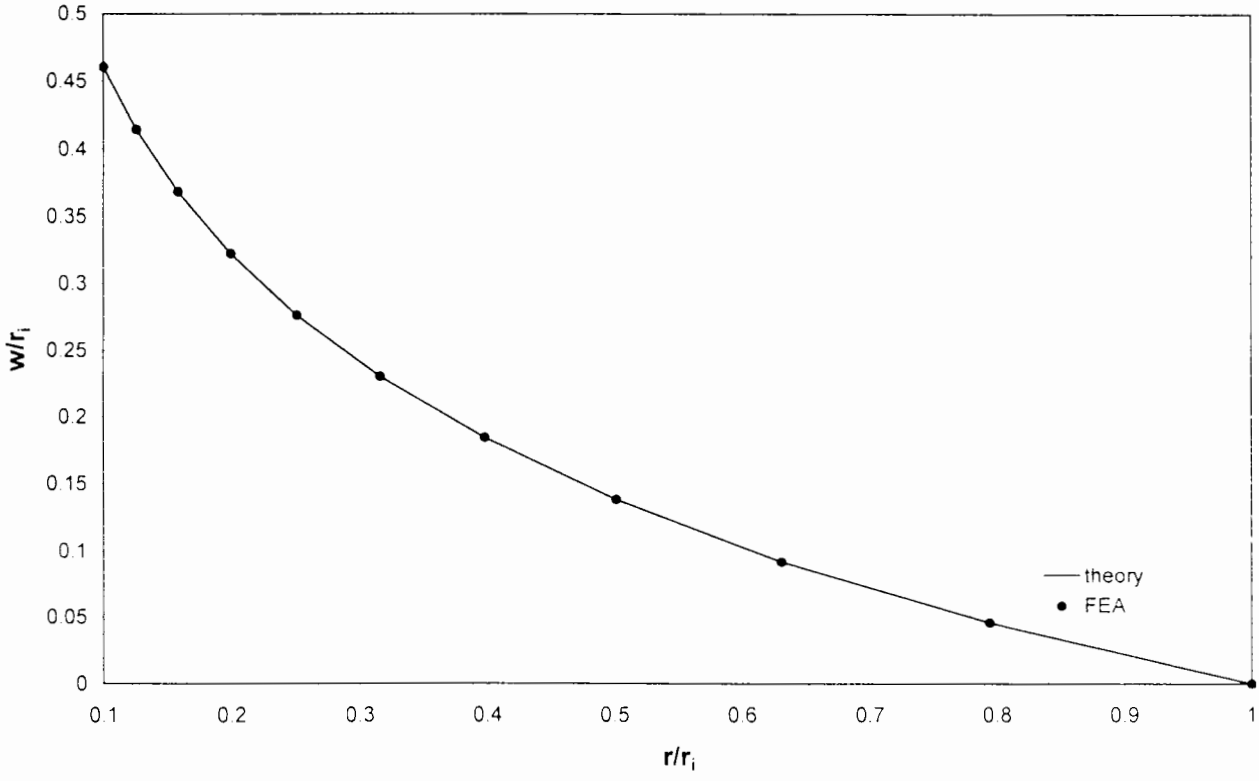

Figure 7.11 - FE elastic pull-out axial displacement variation with radius compared with theory

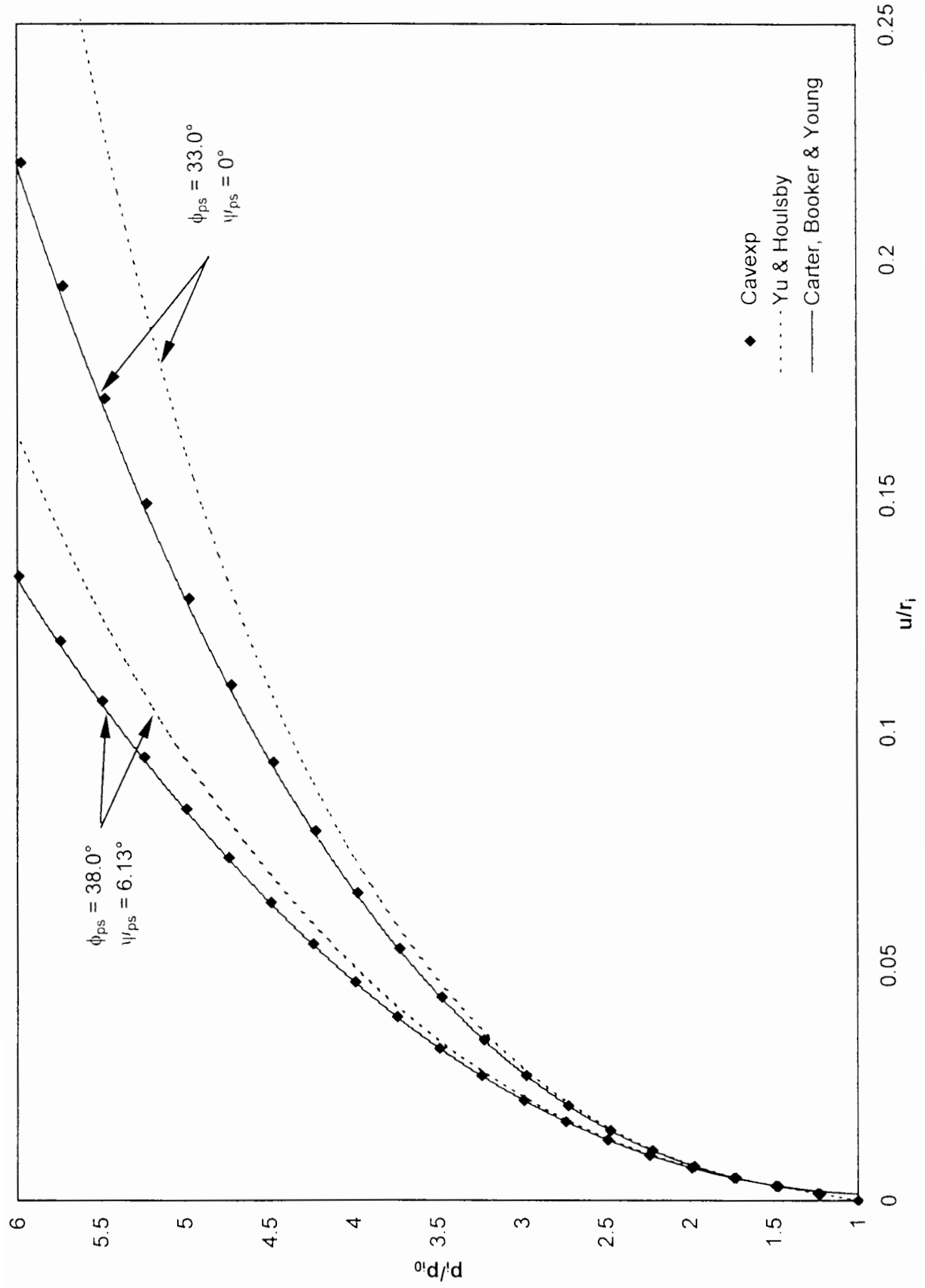

Figure 7.12 – Comparison of different analytical solutions with FE results for dilatant cavity expansion

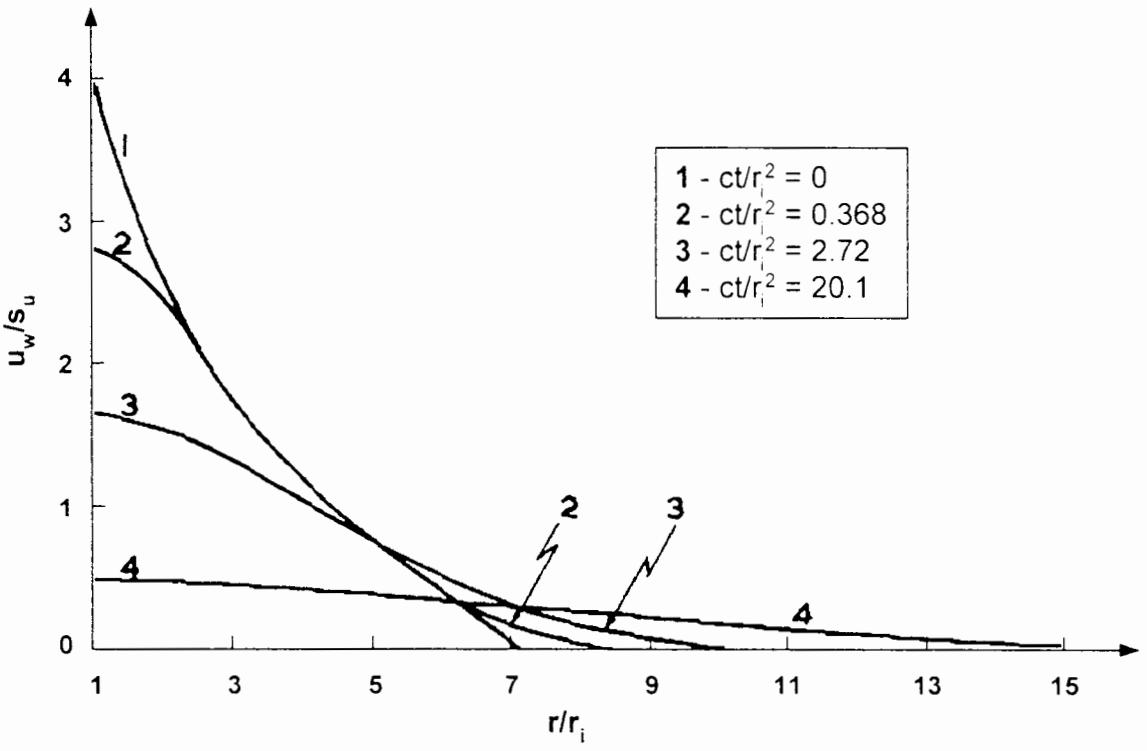

Figure 7.13 – Randolph and Wroth (1979a) solution for pore pressure dissipation following pile driving.

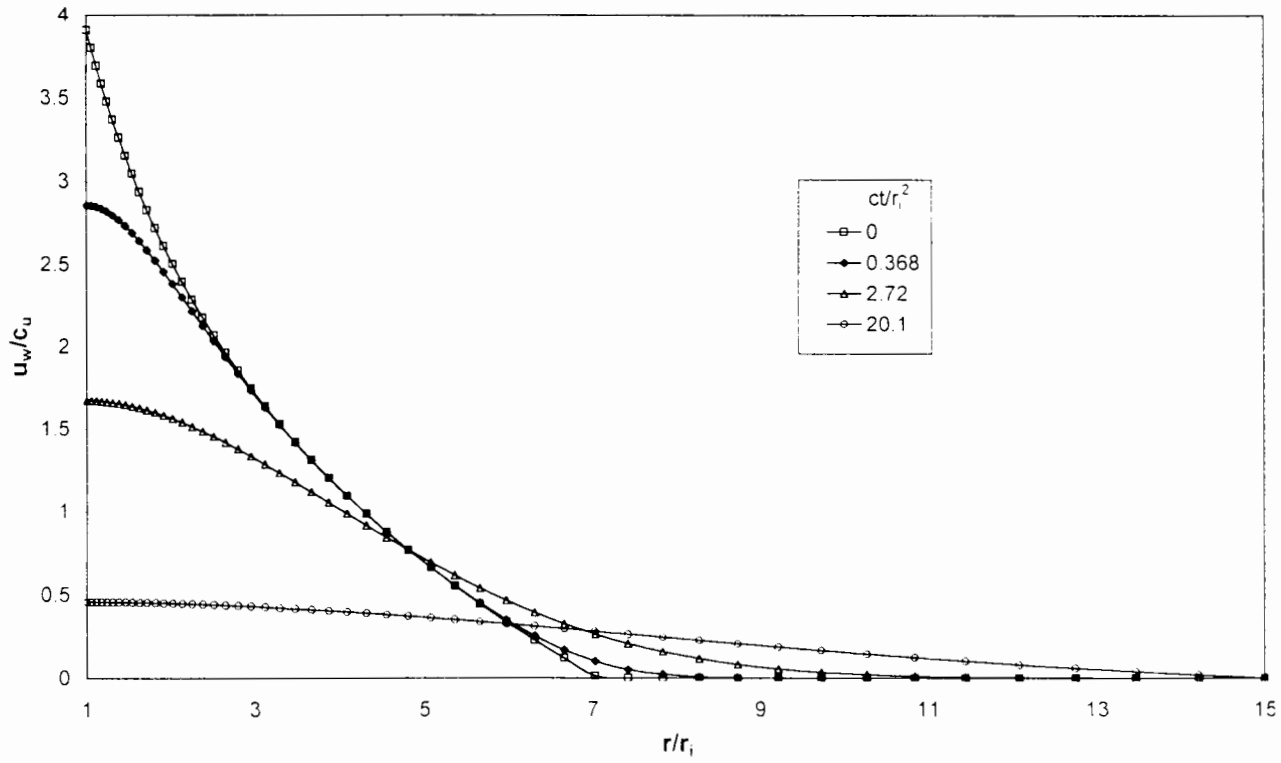

Figure 7.14 – FE results of analysis equivalent to Randolph and Wroth (1979a)

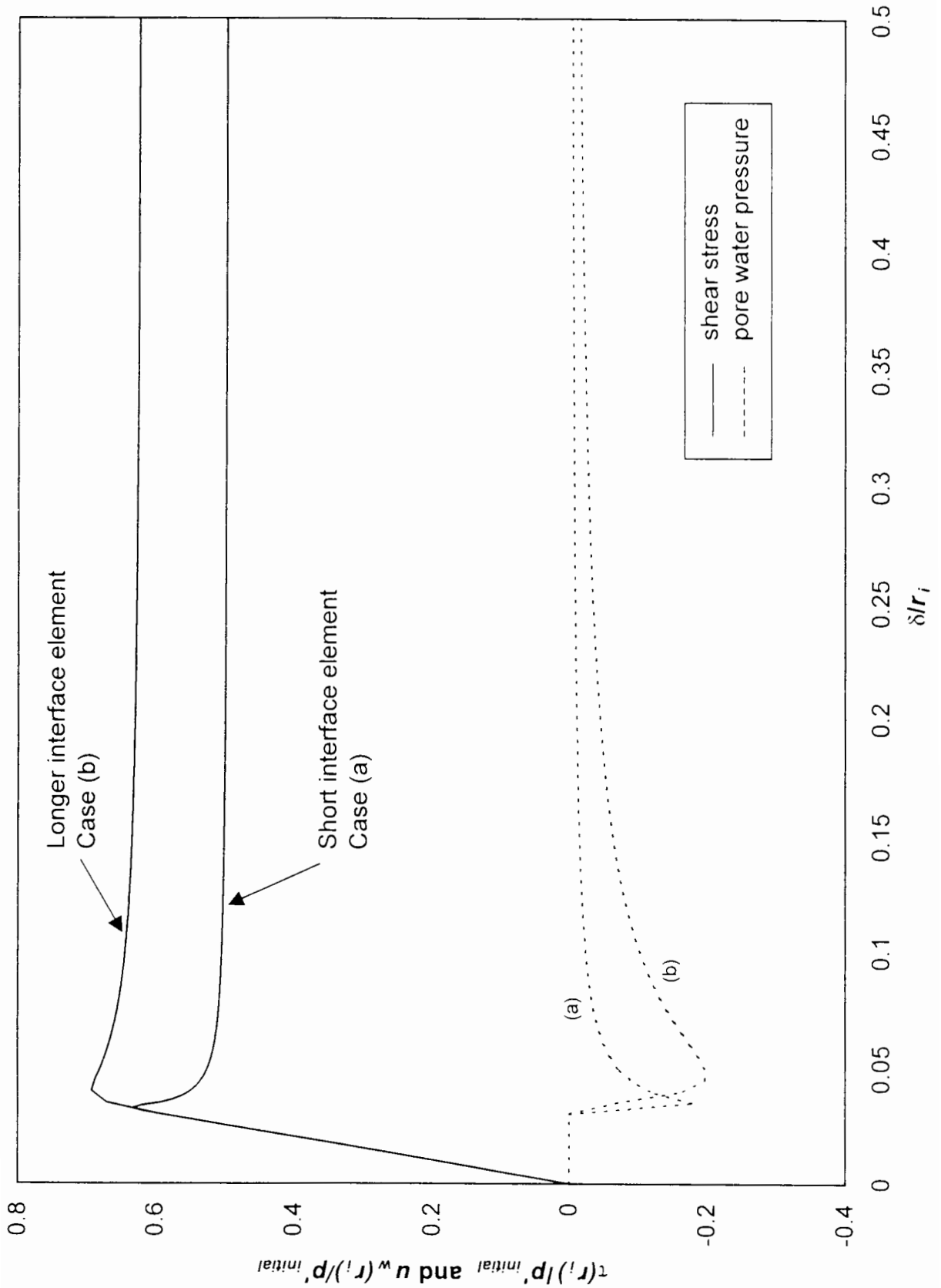

Figure 8.1 – Influence of first element length on FE pull-out analysis

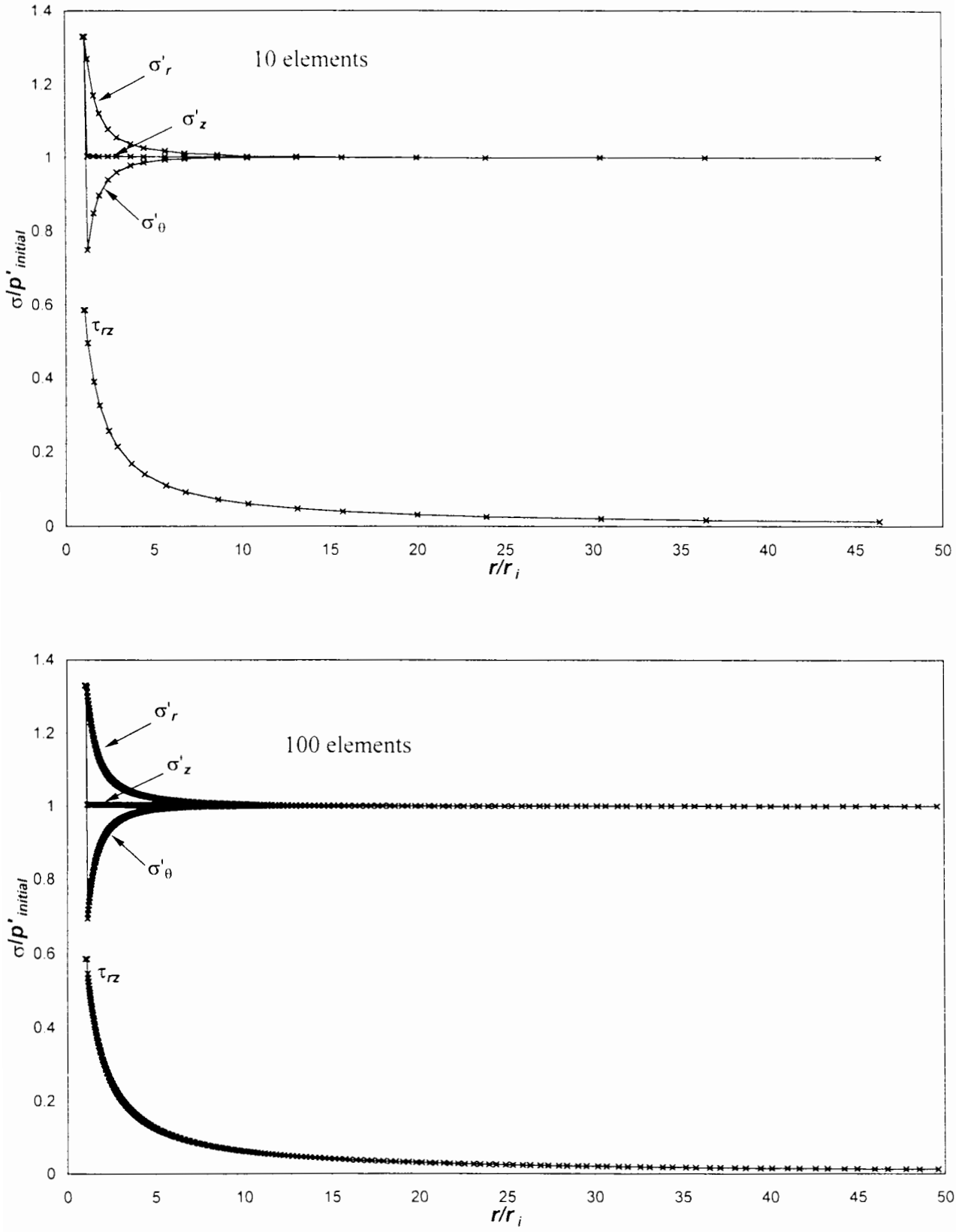

Figure 8.2 – Effective stress distributions following pull-out analyses using 10 and 100 elements

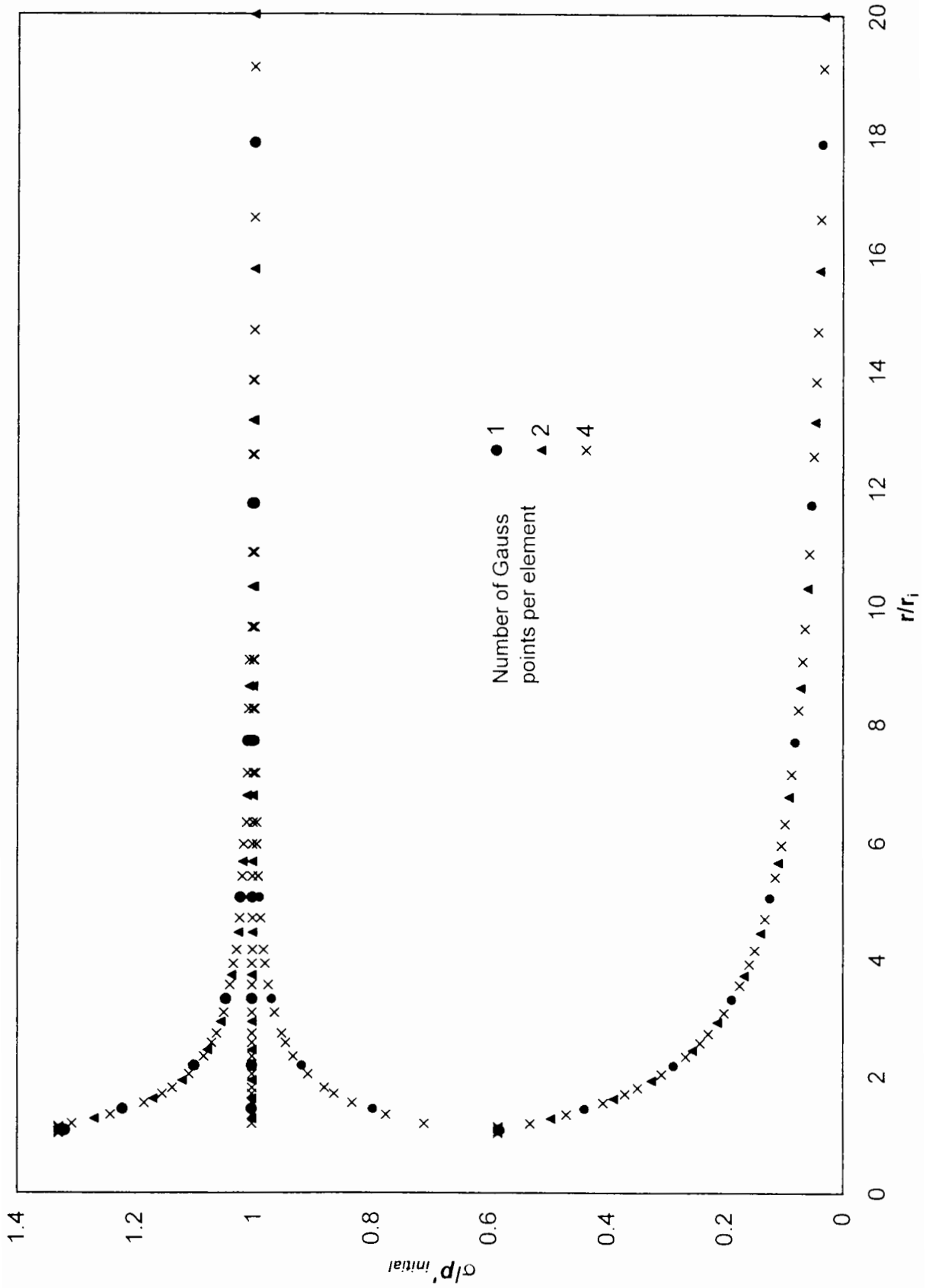

Figure 8.3 – Effective stress distributions following pull-out analyses using 1, 2, and 4 Gauss points per element (10 elements)

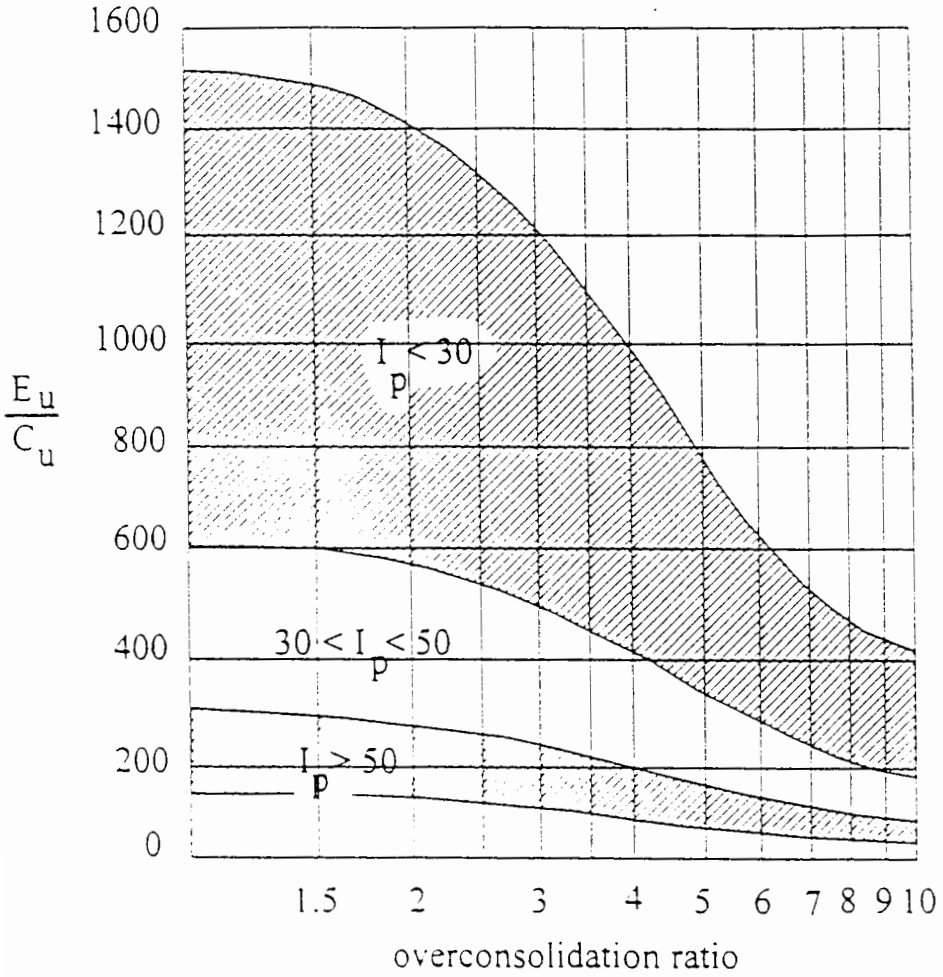

Figure 8.4 – Relationship between undrained elastic modulus and overconsolidation ratio, after Duncan and Buchignani (1976)

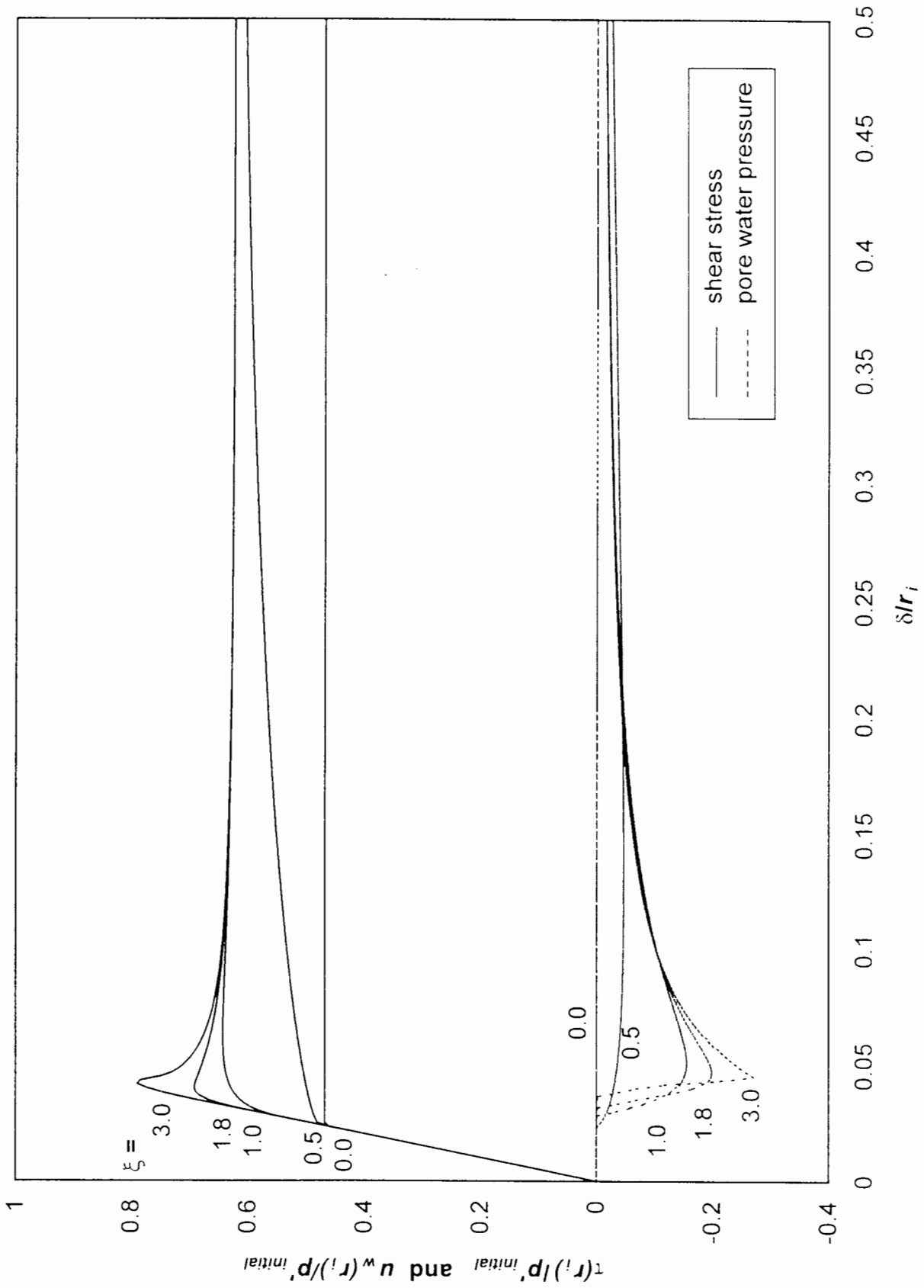

Figure 8.5 – Pull-out analysis results for ξ = 0, 0.5, 1, 1.8, 3

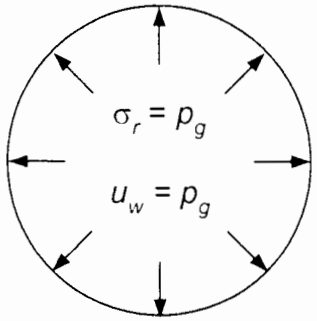

Stages 1 & 2
Grouting

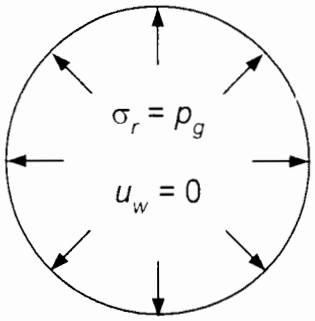

Stage 3
Setting

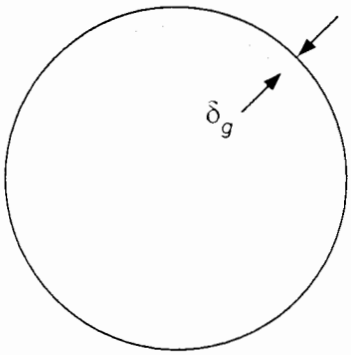

Stage 4
Curing / grout expansion

Figure 8.6 – Idealised installation sequence

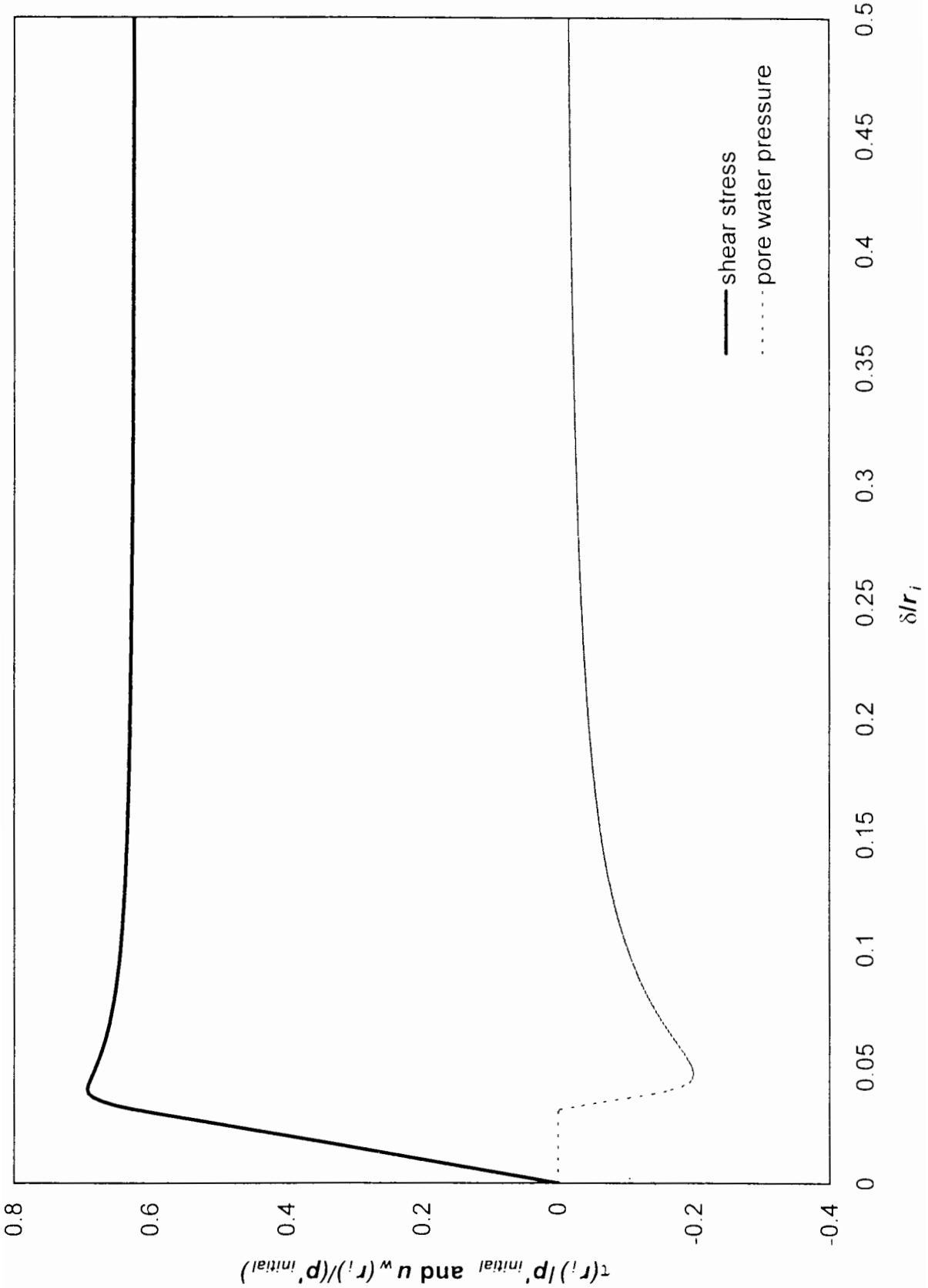

Figure 8.7(a) – Finite element analysis A1. Pull-out curve showing normalised shear stress and pore water pressure at the inner boundary

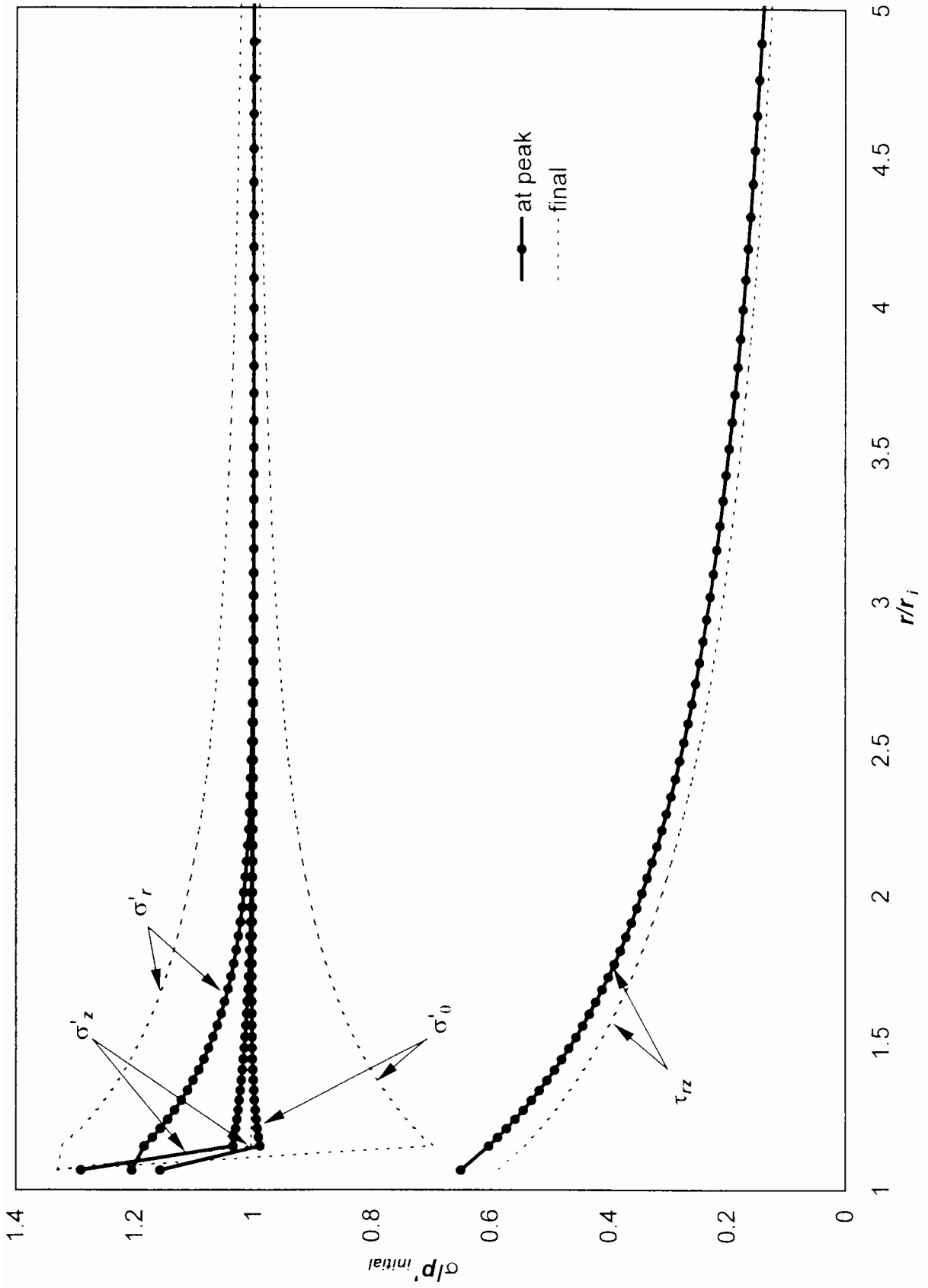

Figure 8.7(b) – Finite element analysis A1

Normalised effective stress distributions at peak and final conditions

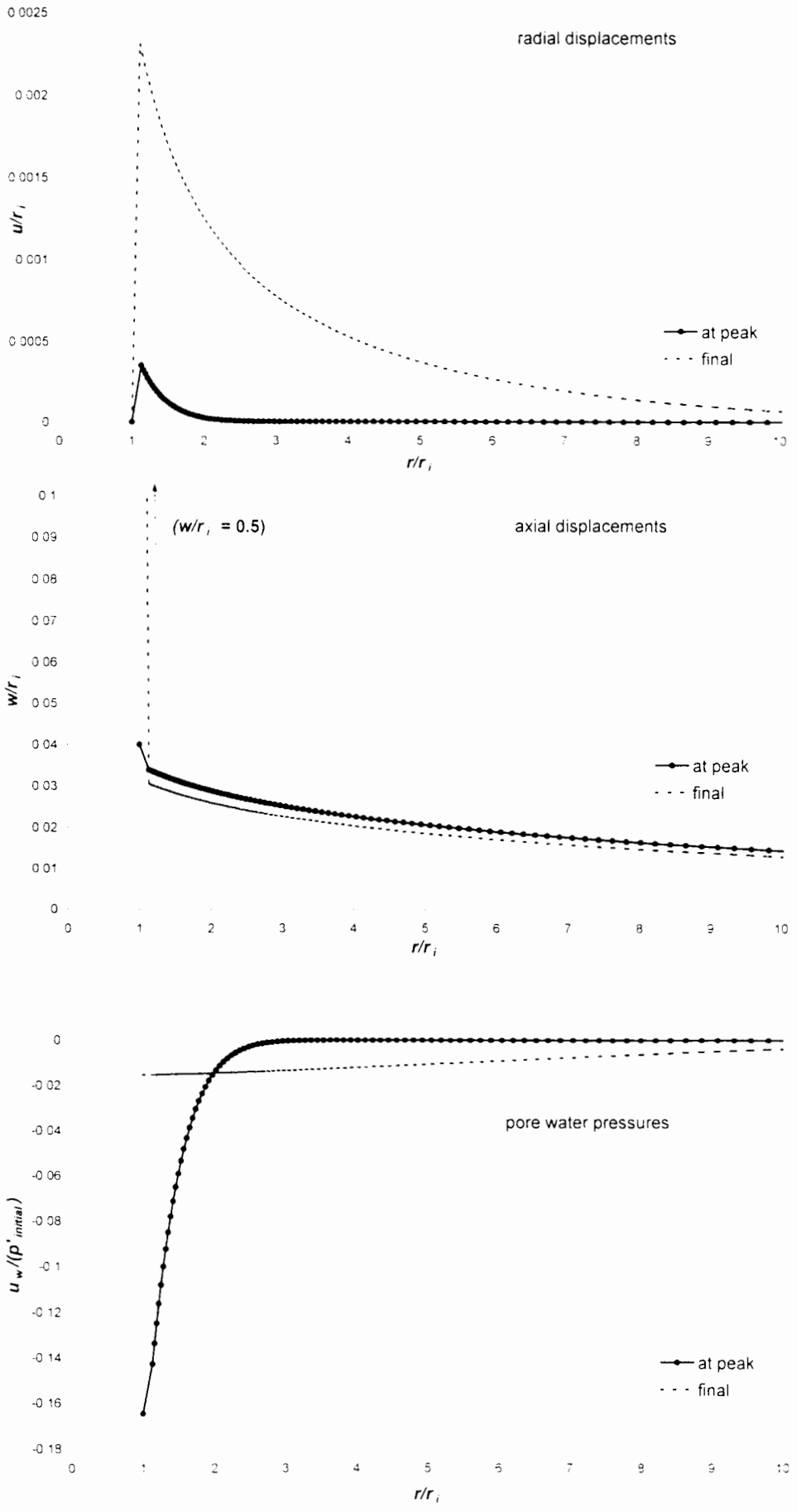

Figure 8.7(c) – Finite element analysis A1. Normalised displacement and pore water pressure distributions at peak and final conditions

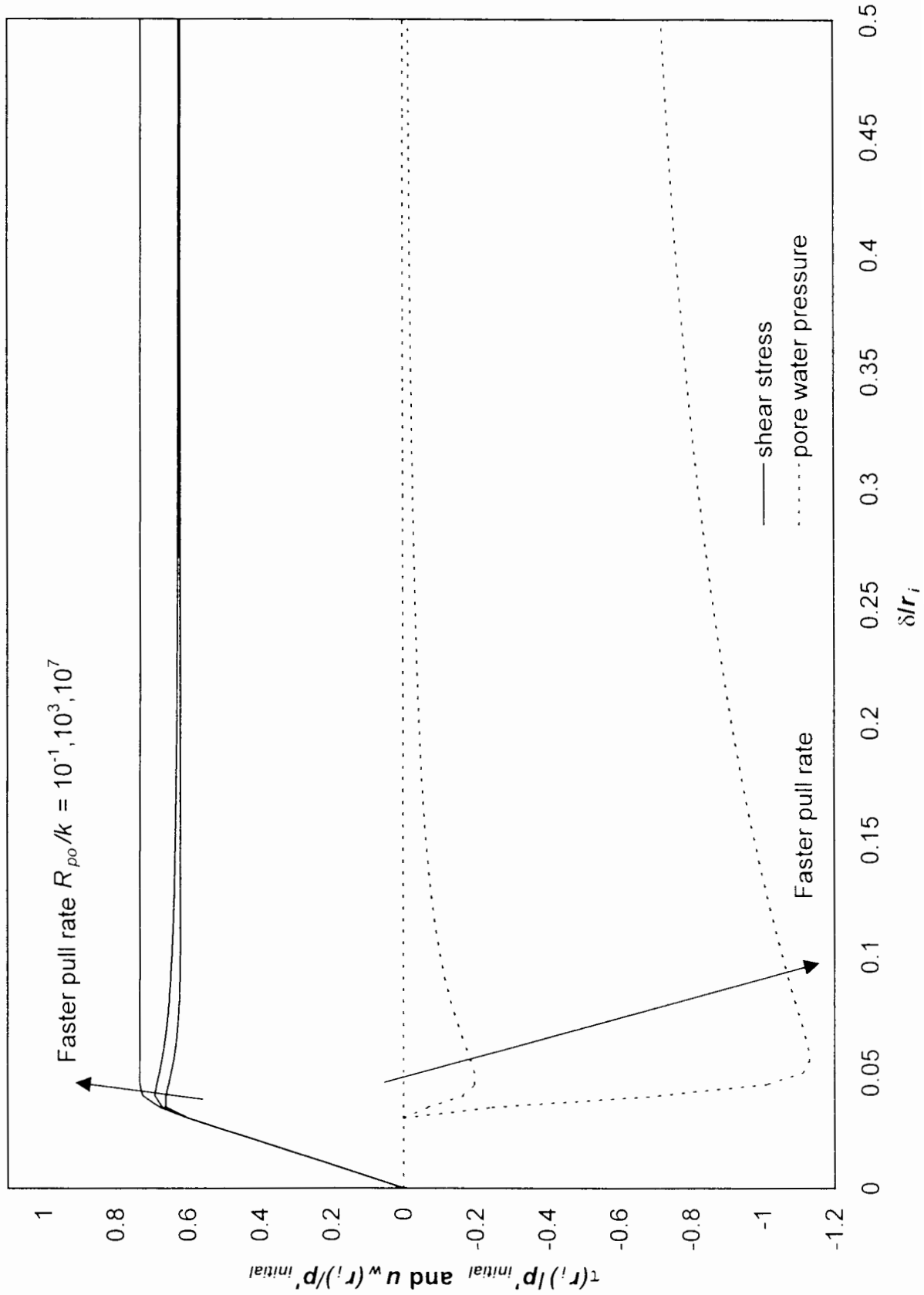

Figure 8.8 – Pull-out curves from finite element analyses at different pull rates

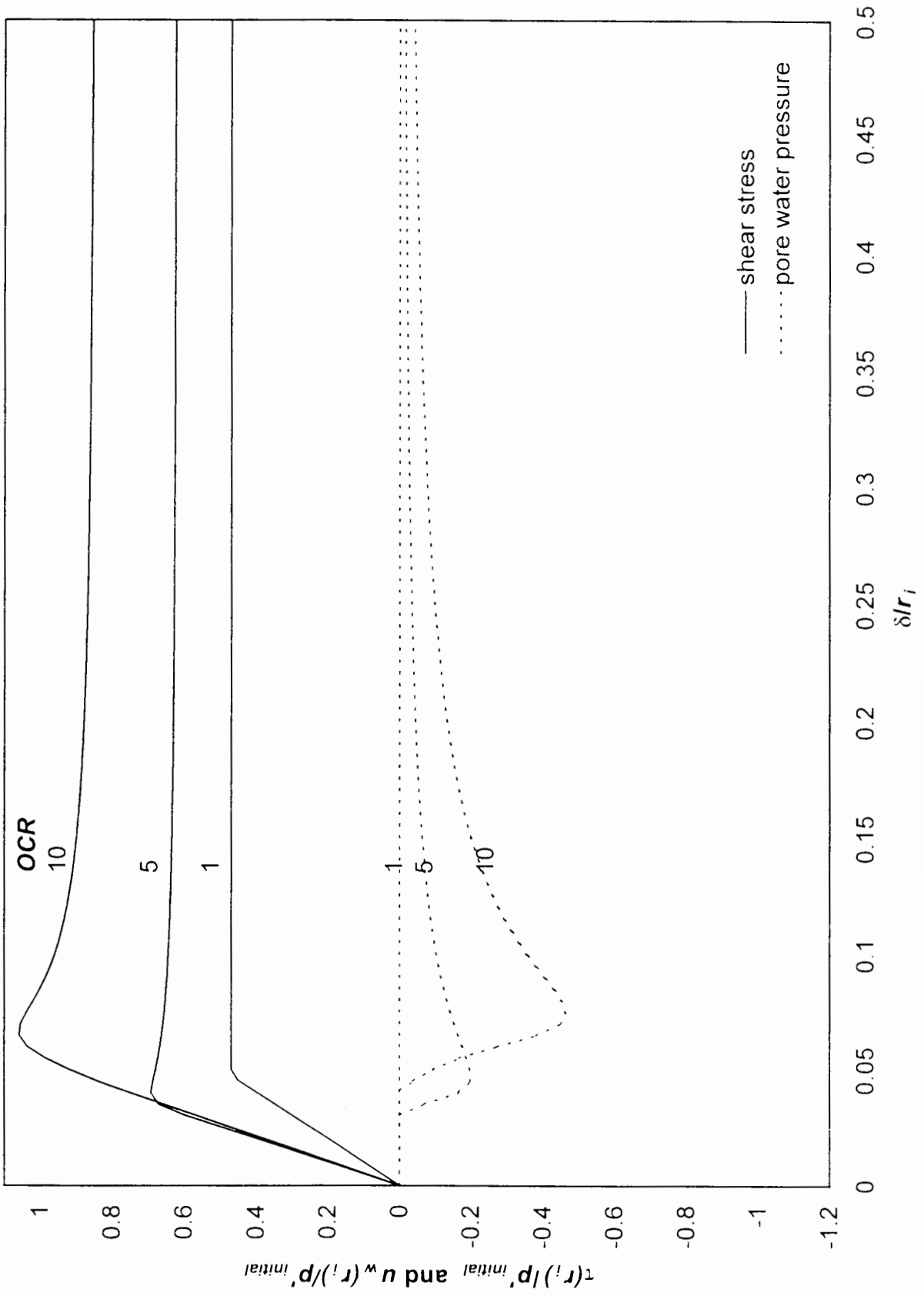

Figure 8.9 – Pull-out curves from finite element analyses at different *OCR*

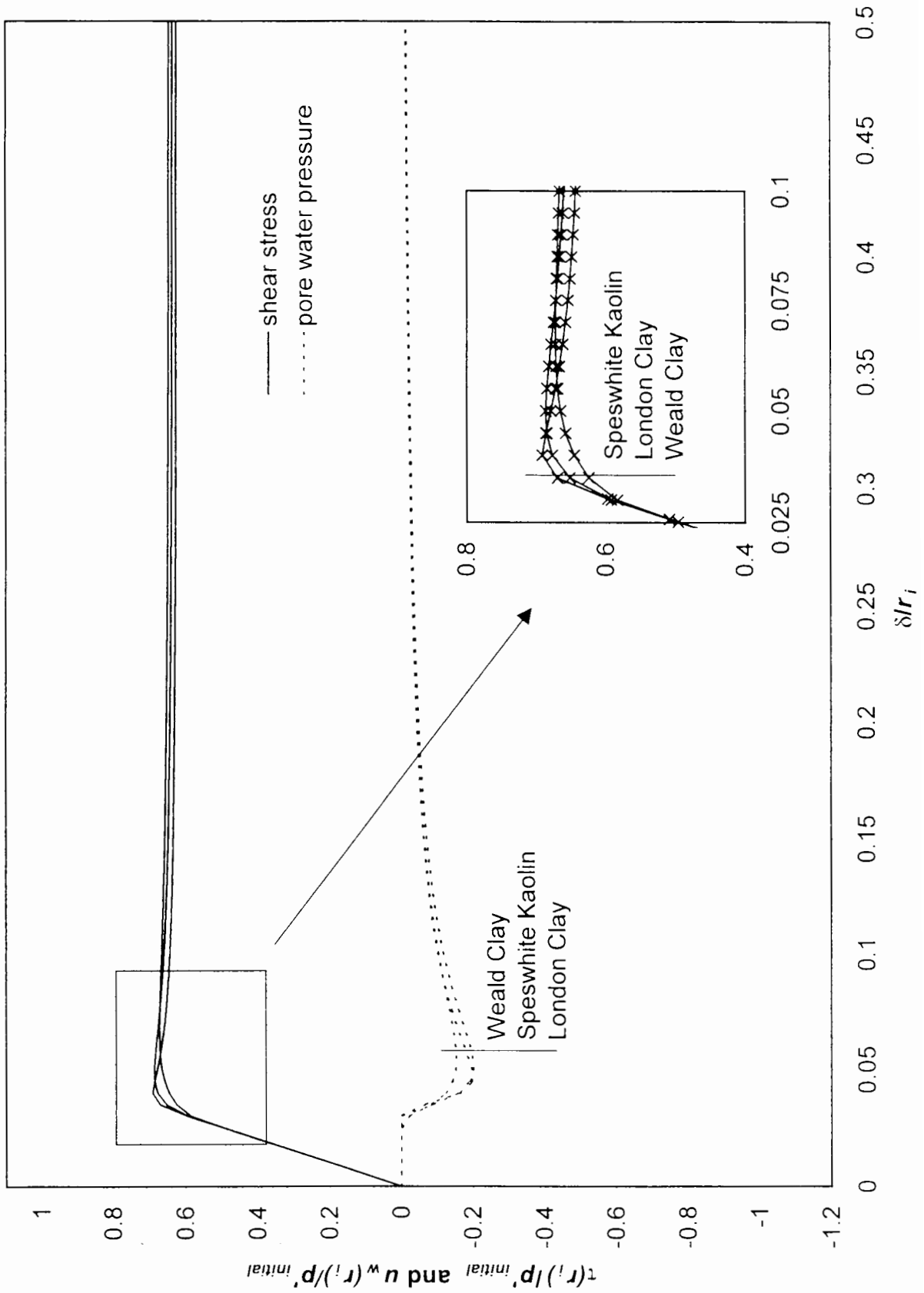

Figure 8.10 – Pull-out curves from finite element analyses performed using different material data sets

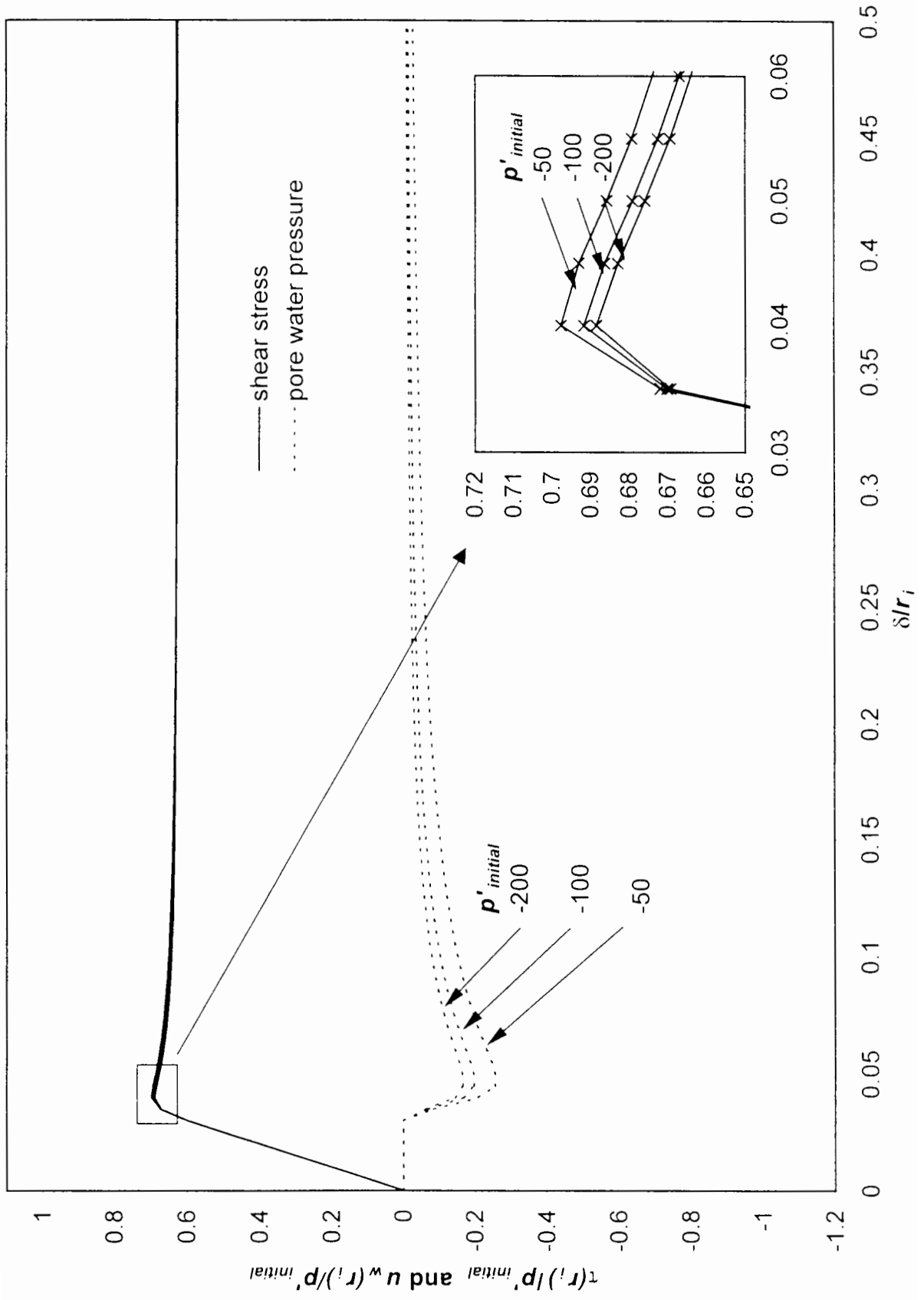

Figure 8.11 – Pull-out curves from finite element analyses at different initial stresses

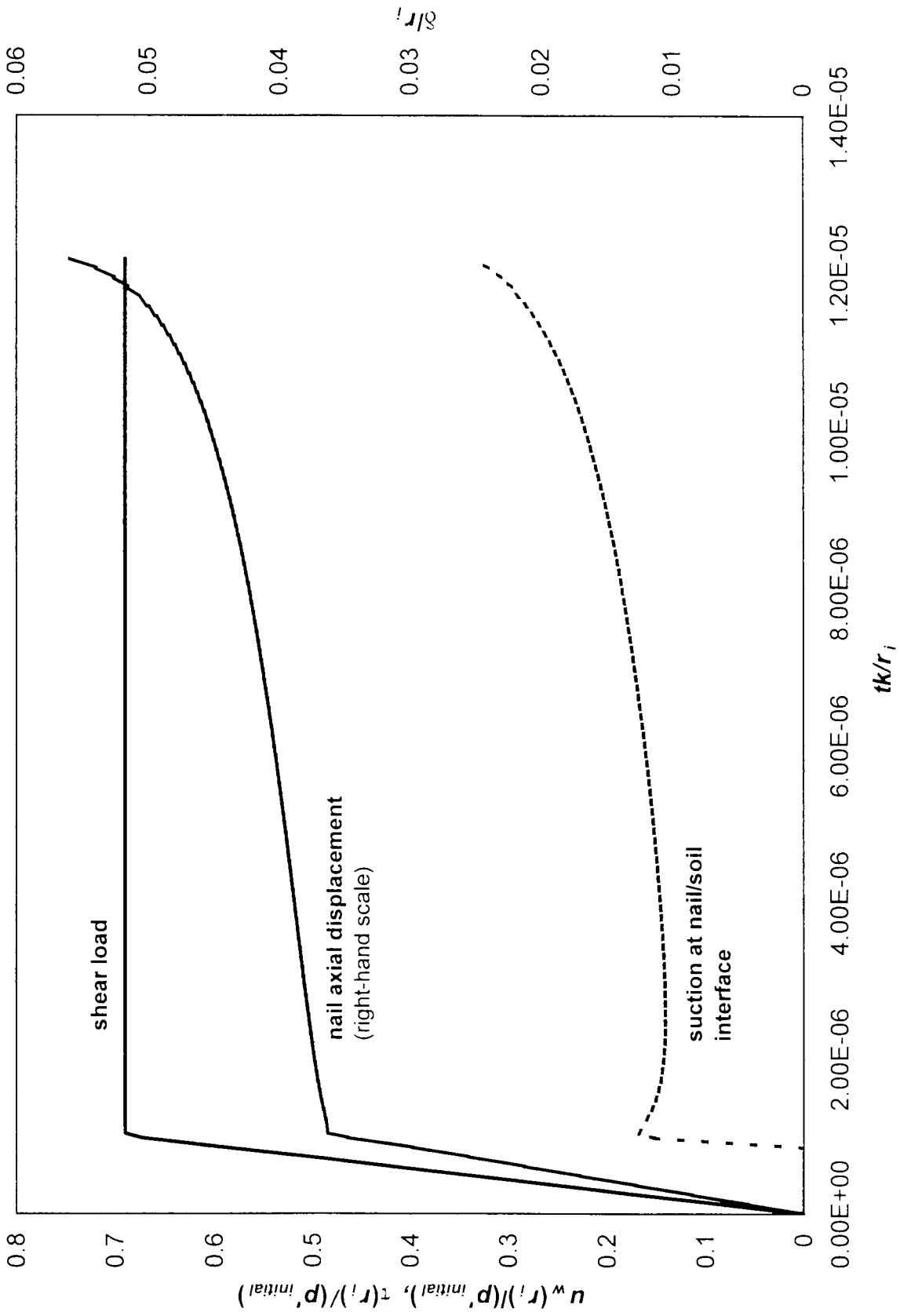

Figure 8.12 – Results from sustained loading finite element analysis B3

(NB pore water suctions shown as positive)

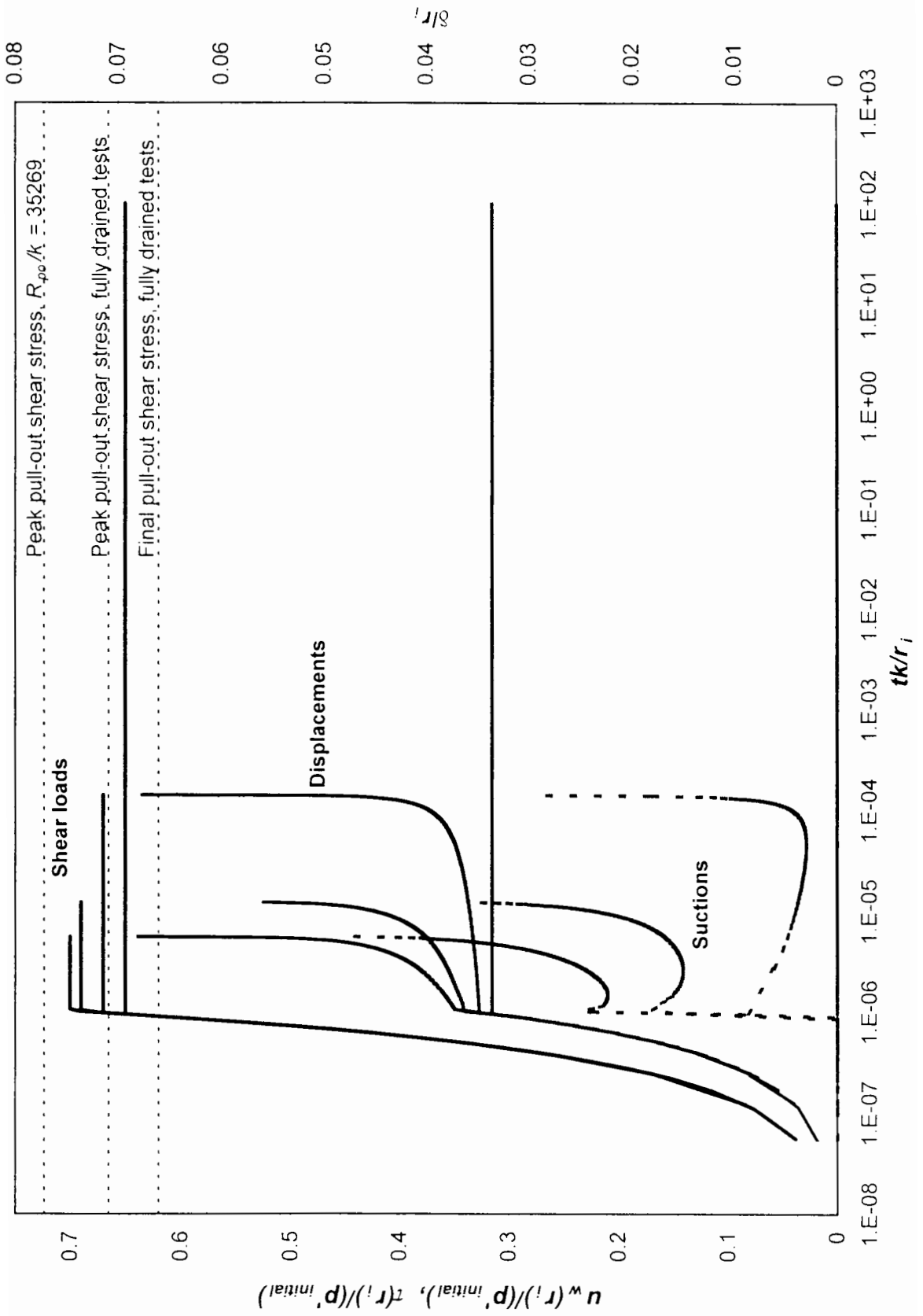

Figure 8.13 – Comparison of results from sustained loading finite element analyses B1-B5 (NB pore water suctions shown as positive)

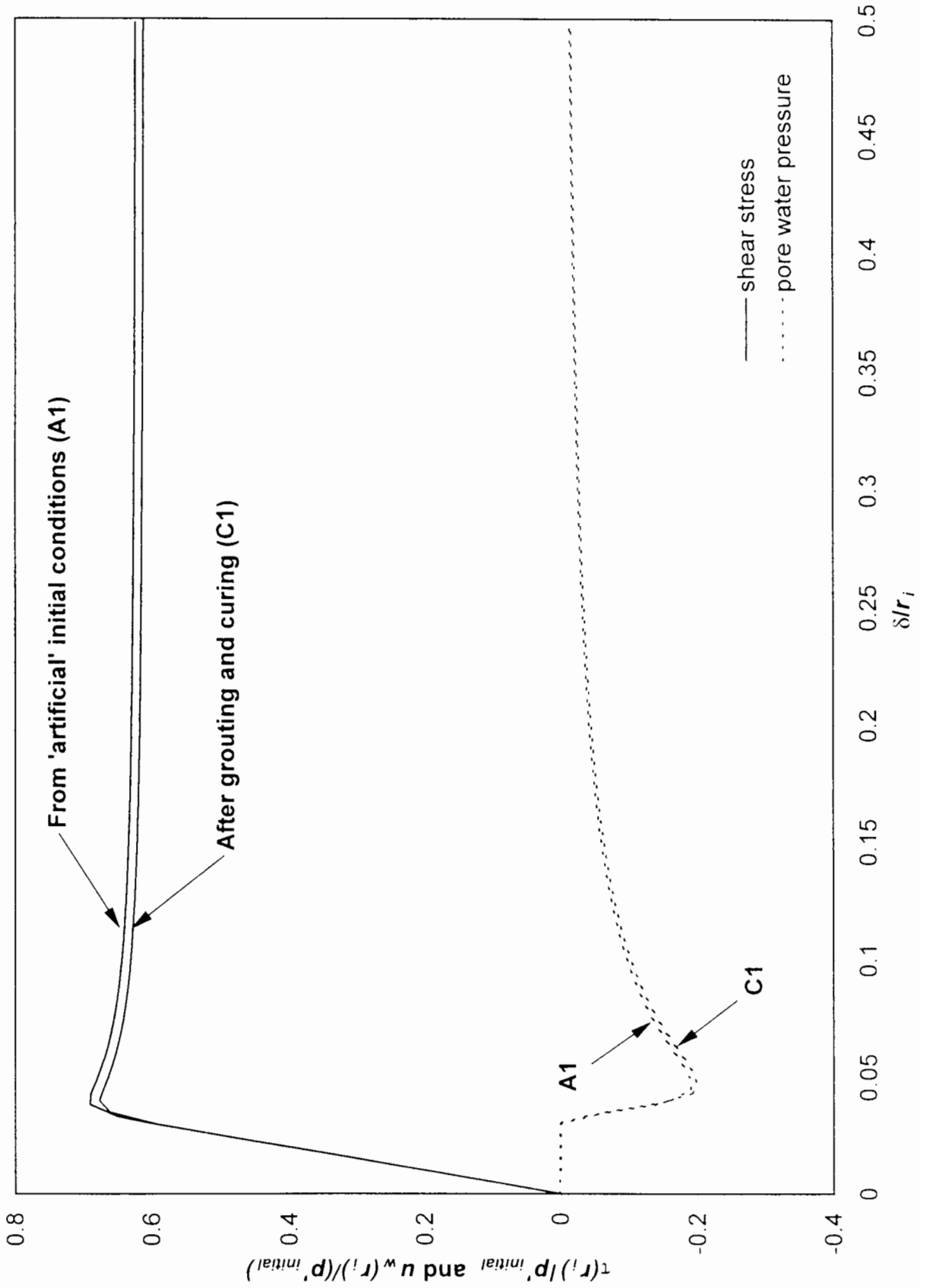

Figure 8.14 – Comparison of results from finite element analyses A1 and C1

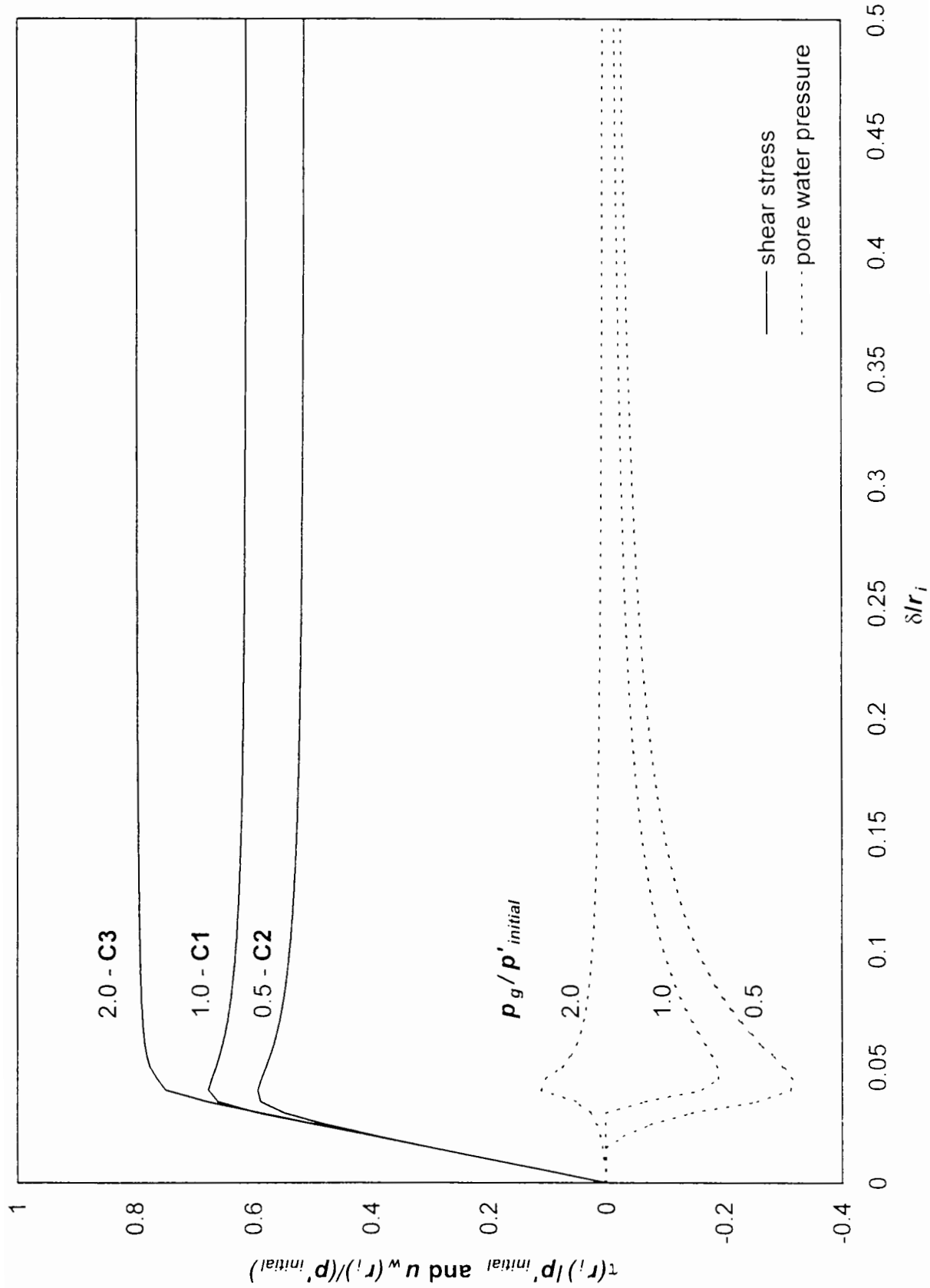

Figure 8.15 – Effect of grouting pressure on finite element analysis prediction of pull-out response

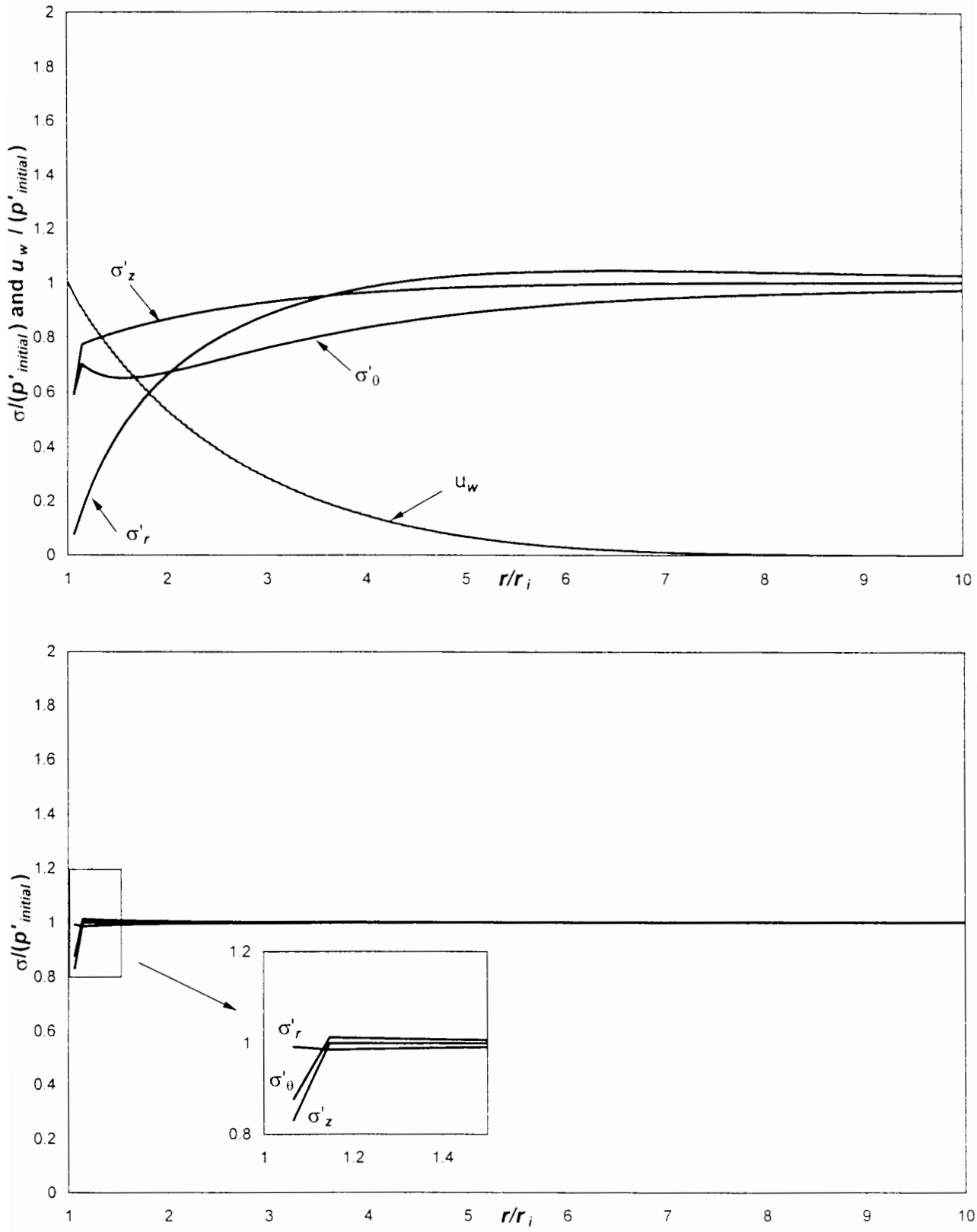

Figure 8.16 – Effective stress distributions during grouting to overburden (top) and after curing (bottom) for finite element analysis C1

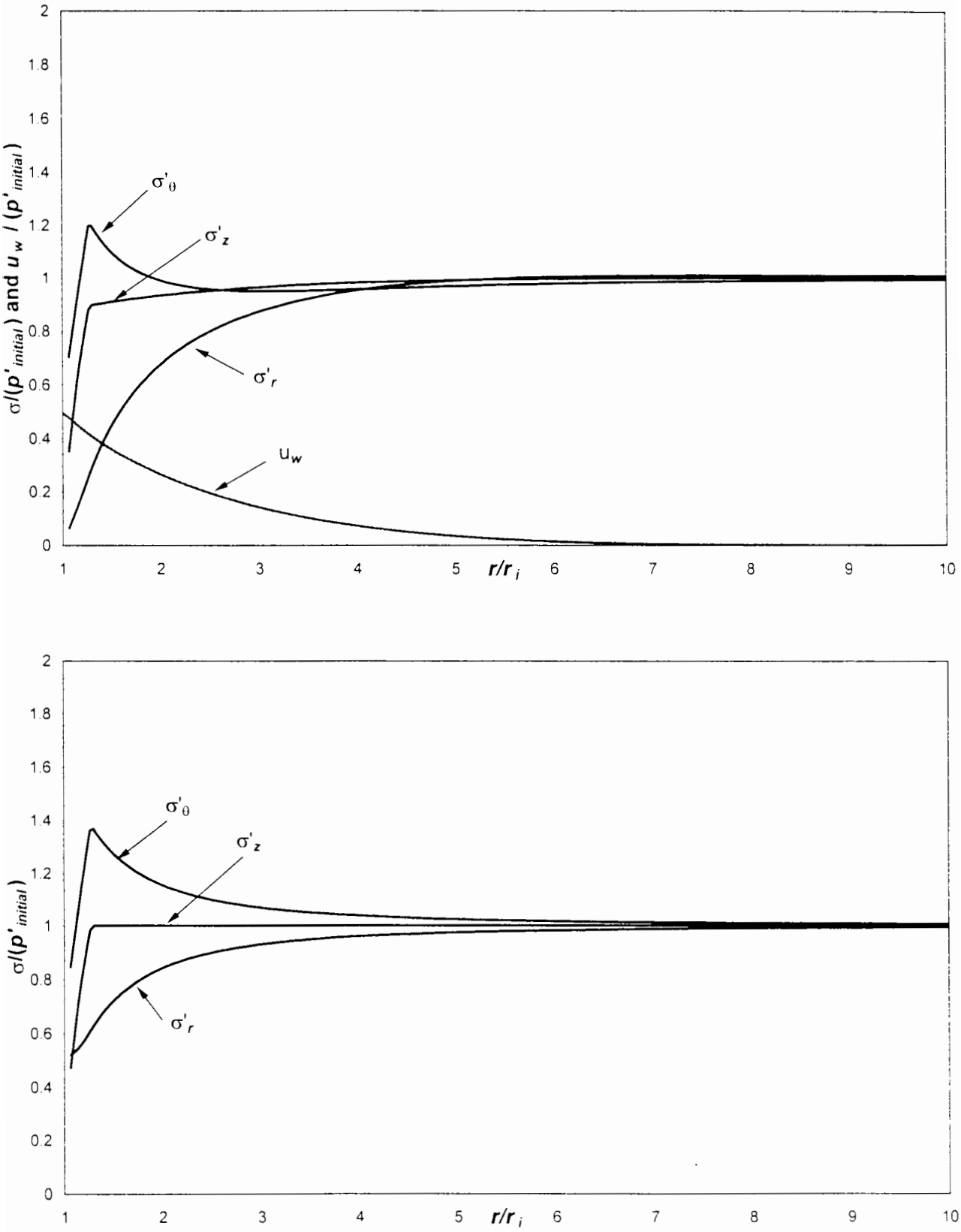

Figure 8.17 – Effective stress distributions during grouting to a level of half the overburden (top) and after curing (bottom) for finite element analysis C2

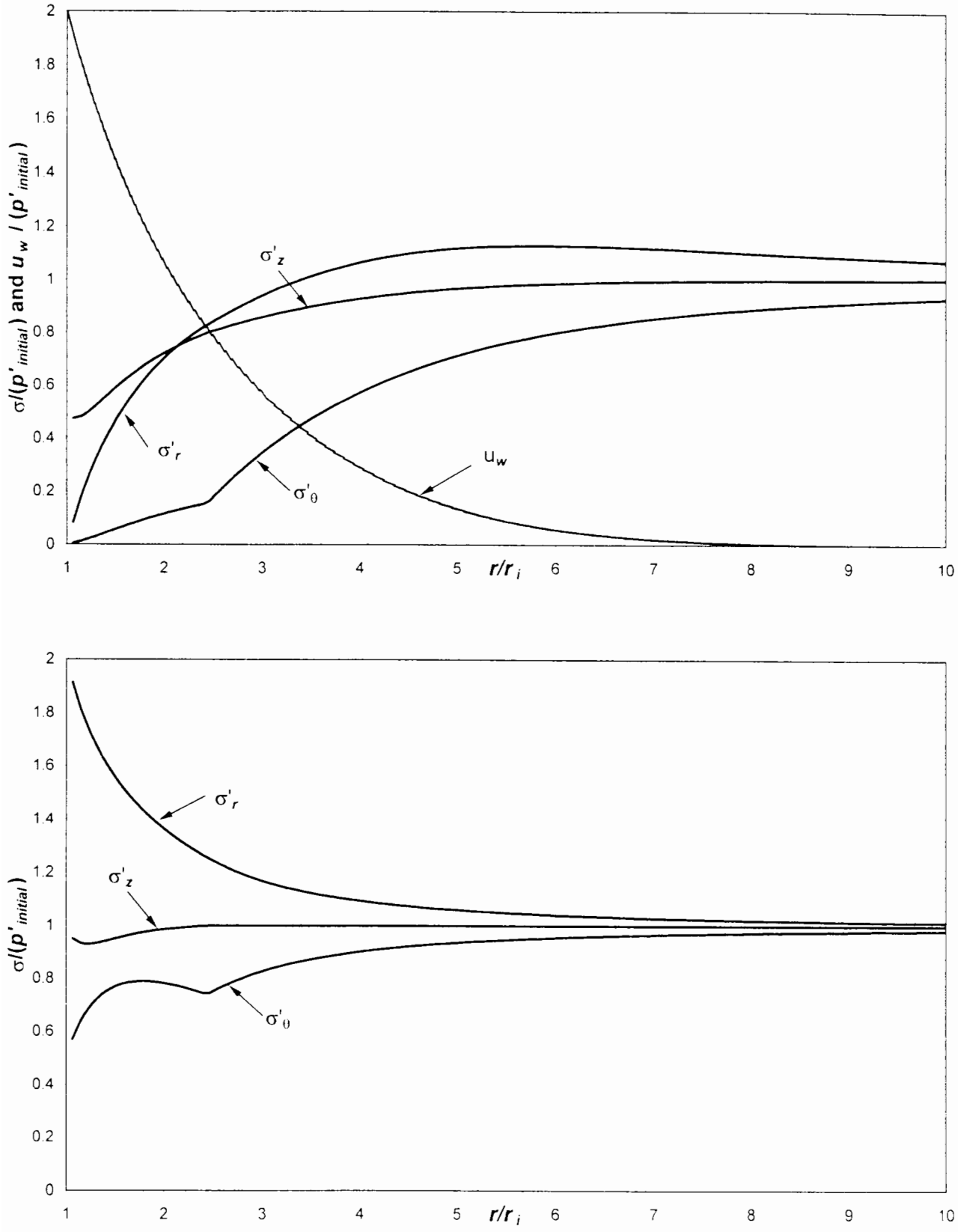

Figure 8.18 – Effective stress distributions during grouting to a level of twice the overburden (top) and after curing (bottom) for finite element analysis C3

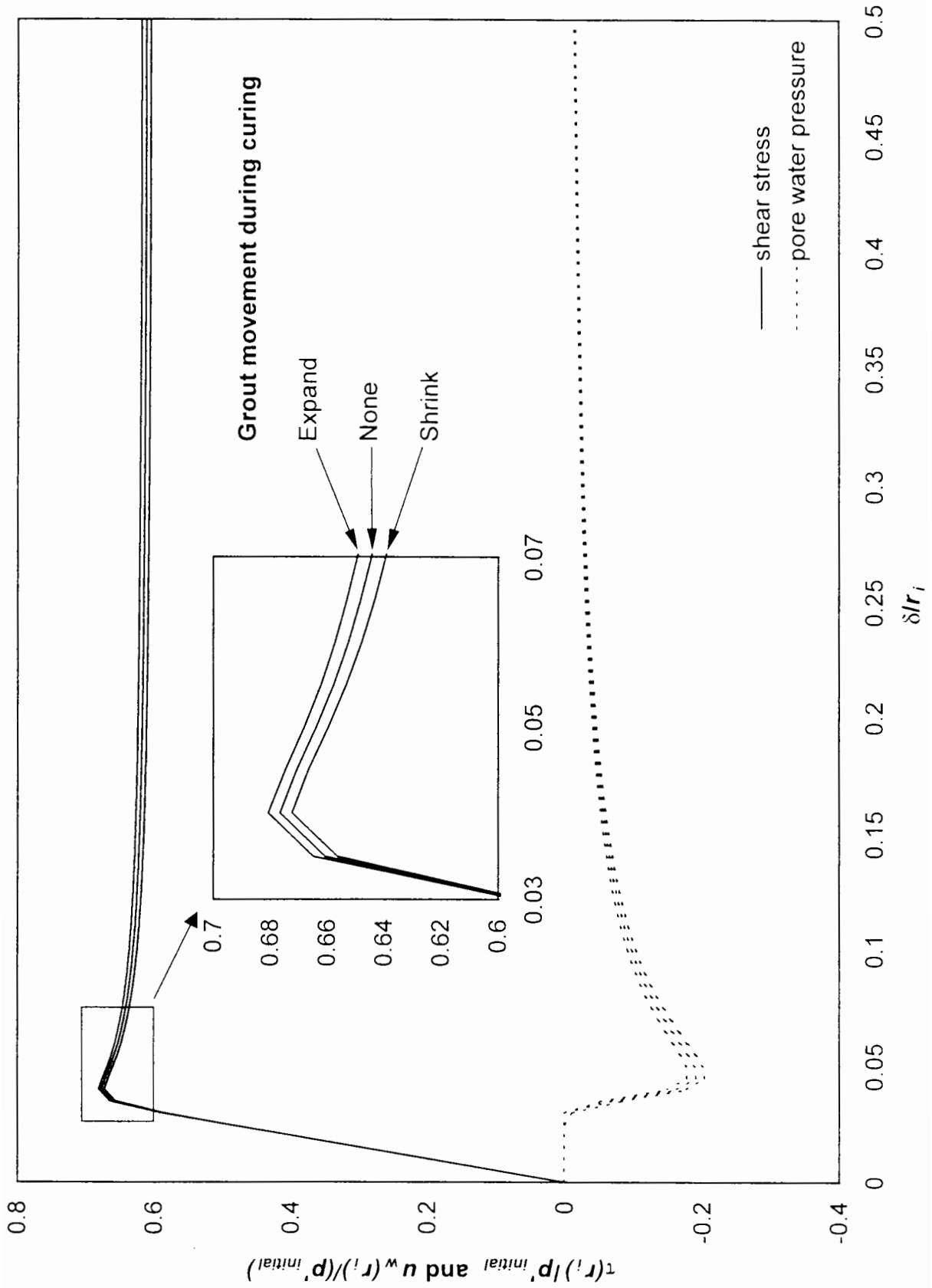

Figure 8.19 – Effect of grout curing movements on finite element analysis prediction of pull-out response

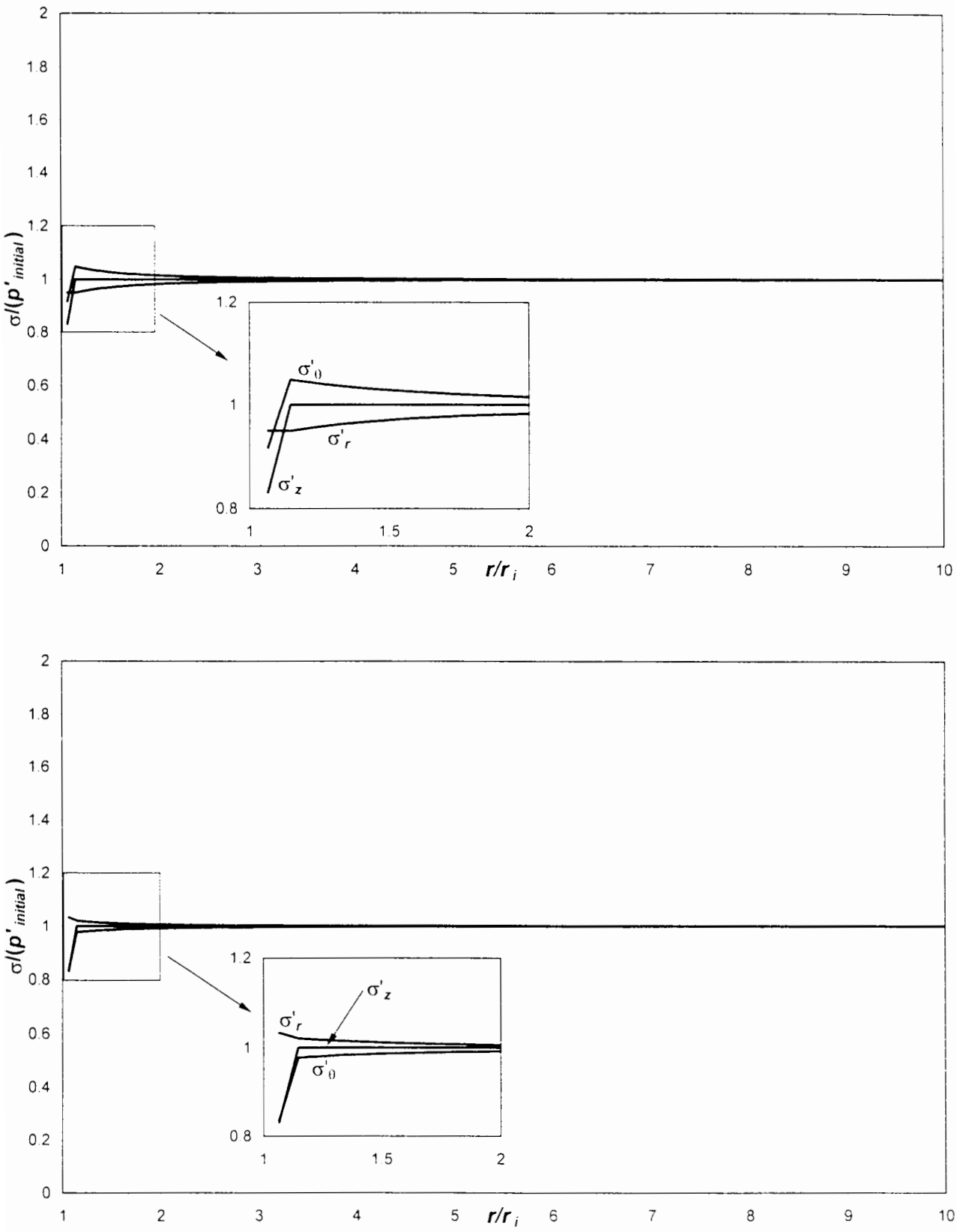

Figure 8.20 – Effective stress distributions after curing of shrinking grout (top) and expanding grout (bottom) for finite element analyses C4 and C5

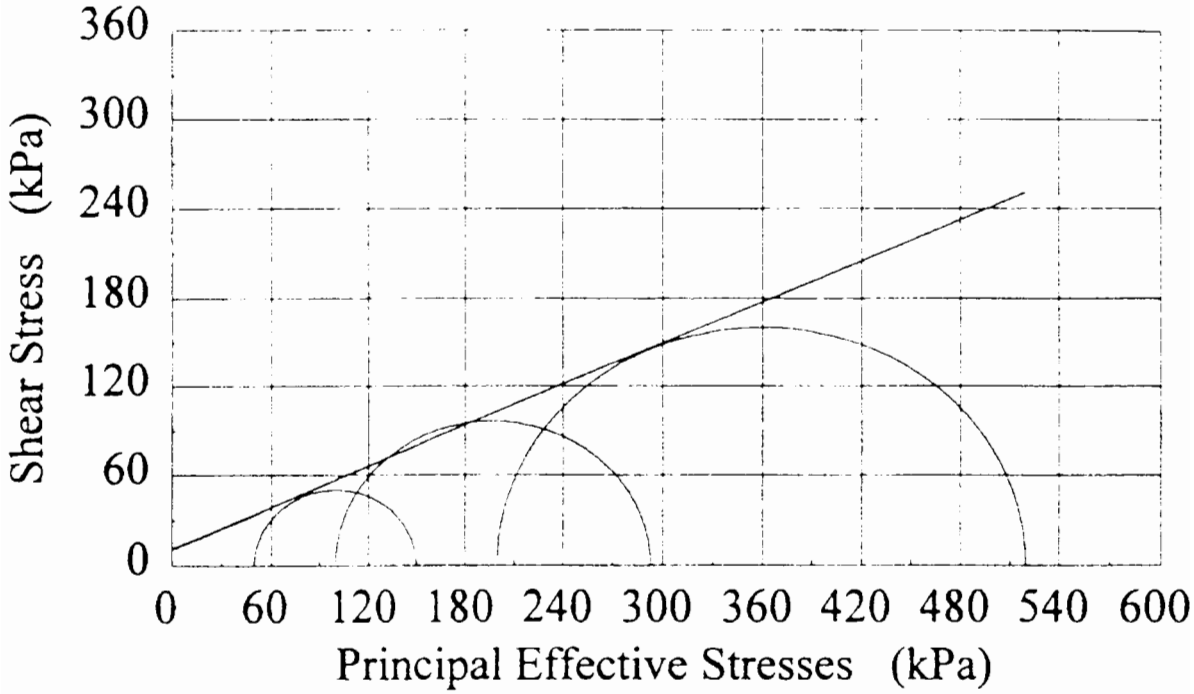

Figure 9.1 – Results from consolidated-drained triaxial tests

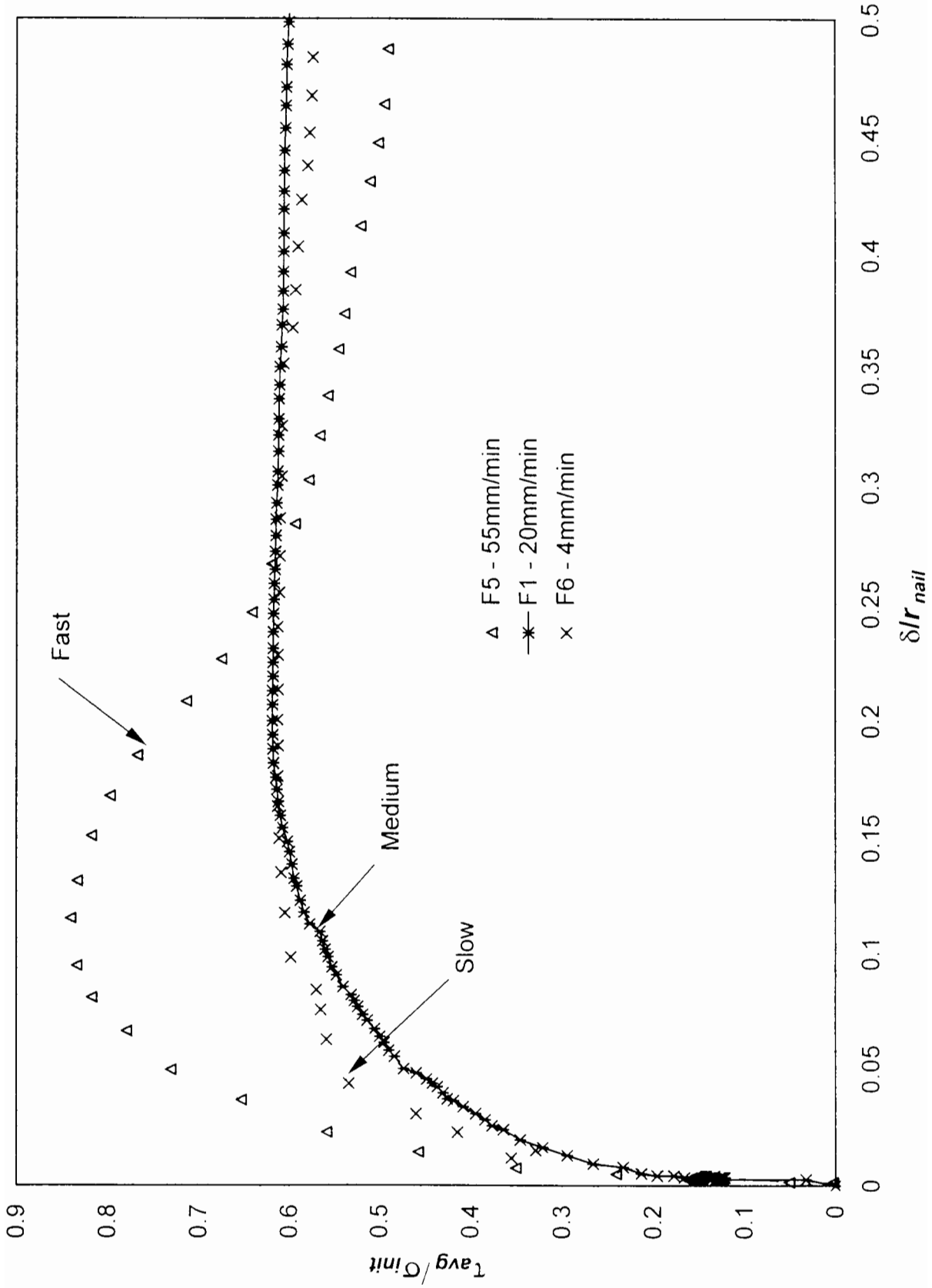

Figure 9.2 – Dimensionless shear stress versus displacement curve for pull-out tests performed at different pull rates

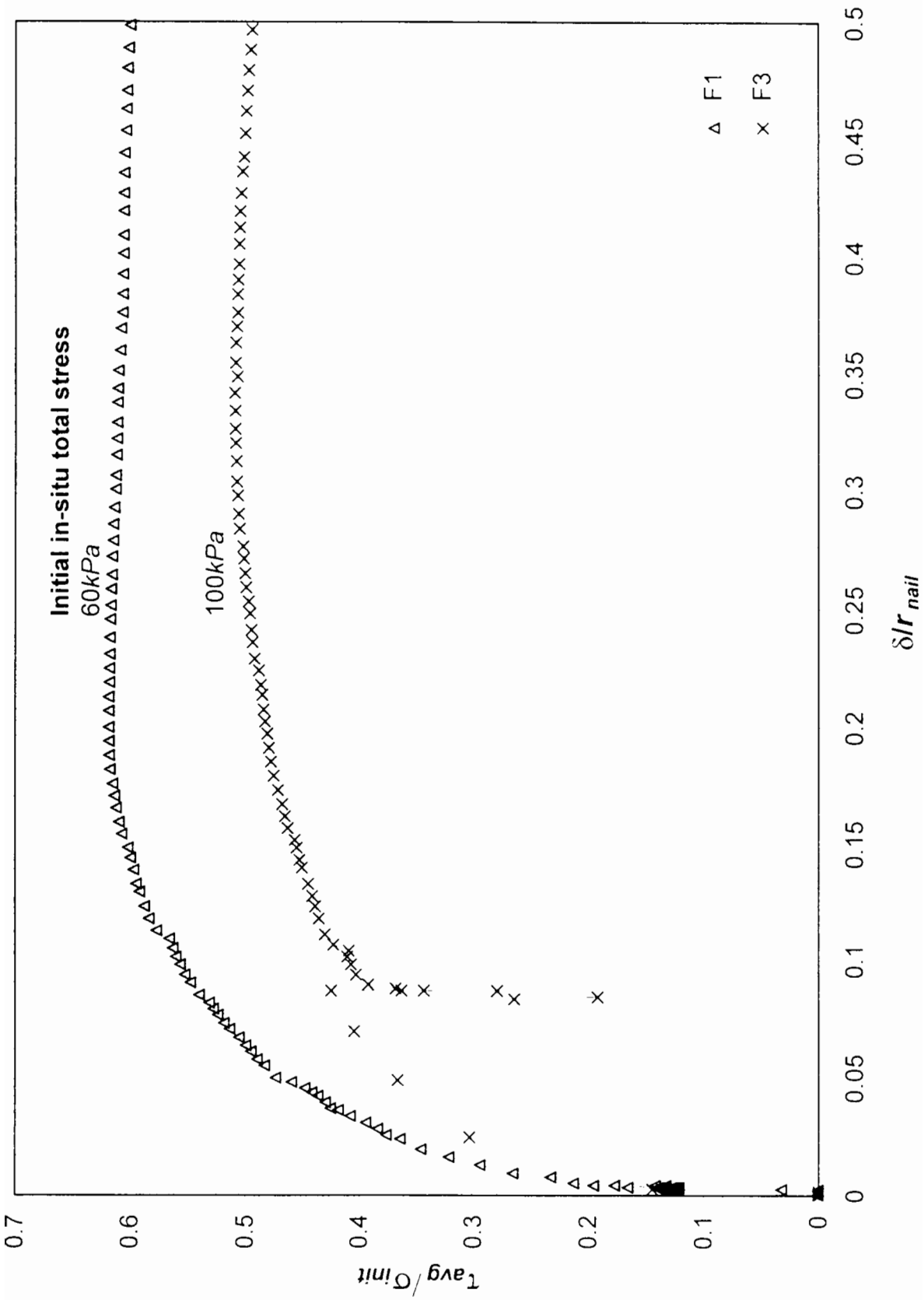

Figure 9.3 - Dimensionless shear stress versus displacement curve for pull-out tests performed at different in-situ stresses

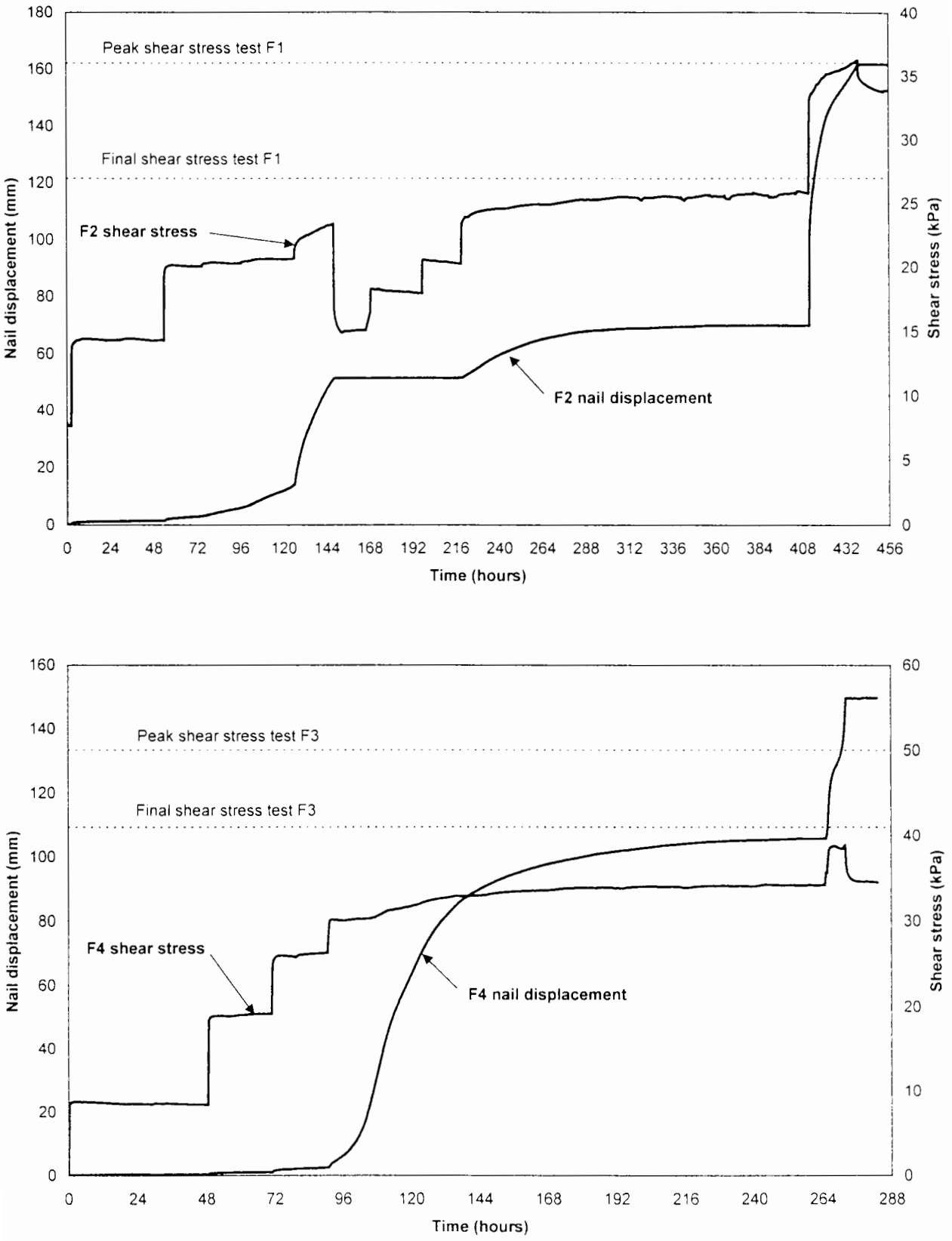

Figure 9.4 – Comparison of sustained loading and pull-out test results

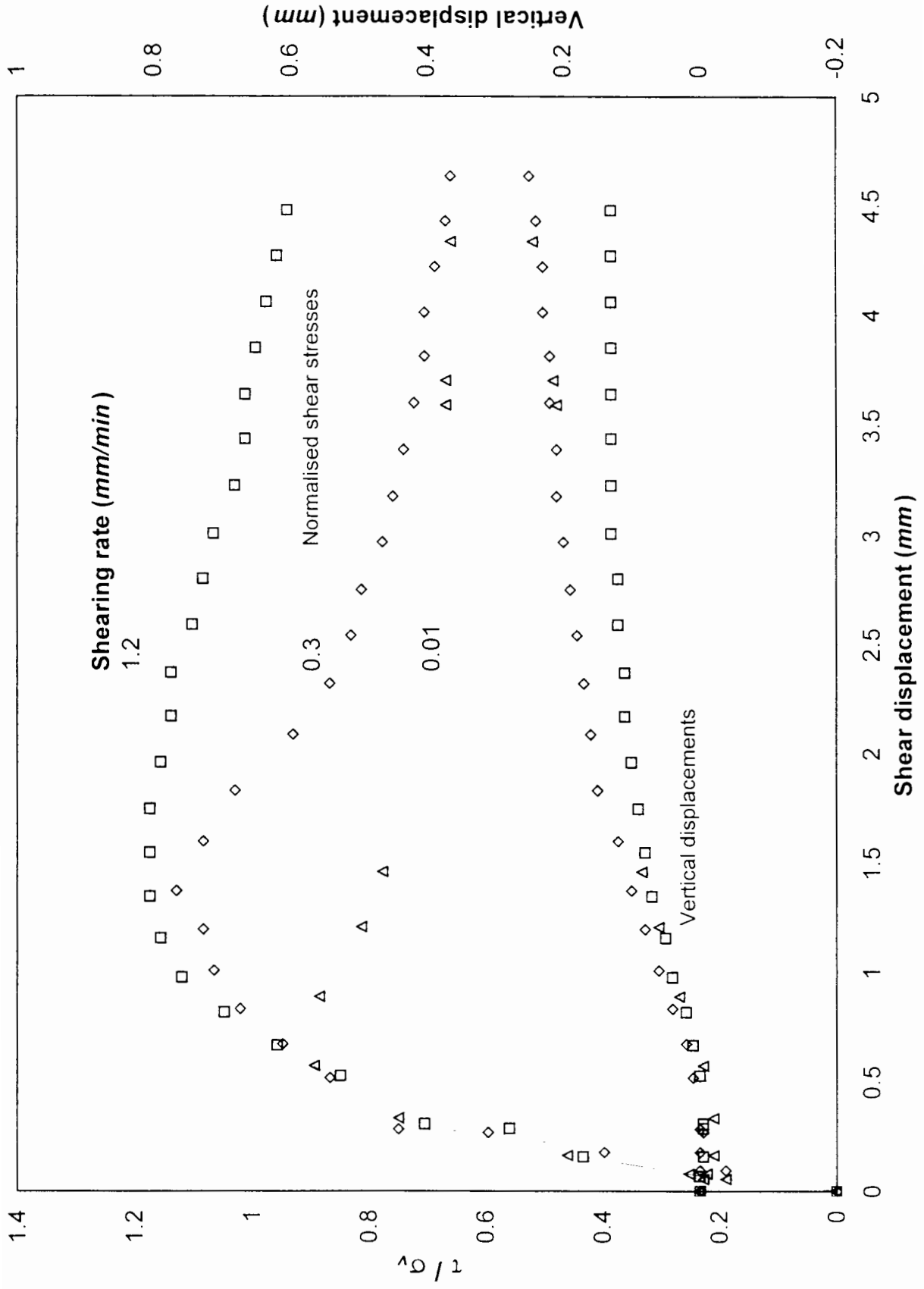

Figure 9.5 – Shear stress versus displacement curve

for interface tests performed at different displacement rates

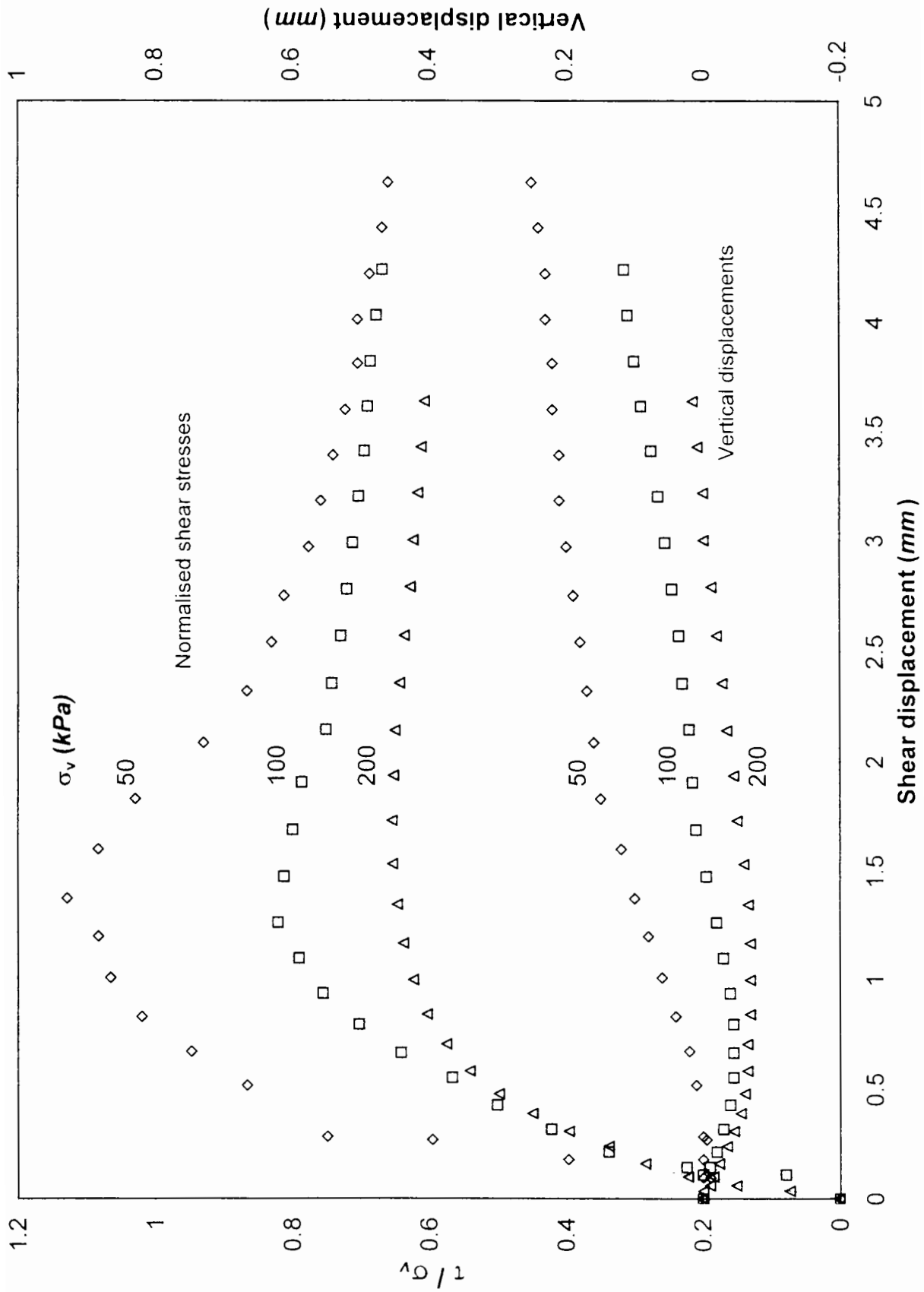

Figure 9.6 – Shear stress versus displacement curve for interface tests performed at different vertical stresses

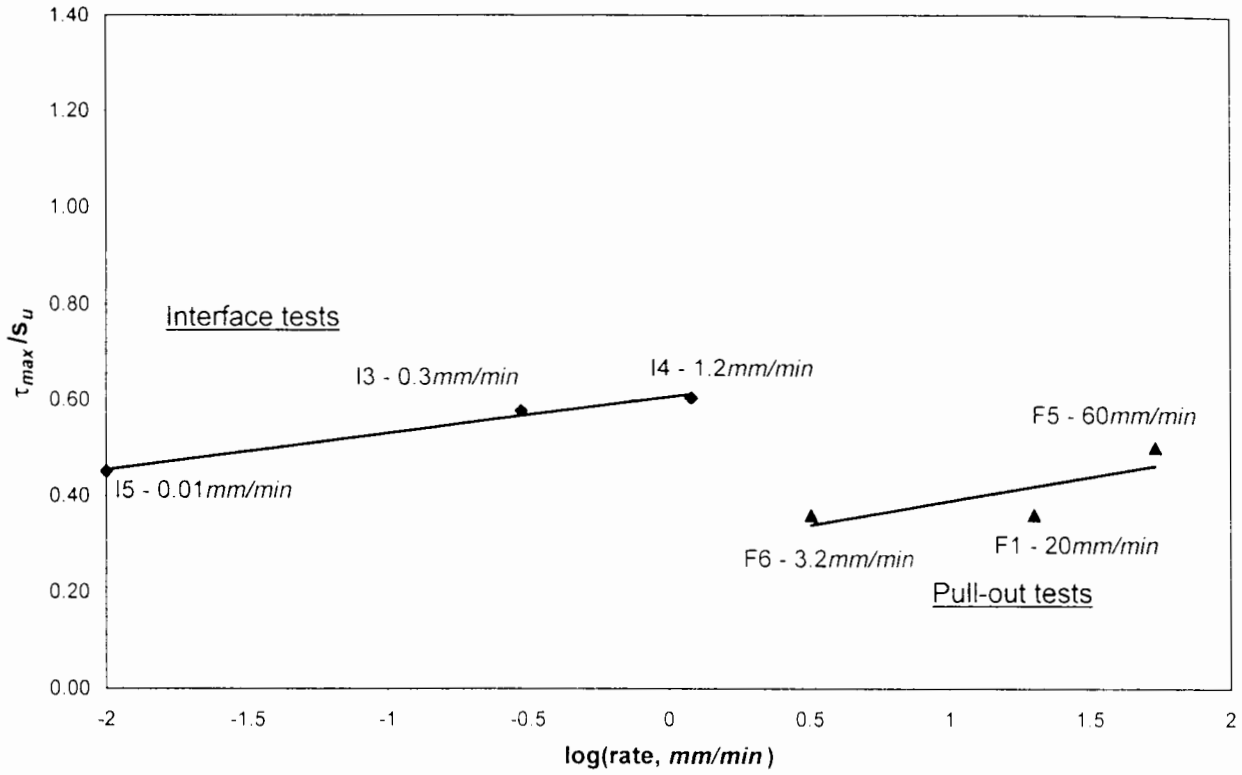

Figure 9.7 – Comparison of interface test and pull-out test results at different rates

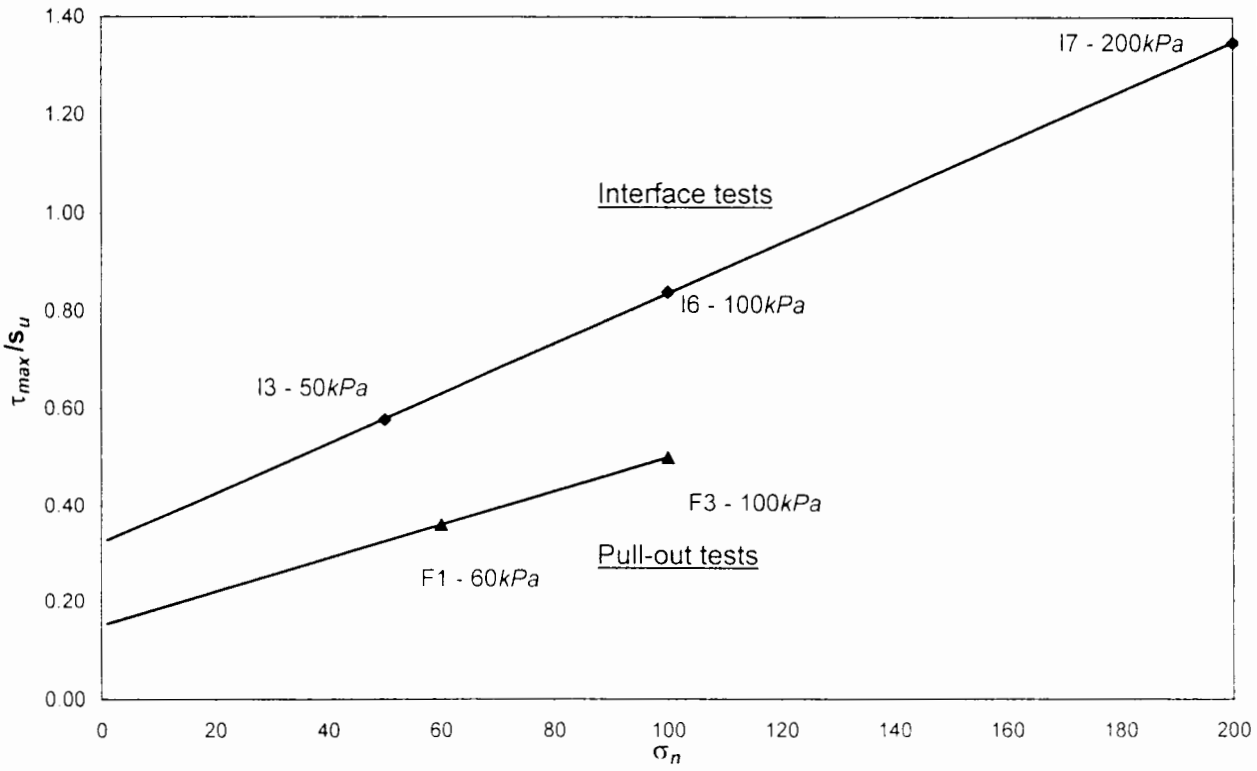

Figure 9.8 – Comparison of interface test and pull-out test results at different stresses

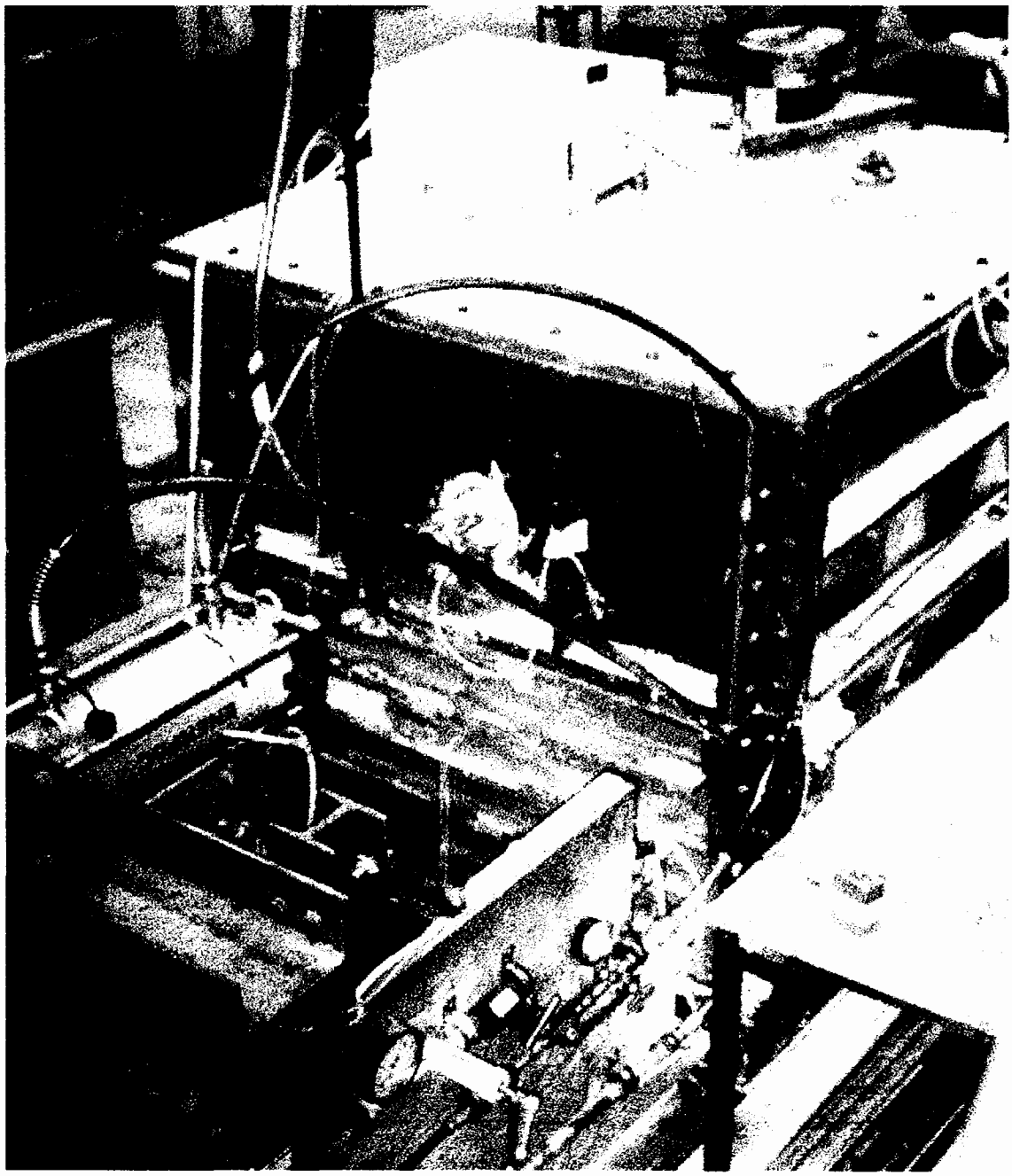

Plate 1

General view of laboratory nailing apparatus (test P5)

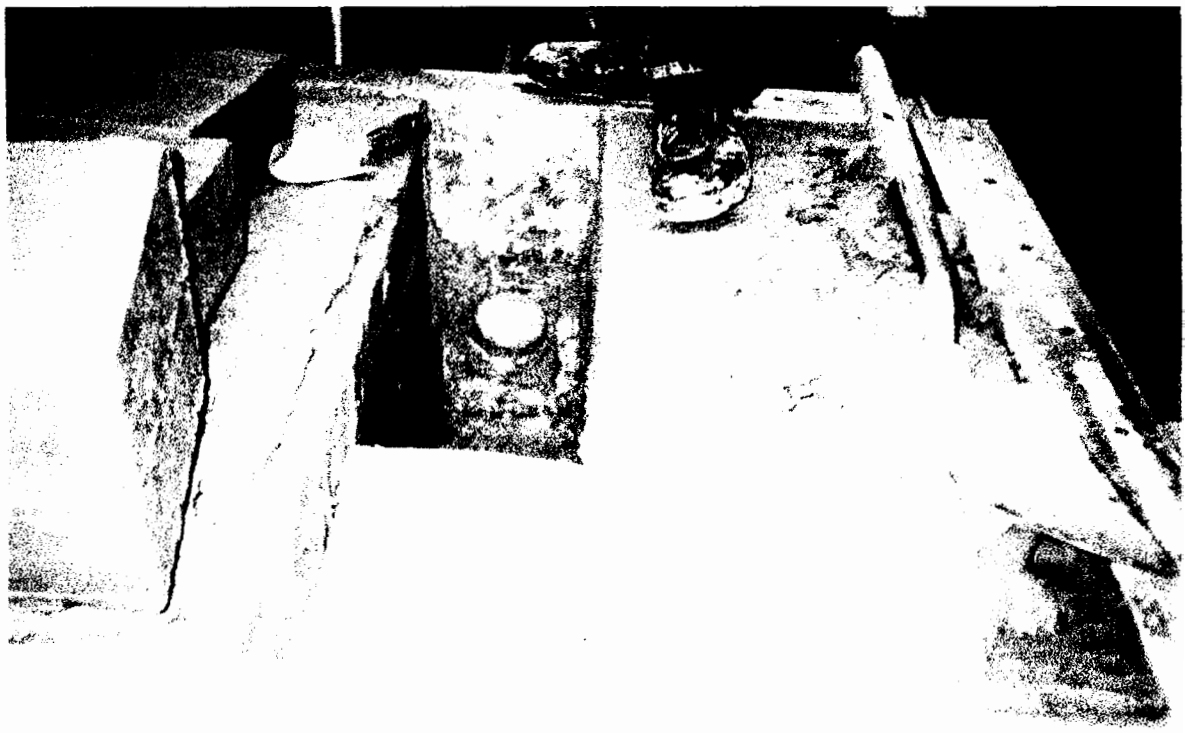

Plate 2

Excavation of trench and refilling with fresh clay blocks before each test

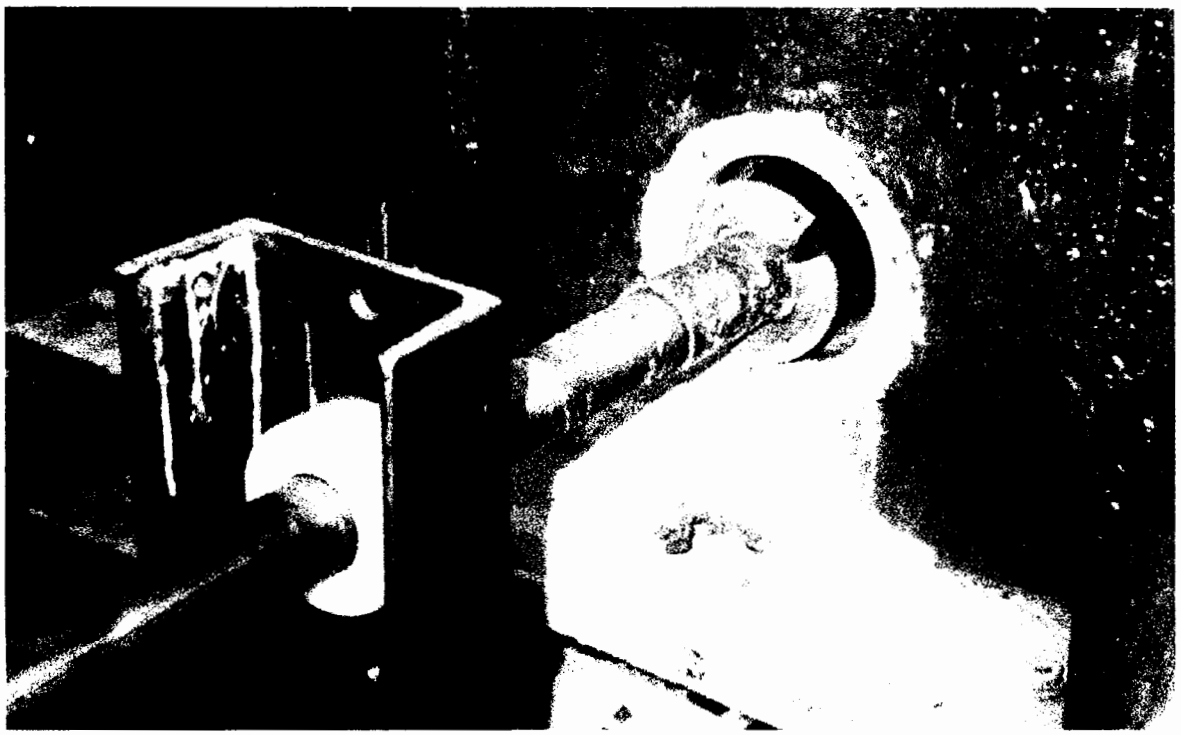

Plate 3 – Second stage drilling using 90*mm* diameter cutter

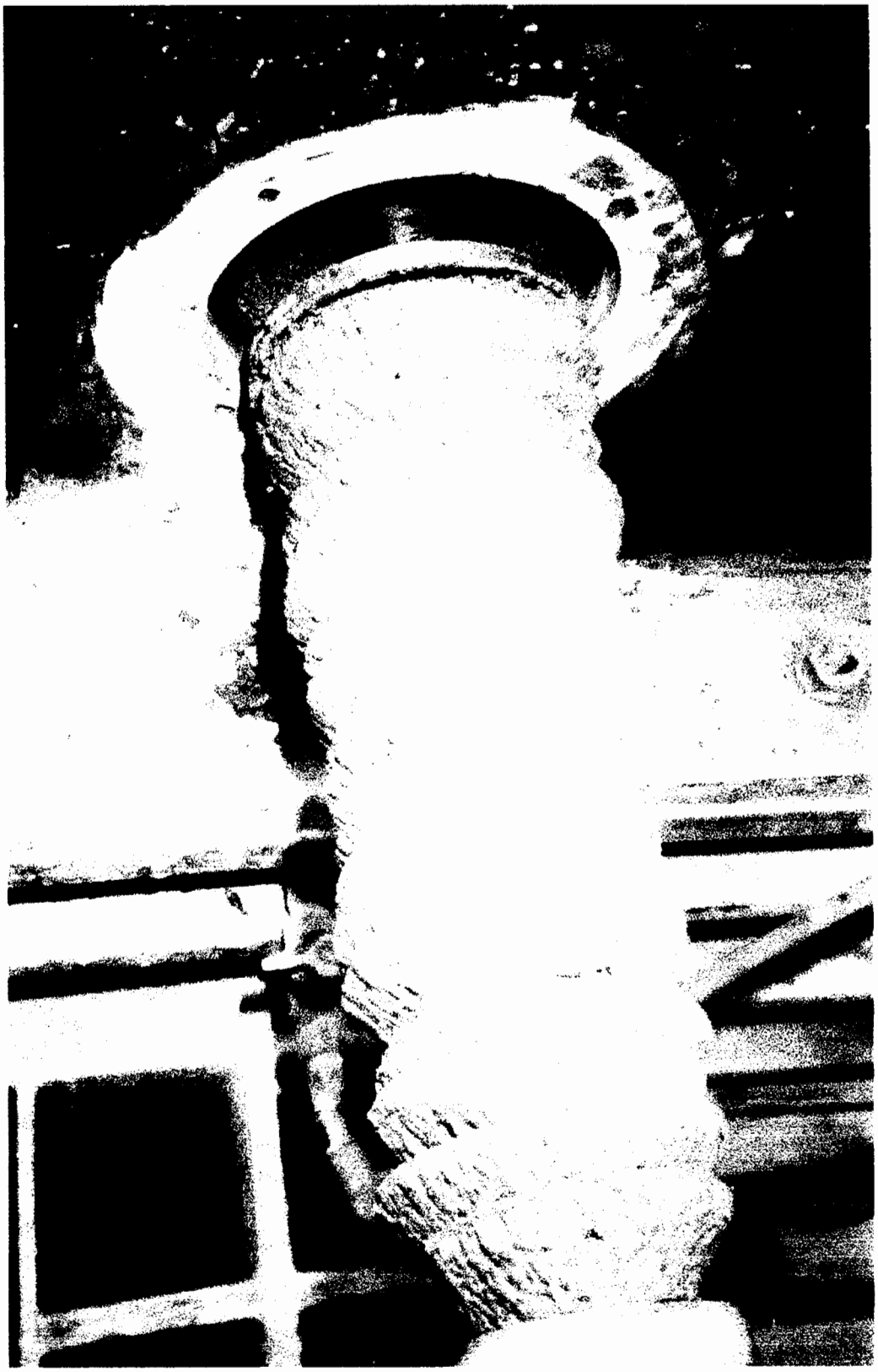

Plate 4

Overhead view of spoil removed during second stage drilling

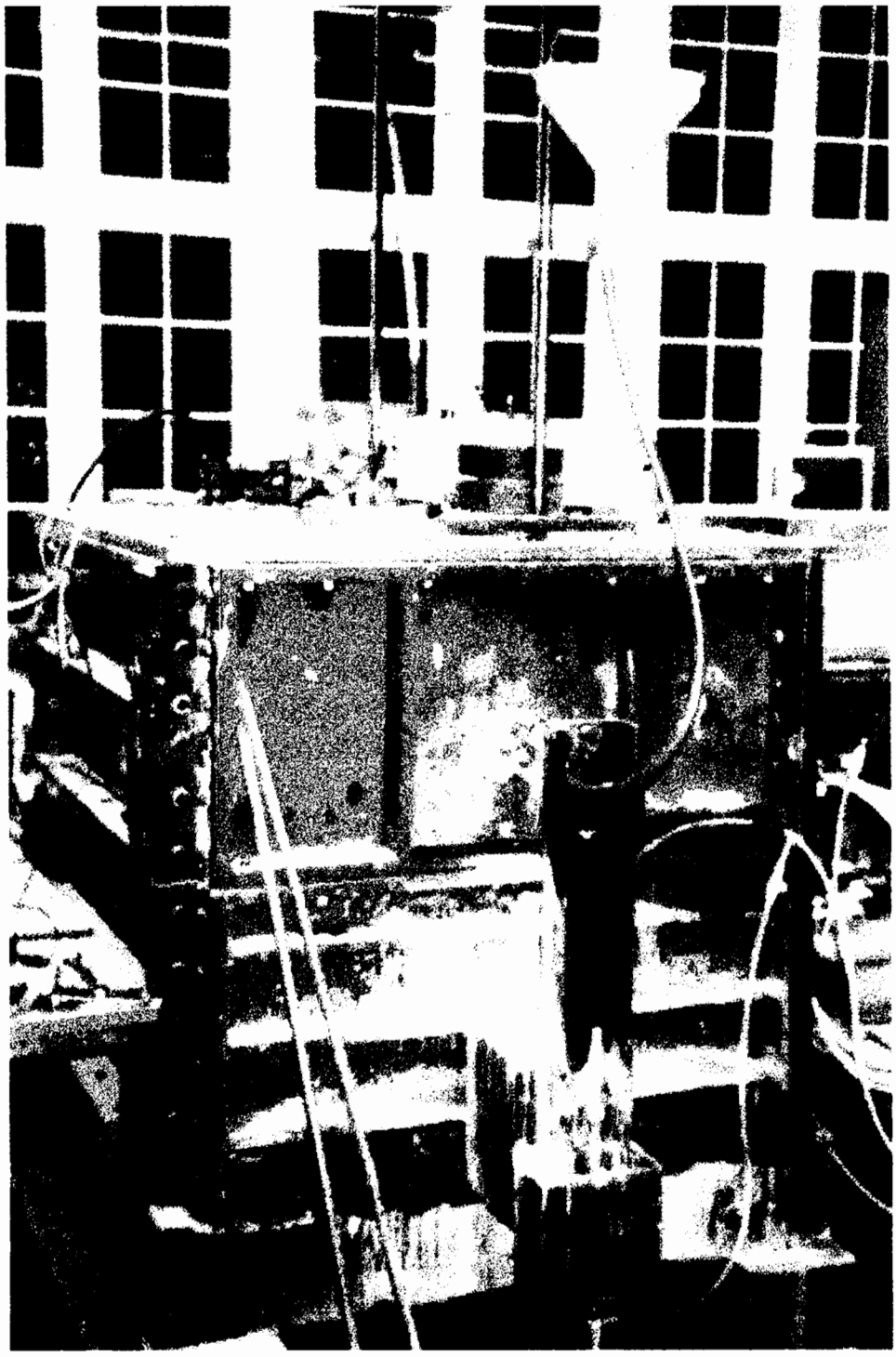

Plate 5

View of laboratory nailing apparatus during grouting (test P5)

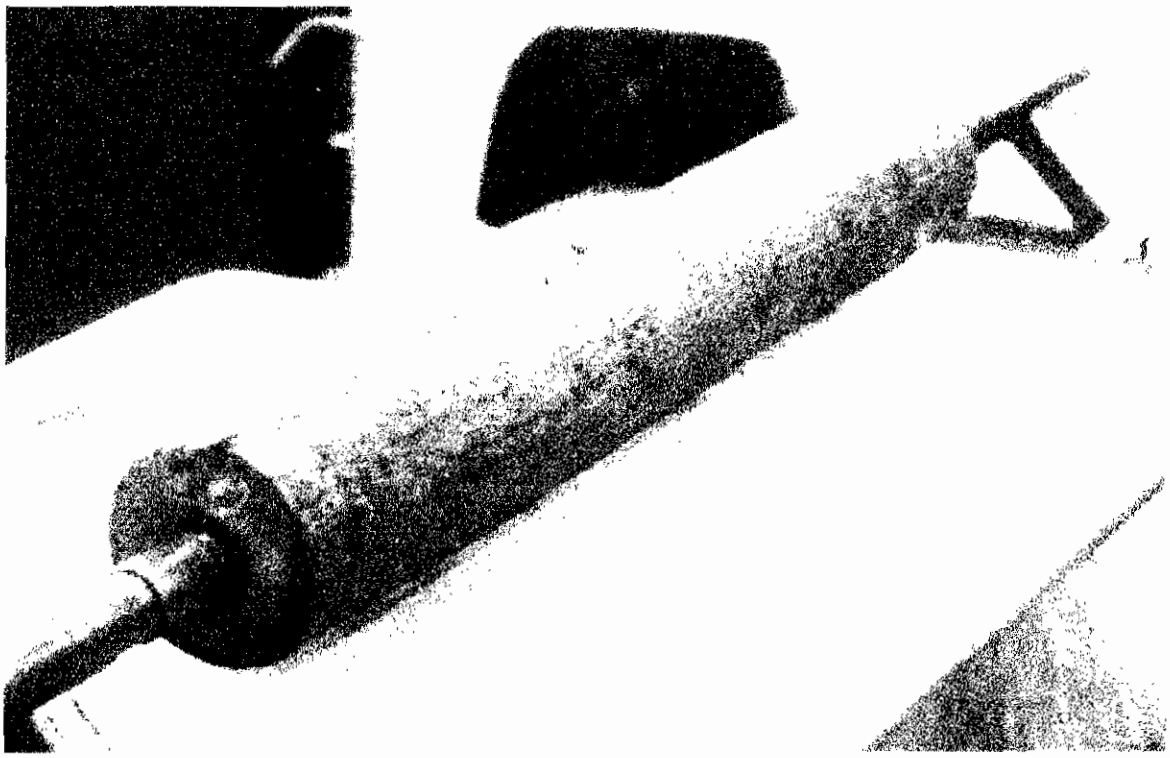

Plate 6 – Nail immediately after removal from apparatus (final test series)

Plate 7 – Nail, a few hours after exhumation